

PhD Dissertation
José Gomis Cebolla
September 2019

**Land surface temperature and evapotranspiration
estimation in the Amazon evergreen forests using
remote sensing data**

Departament de Física de la Terra i Termodinàmica

Programa de Doctorat en Teledetecció

Director: José Antonio Sobrino Rodríguez

Director: Juan Carlos Jiménez Muñoz



To my family

José A. Sobrino Rodríguez, Catedràtic de Física de la Terra, adscrit al Departament de Física de la Terra i Termodinàmica de la Facultat de Física de la Universitat de València,

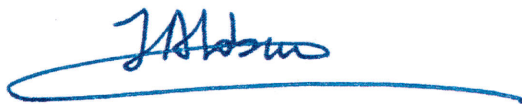
i

Juan Carlos Jiménez Muñoz, Professor titular de Física de la Terra, adscrit al Departament de Física de la Terra i Termodinàmica de la Facultat de Física de la Universitat de València,

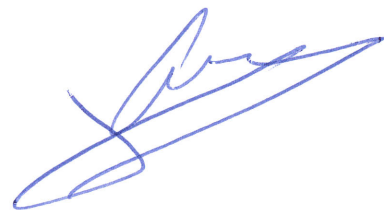
CERTIFIQUEN QUE:

dins del Programa de Doctorat en Teledetecció, José Gomis Cebolla ha realitzat sota la nostra direcció la tesi titulada “**Land surface temperature and evapotranspiration estimation in the Amazon evergreen forests using remote sensing data**”, que es presenta en aquesta memòria per tal d’optar al grau de Doctor per la Universitat de València.

I per tal que així conste a efectes oportuns, i donant el vistiplau per a la presentació d’aquest treball davant el Tribunal de tesi que corresponga, signem el present certificat a València el 17 de setembre de 2019.



José Antonio Sobrino Rodríguez



Juan Carlos Jiménez Muñoz

To perform the present doctoral thesis, the PhD student José Gomis Cebolla obtained the fellowship “Ayudas para la formación de profesorado universitario (FPU) convocatoria 2014” granted by the Ministerio de Educación y Formación Profesional. The research stay was funded by the grant “Ayudas de movilidad para estancias breves y traslados breves convocatoria 2016” from the Ministerio de Educación y Formación Profesional. The research work carried out was funded by the research projects ESP2014-52955-R, PCIN-2015-232 and ESP2017-85770-R of the Ministerio de Economía y Competitividad.

Acknowledgments

In these brief lines, I would like to express my gratitude to all the people and institutions that have been involved in the realization of this PhD dissertation.

Regarding the people, I would like to thank my PhD supervisors José Antonio Sobrino Rodríguez and Juan Carlos Jiménez Muñoz for guiding me in these first steps of my professional career. I also would like to express my gratitude to Dr. Marco Mancini and Dr. Chiara Corbari from DICA department of the University of Milan for giving me the opportunity to perform a research stay in their laboratory. I have also to thank all the colleagues of the Global Change Unit research group that have accompanied me during all these years (Guillem, Yves, Drazen, Susana and Rafa). Thank you all for the enthusiasm for science that you have transmitted me and also for the good moments.

Regarding the institutions I would like to express my gratitude to the University of Valencia particularly the Departament de Física de la Terra i Termodinàmica and the Laboratori de Processament d'Imatges. My special gratitude goes to the Ministerio de Educación y Formación Profesional for the grant received.

INDEX

Acknowledgments	iii
Index	v
List of Figures	xi
List of Tables	xx
List of Acronyms	xxvii
Resum	1
Abstract	25
Introduction	31
I Background	
1.- Cloud detection methods	43
1.1.- Cloud types and classification	45
1.2.- Review of cloud detection methods using passive remote sensing	46
1.3.- MODIS cloud mask algorithms	48
1.3.1.- MOD35	48
1.3.2.- MAIAC	49
1.4.- Reference machine learning and statistical methods for cloud detection	51
1.4.1 Naïve Bayes	51
1.4.2. Linear and Quadratic Discriminant Analysis	52
1.4.3. Random forests	53
1.4.4. Support Vector Machines	53
1.4.5. Multilayer Perceptron	56
1.5.- Probability calibration	58
2.- Land surface temperature retrieval from space	61
2.1. Radiative Transfer Equation	63
2.2. Operative LST algorithms for medium resolution sensors	67
2.2.1.- MODIS	67
2.2.1.1.- Split-window algorithm	67
2.2.1.2.- Day-Night algorithm	68

2.2.1.3.- Temperature Emissivity Separation (TES) method	69
2.2.2.- VIIRS	72
2.2.3.- SLSTR	72
2.3.- LST and LSE algorithms developed at the Global Change Unit	73
2.3.1.- Split-window algorithm (Sobrino and Raissouni (2000))	73
2.3.2.- NDVI threshold method (Sobrino et al. (2008))	74
3. Evapotranspiration retrieval from space	75
3.1.- Turbulent transport of heat and water in the atmosphere	77
3. 2.- The energy budget constraint	81
3.3.- The process of transpiration	82
3.4.- Evapotranspiration retrieval methods using remote sensing data	83
3.5.- Reference remote sensing based evapotranspiration algorithms	86
3.5.1.- PT-JPL	86
3.5.2.- PM-Mu	88
3.5.3.- SEBS	91
3.5.4.- LSASAF	94
3.6.- Observations of Evapotranspiration	97
II Data and methods	
4.- Data description	103
4.1.- Sensors	105
4.1.1.- MODIS	105
4.1.2.- VIIRS	106
4.1.3.- SLSTR	107
4.1.4.- CPR\CALIOP	108
4.2.- Reanalysis and land surface assimilation models	109
4.3.- Study area and in-situ sites	113
4.3.1.- Amazonian region	113
4.3.2.- Manacapuru site	117
4.3.3.- Tambopata site	118

4.3.4.- LBA eddy covariance network	119
5.- Data processing and methodology	125
5.1.- Cloud detection algorithm	127
5.1.1.- Collocated MODIS and CPR/CALIOP orbits	127
5.1.2.- MODIS products	130
5.1.3.- In-situ ground data	132
5.1.4.- Model training and probability calibration	133
5.1.5.- Model testing	134
5.2.- LST retrieval	137
5.2.1.- In-situ data and characterization of uncertainties	137
5.2.2.- Satellite data	141
5.2.3.- Simulations	142
5.2.3.1.- Radiative Transfer codes	143
5.2.3.2.- Atmospheric soundings	143
5.2.3.3.- Emissivity spectra	146
5.2.4.- Algorithms coefficients and sensitivity analysis	146
5.2.5.- T-based validation	148
5.2.6.- R-based validation	149
5.2.7.- Spatial patterns	150
5.3.- Evapotranspiration retrieval	151
5.3.1.- In-situ data	151
5.3.2.- Reanalysis data	153
5.3.3.- Satellite data	154
5.3.4.- Soil data and gap-filling technique	155
5.3.5.- Model configuration	157
5.3.6.- Model evaluation	159
5.3.7.- Reanalysis quality assessment	161
5.3.8.- Sensitivity analysis	162
5.3.9.- Spatial patterns comparison	164

III Results	
6.- MODIS probabilistic cloud masking	169
6.1.- Database description	171
6.2.- Database validation	173
6.3.- Image validation	175
6.4.- In-situ validation	181
6.5.- Discussion	182
7.- LST retrieval algorithm adapted to the Amazon evergreen forests	185
7.1.- Simulated database validation	187
7.2.- T-based validation	191
7.3.- R-based validation	198
7.4.- Spatial patterns	200
7.5.- Discussion	202
8.- Intercomparison of remote-sensing based evapotranspiration algorithms	205
8.1. - Forcing scenario I	207
8.1.1. Algorithm validation	207
8.1.2. Temporal evolution	212
8.2. - Forcing scenario II	214
8.2.1.- Reanalysis quality assessment	214
8.2.2.- Sensitivity analysis	215
8.2.3.- Algorithm validation	217
8.2.4.- Temporal evolution	220
8.2.5.- Spatial patterns	222
8.3.- Discussion	225
8.3.1.- Forcing scenario I	225
8.3.2.- Forcing scenario II	228
Conclusions	231
Appendices	241
References	277

LIST OF FIGURES

Figure 1.1. View of the 10 main cloud types: Cirrus (Ci), Cirrocumulus (Cc), Cirrostratus (Cs), Altocumulus (Ac), Altostratus (As), Nimbostratus (Ns), Stratus (St), Stratocumulus (Sc), Cumulus (Cu), Cumulonimbus (Cb) (<https://cloudatlas.wmo.int/useful-concepts.html>).....45

Figure 1.2. The general flowchart of MAIAC cloud mask algorithm. Here, rectangles represent separate functions, diamond shapes stand for the separate subroutines (algorithms), and round-corner rectangles indicate decision (branching) points. The letters in parentheses show spatial and temporal domains of operations at pixel- (P) and/or block- (B) level, and using the data of the last Tile (T) only or using the full time series of the Queue (Q) (Lyapustin & Wang, 2007). MODIS 1LB data granules are split into 600 km Tiles (T), which are further split into blocks (B) of 25 km x 25 km for the covariance analysis.....50

Figure 1.3. Support vector classifiers. Separable case is shown in panel a). The decision boundary is the solid line, while broken lines bound the shaded maximal margin of width $2M = 2/\|\beta\|$. Panel b) shows the non-separable (overlap) case. The points labeled ξ_j^* are on the wrong side of their margin by an amount $\xi_j^* = M\xi_j$; points on the correct side have $\xi_j^* = 0$. The margin is maximized subject to a total budget $\sum \xi_i \leq ct$. Hence $\sum \xi_j^*$ is the total distance of points on the wrong side of their margin (Hastie et al., 2005).....54

Figure 1.4. Sketch of the mapping of the Support vector machine into higher dimension. In the linearly non-separable case, Support Vector Machine maps the raw data into a higher dimension in order to increase the separability between classes (Mather, 2009).....56

Figure 1.5. Network diagram for the two layer neural network. The input, hidden and output variables are represented by nodes, and the weight parameters are represented by links between the nodes, in which the bias parameters are denoted by links coming from additional input and hidden variables x_0 and z_0 . Arrows denote the direction of information flow through the network during forward propagation (Bishop, 2006).....57

Figure 2.1. Illustration of radiative transfer equation in infrared domain. I_i and R_i are the radiance measured by the channel i at the TOA and ground level, respectively. These radiances can be expressed in terms of TOA (T_i) and ground level (T_g) brightness temperatures. Path 1 represents the radiance observed at ground level attenuated by the atmosphere. Path 2 and 3 represent the upward atmospheric thermal radiance and the upward solar diffusion radiance, respectively. Path 4 represents the radiance emitted directly by the surface. Path 5 and 6 represent the downward atmospheric thermal radiance and solar diffusion radiance reflected by the surface, respectively. Path 7 represents the direct solar radiance reflected by the surface (Li et al. (2013)).....65

- Figure 2.2.** Flow diagram of the TES algorithm in its entirety, including the NEM, RATIO, and MMD modules. Details are included in the text, including information about the refinement of ϵ_{max} (extracted from Hulley et al., 2012).....71
- Figure 3.1.** Airflow can be imagined as a horizontal flow of numerous rotating eddies, that is, turbulent vortices of various sizes, with each eddy having horizontal and vertical components (Wang & Dickinson, 2012).....77
- Figure 3.2.** Temporal evolution of a fair weather boundary layer (ABL) over land under clear sky conditions (a). Sketch of the profiles of mean wind speed, mean potential temperature and the turbulent sensible heat flux in the ABL with depth h (b). Extracted from Brutsaert, 2005 and Moene & Van Dam 2014.....78
- Figure 3.3.** Water pathway through the leaf (Taiz et al., 2015).83
- Figure 3.4.** Chronological line of selected key publications in satellite remote-sensing evapotranspiration model development (adapted from Zhang et al., 2016).....84
- Figure 4.1.** Artistic view of Terra (left) and Aqua (right) platforms.....106
- Figure 4.2.** Artistic view of the Suomi-NPP platform.....107
- Figure 4.3.** SLSTR instrument overview (left) and sketch of the instrument viewing geometry (right).....107
- Figure 4.4.** Artistic view of CloudSat and CALIPSO platforms.....108
- Figure 4.5.** A-Train configuration over time.....109
- Figure 4.6.** Map of the Amazonian evergreen broadleaf forests. The location of Tambopata (in-situ LST) station, together with LBA stations (K34, K67, K83, RJA and CAX) and Manacapuru station (in-situ cloud cover) is also displayed.....113
- Figure 4.7.** Topographic, vegetation, climate and soil conditions for the Amazon Evergreen Forests. Digital Elevation Model (DEM) was extracted from the Shuttle Radar Topography Mission (strm.csi.cgiar.org). Annual NDVI represents the mean NDVI derived from 2000-2014 MAIAC NDVI product. Air temperature (at 2m) was derived from MERRA-2 reanalysis over 2000-2006 years. Precipitation field was calculated from the Tropical Rainfall Measuring Mission (TRMM) data product from 1998-2018. Soil texture was extracted from the Harmonized Soil Word Database (FAO, 2012) according to USDA soil texture classification.....114
- Figure 4.8.** Long-term mean precipitation for January and July superimposed upon the low level (925 hPa) and upper levels (300 hPa) winds. The ITCZ in panels (a) and (b) represent the Intertropical Convergence Zone. In addition, in panel (a) the South American Convergence Zone (SACZ) together with the chaco low (L). In panel (c) Bolivian High and northeast Brazil trough are displayed by letters H and L respectively. (adapted from Garreaud et al., 2009).....116

Figure 4.9. Tambopata test site tower site (perspective from below) together with images of CNR4 net radiometer (lower left) and infrared radiometers (lower right).....	119
Figure 4.10. Monthly averages of the precipitation (blue bars), evapotranspiration (orange line) and Leaf Area Index (LAI). Precipitation and evapotranspiration were obtained from in-situ LBA observations and LAI from the MAIAC NDVI data using Fisher et al. (2008) formulation. In the case of CAX, only precipitation is displayed as there were not enough evapotranspiration observations available.....	122
Figure 5.1. SI-111 and IR120 spectral normalized response.....	138
Figure 5.2. Comparison of in-situ pyrgeometer LST against in-situ radiometer LST. LST radiometer is taken as the average between the two sensors (SI-111 and IR120). Comparison was performed at satellites time overpass.....	140
Figure 5.3. Spatial location of the atmospheric profiles. In green it is displayed the Amazon evergreen broadleaf forests. In red and black are displayed the train and test spatial points.....	144
Figure 5.4. Spectral response functions for the thermal bands of the MODIS, VIIRS and SLSTR sensors in the 8-14 μm window.....	145
Figure 5.5. Simulated daytime and nighttime databases description. Histograms for air temperature, water vapour ($w/\cos\theta$) and view zenith angle are displayed.....	145
Figure 5.6. Hourly energy balance closure for the selected LBA-sites.....	152
Figure 6.1. Histograms of the training dataset viewing conditions: (a) satellite zenith angle and (b) solar zenith angle.....	171
Figure 6.2. Violon plots of the features considered for classification: (a) clear class and (b) cloud class. Values were calculated over the training dataset.....	172
Figure 6.3. Reliability curves for model probability estimation testing: (a) GNB, (b) LDA, (c) QDA, (d) RF, (e) SVM and (f) MLP. For each model pre-calibrated results are displayed in blue and post-calibrated (denoted by iso of isotonic regression) are displayed in orange. Fraction of positives refers to the number of existent cloud instances given a probability threshold value (Mean predicted value).....	174
Figure 6.4. Clear probability estimates of DOY 5 (17:10 UTC time overpass) for the models considered: (d) GNB, (e) LDA, (f) QDA, (g) RF, (h) SVM and (i) MLP. True color image (b) and manually classified image (c) together with its location inside the swath image (a) are also displayed.....	176
Figure 6.5. Probability threshold selection for label assigning. For each model considered Kappa coefficient is calculated considering different probability thresholds values in the range of 0 to 1. MYD35 and MAIAC Kappa values are also displayed.....	177

- Figure 6.6.** Model performance (Kappa value) over each of the manually classified images (image testing dataset). Results correspond to: (a) GNB, (b) LDA, (c) QDA, (d) RF, (e) SVM and (f) MLP models. In each model subplot, model results are displayed in blue and MYD35 and MAIAC in red and green respectively. Image identification is provided in Table 6.2.....179
- Figure 6.7.** Image testing dataset derived cloud cover. Results are displayed for each model considered: (a) GNB, (b) LDA, (c) QDA, (d) RF, (e) SVM and (f) MLP. In each model subplot, cloud cover from the manually classification (REF) is displayed in orange and model, MYD35 and MAIAC in blue, red and green respectively.....179
- Figure 6.8.** Visual intercomparison of models and MYD35/MAIAC cloud masking results for doys 175_1745 (a) and 275_1725 (b). For each doy, results are displayed as follows: (i) Location, (ii) Reference manually classified image, (iii) True color image, (iv) MYD35, (v) MAIAC, (vi) GNB, (vii) LDA, (viii) QDA, (ix) RF, (x) SVM and (xi) MLP results. Cloud and clear labels are displayed in white and green respectively. Non-EBF pixels are displayed in black.....180
- Figure 7.1.** Difference between the temperature derived from the radiosounding and the temperature estimated from the simplified version of the Split-window (T_{rad} and T_{sw}) against the atmospheric path water content ($w/\cos\theta$): a) $TERRA_{DAY}$, b) $TERRA_{NIGHT}$, c) $AQUA_{DAY}$, d) $AQUA_{NIGHT}$, e) $VIIRS_{DAY}$, f) $VIIRS_{NIGHT}$, g) $SLSTR_{DAY}$ and h) $SLSTR_{NIGHT}$189
- Figure 7.2.** Difference between the temperature derived from the radiosounding and the temperature estimated from the simplified version of the Split-window (T_{rad} and T_{sw}) against the sensor view zenith angle a) $TERRA_{DAY}$, b) $TERRA_{NIGHT}$, c) $AQUA_{DAY}$, d) $AQUA_{NIGHT}$, e) $VIIRS_{DAY}$, f) $VIIRS_{NIGHT}$, g) $SLSTR_{DAY}$ and h) $SLSTR_{NIGHT}$190
- Figure 7.3.** Difference between the temperature derived from the radiosounding and the temperature estimated from the generalized version of the Split-window (T_{rad} and T_{sw}) against the atmospheric path water content ($w/\cos\theta$): a) $TERRA_{DAY}$, b) $TERRA_{NIGHT}$, c) $AQUA_{DAY}$, d) $AQUA_{NIGHT}$, e) $VIIRS_{DAY}$, f) $VIIRS_{NIGHT}$, g) $SLSTR_{DAY}$ and h) $SLSTR_{NIGHT}$191
- Figure 7.4.** Difference between the temperature derived from the radiosounding and the temperature estimated from the simplified version of the Split-window (T_{rad} and T_{sw}) against the sensor view zenith angle a) $TERRA_{DAY}$, b) $TERRA_{NIGHT}$, c) $AQUA_{DAY}$, d) $AQUA_{NIGHT}$, e) $VIIRS_{DAY}$, f) $VIIRS_{NIGHT}$, g) $SLSTR_{DAY}$ and h) $SLSTR_{NIGHT}$196

Figure 7.5. Scatterplots in in-situ radiometer LST against estimated LST for the daytime case. MODIS-SW, MODIS-TES and MODIS-DN refers to the LST as extracted from the MXD11_L2, MYD21_L2 product and MXD11C1 product. SW-sim and SW-gen refers to the simplified and generalized SW proposed. a) TERRA platform (1km) , b) AQUA platform (1km), c) TERRA platform (5km), d) AQUA platform (1km), e) VIIRS sensor and f) SLSTR sensor.....196

Figure 7.6. Scatterplots in in-situ pyrgeometer LST against estimated LST for the daytime case. MODIS-SW, MODIS-TES and MODIS-DN refers to the LST as extracted from the MXD11_L2, MYD21_L2 product and MXD11C1 product. SW-sim and SW-gen refers to the simplified and generalized SW proposed. a) TERRA platform (1km) , b) AQUA platform (1km), c) TERRA platform (5km), d) AQUA platform (1km), e) VIIRS sensor and f) SLSTR sensor.....196

Figure 7.7. Scatterplots in in-situ radiometer LST against estimated LST for the nighttime case. MODIS-SW, MODIS-TES and MODIS-DN refers to the LST as extracted from the MXD11_L2, MYD21_L2 product and MXD11C1 product. SW-sim and SW-gen refers to the simplified and generalized SW proposed. a) TERRA platform (1km) , b) AQUA platform (1km), c) TERRA platform (5km), d) AQUA platform (1km), e) VIIRS sensor and f) SLSTR sensor.....197

Figure 7.8. Scatterplots in in-situ radiometer LST against estimated LST for the nighttime case. MODIS-SW, MODIS-TES and MODIS-DN refers to the LST as extracted from the MXD11_L2, MYD21_L2 product and MXD11C1 product. SW-sim and SW-gen refers to the simplified and generalized SW proposed. a) TERRA platform (1km) , b) AQUA platform (1km), c) TERRA platform (5km), d) AQUA platform (1km), e) VIIRS sensor and f) SLSTR sensor.....197

Figure 7.9. Determination of the optimal threshold value for ΔT_{b32} ($T_{MOD32} - T_{SIM32}$). ΔT_{b32} is represented against the difference between the T_R (derived from the R-based method) and $T_{IN-SITU}$ as derived in the section 5.1.....199

Figure 7.10. Simulated R-based T_R against estimated temperature. Red cross refers to MODIS operative algorithms. Blue circle refers to the proposed SW algorithm. a) TERRA 1km, b) AQUA 1km, c) TERRA 5 km and d) AQUA 5 km. MODIS 1km algorithm is MODIS-SW and MODIS 5km algorithm is MODIS-DN. Results include mean \pm bias, correlation coefficient, N: total number of points and S: number of spatial points with data. The line 1:1 is also represented.....200

Figure 7.11. Spatial patterns of LST (left image) and Number of clear sky days (right image) for TERRA. For every panel the results are shown using rows as seasons (JFM, AMJ, JAS and OND.) and columns as cloud masks filtering (MOD35, QC and MAIAC).
.....201

- Figure 7.12.** Spatial patterns of LST (left image) and Number of clear sky days (right image) for AQUA. For every panel the results are shown using rows as seasons (JFM, AMJ, JAS and OND.) and columns as cloud masks filtering (MOD35, QC and MAIAC).....201
- Figure 7.13.** Spatial patterns of LST (left image) and Number of clear sky days (right image) for VIIRS sensor. Only confident clear pixels were considered for LST retrieval. For every panel the results are shown: JFM, AMJ, JAS and OND.....202
- Figure 8.1.** Scatterplots of model ET estimate against in-situ ET uncorrected observations. Bias, RMSE, R, and S metrics were calculated considering observations from all the stations. Metrics derived considering corrected ET values (Bowen Ratio/Energy Residual) are presented between parenthesis.....207
- Figure 8.2.** Validation of other fluxes provided by the ET models considered: a) daytime PM-Mu Rn b) nighttime PM-Mu Rn c) daytime LSASAF Rn, d) daytime LSASAF H e) SEBS H for TERRA platform, f) SEBS LE for TERRA platform, g) SEBS H for AQUA platform, h) SEBS LE for AQUA platform. Bias, RMSE, R, and S metrics were calculated considering observations from all the stations. Metrics derived considering corrected ET values (Bowen Ratio/Energy Residual) are presented between parenthesis.....210
- Figure 8.3.** Taylor diagrams for the LBA in-situ stations. Models are represented by colors and evapotranspiration corrections by shapes (triangle – ET (uncorrected ET values), square – BR (Bowen Ratio) and circle – ER (Energy Residual)).....212
- Figure 8.4.** Time series of ET model monthly mean values. In-situ ET observations are represented by the shadowed area (lower, intermediate and upper limit indicating uncorrected, BR and ER ET observations respectively).....213
- Figure 8.5.** Sobol sensitivity analysis for the models considered. Temporal resolution of model inputs is indicated by a subscript (day refers to daytime, night to nighttime and hour to hourly values at the time of satellite overpass).....216
- Figure 8.6.** Bias analysis for the models considered. Bias was calculated as the difference between perturbed values and unperturbed values. Only radiation variables being responsible of the model variability were considered for perturbation. For SEBS, SR_{inhour} was also included in the analysis.....217
- Figure 8.7.** Scatterplots of ET derived from the selected models (scenario II) against in-situ measurements considering all stations. For each model, bias, RMSE, R and S, together with the number of points available for validation are shown. Metrics derived considering Bowen Ratio/Energy Residual method are presented between parenthesis.....218
- Figure 8.8.** Taylor diagrams for individual station considering reanalysis forcing.....220

- Figure 8.9.** Time series of ET model monthly mean values for each combination (model + reanalysis) considered. In-situ ET observations are represented by the shadowed area (lower, intermediate and upper limit indicating uncorrected, BR and ER ET observations respectively).....221
- Figure 8.10.** Annual cumulative ET (year 2004) spatial patterns (deviation from the ensemble mean).....223
- Figure 8.11.** R^2 value derived from the linear regression of ET model estimates against model inputs (MERRA-forcing). Radiation inputs refer to Rn_{24} (PT-JPL and SEBS-GF) and SR_{in} (PM-Mu and LSASAF). Temperature and humidity inputs refer to T_a and ea forced at the temporal scale indicated by the models. Soil moisture refers to the root zone soil moisture for LSASAF model. Non significant values ($p < 0.05$) are displayed in black.....224
- Figure 8.12.** Temporal evolution of zonal mean values for the Amazonian region.....225

LIST OF TABLES

Table 1.1. Approximate heights of each level, and the genus occurring in each (adapted from https://cloudatlas.wmo.int/home.html).....	46
Table 1.2. MODIS cloud test executed for a given processing path: daytime ocean (DO), nighttime ocean (NO), daytime land (DL), nighttime land (NL), polar daytime (PD), polar nighttime (NP), coastal daytime (CD), coastal nighttime (CN), desert daytime (DD) and desert nighttime (DN) (Ackerman et al., 2010).....	49
Table 3.1. Summary of the existing major satellite-based evapotranspiration retrieval methods (adapted from Zhang et al., 2016).....	85
Table 3.2. Biome Properties Look-Up Table (BPLUT) for MODIS ET. ENF: evergreen needleleaf forest; EBF evergreen broadleaf forest; DNF deciduous needleleaf forest; DBF deciduous broadleaf forest; MF mixed forest; WL woody savannas; SV savannas; CSH closed shrubland; OSH open shrubland; Grass grassland, urban built-up or sparsely vegetated; Crop cropland (adapted from Mu et al. (2011)).....	91
Table 3.3. Vegetation type considered in the LSASAF algorithm and associated parameters: minimum stomatal resistance (r_{smin}), coefficient for the dependency of canopy resistance on water vapour pressure deficit (g_D) and root distribution per vegetation type in % over the four soil layers (R_k). In the case of R_k , from left to right values correspond to increasing values of depth.....	97
Table 3.4. Summary of the λE observation and estimation methods (extracted from Wang & Dickinson, 2012). * depend on measurement height above the canopy and wind speed.....	100
Table 4.1. Technical characteristics of MODIS sensor. SNR refers to signal to noise ration and NET to noise-equivalent temperature difference.....	105
Table 4.2. Technical characterization of VIIRS sensor. SNR refers to signal to noise ration and NET to noise-equivalent temperature difference.....	106
Table 4.3. Technical characterization of SLSTR sensor.....	107
Table 4.4. Technical characterization of CPR and CALIOP sensors.....	109
Table 4.5. MERRA-2 and ERA-Interim comparison table.....	111
Table 4.6. Site descriptions. Table was adapted from Gonçalves et al., 2013, Restrepo-Coupe et al., 2013 and El-Masri et al., 2013. Soil texture was extracted from the Harmonized Soil Word Database (FAO, 2012) according to USDA soil texture classification.....	123
Table 5.1. Products and layers used for reference database creation.....	129
Table 5.2. MODIS products and layers selected used in the present study.....	131
Table 5.3. Time period used for Image-testing and in-situ testing.....	131

Table 5.4. Parameter search space and optimal values for the parameters of the models that need to be optimized during the training process.....	134
Table 5.5. Confusion matrix and derived metrics for comparison of model predictions and true label predictions.....	135
Table 5.6. Testing strategy for model performance testing and comparison.....	136
Table 5.7. List of satellite products and layers selected used in this section. X can take values of O or Y, referring to MOD (TERRA platform) or MYD (AQUA platform) respectively.....	142
Table 5.8. List of validated algorithms according to the scenarios considered.....	148
Table 5.9. List of reanalysis variables according to model inputs.....	154
Table 5.10. Land surface variables derived from MODIS remote sensing data.....	155
Table 5.11. Soil moisture retention properties assigned to each HSWD texture class (extracted from Anderson et al., 2007).....	156
Table 5.12. Gap-filling process for days with no ET estimate (extracted from Anderson et al., 2007).....	157
Table 5.13. List of required data and parameters for evapotranspiration models as used in the present study. Static fields are indicated with an asterisk (*). Models were forced considering the temporal resolution indicated.....	160
Table 5.14. List of data sources and variables used in the two forcing scenarios considered.....	161
Table 5.15. List of data sources and variables used in the two forcing scenarios considered. Radiation inputs are given in W/m^2 , temperature inputs in K, humidity inputs in Pa and wind speed in m/s.....	164
Table 6.1. Confusion matrix in percentage of CPR/CALIOP and MYD35 cloud masks. CPR/CALIOP is used as reference data. Results are calculated over the training dataset.....	173
Table 6.2. Test overall accuracy and Kappa coefficient metrics for the classifiers considered. The training and testing computational cost is also presented.....	175
Table 6.3. Probability threshold selected together with its associated Kappa value for the models considered. Computational cost at image level is also presented. MYD35 and MAIAC Kappa values are also provided.....	177
Table 6.4. Model performance (Kappa coefficient and OA metrics) under three different view zenith angle (vza) ranges.....	178

Table 6.5. In-situ testing results of MYD35, MAIAC, GNB, LDA, QDA, RF, SVM and MLP algorithms. Results are presented using confusion matrices together with OA and Kappa coefficient values. Samples in confusion matrices represent available days (i.e. for each day a prediction of clear/cloud in the station is obtained).....	181
Table 7.1. Coefficients of the split-window for MODIS (TERRA and AQUA platforms), VIIRS and SLSTR cases. Both daytime and nighttime values are presented. In addition, individual contributions to the total uncertainty in LST are also given: standard error of the algorithm (δ_{alg}), uncertainty due to the Noise Equivalent Delta Temperature ($\delta_{NE\Delta T}$), contribution of the uncertainty in the emissivity (δ_{ϵ}) and contribution of the uncertainty in the total atmospheric water vapour (δ_w). Uncertainties of 0.1 K, 0.01 and 0.5 cm for brightness temperatures, emissivity and water vapour have been considered, respectively.....	188
Table 7.2. Validation of the generalized and simplified split-window algorithms for the independent simulated dataset. Subscripts gen and simpl refers to the generalized and simplified versions of the algorithms.....	189
Table 7.3 . Daytime validation results of the LST algorithms considered in this study at Tambopata in-situ station. Metrics presented correspond to the bias, standard deviation and RMSE value together with the correlation coefficient and the number of points used to perform the validation. Validation is performed separately for the radiometer and pyrgeometer. In bold, it is highlighted the best performing algorithm for each sensor.....	194
Table 7.4 . Nighttime validation results of the LST algorithms considered in this study at Tambopata in-situ station. Metrics presented correspond to the bias, standard deviation and RMSE value together with the correlation coefficient and the number of points used to perform the validation. Validation is performed separately for the radiometer and pyrgeometer. In bold, it is highlighted the best performing algorithm for each sensor.....	195
Table 7.5. Error metrics derived from the comparison of in situ LST against reference LST obtained with the R-based method over the Tambopata test site considering a threshold of $-0.2K < \Delta T_{b32} < 0.4K$. RMSE: Root Mean Square Error, MAE: N: number of data points.....	199
Table 8.1. Bias, RMSE, correlation coefficient (R), Taylor skill score (S) metrics together with the number of available points (N) for the individual station validation. Values refer to the mean value \pm standard deviation of the validation values from the uncorrected case and the Bowen Ratio and Energy Residual case.....	211
Table 8.2. Bias, RMSE and R values derived from the comparison of in-situ inputs against reanalysis inputs. The temporal resolution of the inputs is indicated by a subscript (day refers to daytime, night to nighttime and hour to hourly values at the time of satellite overpass).....	215

Table 8.3. Bias, RMSE, correlation coefficient (R), Taylor skill score (S) metrics together with the number of available points (N) for the individual station validation (scenario II). Values refer to the mean value of the validation values from the uncorrected case and the Bowen Ratio and Energy Residual case.....	219
---	-----

LIST OF ACRONYMS

20CR	20 century reanalysis
3D-VAR	Three-dimensional variational analysis
4D-VAR	Four-dimensional variational analysis
AATSR	Advanced Along-Track Scanning Radiometer
ABL	Atmospheric Boundary Layer
ACCA	Automated Cloud-Cover Assessment
AFRL	Air Force Research Laboratory
AMF-1	ARM Mobile Facility One
ANOVA	Analysis of variance
APAR	Absorbed PAR
ARM	Atmospheric Radiation Measurement
ASL	Atmospheric Surface Layer
ASTER	Advanced Spaceborne Thermal Emission and Reflection Radiometer
AVHRR	Advanced Very High Resolution Radiometer
BAS	Bulk Atmospheric Boundary Layer Similary
BR	Bowen Ratio
BRDF	Bidirectional reflectance distribution function
CALIOP	Cloud Aerosol Lidar with Orthogonal Polarization
CALIPSO	Cloud-Aerosol Lidar and Infrared Pathfinder Satellite Observation
CAX	Caxiuana LBA station
CCSM	Community Climate System Model
CFSR	Climate Forecast System Reanalysis
CLM	Community Land Model
CPR	Cloud Profiling Radar
DEM	Digital Elevation Model
DN	Day-Night
EC	Eddy-covariance
ECMWF	European Centre for Medium-range Weather Forecasts
EDR	Environmental Data Record
ENSO	El-Niño-Southern-Oscillation

EO	Earth Observation
ER	Energy Residual
ERA	ECMWF ReAnalysis
ET	Evapotranspiration
EVI	Enhanced Vegetation Index
FAO	Food Agriculture Organization
GCU	Global Change Unit
GLDAS	Global Land Assimilation System
GNB	Gaussian Naïve Bayes
HSWD	Harmonized Soil Word Database
IFS	Integrated Forecast System
IGBP	International Geosphere-Biosphere Programme
IPAR	Intercepted PAR
ISLSCP	International Satellite Land-Surface Climatology Project
ITCZ	Intertropical convergence zone
JHU	Johns Hopkins University
JPL	Jet Propulsion Laboratory
JPSS	Joint Polar Satellite System
JRA-25	Japanese 25-year ReAnalysis
K34	Manaus kilometre 34 LBA station
K67	Santarem kilometre 67 LBA station
K83	Santarem kilometre 83 LBA station
LAI	Leaf Area Index
LBA	Large-Scale Biosphere-Atmosphere Experiment
LDA	Linear Discriminant Analysis
LIS	Land Information System
LSASAF	Satellite Application Facility on Land Surface Analysis
LSE	Land Surface Emissivity
LSM	land surface model
LST	Land Surface Temperature

MAIAC	Multi-Angle Implementation of the Atmospheric Correction
MAOS	ARM Mobile Aerosol Observing System
MERRA-2	Modern-Era Retrospective analysis for Research and Application
MIR	Middle-Infrared-Spectrum
MLP	Multilayer Perceptron
MMD	Maximum–minimum apparent emissivity difference method
MODIS	Moderate Resolution Imaging Spectroradiometer
MODTRAN	MODerate resolution atmospheric TRANsmission
MOS	Monin-Obukhov Similarity
MOST	Monin-Obukhov similarity theory
MSI	MultiSpectral Instrument
NASA	National Aeronautics and Space Administration
NASA/DAO	NASA data assimilation office
NCAR	National Center for Atmospheric Research
NCEP	National Centers for Environmental Prediction
NDVI	Normalized Difference Vegetation Index
NDVI^{THM}	NDVI Threshold method
NEM	Normalization emissivity method
NIR	Near Infrared spectrum
NOAA	National Oceanic and Atmospheric Administration
NSIDC	National Snow and Ice Data Center
NWP	Numerical Weather Prediction model
PAR	Photosynthesis Active Radiation
PDO	Pacific Decadal Oscillation
PET	Potential evapotranspiration
PM-Mu	Penman-Monteith MODIS operative parametrization
PT-JPL	Priestley-Taylor Jet Propulsion Laboratory
QDA	Quadratic Discriminant Analysis
RF	Random Forests
RH	Relative Humidity

RJA	Reserva Jarú LBA station
RMSE	Root Mean Square Error
RTE	Radiative Transfer Equation
RTM	Radiative Transfer Model
RVI	Ratio vegetation index
SACZ	South Atlantic Convergence Zone
SASM	South American Monsoon System
SAVI	Soil Adjusted Vegetation Index
SEBS	Surface Energy Balance System
SEVIRI	Spinning Enhanced Visible and InfraRed
SLSTR	Sea and Land Surface Temperature Radiometer
SR	Spectral ratio
SSI	Spectral Sciences, Inc.
SST	Sea Surface Temperature
SVAT	Soil Vegetation Atmosphere Transfer
SVM	Support Vector Machine
SW	Split-Window
TES	Temperature-Emissivity-Separation
TIR	Thermal Infrared spectrum
TOA	Top-of-Atmosphere
TRMM	Tropical Rainfall Measuring Mission
USDA	United States Department of Agriculture
USGS	United States Geological Survey
VIC	Variable Infiltration Capacity model
VIIRS	Visible Infrared Imaging Radiometer Suite Sensor
VIS	Visible spectrum
VPD	vapour pressure deficit
VZA	View zenith angle
WMO	World Meteorological Organization
WV	Water vapour

RESUM

Introducció

Els boscos amazònics, representen el 40% de la superfície forestal tropical global (Aragão et al., 2014). Contenen al voltant d'una quarta part de les espècies terrestres del món (Dirzo & Raven, 2003) i produeixen el 15% de la fotosíntesi global (Malhi, 2008). Addicionalment, juguen un paper important en el cicle hidrològic de la regió (Marengo et al., 2018).

Tenint en compte la importància d'aquest ecosistema juntament amb la situació actual d'escalfament global, el seguiment dels possibles canvis efectuats en aquests boscos és d'especial importància. L'ús d'imatges de satèl·lits es presenta com una via atractiva per tal d'acomplir aquest objectiu. En particular, el sensor Moderate Resolution Imaging Spectroradiometer (MODIS) a bord dels satèl·lits TERRA i AQUA es troba entre les principals eines actuals per al seguiment d'aquesta regió (Jiménez-Muñoz et al., 2015). L'ús de dades de teledetecció en aquesta regió, no obstant presenta una sèrie de limitacions entre les que destaca l'efecte de la possible contaminació per núvols introduïda per una deficient detecció d'aquests. Entre les variables que es poden utilitzar per al seguiment d'aquests boscos (i que poden ser estimades mitjançant dades de teledetecció) destaquen la temperatura de la vegetació i l'evapotranspiració. La temperatura de vegetació està directament relacionada amb la fisiologia vegetal. A més, alguns estudis han demostrat la relació existent entre aquesta variable i la capacitat d'absorció de CO₂ i la pèrdua de biomassa d'aquests boscos. Per un altra banda, l'evapotranspiració connecta els intercanvis d'aigua, carboni i energia superficial d'aquests boscos. Com respondrà aquesta variable al canvi del clima és fonamental per entendre l'estabilitat d'aquests boscos (Cox et al., 2000).

Arran de la importància dels temes esmentats prèviament, les activitats de recerca realitzades durant aquest període de doctorat es poden agrupar en tres **objectius principals**:

- I. Detecció dels núvols mitjançant mètodes basats en l'aprenentatge màquina.
- II. Estimació i validació de temperatura de la superfície terrestre (TST) per a diferents sensors de resolució mitjana.
- III. Estimació de l'evapotranspiració a partir de diferents models de teledetecció.

Cal destacar ací que els objectius I i II s'han centrat en l'ús de dades del sensor MODIS, en canvi l'objectiu II ha sigut expandit a altres dos sensors: Visible Infrared Imaging Radiometer Suite (VIIRS) i Sea and Land Surface Temperature Radiometer (SLSTR).

Per tal d'assolir els objectius esmentats anteriorment, aquesta tesi s'ha estructurat en tres parts diferents: introducció teòrica o background (part I), dades i mètodes (part II) i resultats (part III). A continuació es presenta un breu resum d'aquestes parts.

I. Introducció teòrica

1. Mètodes de detecció de núvols

En aquest capítol ens hem centrat en descriure l'estat de l'art dels mètodes de detecció de núvols en imatges de satèl·lit. Per una part trobem els mètodes de base física (Ackerman et al., 1998; Irish et al., 2000, 2006; Zhu & Woodcock 2012; Godin, 2014). I per altra banda, trobem els mètodes de base estadística (o d'aprenentatge màquina) entre els quals podem destacar els següents treballs: Gomez-Chova et al. (2007), Amato et al. (2008), Ricciardelli et al. (2008), Heidinger et al. (2012), Ishida et al. (2018), Chen et al. (2018), Chai et al. (2019).

Pel que fa al sensor MODIS, les màscares de núvols de referència són MOD35 (Ackerman et al., 1998) i MAIAC (Lyapustin et al., 2008). Aquests es poden classificar dins del primer grup. No obstant MAIAC, es beneficia de l'ús d'informació temporal (Lyapustin et al., 2008). Apart d'aquests algorismes, en el present treball també s'ha considerat l'ús dels següents algorismes: Gaussian Naïve Bayes (GNB), Linear Discriminant Analysis (LDA), Quadratic Discriminant Analysis (QDA), Random Forests (RF), Support Vector Machines (SVM) i Multilayer Perceptron (MLP). La formulació teòrica d'aquests mètodes es presenta en la secció 1.4. Addicionalment, també es descriu els algorismes de calibratge de probabilitat emprats: el mètode de Platt (Platt, 1999) i la regressió isotònica (Zadrozny & Elkan, 2001-2002).

2. Estimació de la TST des de satèl·lit

En aquest capítol, ens hem centrat en descriure els algorismes utilitzats en els productes de temperatura dels sensors MODIS, VIIRS i SLSTR. Pel que fa a MODIS existeixen 3 algorismes diferents: l'algoritme Split-window (Wan & Dozier, 1996), l'algoritme dia-nit (Wan & Li, 1997) i l'algoritme Temperature-Emissivity-Separation (TES) (Hulley et al., 2012). Aquests corresponen als productes: MOD11A1, MOD11C1 i MOD21 respectivament. Addicionalment, també es presenta l'algoritme Split-Window (SW) d'estimació de temperatura utilitzat. Aquest ha sigut desenvolupat en el grup de recerca Unitat de Canvi Global i correspon a la formulació matemàtica de Sobrino & Raissouni (2000). Aquest es tracta d'un algoritme de tipus SW, que relaciona la TST amb la temperatura de brillantor i l'emissivitat de les bandes 11 μ m i 12 μ m. Els diferents coeficients han sigut obtinguts a partir de simulacions.

3. Estimació de l'evapotranspiració des de satèl·lit

En aquest capítol, ens hem centrat en descriure els processos que es produeixen en la capa superficial de l'atmosfera. Dins d'aquesta, el transport de calor, aigua (massa) i impuls entre diferents nivells de l'atmosfera pot ser descrit mitjançant la teoria K (Brustaert, 1982). Aquesta permet obtenir les expressions dels perfils de vent, temperatura i vapor

d'aigua de l'aire en condicions estables (Equacions 3.8-3.10) i inestables (Equacions 3.14-3.16). Addicionalment, també ens hem centrat en descriure breument l'estat de l'art de l'estimació de l'evapotranspiració des de satèl·lit. Entre els algorismes existents trobem: els mètodes residuals (1 font o 2 fonts), els mètodes contextuals, els mètodes Penman-Monteith i Priestley-Taylor, els mètodes empírics i altres mètodes que fan ús del balanç hídric o de la vinculació amb el balanç del carboni. A més a més, la formulació matemàtica dels algorismes seleccionats es presenta també en aquest capítol. Aquests en són quatre: Priestley-Taylor Jet Propulsion Laboratory (PT-JPL), ii) Penman-Monteith MODIS (PM-Mu), iii) Surface Energy Balance System (SEBS), i iv) Satellite Application Facility on Land Surface Analysis (LSASAF).

II. Dades i mètodes

4. Dades

4.1. - Sensors

Les dades de teledetecció utilitzades en aquesta tesi provenen dels sensors MODIS, VIIRS, SLSTR. Aquests es tracten de sensors passius a bord de satèl·lits d'òrbita polar. En les Taules 4.1-4.3 es presenten les característiques tècniques d'aquests incloent la resolució temporal, radiomètrica, espacial i espectral. Addicionalment, per al primer objectiu del treball també s'han utilitzat dades dels sensors Cloud Profiling radar (CPR) que es tracta d'un radar de 94 Hz i Cloud-Aerosol Lidar with Orthogonal Polarization (CALIOP) que es tracta d'un lidar operant en les longituds de 532 nm i 1064 nm. A la Taula 4.4 es detallen les característiques tècniques d'aquests dos sensors.

4.2. – Reanàlisis meteorològics

Entre les dades meteorològiques utilitzades en aquesta tesi estan les dels reanàlisis MERRA-2 (Bosilovich et al., 2015; Gelaro et al., 2017), ERA-Interim (Berrisford et al., 2009; Dee et al., 2011) així com les del Global Land Assimilation system (GLDAS-2.1) (Rodell et al., 2004). Descripcions tècniques d'aquests es presenten en la Taula 4.5. MERRA-2 proporciona dades a escala horaria amb una resolució espacial de $0,5^{\circ} \times 0,65^{\circ}$ mentre que ERA-Interim i GLDAS-2.1 proporcionen dades a escala tres hores amb una resolució espacial de $0,75^{\circ} \times 0,75^{\circ}$ i $0,25^{\circ} \times 0,25^{\circ}$ respectivament.

4.3.- Regió d'estudi i estacions in-situ

4.3.1.- Regió amazònica

En la Figura 4.6, es mostren els boscos tropicals de l'Amazones tal i com han sigut definits en aquest estudi. En la Figura 4.7 es presenta una descripció de les característiques de la regió: topografia, vegetació, temperatura anual mitjana, precipitació anual i caracterització dels sòls. Tal i com es pot observar, en termes generals es tracta d'una regió relativament plana (exceptuant els Andes) amb un clima càlid i humit amb vegetació verda i abundant.

4.3.2.- Estació de Manacapuru

Les mesures in-situ utilitzades per a la validació dels resultats dels núvols pertanyen a l'Amazon Green Ocean (GoAmazon2014 / 5) Experiment realitzat des del gener del 2014 fins al 31 de desembre del 2015. De les diferents estacions de mesura, s'han utilitzat dades de l'instal·lació T3 (3.2130°S, 60.5981° W). En particular, s'ha fet ús de les dades de l'instrument total Sky Imager (TSI-880). Aquest és un sistema automatitzat d'imatges del cel a tot color que proporciona el processament i visualització en temps real de les condicions de cel durant el dia. Les especificacions del sensor es troben en l'apèndix A.1.

4.3.3.- Estació de Tambopata

L'estació de Tambopata (12.832 S, 69.282 W) es troba situada a l'Amazònia peruana (Madre de Dios, Perú). Aquest lloc té una elevació d'uns 225 metres sobre el nivell del mar. Té una precipitació anual de 2580 mm / any i la temperatura mitjana anual és d'uns 299.2 K. L'estació està situada en una zona homogènia caracteritzada per un bosc tropical dens. La instrumentació de l'estació consta de dos radiòmetres infrarojos (SI-111 i IR120) i un radiòmetre net CNR4 (Figura 4.9). Els 3 sensors s'integren directament al cos de l'instrument. Per obtenir una descripció detallada de les especificacions tècniques del sensor, consulteu l'apèndix A.1.

4.3.4.- Xarxa d'estacions LBA

Les dades d'evapotranspiració foren obtingudes del programa Large-Biosphere-Atmosphere (LBA). Durant aquest es va establir una xarxa de torres de fluxos turbulents a l'entorn de l'Amazònia brasilera (Saleska et al., 2013). En la present dissertació, vàrem utilitzar dades de cinc estacions (Figura 4.6, Taula 4.6): K34, K67, K83, CAX i RJA. Per a una descripció de la instrumentació en cada estació consulteu l'apèndix A.1. En la

Figura 4.10 es mostra l'evolució mensual de la vegetació, evapotranspiració i precipitació.

5. Metodologia

5.1.- Algoritme de detecció de núvols

5.1.1.- Òrbites MODIS i CPR/CALIOP

Per tal de generar la base de dades de referència que servirà per tal d'entrenar els models estadístics s'han utilitzat els següents productes CloudSat: 2B-CLDCLASS-LIDAR, MODIS-AUX, 2B-GEOPROF i 2B-FLXHR-LIDAR. A la Taula 5.1 es presenten les capes seleccionades dels diferents productes. Per a cada producte, es van descarregar un total de 1002 òrbites referents al període temporal de 2007 i l'extensió geogràfica de 80°W-45°W, 10°N-20°S. Per tal d'eliminar totes aquelles dades que no foren vàlides s'aplica el següent processament: 1) eliminació dels píxels de mar, 2) eliminació dels píxels nocturns i píxels que no correspongueren a la classe "Evergreen Broadleaf Forest" i 3) eliminació dels píxels no vàlids. Després del processament inicial, la base de dades resulta en un total de 477.415 mostres. Aquestes tenen associades una etiqueta (núvol o no-núvol) i les 7 característiques considerades per a la discriminació dels núvols. Aquestes són: B1, B3, B4, B7, B26, $(B2-B1) / (B1 + B2)$ i $B2 / B1$. On els números fan referència a les bandes de MODIS. Finalment, la base de dades es va dividir aleatòriament en dos conjunts diferenciats de dades (tren i test). Es va utilitzar una proporció 2/3 i 1/3 respectivament.

5.1.2- Productes MODIS

En la Taula 5.2 es presenten productes MODIS a nivell d'imatge considerats a l'estudi. També es mostren les capes seleccionades. Aquest productes s'utilitzaren en la validació a nivell d'imatge i a nivell in-situ. Per al primer cas, tan sols s'utilitzaren 20 imatges referents a l'any 2014 (és a dir 20 dies). Es mostren en la Taula 5.3. Aquestes tenen com a objectiu generar una base de referència d'imatges que pogués servir per validar els diferents algoritmes considerats així com els productes oficials. Açò es va aconseguir mitjançant la classificació manual de les imatges. Aquesta fou realitzada amb el software ENVI.

5.1.3- Dades in-situ

Hem utilitzat el producte maotsiskycoverM1.b1. Aquest proporciona el percentatge de núvols opacs i prims que hi ha a les imatges enregistrades. Es va obtenir una fracció total del núvol sumant aquests dos percentatges. Per tenir en compte les diferents resolucions espacials i temporals, es va fer la mitjana de les mesures de fracció de núvol in situ durant els 5 minuts de durada del pas de satèl·lit MODIS. Per discriminar les ocurrencies de no-núvol de les de núvol es va considerar un llindar del 25% de la fracció de núvol (no-núvol $<25\%$ i núvol $\geq 25\%$). Aquest valor de llindar fou seleccionat per no restringir completament els casos de no-núvol.

5.1.4. – Aprenentatge dels models i calibratge de la probabilitat

El conjunt de dades de train va ser dividit en dos conjunts diferents (train + calibration) amb la finalitat de no crear un biaix en els models. La mateixa proporció 2/3 i 1/3 fou considerada. Les bases de dades resultants estan compostes per un total de 214311 mostres per a train i 105557 per a calibration. L'aprenentatge (train) per als models GNB, LDA i QDA consisteix en estimar els paràmetres requerits a partir del conjunt de dades. En el cas de RF, SVM i MLP els diferents paràmetres involucrats han de ser optimitzats. Per a cada model, es van provar diferents combinacions de paràmetres i es va seleccionar la millor combinació mitjançant una validació creuada (5-K fold). Els paràmetres podien variar d'acord amb l'espai de paràmetres pre-definit en la Taula 5.4. El calibratge de la probabilitat proporcionada pels models es va validar mitjançant el sub-conjunt de dades de calibration. Es va considerar per a tal fi una regressió isotònica (Zadrozny & Elkan 2002–2001). Per tal d'implementar aquesta metodologia es va utilitzar el paquet de Python Sklearn (Pedregosa et al., 2011).

5.1.5- Validació dels models

L'avaluació dels models es va realitzar mitjançant matrius de confusió i estadístics derivats (precisió global (OA) i el coeficient Kappa). Addicionalment, els models també foren avaluats en termes del cost computacional associat (diferència de temps entre inici i final del càlcul). Per a tal fi, es va servir un ordinador amb 8 GB de RAM i un processador Intel Core i3-6100. L'avaluació de les probabilitats estimades s'ha realitzat mitjançant corbes de fiabilitat (reliability curves). La metodologia emprada per a la validació dels models s'agrupa en tres blocs. En el primer, la validació es va realitzar sobre el conjunt de dades test. Addicionalment, també s'avaluaren les probabilitats. En el segon bloc, la validació es va realitzar sobre les 20 imatges classificades manualment. Per tal d'assignar prediccions (dels model obtenim valors continus de probabilitat) el valor llindar emprat va ser optimitzat a partir de la base de dades. A més a més, en aquest bloc

també es va procedir a la comparació dels resultats amb les màscares de referència de MODIS (MYD35 i MAIAC). En el tercer bloc, els resultats dels models i les màscares MODIS foren validats utilitzant les dades in-situ.

5.2.- Estimació de la TST

5.2.1.- Dades in-situ i caracterització de la incertesa

Pel que fa als dos radiòmetres la TST ha sigut obtinguda a partir de l'Equació 5.4. En aquesta el valor de l'emissivitat ϵ_λ s'ha pres igual a 0.99 i la radiància descendent L_λ^\downarrow s'ha obtingut a partir de simulacions MODTRAN utilitzant perfils atmosfèrics com a input. Per a la validació, es va considerar la mitjana del valor proporcionat per ambdós sensors. Una estimació de les diferents contribucions de la incertesa dels valors in-situ de la TST va proporcionar un valor de 0.5 K (<1K). Pel que fa al pirogeòmetre la LST va ser calculada mitjançant l'Equació 5.5. La incertesa d'aquesta mesura va ser obtinguda mitjançant un càlcul d'errors d'acord amb l'Equació 5.6. La incertesa ve determinada per la pròpia incertesa de l'instrument proporcionada pel fabricant. Finalment, a partir de la comparació amb els valors de TST dels radiòmetres es va assumir un valor de 0.8 K (<1K).

5.2.2.- Dades de satèl·lit

En la Taula 5.7 es presenta la llista de productes MODIS utilitzats i les capes seleccionades. Per a la validació de MODIS i VIIRS es descarregaren els productes M(OY)D021KM, M(OY)D03, M(OY)D07_L2, M(OY)D05_L2, M(OY)D_35_L2, M(OY)D11_L2, MYD21, M(OY)D11C1, MAIAC(TA)BRF/MCD19A1, VNP03MOD, VNP02MOD i VNP21 per a l'estació in-situ des de desembre 2014 fins a març 2019. Pel que fa al sensor SLSTR es descarregaren per al període Juliol-Agost 2017 dades dels productes L1_RBT i L2_LST. El processament inicial va consistir en l'extracció del valor de l'estació dels diferents productes.

5.2.3.- Simulacions

Per tal de simular els paràmetres atmosfèrics necessaris (transmissivitat i radiància descendent) s'utilitzà el codi de transferència radiativa MODTRAN 5.2.0 (Berk et al., 2008) considerant com a input els perfils atmosfèrics del producte M(OY)D07_L2. Aquest procés de simulació es va utilitzar de dues formes diferents: 1) obtenir el valor de

L_{λ}^{\downarrow} per tal de corregir la temperatura in-situ (Equació 5.4). 2) generar la base de dades de temperatures de brillantor a partir de la qual s'han obtingut els coeficients dels algorismes proposats en aquest treball. Amb aquest fi, es van seleccionar 1118 punts espacials aleatoris distribuïts en la regió d'estudi (Figura 5.3). Els perfils atmosfèrics lliures de núvols durant el període 2014-2016 es varen utilitzar en les simulacions. Aquestes es feren utilitzant l'angle d'observació indicant pel sensor MODIS i considerant com a TST la temperatura de l'aire de la primera capa del perfil. Els valors de canal s'obtingueren utilitzant la resposta espectral dels sensors mostrada en la Figura 5.4. Per tal d'obtenir les temperatures de brillantor tan sols resta saber el valor de l'emissivitat. Aquests foren extrets de la llibreria espectral ASTER (Baldrige et al., 2009). Se seleccionaren els espectres de vegetació de gespa, coníferes i caducifoli.

5.2.4.- Obtenció dels coeficients de l'algorisme i anàlisi de sensibilitat

Les bases de dades resultant (TERRA-dia, AQUA-dia, TERRA-nit, AQUA-nit) consten d'aproximadament 542000, 870000, 650000 i 680000 punts respectivament. Aquests conjunts de dades es van dividir en train (70%) i test (30%). Train es va utilitzar per tal d'obtenir els coeficients dels algorismes i test com a validació independent. 2 versions de l'algorisme es van considerar: una versió generalitzada on s'han obtingut els 6 coeficients de l'algorisme, i una versió simplificada amb 3 (és a dir s'han eliminat contribucions de vapor d'aigua i emissivitat). La incertesa d'aquests algorismes fou avaluada utilitzant les equacions 5.7 -5.13.

5.2.5.- Validació T-based

Aquesta validació ha consistit en la comparació directa dels valors de TST dels productes considerats amb els valors in-situ proporcionats per l'estació. La validació es va realitzar per separat en condicions diürnes i nocturnes. Per al cas del SW generalitzat, es va suposar ϵ un valor fix de 0.99 i $\Delta\epsilon$ un valor de 0.005 per a tots els tres sensors. El vapor d'aigua de tots els tres sensors va ser extret directament del producte M(OY)D05_L2. A efectes pràctics, els valors diürns de TST es van filtrar per núvols mitjançant les màscares de núvol M(OY)D35_L2 i MAIAC en el cas del sensor MODIS. Els valors de TST nocturns es van filtrar mitjançant M(OY)D35_L2. Per al sensor VIIRS, les estimacions de LST diürnes i nocturnes es van filtrar mitjançant la màscara de núvol VNP35_L2 tal com incrustada al producte VNP21. En el cas de SLSTR, es van descartar possibles valors de TST contaminats per núvols considerant només valors amb una diferència màxima de 6 K amb valors TST in situ. Aquest filtre addicional també es va aplicar a MODIS i VIIRS. Per analitzar els possibles efectes d'aquesta restricció, també es van obtenir resultats per a una diferència màxima de 15 K i 3 K (Apèndix A.3).

5.2.6.- Validació R-based

A causa del cost addicional de descàrrega i processament, la validació R-based es va restringir al cas diürn per a MODIS. En particular, tan sols per als algoritmes MODIS-SW, MODIS dia-nit i per a la versió simplificada de l'algoritme proposat. Com a dades de validació es seleccionaren 100 punts de les bases test descrites anteriorment. Els valors de temperatura de brillantor de les bandes 31 i 32, així com els valors de TST s'obtingueren dels productes de la Taula 5.7. S'utilitza la màscara de núvols del producte MAIAC(TA)BRF per tal de descartar els píxels contaminats. El període de validació considerat és des de desembre del 2014 fins al desembre del 2016. El valor d'emissivitat es va suposar en 0.99. Per tal de trobar el valor del llindar òptim $\delta (T_{11} - T_{12})$ s'utilitzaren els valors LST de l'estació Tambopata com a referència.

5.2.7.- Patrons espacials

Per tal de completar la validació per al cas particular MODIS (dia), es va realitzar una comparació entre els patrons espacials del número de dies sense núvols i LST obtinguts del producte estàndard MODIS i l'algoritme SW simplificat. Les estacions incloses en l'anàlisi van ser JFM (gener-febrer-març), AMJ (abril-maig-juny), JAS (juliol-agost-setembre) i OND (octubre-novembre-desembre). La comparació es va realitzar per a l'any 2014. S'utilitzaren tres nivells diferents: i) la màscara de núvols MOD35 inclosa en el producte MOD11 sense cap tipus de discriminació QA addicional (TST no produïda a causa dels núvols), ii) la màscara de núvol MOD35 tal com està inclosa en el producte MOD11 i el filtre addicional basat en la capa QC (TST no produït a causa dels núvols + TST va produir una altra qualitat) (Nishida et al., 2003; Williamson et al., 2013) i iii) la màscara de núvols MAIAC. Addicionalment, es va ampliar la validació de patrons espacials repetint aquest mateix procediment mitjançant dades de la suite VIIRS.

5.3. – Estimació de l'evapotranspiració

5.3.1.- Dades in-situ

Una descripció general de les dades de les estacions in-situ utilitzades es pot trobar en Saleska et al. (2013). Per tal d'obtenir els valors diaris d'evapotranspiració (ET) se sumaren els valors d'ET horaris. S'excloueren aquells valors que no tenien al mínim 20 observacions. Els models varen ser validats utilitzant aquests valors. No obstant, per tal de tenir en compte el problema del tancament del balanç d'energia es consideraren dues correccions : Bowen Ratio (BR) i Energy Residual (ER). Els valors d'ET corregits horaris se sumaren per tal d'obtenir el valor diari. D'aquests valors corregits es descartaren

aquells que compliren que el ratio entre corregit/no-corregit fora menor a 0.5 o major que 2 (Ershadi et al., 2014). A part de les observacions dels fluxos turbulents també s'utilitzaren els valors de radiació neta (R_n), radiació incident d'ona curta i llarga (SR_{in} , LR_{in}) i els valors de temperatura (T_a), pressió de vapor de l'aigua (e_a) velocitat del vent (W_s) i pressió de l'aire (P). Aquests valors a escala horària foren agregats a escala diària, diürna o nocturna depenent de les exigències del model.

5.3.2.- Dades de reanàlisi

Les dades meteorològiques a escala regional foren obtingudes dels reanàlisis: MERRA-2, ERA-Interim and GLDAS-2.1. La Taula 5.9 presenta les variables de reanàlisi de les que es deriven les inputs dels models. Les variables de reanàlisi de MERRA-2 es van obtenir dels productes M2T1NXRAD, M2T1NXSLV i M2T1NXLND. Les dades de GLDAS-2.1 es van derivar del producte GLDAS_NOAH025_3H. En el cas de ERA-Interim, s'obtingueren directament de la plataforma de descàrrega. Aquests valors a escala horària foren agregats a escala diària, diürna o nocturna depenent de les exigències del model. En el cas de SEBS, els valor instantanis s'obtingueren a partir de la interpolació lineal entre els dos valors horaris més pròxims al pas del satèl·lit. Per tal de reduir l'escala espacial (1km i 5km) es va fer ús d'una interpolació gaussiana entre els veïns més pròxims.

5.3.3.- Dades de satèl·lit

Les dades de satèl·lit utilitzades en aquest apartat són: l'altura de la vegetació (h), la fracció de vegetació (f_c), l'emissivitat, la TST, l'albedo i el Normalized Difference Vegetation Index (NDVI). En la Taula 5.10 s'especifica el procediment seguit per tal d'obtenir aquestes variables.

5.3.4.- Dades del sòl i mètode gap-filling

A causa de la seua dependència amb la TST, el model SEBS presenta un número molt limitat d'observacions en comparació als altres models. Per tal d'alleugerir aquest problema, es considerarà un mètode de gap-filling per als dies amb núvols. Per tal d'aplicar aquest mètode es necessita de les propietats del sòl "wilting point" i "field capacity". Aquestes foren obtingudes a partir de l'Harmonized World Soil Database (HWSD) (FAO,2012) juntament amb la indexació proposada en Anderson et al. (2007).

El mètode gap-filling es basa en la relació existent entre la fracció d'evapotranspiració potencial (f_{PET}) i la fracció d'aigua disponible per la planta (f_{AW}). Aquesta relació ve donada per les equacions 5.21 a 5.23. El procediment es troba detallat en la Taula 5.12.

5.3.5- Configuració dels models

PT-JPL:

- La temperatura òptima de creixement ha sigut fixada a 25°C. Aquest valor ha sigut aplicat prèviament en la modelització a escala global (Yuan et al., 2010; García et al., 2013).
- En el càlcul de la humitat relativa tant per a e_a com e_s s'utilitzaren els valors a migdia.
- El model PT-JPL ha sigut aplicat a escala diària. El valor de G ha sigut negligit.

PM-Mu:

- Per tal de facilitar la implementació el valor de f_c ha sigut el mateix que l'utilitzat en la resta de models (és a dir no s'ha utilitzat el f_{apar}).
- NDVI i l'albedo s'han obtingut dels productes MAIAC.
- Els valors d'ET nocturns negatius foren descartats en el càlcul diari.

SEBS:

- S'utilitza la parametrització per a vegetació alta de Timmermans et al. (2013).
- Es va considerar una fracció evaporativa constant per tal de passar els valors horaris a diaris.
- Estimacions de SEBS en dies amb núvols foren proporcionades pel mètode gap-filling. Per tal de facilitar la notació aquesta versió s'anomena com SEBS-GF.
- Els valors diaris d'ET corresponen al valor mitjà entre els obtinguts per TERRA i AQUA.

LSASAF:

- Per tal de reduir el cost computacional associat, el model ha sigut forçat a escala diària en comptes d'horària. En particular, tan sols s'ha considerat el forçament diürn. La contribució de G fou negligida.
- λE fou calculada com la suma $\lambda E_c f_c + \lambda E_s (1 - f_c)$. Les classes EBF i sòl (Ghilain et al., 2011) foren seleccionades per a aquest càlcul.
- Es va considerar un valor representatiu de z_{0m} igual a 2.5 i 0.001 per als bosc i el sòl nu. z_{0h} es va calcular a partir de $0.1z_{0m}$ i d_0 com $\frac{2h}{3}$.

5.3.6- Avaluació dels models

En la Taula 5.13 es presenten els inputs necessaris per a cada model. Aquest han sigut forçats a la resolució temporal indicada en aquesta taula. Els models foren validats d'acord amb dos escenaris diferents (Taula 5.14). En l'escenari I, els models foren forçats amb els inputs de les estacions i dades de satèl·lit. En canvi, en l'escenari II, els models foren forçats amb dades de reanàlisi i satèl·lit. A causa de la falta de mesures, en alguns casos com en el model LSASAF s'ha hagut d'utilitzar dades d'humitat del sòl de reanàlisi en l'escenari I. Així també, per a algunes estacions alguns models no s'han pogut fer funcionar. Els estadístics utilitzats en aquesta avaluació han sigut el biaix, la desviació estàndard, el Root Mean Square Error (RMSE), el coeficient de correlació i el coeficient de Taylor. Addicionalment, també s'ha fet ús de diagrames de Taylor.

5.3.7- Avaluació de la qualitat dels reanàlisis

La qualitat dels reanàlisis fou avaluada mitjançant comparació directa dels inputs proporcionats per aquests models amb els inputs meteorològics de les estacions. S'han utilitzat els mateixos estadístics que en l'apartat anterior. El factor que més afecta a la incertesa d'aquestes mesures és la discrepància espacial existent entre aquests dos tipus de dades.

5.3.8- Anàlisi de sensibilitat

Els efectes de la incertesa dels inputs de reanàlisi en els outputs del models d'ET ha sigut avaluada mitjançant un anàlisi de sensibilitat global. Entre els diferents mètodes existents s'ha fet ús del mètode de Sobol (Sobol, 2001, Saltelli et al., 2010). Aquest mètode està basat en una descomposició Analysis of Variance (ANOVA). Com a resultat proporciona una sèrie d'índexs que quantifiquen la contribució independent de cada variable (índex primer), així com la interacció entre dues variables (índex segon). Aquests efectes es poden observar conjuntament mitjançant l'índex total.

5.3.9- Comparació de patrons espacials

Les discrepàncies entre els models també han sigut avaluades mitjançant la comparació dels patrons espacials de l'ET acumulada anualment. Açò s'ha aconseguit mitjançant una simple diferència d'imatges i analitzant els valors mitjans zonals a escala mensual. A part dels models considerats també es van incloure en la comparació els següents models: GLEAM (Miralles et al., 2011; Martens et al., 2017), MERRA-Land (Reiche et al., 2011),

ERA-Interim i GLDAS-2.1. Addicionalment, els models també foren comparats amb els corresponents inputs mitjançant regressió lineal.

III. Resultats

6. Detecció de núvols en imatges MODIS utilitzant una aproximació probabilística

6.1. Descripció de la base de dades

En la Figura 6.1 es presenten les condicions d'observació de la base de dades considerada per tal d'aprendre els models. Es fa palès ací el rang tan restringit de l'angle d'observació (al voltant de 17-19°). Aquest problema encara que no impedeix el desenvolupament del treball necessita de l'avaluació del seu impacte. En la Taula 6.1, es presenta una comparació de les dues màscares de núvols de referència utilitzades. S'observa que aquestes classifiquen igualment un 78.3% (14.85% + 63.45%) del total de les mostres. El 21.7% restant representa les possibles classificacions errònies. D'aquestes el 19.18% corresponen a instàncies on MYD35 classifica com a no-núvol i CPR/CALIOP com a núvol. En la base de dades definitiva, els núvols representen un 81% i els no-núvol o vegetació un 19%.

6.2 Validació amb la base de dades

En la Figura 6.3 es presenten les corbes de fiabilitat (reliability curves). Es pot observar com MLP és l'únic model que proporciona probabilitats ben calibrades. Pel que fa a GNB, QDA i SVM les estimacions tendeixen a ser optimistes. LDA i RF presenten una forma sigmoïdal. En la Taula 6.2, es presenta els estadístics OA i Kappa. Centrant-nos en les prediccions obtingudes una vegada calibrades les probabilitats tenim que tots els models són capaços de reproduir òptimament la base de dades. En particular, RF, SVM i MLP presenten un millor funcionament que GNB, LDA i QDA. Pel que fa al cost computacionals, tots els models són eficients. El cost es va calcular amb un total de 214311 mostres.

6.3 Validació amb imatges

En la Figura 6.5, es presenta la selecció del valor llindar utilitzat per a discriminar entre núvol i no-núvol. El valor màxim de Kappa referent al valor llindar es presenta en la Taula 6.3. També es mostren els valors de MYD35 i MAIAC. Com es pot observar, el grup

GNB-LDA-QDA proporciona valors més elevats de Kappa que el grup RF-SVM-MLP. En particular, LDA proporciona el valor màxim (0.722). Tots els models són capaços de millorar els resultats de MYD35 i MAIAC. En la Taula 6.4, es presenten els resultats per a diferents rangs de visió (angle zenital). Es comprova com els resultats empitjoren a mesura que augmenta l'angle. El grup GNB-LDA-QDA continua proporcionant valors dels estadístics més elevats. En termes del cost computacional tots els models són eficients. La validació continua amb l'avaluació de l'estadístic Kappa per a cada imatge individual (Figura 6.6). A més, en la Figura 6.7 es mostra la comparació de la cobertura nuvolosa d'aquestes imatges. S'observa com MYD35 i MAIAC tendeixen a subestimar i sobreestimar aquesta respectivament. En la Figura 6.8, es presenta una comparació visual per a un conjunt de 2 imatges.

6.4 Validació amb dades in-situ

En la Taula 6.5 es presenten els resultats de la validació in-situ. La validació es va realitzar sobre un conjunt de 110 dies. La distribució de núvol i no-núvol correspon a un 95% i 5% respectivament. Encara que aquestes classes clarament no es troben equilibrades, s'assumeix que aquesta és la distribució de l'estació. MYD35 estima la presència de no-núvols com el 15% mentre que MAIAC el 2.7%. Els models proporcionen valors entre 4% i 5%. S'observa (Taula 6.5) que tots els models classifiquen bé els núvols, la principal discrepància ve a l'hora de la classe no-núvol. En termes del coeficient Kappa, els models proporcionen millors resultats que MYD35 i MAIAC. El millor funcionament el proporciona MLP, seguit per LDA, SVM, RF, GNB i QDA.

7. Algoritme d'estimació de la TST adaptat als boscos tropicals de l'Amazones

7.1.- Validació amb la base de dades simulades

En la Taula 7.1 es presenta l'anàlisi de sensibilitat dels algorismes. Per a la versió simplificada del SW, l'error total de LST es mou entre 0.520 K i 0.896 K. Per a la versió generalitzada l'error varia entre 0.841 i 1.695 K. L'augment resulta de la consideració addicional de les contribucions d'emissivitat i vapor d'aigua. Un 1% d'emissivitat contribueix entre 0.732 i 1.549 K. El vapor d'aigua presenta una contribució menor amb 0.184 K. Els resultats de la validació amb les dades test es presenten en la Taula 7.2 i les figures 7.1-7.4. Exceptuant el cas de VIIRS SW generalitzat, tots els algorismes tenen un biaix nul i valor de coeficient de correlació majors que 0.9. El RMSE varia entre 0.36 i 1.0 K amb valors superiors en condicions diürnes. En termes del vapor d'aigua i de l'angle d'observació es mostra que el SW simplificat és més estable que el SW generalitzat.

7.2.- Validació T-based

Els resultats de la validació T-based es recullen en les Taules 7.3 i 7.4. Començant per la validació diürna, per a TERRA els algoritmes MODIS-SW i MODIS-DN tenen un RMSE entre 2.7 K i 2.9 K. L'algoritme SW generalitza no proporciona una millora dels resultats. L'algoritme SW simplificat millora els productes MODIS amb una diferència en RMSE fins a 0.8 K. Per a AQUA, MODIS SW i MODIS-TES proporcionen valors semblants de RMSE (2.3 K i 2.9 K), no obstant amb un biaix negatiu i positiu respectivament. MODIS-DN presenta un RMSE de 2.66 i 3.05 K. Ambdós algoritmes SW (generalitzat i simplificat) milloren els resultats dels productes MODIS. El valor menor de RMSE s'obté per a la versió simplificada (1.68 K i 1.90K per a radiòmetres i pirgeòmetre, respectivament). Per a VIIRS, la versió SW simplificada millora la versió SW generalitzada amb una reducció entre 0.4 K i aproximadament 0.5 K de RMSE. No obstant, VIIRS-TES és l'algoritme que proporciona un millor funcionament (reducció entre 0.2 K i 0.4 K de RMSE respecte SW simplificat). Per a SLSTR, l'algoritme operatiu funciona millor que la resta d'algoritmes considerats amb una diferència màxima de RMSE de 0.68 K respecte del SW simplificat. Passant a la validació nocturna, s'observa que generalment els valors de RMSE decreixen en un rang entre 0.7 K i 2 K. Per a TERRA, MODIS-SW funciona millor que MODIS-DN (RMSE al voltant d'1.3 K enfront d'un valor al voltant de 1.6 K). L'algoritme SW simplificat és capaç de millorar la resta dels algoritme amb valors de RMSE diferència fins a 0.5 K. Per a AQUA, MODIS-TES funciona pitjor que MODIS-SW i MODIS-DN. El primer té un valor RMSE de 1.8 K -2 K enfront de 1.2 K-1.3 K per a SW i 1.3 K -1.7 K per a DN. Els dos algoritmes SW proposats són capaços de millorar aquests resultats, sent la versió simplificada la millor d'ambdós. Per a VIIRS, l'algoritme SW proporciona els valors mínims de RMSE de tots els algoritmes considerats (0.88 K -0.98 K). Per a SLSTR, conclusions anàlogues al cas diürn s'han obtingut. No obstant, la diferència entre l'algoritme operatiu i el SW proposat s'ha reduït.

7.3.- Validació R-based

Utilitzant les dades in-situ de Tambopata i considerant una diferència màxima de $\pm 1\text{K}$ per a s'obtenen els següents valors llindars $-0.1\text{K} < (T_{12_{obs}} - T_{12_{sim}}) < 0.3\text{K}$. No obstant, tenint en compte la limitació imposada per l'abundant cobertura nuvolosa els valors llindars finalment foren $-0.2\text{K} < (T_{12_{obs}} - T_{12_{sim}}) < 0.4\text{K}$. Aquests proporcionen una diferència menor que $\pm 2\text{K}$. En la Figura 7.10 es presenten els resultats de la validació R-based. S'observa com l'algoritme proposat presenta un valor menor del biaix i de desviació estandard. La diferència en termes de RMSE és d'aproximadament 0.9 K, 1.7 K, 0.7 K i 1.5 K per a MODIS-SW TERRA, MODIS-SW AQUA, MODIS-DN TERRA i MODIS-DN AQUA.

7.4.- Patrons espacials

Observant els patrons espacials de les Figures 7.11 i 7.12 es comprova que la diferència en els patrons de TST entre MOD35 i QC/MAIAC prové de l'eliminació de la contaminació dels núvols. No obstant açò redueix el número de dies disponibles. Pel que fa a la comparació entre QC i MAIAC es comprova que ambdós reproduïxen patrons similars. Addicionalment, en la Figura 7.13 es presenten els resultats anàlegs per a VIIRS. S'observa certa similitud entre VIIRS i AQUA per al cas de la TST.

8. Comparació d'algoritmes d'estimació de l'evapotranspiració basats en dades de teledetecció

8.1.- Escenari I

8.1.1. Validació dels algoritmes

En la Figura 8.1, es presenta la validació dels algoritmes. Els models proporcionen valors de R entre 0.5 i 0.9. Els valors de l'estadístic S es mouen entre 0.7 i 0.9 i el RMSE entre 0.55-1.25 mm/dia. Els models mostren un funcionament similar, no obstant això PT-JPL presenta els valors més elevats de R (0.65-0.88) en comparació amb PM-Mu (0.56-0.74), SEBS (0.56-0.77), SEBS-GF (0.58-0.76) i LSASAF (0.53-0.69). A més, PT-JPL proporciona els millors resultats considerant valors in-situ corregits (RMSE = 0.55 mm/dia, R = 0.88 i S = 0.91), seguit de SEBS, SEBS-GF i PM-Mu. El pitjor funcionament s'obté per a LSASAF (RMSE = 1.50 mm/dia, R = 0.55 i S = 0.77). Els resultats de la validació individual de les estacions es presenta amb diagrames Taylor en la Figura 8.3. Considerant valor in-situ corregits, PT-JPL funciona millor que la resta de models (més pròxim al punt d'observació). Pel que fa als valors no corregits tots els models presenten un funcionament similar.

8.1.2. Evolució temporal

L'anàlisi de l'evolució temporal es presenta en la Figura 8.4. S'observa que els models són capaços de seguir l'evolució dels valors in-situ, obtenint valors màxims en setembre. LSASAF no obstant presenta el pic en Agost, cal dir no obstant que les estacions K67 i CAX no foren incloses a causa de la falta de dades. Al llarg de l'any, PT-JPL, SEBS i SEBS-GF es troben dins del rang preestablert pels valors in-situ. En canvi, LSASAF i PM-Mu presenten una subestimació i sobreestimació dels valors respectivament.

8.2.- Escenari II

8.2.1. Avaluació de la qualitat dels reanàlisis i anàlisi de sensibilitat

En la Taula 8.2 es presenta la validació dels reanàlisis considerats. Generalment, els inputs de velocitat de vent presenten una incertesa més elevada (60% d'error relatiu). Els inputs de radiació un 30%, els d'humitat un 15% i els de temperatura un 10%. Pel que fa a la radiació, es comprova que la diferència més important entre els reanàlisis és el biaix proporcionat. MERRA-2 sobreestima R_{n24} , SR_{inday} i SR_{inhour} i subestima LR_{inday} i LR_{inhour} . El mateix comportament s'observa per a GLDAS-2.1, no obstant aquest sobreestima SR_{inday} . ERA-Interim sobreestima els valors instantanis mentre que subestima els valors diürns i diaris. Pel que fa a l'anàlisi de sensibilitat, es comprova que la variabilitat dels inputs de radiació és el factor dominant que explica la variabilitat de l'ET.

8.2.3. Validació dels algoritmes

En la Figura 8.7 es presenten els resultats de l'escenari II. S'observa una clara deterioració del funcionament dels models respecte de l'escenari anterior (R (0.2-0.3) i S (0.5-0.7) han disminuït mentre que el RMSE ha augmentat (1.1-1.7 mm/dia)). Tenint en compte la incertesa dels reanàlisis aquest era un resultat esperat. Cal destacar que es troba una clara relació entre la sobreestimació i subestimació dels inputs de radiació observada en l'apartat anterior amb l'observada en aquest. Pel que fa als resultats de les estacions individuals es presenten en la Taula 8.3 i Figura 8.8. En aquest escenari, no hi ha cap combinació de model+reanàlisi en particular que proporcione els millors resultats.

8.2.4. Evolució temporal

Els resultats d'aquesta secció es presenten en la Figura 8.9. Per a PT-JPL, MERRA-2 i GLDAS-2.1 sobreestimen els valors in-situ, en canvi ERA-Interim els subestima. Per a PM-Mu, MERRA-2 proporciona la major coincidència amb els valors in-situ. ERA-Interim i GLDAS-2.1 subestimen els valors in-situ. Pel que fa a SEBS-GF, MERRA-2/GLDAS-2.1 i ERA-Interim proporcionen una desviació positiva i negativa respectivament. Per a LSASAF, la màxima discrepància s'obté per a MERRA-2, no obstant açò resulta amb un millor acord amb les dades in-situ.

8.2.5. Comparació de patrons espacials

De la Figura 8.10 es pot comprovar com discrepàncies entre els reanàlisis considerats poden induir una diferència major de 500 mm/any en el valor anual cumulatiu d'ET. En particular, les desviacions negatives màximes s'obtenen per a LSASAF-ERA i LSASAF-

GLDAS seguits per LSASAF-MERRA, PM-Mu-ERA i PM-Mu-GLDAS. Les desviacions positives màximes s'obtenen per a MERRA-2 i GLDAS-2.1 seguits per PT-JPL-GLDAS i SEBS-GF-GLDAS. A partir de la Figura 8.11, es pot comprovar com la contribució màxima als patrons espacials prové dels inputs de radiació. Pel que fa a l'evolució temporal (Figura 8.12) els models segueixen el mateix patró espacial encara que proporcionant valors absoluts diferents.

Conclusions

En aquest apartat, presentem les principals conclusions derivades d'aquest estudi. S'han organitzat segons les tres línies de recerca seguides.

Pel que fa al **primer objectiu** les principals conclusions han sigut:

- Les observacions simultànies dels sensors CPR/CALIOP i MODIS poden ser utilitzades com a base de dades de referència per tal d'aprendre algoritmes supervisats. No obstant la base resultant es troba restringida a unes condicions d'observació limitades. En aquest treball, hem fet ús d'una aproximació probabilística (estimació de les probabilitats en comptes de prediccions) per tal d'evitar aquest problema.
- La validació utilitzant imatges ha demostrat que els mètodes probabilístics (LDA, GNB i en una mesura menor QDA) proporcionen millor resultats que RF, SVM i MLP. Aquest fet resulta d'haver heretat les deficiències de la base de dades generada.
- La metodologia emprada millora els resultats de les màscares MODIS ja que es capaç de corregir les deficiències observades en els productes MYD35 i MAIAC (subestimació i una sobreestimació de la cobertura dels núvols, respectivament).
- Els models presenten un bon equilibri entre la exactitud dels resultats i el cost computacional associat. En particular, LDA destaca entre la resta de models obtenint el valor màxim del coeficient Kappa i el menor cost associat.
- La implementació de la metodologia emprada és directa i pot ser adaptada a altres regions amb requeriments mínims. Les dades CPR/CALIOP i MODIS són proporcionades directament per l'equip CloudSat. A més, aquesta metodologia pot ser adaptada fàcilment a altres sensors com VIIRS.

Pel que fa al **segon objectiu**, les conclusions principals han sigut:

- La incertesa dels radiòmetres infrarojos SI-100 i IR-120 ha sigut inferior a 1K. A més de la comparació amb les dades del sensor CNR4 s'ha obtingut un RMSE de 0.8 K. Complint així els requisits del llocs de validació de TST.

- A partir de la validació amb dades simulades independents, es va comprovar que per a la regió d'estudi considerada l'algoritme SW simplificat proporciona millor resultats que el general (reducció del RMSE entre 0.1-0.4 K i més estabilitat per a angles de visió més grans i per a un contingut de vapor d'aigua major).

- De la validació T-based s'han obtingut les següents conclusions:

- Per a MODIS-TERRA, els algoritmes MODIS-SW i MODIS-DN proporcionen un RMSE de fins a 2.70 K -2.83 K en el cas diürn i d'1.40 K - 1.70 K per al cas nocturn. Per al dia el SW generalitzat no va proporcionar una millora dels resultats. A la nit en canvi, s'obté una disminució de fins a 0.1 K en el RMSE. El SW simplificat sí que millora els algoritmes MODIS tant al dia com a la nit amb una disminució de 0.2 K – 0.8 K de RMSE.

- Per a MODIS-AQUA, durant el dia MODIS-SW i MODIS-TES tenen un funcionament similar (valors RMSE al voltant de 2.3 K per al radiòmetre i 2.9 K per al radiòmetre net CNR4). MODIS-DN presenta uns resultats pitjors amb un RMSE de 2.66 K i 3.05 K respectivament. A la nit, MODIS-TES proporciona el pitjor funcionament de tots els algoritmes MODIS, amb una diferència en RMSE que oscil·la entre 0.1 K i 0.7 K. MODIS-TES sobreestima els valors de TST in-situ (biaix positiu) mentre que MODIS-SW i MODIS-DN presenten un biaix negatiu. Tant el algoritme SW generalitzat com simplificat són capaços de millorar els resultats de la validació amb una disminució de RMSE fins a 1.3 K. La versió simplificada és la que millor resultats proporciona.

- Per a VIIRS es va comprovar que l'algoritme SW simplificat millora l'algoritme SW general, amb diferències d'aproximadament 0.2 K-0.5 K en el RMSE. Durant el dia, VIIRS-TES proporciona el millor funcionament amb una diferència de 0.2 K a 0.3 K respecte a l'algoritme SW simplificat. No obstant això, durant la nit, VIIRS-TES no supera aquest últim. S'obté una diferència de 0.7 K a 0.8 K en RMSE.

- Per a SLSTR, el producte L2 proporciona un millor acord amb les observacions in situ que el que presenta l'algoritme SW simplificat (diferència d'aproximadament 0.6 K en RMSE diürn i una diferència de 0.07 K en RMSE nocturn). El SW generalitzat proporciona un pitjor funcionament.

No obstant, cal recordar que la validació s'ha realitzat sobre un conjunt de dades menor.

- La validació amb el mètode R-based s'ha mostrat com una alternativa vàlida al T-based. La incertesa associada es trobava dins dels límits de 2 K. A causa de limitacions pràctiques, aquest mètode només es va aplicar a la validació diürna de MODIS. El SW simplificat proposat redueix la incertesa en l'estimació de LST (RMSE) en 0.7 a 1.7 K en comparació amb algoritmes operatius MODIS.

- A partir de la comparació de patrons espacials, es va veure que la diferència revelada en els patrons de TST entre MOD35 i QC / MAIAC deriva de la correcció de l'efecte de contaminació dels núvols.

Pel que fa al **tercer objectiu**, les conclusions principals han sigut:

- S'ha comprovat que quan s'utilitzen dades amb una incertesa menor (escenari I), es pot obtenir valors de RMSE inferiors a 1 mm/dia. Demostrant per tant la capacitat de les dades MODIS per d'estimar l'ET en la regió.

- En l'escenari I, els models considerats presenten un rang de biaix entre -1.08 i 0.92 mm/dia amb un rang de RMSE entre 0.55 i 1.50 mm/dia. Els valors de R es mouen entre 0.55 i 0.88. Entre aquests models, PT-JPL va proporcionar el rang de valor R més alt (0.65-0.88) i el millor funcionament, tenint en compte la correcció "energy residual" (RMSE = 0.55 mm / dia i R = 0.88). A més, va donar el punt més proper al punt d'observació en el diagrama de Taylor.

- LSASAF proporciona una clara subestimació en comparació amb la resta de models. Els motius principals atribuïts a aquest comportament són l'ús de dades d'humitat del sòl obtingudes de reanàlisi (descripció problemàtica en la regió + desajust espacial entre les dades). S'ha comprovat que aquest problema es redueix quan s'inclou un terme d'intercepció.

- PM-Mu presenta un funcionament similar al PT-JPL (és a dir, una diferència de RMSE d'aproximadament 0.2 mm / dia i una desviació màxima de 0,1 en valor R). No obstant això, es va comprovar que els valors d'entrada difereixen dels seus valors òptims (f_c i R_n). No obstant, utilitzant el valor de f_{apar} en comptes de f_c la sobreestimació es redueix.

- SEBS proporciona uns resultats similars a PT-JPL. Tot i això, pel fet de dependre de les observacions de TST, les estimacions de SEBS estan limitades per la cobertura nuvolosa continuada de la regió. S'obté una disminució dràstica (d'un factor 4) del nombre d'estimacions disponibles respecte del model PT-JPL. Per tal d'evitar aquest problema es va considerar l'ús d'un mètode de gap-filling (Anderson et al., 2007) per tal de proporcionar estimacions en els dies amb núvols. Malgrat que es va produir un increment del número d'estimacions, es va observar una subestimació respecte dels valors de SEBS.

- En l'escenari II, el RMSE presenta valors superiors a 1 mm/dia. A més s'obté una correlació deficient (valor R màxim al voltant de 0.3). Aquests pitjors resultats s'expliquen principalment per la incertesa d'aquestes dades. La validació d'aquests inputs es va realitzar mitjançant la comparació directa entre els inputs de les estacions in-situ i les de reanàlisi. La velocitat del vent és la variable amb més incertesa amb un error relatiu superior al 60%, seguit per els inputs de radiació amb un 30%, els d'humitat amb un 15% i els de temperatura amb un 10%.

- Per analitzar l'impacte de la incertesa del reanàlisi sobre la incertesa del model es va fer un anàlisi de la sensibilitat de Sobol. A partir d'aquesta anàlisi, es va trobar que la incertesa dels inputs de radiació governaven la incertesa del model.

-Respecte dels inputs de radiació s'ha comprovat que MERRA-2 tendeix a sobreestimar la radiació neta diària i la radiació solar descendent. ERA-Interim tendeix a subestimar ambdues variables, i GLDAS-2.1 tendeix a sobreestimar la radiació neta diària mentre que subestima la radiació solar descendent. Els biaixos d'aquestes variables es tradueixen directament en biaixos en les estimacions d'ET. A més, les discrepàncies entre aquestes entrades expliquen discrepàncies entre els models d'ET.

ABSTRACT

Amazonian tropical forests play a significant role in global water, carbon and energy cycles. Considering the relevance of this biome and the climate change projections which predict a hotter and drier climate for the region, the monitoring of the vegetation status of these forests becomes of significant importance. In this context, vegetation temperature and evapotranspiration (ET) can be considered as key variables. Vegetation temperature is directly linked with plant physiology. In addition, some studies have shown the existing relationship between this variable and the CO₂ absorption capacity and biomass loss of these forests. Evapotranspiration resulting from the combined processes of transpiration and evaporation links the terrestrial water, carbon and surface energy exchanges of these forests. How this variable will response to the changing climate is critical to understand the stability of these forests. Satellite remote sensing is presented as a feasible means in order to provide accurate spatially-distributed estimates of these variables. Nevertheless, the use of satellite passive imagery for analysing this region still has some limitations being of special importance the proper cloud masking of the satellite data which becomes a difficult task due to the continuous cloud cover of the region.

Under the light of the aforementioned issues, the present doctoral thesis is aimed at estimating the land surface temperature and evapotranspiration of the Amazonian tropical forests using remote sensing data. In addition, as cloud screening of satellite imagery is a critical step in the processing chain of the previous magnitudes and becomes of special importance for the study region this topic has also been included in this thesis. We have mainly focus on the use of data from the Moderate Resolution Imaging Spectroradiometer (MODIS) which is amongst major tools for studying this region. Regarding the cloud detection topic, the potential of supervised learning algorithms for cloud masking was studied in order to overcome the cloud contamination issue of the current satellite products. Models considered were: Gaussian Naïve Bayes (GNB), Linear Discriminant Analysis (LDA), Quadratic Discriminant Analysis (QDA), Random Forests (RF), Support Vector Machine (SVM) and Multilayer Perceptron (MLP). These algorithms are able to provide a continuous measure of cloud masking uncertainty (i.e. a probability estimate of each pixel belonging to clear and cloudy class) and therefore can be used under the light of a probabilistic approach. Reference dataset (a priori knowledge) requirement was satisfied by considering the collocation of Cloud Profiling Radar (CPR) and Cloud Aerosol Lidar with Orthogonal Polarization (CALIOP) observations with MODIS sensor. Model performance was tested using three independent datasets: 1) collocated CPR/CALIOP and MODIS data, 2) MODIS manually classified images and 3) in-situ ground data. For the case of satellite image and in-situ testing, results were additionally compared to current operative MYD35 (version 6.1) and Multi-Angle Implementation of the Atmospheric Correction (MAIAC) cloud masking algorithms. These results showed that machine learning algorithms were able to improve MODIS operative cloud masking performance over the region. MYD35 and MAIAC tended to underestimate and overestimate the cloud cover, respectively. Amongst the models considered, LDA stood out as the best candidate because of its maximum accuracy (difference in Kappa coefficient of 0.293/0.155 (MYD35 /MAIAC respectively)) and minimum computational associated.

Regarding the estimation of land surface temperature (LST), the aim of this study was to generate specific LST products for the Amazonian tropical forests. This goal was accomplished by using a tuned split-window (SW) equation. Validation of the LST products was obtained by direct comparison between LST estimates as derived from the algorithms and two types of different LST observations: in-situ LST (T-based validation) and LST derived from the R-based method. In addition, LST algorithms were validated using independent simulated data. In-situ LST was retrieved from two infrared radiometers (SI-100 and IR-120) and a CNR4 net radiometer, situated at Tambopata test site (12.832 S, 62.282 W) in the Peruvian Amazon. Apart from this, current satellite LST products were also validated and compared to the tuned split-window. Although we have mainly focus on MODIS LST products which derive from three different LST algorithms: split-window, day and night (DN) and Temperature Emissivity Separation (TES), we have also considered the inclusion of the Visible Infrared Imaging Radiometer Suite (VIIRS) sensor. In addition, a first assessment of the Sea and Land Surface Temperature Radiometer (SLSTR) is presented. Validation was performed separately for daytime and nighttime conditions. For MODIS sensor, current LST products showed Root Mean Square Errors (RMSE) in LST estimations between 2 K and 3K for daytime and 1 K and 2 K for nighttime. In the best case (with a restrictive cloud screening) RMSE errors decrease to values below 2K and around 1 K, respectively. The proposed LST showed RMSE values of 1K to approximately 2 K and 0.7-1.5 K (below 1.5 K and below 1 K in the best case) for daytime and nighttime conditions, thus improving current LST MODIS products. This is also in agreement with the R-based validation results, which show a RMSE reduction of 0.7 K to 1.7 K in comparison to MODIS LST products. For the case of VIIRS sensor daytime conditions, VIIRS-TES algorithm provide the best performance with a difference of 0.2 K to around 0.3 K in RMSE regarding the split window algorithm (in the best case it reduces to 0.2 K). All VIIRS LST products considered have RMSE values between 2 K and 3K. At nighttime, however VIIRS-TES is not able to outperform the SW algorithm. A difference of 0.7 K to 0.8 K in RMSE is obtained. Contrary to MODIS and the SW LST products, VIIRS-TES tends to overestimate in-situ LST values. Regarding SLSTR sensor, the L2 product provides a better agreement with in-situ observations than the proposed algorithm (daytime difference in RMSE around 0.6 K and up 0.07 K at nighttime).

In the estimation of the ET, we focused on the evaluation of four commonly used remote-sensing based ET models. These were: i) Priestley-Taylor Jet Propulsion Laboratory (PT-JPL), ii) Penman-Monteith MODIS operative parametrization (PM-Mu), iii) Surface Energy Balance System (SEBS), and iv) Satellite Application Facility on Land Surface Analysis (LSASAF). These models were forced using remote-sensing data from MODIS and two ancillary meteorological data sources: i) in-situ data extracted from Large-Scale Biosphere-Atmosphere Experiment (LBA) stations (scenario I), and ii) three reanalysis datasets (scenario II), including Modern-Era Retrospective analysis for Research and Application (MERRA-2), European Centre for Medium-range Weather Forecasts (ECMWF) Re-Analysis-Interim (ERA-Interim), and Global Land Assimilation System (GLDAS-2.1). Performance of algorithms under the two scenarios was validated using

in-situ eddy-covariance measurements. For scenario I, PT-JPL provided the best agreement with in-situ ET observations (RMSE = 0.55 mm/day, R = 0.88). Neglecting water canopy evaporation resulted in an underestimation of ET measurements for LSASAF. SEBS performance was similar to that of PT-JPL, nevertheless SEBS estimates were limited by the continuous cloud cover of the region. A physically-based ET gap-filling method was used in order to alleviate this issue. PM-Mu also with a similar performance to PT-JPL tended to overestimate in-situ ET observations. For scenario II, quality assessment of reanalysis input data demonstrated that MERRA-2, ERA-Interim and GLDAS-2.1 contain biases that impact model performance. In particular, biases in radiation inputs were found the main responsible of the observed biases in ET estimates. For the region, MERRA-2 tends to overestimate daily net radiation and incoming solar radiation. ERA-Interim tends to underestimate both variables, and GLDAS-2.1 tends to overestimate daily radiation while underestimating incoming solar radiation. Discrepancies amongst these inputs resulted in large absolute deviations in spatial patterns (deviations greater than 500 mm/year) and temporal patterns.

INTRODUCTION

Overview and problem statement

The Amazon forests, with approximately 5.3 million km², represent the 40 % of the global tropical forest area (Aragão et al., 2014). It contains around a quarter of the world's terrestrial species (Dirzo & Raven, 2003) with approximately 16000 tree species (ter Steege *et al.*, 2013). Fifteen percent of the global photosynthesis occurs in these forests (Malhi, 2008) and they store an estimated 120 billion tons of carbon (Phillips et al., 2009; Atkinson et al., 2011) which is equivalent to more than 10 years' worth of global fossil-fuel emissions (Davidson et al., 2012). In addition, these forests have an important role in maintaining local and regional rainfall and contribute to the hydrological cycle by means of moisture transport inside and outside the region (Marengo et al., 2018). These forests release large amounts of water vapour to the atmosphere via evapotranspiration, which ranges from 35% to over 80% of the precipitation of the region (see Marengo et al., 2018 and references therein). In addition, moisture is transported to the La Plata basin and Southeastern regions by means of the South American low-level jet east to the Andes representing a significant source of precipitation (Marengo et al., 2004; Zemp et al., 2014). Apart from this, Amazon ecosystem additionally mediates the approximately 20% of water inflow into the oceans through the Amazon river (Nobre et al., 2016).

The climate of Amazonia has become more extreme during the last few decades. Analysis of air temperature trends revealed a warming of 0.5°C since 1980 (Jiménez et al., 2018). Rainfall trends show statistically significant negative values for the southern Amazonia (Espinoza et al., 2019) with a 25% of reduction in rainfall between 2000 and 2012 (Hilker et al., 2014). Over this same region, several studies show an increase in the length and intensity of the dry season (Fu et al., 2013; Marengo et al., 2011). In addition, in the recent years there have been several extreme climatic events: three mega-floods were detected in 2009, 2012 and 2014 and three mega-droughts in 2005, 2010 and 2016 (Marengo & Espinoza, 2016). In particular, these three droughts have been of particular importance because the strong impacts they have had on the rainforests and its carbon cycle. Both 2005 and 2010 droughts led to losses of biomass resulting from increased mortality rates and small declines in growth during and after drought events (Feldpausch et al., 2016). At basin scale they also impacted the exchange of CO₂ between the vegetation and the atmosphere by reversing the long-term carbon sink of these forests and becoming the vegetation a net source of CO₂ (Phillips et al., 2009; Gatti et al., 2014; Feldpausch et al., 2016). The 2016 drought experienced record-breaking warming (Jiménez-Muñoz et al., 2016b). In addition, the net forest carbon balance was also altered by the increased tree mortality and the reduced net primary productivity (Leitold et al., 2018).

Deforestation and forests fire are additional drivers of change in the Amazon region (Marengo et al., 2018). Substantial losses of these forests by deforestation are expected to impact the land-atmosphere energy exchange and precipitation at regional scale (Werth & Avissar, 2002; Sampaio et al., 2007; Bagley et al., 2014) as well as the global carbon balance via an alteration of global CO₂ concentration (Betts et al., 2004; Phillips et al.,

2009). Fires are able to alter forests characteristics. They promote the establishment of fire-adapted species thus leading to a more savannah-like ecosystem (Nepstad et al., 2008). An increase in frequency and severity of fires is associated to an increase in tree mortality (Balch et al., 2011; Brando et al., 2014). In addition, fires can also affect regional climate (Andreae et al., 2004) because of the aerosol particles emitted during fire combustion. Of particular concern for the region is the role that could play the combined effects of repeated droughts and deforestation in combination with fire, which according to some studies have the potential to cause the collapse of the rainforest ecosystem (Cox et al., 2000, 2004, 2008). Various studies have suggested the shift of the Amazon forest into a drier savanna-like biome (Oyama & Nobre, 2003; Sampaio et al., 2007 among others) as a consequence of the drastic reduction of rainfall due to increase deforestation. This Amazon dieback is thought to occur after passing after a tipping point, which has been associated with a critical threshold of drought linked to the global warming or deforestation exceeding a certain threshold value (Marengo et al., 2018 and references therein). Although several observational and modelling studies have pointed to some degree of forest resilience (Brando et al., 2008; da Costa et al., 2010; Ramming et al., 2010; Huntingford et al., 2013) it is still uncertain whether or not future climate change and other anthropogenic stressors will lead to this possible dieback scenario (Marengo et al., 2018).

In this context, an accurate monitoring of the vegetation changes is of special importance. Satellite remote sensing is the only viable means in order to observe these forests in a spatially comprehensive and temporally frequent fashion. In particular, the MODIS on board the National Aeronautics and Space Administration (NASA) Terra and Aqua Earth Observation (EO) polar orbiting system satellites since 2000 and 2002 providing multiple day products is among today's major tools for the climate monitoring of this region (Hilker et al., 2015, Jiménez-Muñoz et al., 2015). The most common approach for analysing vegetation dynamics for phenology and drought assessment has been the use of time-series analysis of vegetation indices such as the Enhanced Vegetation Index (EVI) and the Normalized Difference Vegetation Index (NDVI) (Saleska et al., 2007; Samanta et al., 2010; Atkinson et al., 2011; Samanta et al., 2012; Hilker et al., 2012, 2014, among others). Nevertheless, results and conclusions for these studies have been controversial. Several studies suggest that MODIS surface reflectance uncertainties is likely to cause these discrepancies (Asner & Alencar et al., 2010; Samanta et al., 2012).

Less attention however has been paid to the use of other variables such as vegetation temperature, which being linked with plant physiology is a key variable in the understanding of the vegetation dynamics. In particular, some studies have investigated the relationship between this variable and the CO₂ absorption capacity, showing that an increase in temperature could result in a negative impact on tropical forest CO₂ uptake and productivity (Clark et al., 2003; Doughty & Goulden, 2008). Also, anomalous high values have been proved to be more important than precipitation deficits in causing losses of biomass during drought periods (Galbraith et al., 2010). In Toomey et al. (2011) it was suggested that heat stress played an important role in the 2005 and 2010 droughts and that

models should incorporate both heat and moisture stress in order to predict drought effects on these forests. Jiménez-Muñoz et al. (2013, 2015, 2016ab) and Jimenez et al. (2018) pointed out the valuable information that could be derived from monitoring land surface temperature anomalies for the region. These studies are the basis of the development of the Thermal Amazoni@ project (ipl.uv.es/thamazon), a prototype platform for the dissemination and friendly visualization of LST and thermal indices maps (Jiménez-Muñoz et al., 2015). This monitoring system is expected to be relaunched with updated and improved information extracted from the LST and ET products developed in this thesis.

Thermal remote sensing (as optical remote sensing) does have some important limitations mainly due to imperfect cloud masking and atmospheric correction. Regarding the first limitation, the proper cloud detection of clouds in satellite imagery is a critical step in any remote-sensing processing chain in order to ensure accuracy in the provided results. Due to the continuous cloud coverage of the region of study (cloud cover may be as high as 70% during the dry season and greater than 90% for the wet season (Hilker et al., 2012)) this becomes of crucial importance. For the particular case of MODIS sensor, cloud detection is accomplished using MODIS operative cloud mask MOD35 (MYD35) which uses a threshold based approach (Ackerman et al., 1998). An alternative suite of products is developed by the MAIAC algorithm which uses a multi-temporal approach in order to detect clouds (Lyapustin et al., 2008). Several issues in the performance of this MOD35 (MYD35) cloud mask were reported globally. Overestimation in some global regions was found in Liu et al. (2013). Biases related to land cover were determined by Leinenkugel et al. (2013) and Wilson et al. (2014). Deficient cloud masking has been identified as one of the main factors affecting accuracy of MODIS downstream products (Crosson et al., 2012; Williamson et al., 2013). For Amazonian region, cloud contamination impacts on surface variable retrieval were reported by Hilker et al. (2012), Gomis-Cebolla et al. (2018). In order to solve operative cloud mask deficiencies in the recent years machine learning algorithms have emerged as an alternative candidates for satellite cloud masking. In particular, for the MODIS sensor, ensembles of decision trees (Kilpatrick et al., 2018), support vector machines (Ishida et al., 2018) and neural networks (Chen et al., 2018) were able to outperform MODIS cloud mask detection accuracy. Other algorithms have been successfully applied to a wide range of sensors (we refer the reader to chapter 1 for a bibliographic review of the applications of these methods). Main issue about these methods is that they are based on a supervised approach (i.e. they need accurate reference data in order to learn the models). Several studies have pointed out the potential use of active sensors such as the Cloud Profiling radar (CPR) onboard CloudSat platform and the Cloud-Aerosol Lidar and Infrared Pathfinder Satellite Observation (CALIOP) onboard the Cloud-Aerosol Lidar and Infrared Pathfinder Satellite Observation (CALIPSO) platform in order to provide a reference cloud dataset and thus overcome this issue.

Regarding the second limitation, estimation of land surface temperature can be obtained by a wide variety of methods depending on sensor characteristics (Li et al., 2013). In

particular, operational land surface temperature products are currently available from a variety of instruments. For the particular case of MODIS sensor, three different LST products exist which are based on the Generalized Split-Window (Wan & Dozier et al., 1996), the Day-Night (DN) algorithm (Wan & Li, 1997) and the Temperature-Emissivity-Method (Matsunaga et al., 1994; Gillespie et al., 1995) respectively. VIIRS sensor considered the successor of MODIS provides two products which are based on the single split-window algorithm of Yu et al. (2005) and the TES algorithm. The SLSTR developed by the European Space Agency uses the algorithm of Prata (2002). Nevertheless, the performance of these products over the region is not well documented due mainly due to the scarcity on in-situ LST measurements that can be used for validation. This, can be achieved by direct ground comparison of satellite LST estimates and in-situ LST observations, which is called T-based validation. Additional techniques exist that can overcome the need of in-situ observations such as the R-based method proposed in Wan & Li (2008). In order to escape from the possible limitations that offer the current LST products, alternative retrieval algorithms can be applied. Among the possible candidates the Sobrino & Raissouni (2000) formulation which was developed by the Global Change Unit (GCU) meet all the requirements for this task. This method (and also the operative ones) makes use of simulated at-sensor brightness temperature values databases in order to derive the algorithm coefficients. The success of the retrieval algorithm heavily relies on the accuracy of the simulated values. Therefore, using a specific database that properly represents the study region conditions would help to refine the LST estimations for this region.

Apart from the land surface temperature there are other key variables that explain the functioning of these forests. As pointed out before, evapotranspiration represents a major contribution to the water and energy exchanges of the region. In particular, the response of this variable to the changing climate is critical to understand the stability of these forests in the larger global system (Cox et al., 2000). Accurate knowledge of temporal and spatial variations of this variable is therefore of crucial importance for the complete understanding of the functioning of these forests. Nevertheless, estimation of tropical evapotranspiration is hindered by the lack of continuous and spatially dense ground-based measurements in the region. Although understanding of Amazonian forest processes has greatly advanced through the establishment of a network of eddy covariance flux towers across the Brazilian Amazon, providing continuous measurements of energy water and carbon fluxes in the context of the LBA program (Araujo et al., 2002), these measurements are temporally limited and represent point-scale information only. Remote sensing driven models are presented as an alternative feasible means to overcome this issue and provide spatially distributed ET information at regional and global scale (Mu et al., 2007, 2011; Fisher et al., 2008; Miralles et al., 2011). In order provide evapotranspiration estimates these models generally require three categories of inputs: land surface variables, surface radiation and surface meteorology inputs. At regional and global scale, land surface variables could be obtained from MODIS sensor while surface radiation/meteorology inputs are commonly derived from reanalysis models. As pointed out in Badgley et al. (2015) the quality of the derived evapotranspiration and its potential

biases is directly impacted by the uncertainty from these coarser reanalysis data. How uncertainty derived from the model assumptions (i.e. model uncertainty) in conjunction with the uncertainty derived from the difference in these input datasets is able to explain the observed variability in the estimations is a major difficulty for the accurate retrieval of this variable.

This doctoral research has been conducted in the Global Change Unit (GCU), a research group with an extensive experience in the field of thermal remote sensing including LST and ET retrieval from remote sensing data. In this thesis we present for the first time in this research group the application and development of LST and ET algorithms over the large vegetated area of the Amazon forests.

Objectives of the thesis

The aforementioned issues highlight the key role of the Amazon ecosystem in the global climate and global carbon and water cycles, as well as the potential of thermal remote sensing techniques for the monitoring of surface processes over this region. Therefore, the research activities performed during this doctoral period can be linked to three main objectives:

- I. Cloud masking using machine learning based methods.
- II. LST estimation and validation for different medium resolution sensors.
- III. Estimation of evapotranspiration from different remote-sensing models.

The accomplishment of these objectives was performed by breaking them down into the following specific objectives.

I. Cloud masking using machine learning based methods

- Evaluate the suitability of supervised machine learning methods for providing alternative MODIS cloud masking over the study region.
- Evaluate the use of collocated simultaneous observations between CPR/CALIOP and MODIS sensors as a source of training data.
- Derive of a continuous measure of cloud masking uncertainty (i.e. probability estimates) from the models that can be tuned to adapt user conditions.
- Compare the performance of six supervised methods: GNB, LDA, QDA, RF, SVM and MLP.
- Validate the models results by visual inter-comparison with images and in-situ cloud data.
- Compare the performance of the proposed approach with MODIS operational cloud masking methodologies (MYD35 and MAIAC).

II. LST estimation and validation for different medium resolution sensors

- Generate a database of simulated brightness temperatures that properly represents the atmospheric conditions of the study region.
- Based on the split-window algorithm (Sobrino & Raissouni, 2000) use the previous database in order to retrieve new algorithm coefficients for each of the sensors considered: MODIS, VIIRS and SLSTR.
- Validate the derived tuned algorithm using in-situ LST corrected for emissivity and atmospheric effects.
- Validate the current LST products for MODIS, VIIRS and SLSTR sensors and compare the results with the tuned split-window.
- Expand the validation to other spatial points using the R-based validation method for MODIS sensor.
- Compare the LST estimated from the SW and for the operational MODIS LST products at image scale by visual comparison of the spatial patterns.

III. Estimation of evapotranspiration from different remote-sensing models

- Estimate the evapotranspiration using remote-based models. In particular: PT-JPL, PM-Mu, SEBS and LSASAF algorithm.
- Validate and compare the model performance using in-situ eddy covariance data from the LBA network (scenario I).
- Consider the impact of coarse reanalysis data in the performance at image (regional) scale (scenario II) by assessing model estimates and reanalysis inputs.
- Perform a sensitivity analysis on the models in order to obtain the variable that contributes the most to model variability in scenario II.
- Compare the evapotranspiration estimates from the models considered at image scale by visual comparison of the spatial patterns and zonal means.

Thesis outline

In order to accomplish the previously stated objectives, this thesis has been structured into three main parts: background (Part I), data and methods (Part II) and results (Part III).

- **Part I** is dedicated to introduce the required background related with the methods for cloud detection using satellite imagery and the retrieval of land surface temperature and evapotranspiration from space. Chapter one is dedicated to cloud detection. After a brief review of the state-of-the-art on the topic focusing on MODIS operative cloud masks it provides a description of the supervised learning algorithms employed in this thesis together with the methodology to obtain well-calibrated probabilities. Chapter two reviews the general aspects of the radiative transfer equation in the thermal range of the electromagnetic spectrum and gives a short compilation of the current land surface temperature and emissivity

retrieval algorithms focusing on MODIS, VIIRS and SLSTR sensors. In addition, it presents the split-window technique used in this work. Chapter three provides a brief description of the water transport in the atmosphere together with an overview of the algorithms selected for evapotranspiration retrieval using remote sensing data.

- **Part II** deals with the description of the data and methodology employed. Chapter four provides an overview of the satellite sensors and meteorological reanalysis and land surface assimilation models from which we have used data. In addition, the region of study (Amazonian region) is defined and the in-situ test sites together with its instrumentation are presented. In particular, the Manacapuru test site was used for cloud mask validation, the Tambopata test site was employed in land surface temperature validations tasks and the five eddy-covariance sites belonging to the Large-Biosphere-Atmosphere network for evapotranspiration estimates validation. Chapter five addresses the data processing and methodology followed in this thesis. It is divided into the three sections corresponding to the three general objectives stated in the previous section. In section I, firstly the preprocessing of the data employed in the proposed cloud scheme is provided. In particular we used: 1) collocated MODIS and CPR/CALIOP orbits, 2) MODIS products and 3) Manacapuru test site in-situ ground cloud cover fraction derived from the Total Sky Imager. Secondly, the training and probability calibration of the six supervised classifications considered for cloud detection evaluation is provided. Finally, the methodology and statistical metrics for model evaluation are given. Section two starts with the correction of in-situ LST derived from the infrared radiometers and net radiometers installed in Tambopata test site followed by the presentation of the MODIS, VIIRS and SLSTR products employed. Then the methodology followed for the generation of simulated database of brightness temperatures, which will be used for split-window coefficients retrieval, is explained. The section ends with the validation methodology of the current satellite products and the tuned split-window algorithm derived. Two methods were used: T-based and R-based validation. Spatial patterns were also used for comparison. Section three is dedicated to the evapotranspiration retrieval methodology. Firstly, it presents the pre-processing of the in-situ eddy covariance data of the LBA sites. Secondly, it presents the processing of the reanalysis data and satellite products used. Thirdly, the soil data and the gap-filling technique aimed at providing SEBS evapotranspiration estimates for cloudy days are detailed. Next points deal with specific details on the model configuration employed and the evaluation methodology of model evapotranspiration estimates and reanalysis meteorological inputs. In particular, two different scenarios were considered depending on the meteorological data used: i) using in-situ data from LBA networks (scenario I) and ii) reanalysis datasets (scenario II). The section ends with the sensitivity analysis performed and the methodology used for the comparison of the spatial patterns.

- **Part III** addresses the results derived from the application of the methodology described in Part II. It consists in three chapters, each corresponding to a specific objective of the thesis. Chapter six presents the validation results of the probabilistic cloud masking approach followed. Apart from validation over the generated database derived from collocated satellite measurements, its performance is compared at image and in-situ scale with operative MODIS cloud masks. Discussion of these results concludes the chapter. Chapter seven presents the results of the split-window LST retrieval algorithm and its comparison with the current operative LST products for MODIS, VIIRS and SLSTR sensors. Apart from the T-based and R-based validation results, the split-window algorithm was also evaluated over the generated simulated database. For the special case of MODIS and VIIRS sensors split-window results were also compared to current products by visual comparison of the spatial patterns. The chapter concludes with the discussion of the results. Chapter eight is devoted to the intercomparison of remote-sensing based evapotranspiration algorithms. Results are presented separately for each scenario and consists of the validation of the algorithms and the comparison of the temporal evolution. Scenario II also include the results from the reanalysis quality assessment, the sensitivity analysis and the spatial patterns comparison. A brief discussion of the two scenarios is given at the end of the chapter.

The thesis ends summarizing the main conclusion and findings of the research. The work is closed by a series of appendices. Appendices A.1 to A.4 contain supplementary information from the description of the test sites and the results section. Appendix B lists the scientific articles published in relation with this thesis.

I. BACKGROUND

1. - CLOUD DETECTION METHODS

1.1. - Cloud types and classification

According to the World Meteorological Organization (WMO), a cloud is defined as a hydrometeor consisting of minute particles of liquid water or ice, or of both, suspended in the atmosphere and usually not touching the ground. It may also include larger particles of liquid water or ice, as well as non-aqueous liquid or solid particles such as those present in fumes, smokes or dust (WMO, 2017).

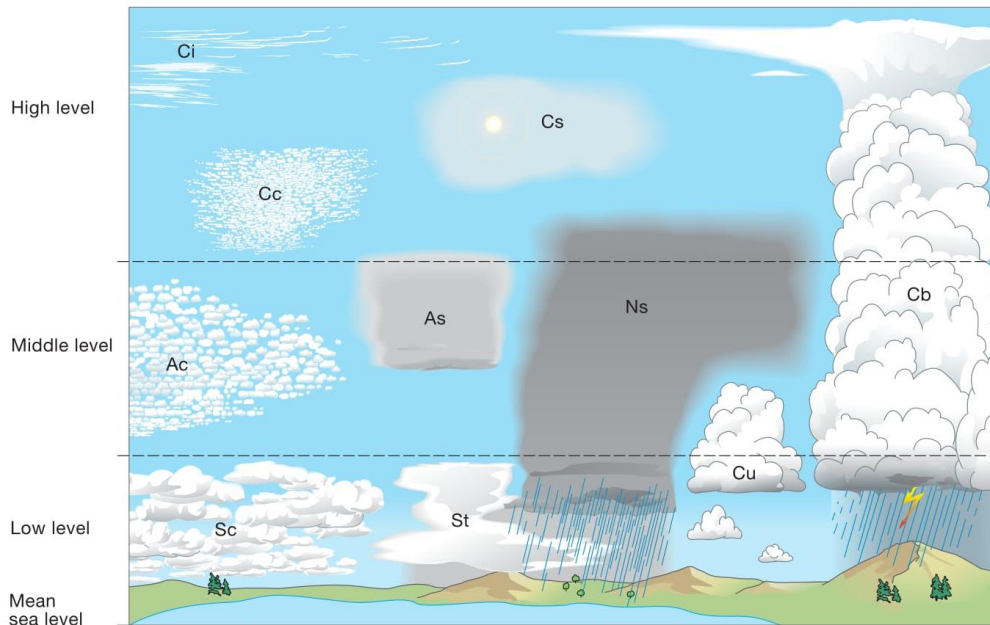


Figure 1.1: View of the 10 main cloud types: Cirrus (Ci), Cirrocumulus (Cc), Cirrostratus (Cs), Altostratus (As), Nimbostratus (Ns), Stratus (St), Stratocumulus (Sc), Cumulus (Cu), Cumulonimbus (Cb) (<https://cloudatlas.wmo.int/useful-concepts.html>).

The International Cloud Atlas of the WMO classifies cloud based on: 1) the genus, which is the main characteristic form of the cloud. 10 different types of genus exist (Figure 1.1), 2) the species, which is related to the shape of the clouds or their internal structure, 3) the varieties that define the special characteristics of the arrangement and transparency of the genus, 4) the supplementary features and accessory clouds that form near them and 5) the mother cloud, which provides the origin of the cloud (WMO, 2017). This classification is similar to the one used in plant and animal classification, and hence it also uses Latin names. It was originally developed by Howard (1804).

The 10 genus of clouds typically occur at certain ranges of heights in the troposphere (Figure 1.1). According to this, clouds are classified also by altitude: low, middle and high clouds (Table 1.1).

Table 1.1. Approximate heights of each level, and the genus occurring in each (adapted from <https://cloudatlas.wmo.int/home.html>).

Level	Genera	Composition	Polar region	Temperate region	Tropical region
High	Cirrus (Ci)	Ice crystals	3 – 8 km	5 – 13 km	6 – 18 km
	Cirrocumulus (Cc)				
	Cirrostratus (Cs)				
Middle	Altostratus (As)	Water	2 – 4km	2 – 7 km	2 – 8 km
	Nimbostratus (Ns)				
	Altostratus (As)				
Low	Stratus (St)	Water	2 km	2 km	2 km
	Stratocumulus (Sc)				
	Cumulus (Cu)				
	Cumulonimbus (Cb)				

1.2. - Review of cloud detection methods using passive remote sensing

The presence of clouds strongly affects the retrieval accuracy of atmospheric and surface parameters from passive satellite sensors. In the visible (VIS) and near infrared (NIR) parts of the electromagnetic spectrum clouds contribute to the sensor signal by attenuating the surface radiation and by reflecting radiation while in thermal infrared (TIR) region the cloud-emitted radiation superimposes the earth-emitted radiation. Depending on the characteristics of the cloud, its radiation can completely overwhelm the target radiation, thus impeding the solar radiation reaching the surface in the VIS/NIR or blocking the surface contribution in the TIR. Thus, either surface or cloud parameters retrieval need an accurate cloud identification in order to correctly separate the surface from the clouds and ensure accuracy in the results. To do so, a set of features that maximize the difference between clouds and the underlying surface is used. These features are derived from the different spectral, spatial and temporal response between clouds and others surfaces.

Cloud masking approaches differ in the way the algorithm considers these features. A major division can be made between the physically based and statistically based. In the first group, the common approach is a rule-based classification based on the physical properties of the clouds. It consists in applying a series of thresholds test on different physical features (e.g. albedo, brightness temperature). These thresholds may be static or adaptative (Di Vittorio & Emery, 2002) empirically derived or pre-calculated using radiative transfer models (RTM). Test results can be combined resulting into a binary flag or into a few cloud confidence categories (Ackerman et al., 1998). Most of the operational cloud masking applications of current earth orbiting sensors, such as MODIS (Ackerman et al., 1998), VIIRS (Godin, 2014) or Copernicus Sentinel-sensors follow this approach. In this group, it is worth noting the well-known cloud detection for LANDSAT, Fmask

(Zhu & Woodcock, 2012), which has also been applied to Sentinel-2 images (Frantz et al., 2018) and the automated cloud-cover assessment algorithm (ACCA) (Irish et al., 2000, 2006) which is also applied for LANDSAT. Other threshold based tests which are not implemented in an operational chain but they are worth mentioning are: Vemury et al. (2001), Hutchison et al. (2005), Yang et al. (2007), Luo et al. (2008), Scaramuzza et al. (2011), Sun et al. (2016) and Zhai et al. (2018). Apart from these spectral thresholds, spatial information has also been incorporated in the cloud detection method in order to improve cloud detection and classification accuracy (Christodolou et al., 2003; Li et al., 2017). Besides, several algorithms that take advantage of multi-temporal information have been proposed (Lyapustin et al., 2008; Hagolle et al., 2010; Liu et al., 2013; Zhu & Woodcock, 2014).

Statistically based cloud masking approaches differ from the physically based methods in the sense that they infer from the totality of the features considered (i.e. not individual features) the statistical properties of the underlying clear and cloudy classes considered. In the past decades, several researches has been made on this topic. For simplification, we also include in this group the machine learning techniques. In the literature we find the application of Bayesian methods to Advanced Along-Track Scanning Radiometer (AATSR) in Bulgin et al. (2018), Hollstein et al. (2014), and for the National Oceanic and Atmospheric Administration (NOAA)'s Advanced Very High Resolution Radiometer (AVHRR) in Heidinger et al. (2012) and Karlsson et al. (2015). Discriminant analysis methods were applied to the Spinning Enhanced Visible and InfraRed Imager (SEVIRI) in Amato et al. (2008). Maximum Likelihood Classification was applied in Li et al. (2003) for MODIS sensor. K-NN (nearest neighbour) was used in Ricciardelli et al. (2008) for METEOSAT Second Generation. Some examples of the SVM are Mazzoni et al. (2007), Lee et al. (2004) and Ishida et al. (2018). This latter was based on MODIS data. Neural networks have been widely applied. Some examples are: Tian (2000), Saitwal et al. (2003), Lafont et al. (2006), Jang et al. (2006), Liu et al. (2009) and more recently Hughes & Hayes (2014) for LANDSAT and Chen et al. (2018) for MODIS sensor. Other techniques include Fuzzy Logic introduced in Ghosh et al. (2006), and random forests, decision trees or stochastic gradient descent in Hollstein et al. (2016) for Sentinel-2 MultiSpectral Instrument (MSI). These previous techniques, require a reference database containing features and associated labels (clouds or clear), in order to learn the models. They are referred as supervised techniques. On the contrary unsupervised techniques do not need a labelled dataset, the algorithm acts on the information without previous guidance. The work of Gomez-Chova et al. (2007) stands out in this group apart from other techniques such as Markov Random Fields (Le-Hégarat-Masclé & André, 2009). In addition to all these methods, as a subset of machine learning methods, deep learning-based cloud detection methods benefiting from the application of deep convolutional features have achieved high accuracies in image classification tasks (Li et al., 2019; Chai et al., 2019).

For supervised techniques, in order to overcome the issue of needing training data synthetic datasets derived from RTM simulations (Chen et al. 2018) or collocated cloud data from other sensors in a common approach used (Heidinger et al., 2012; Musial et al.,

2014; Hollstein et al., 2014). For the particular case of sensors on-board the A-Train constellation, the CloudSat satellite, carrying CPR radar-sensor, and CALIPSO satellite carrying a CALIOP lidar-sensor, have been used successfully for this task for AVHRR sensor (Heidinger et al., 2012; Karlsson et al., 2015).

1.3. - MODIS cloud mask algorithms

MODIS cloud detection is currently accomplished by the MOD35 operative cloud mask. Alternative cloud masking is applied in the MAIAC suite products available as a part of the version 6 of MODIS products. In the following a brief description of these algorithms as extracted from the respective algorithm theoretical basis document (Ackerman et al., 2010; Lyapustin & Wang, 2007)) is provided.

1.3.1. - MOD35

MOD35 cloud detection algorithm uses a combination of variety of spectral and spatial variability thresholds in order to provide the level of confidence of a pixel being clear (Ackerman et al., 1998). Briefly, the process is as follows: a pixel is assigned to a particular domain according to the surface type (water, land, snow, coastline and desert) and illumination characteristics (daytime or nighttime). Next, a series of threshold tests are applied, returning each test with a confidence level (from 0 (low) to 1 (high)) that the pixel is clear. The election of the particular tests employed is determined by the former assignation of the pixel to a specific domain (Table 1.2). These test results are arranged into five different groups according to their cloud distinction capability. A minimum confidence level of all the tests grouped together is considered representative of each group (i.e. $G_{j=1,..,5} = \min[F_i]$, where F_i are the test results within a group, and $G_{j=1,..,5}$ are the group confidences). Eventually, the product of all these minimum values give the definitive confidence of the pixel being clear. This level is assessed using four different categories: confident clear (>99%), probably clear (>95%), uncertain/probably cloudy (>66%) and cloudy (<66%).

Inputs to the cloud masking algorithm include level 1B MODIS radiance data (channels, B1, B2, B4, B5, B6, B7, B17, B18, B19, B20, B22, B26, B27, B28, B29, B31, B32, B33 and B35) together with ancillary data: viewing geometry, land water map and topography from MOD03 product. Apart from daily snow/ice map provided by National Snow and Ice Data Center (NSIDC) and daily sea ice concentration product from NOAA.

Table 1.2. MODIS cloud test executed for a given processing path: daytime ocean (DO), nighttime ocean (NO), daytime land (DL), nighttime land (NL), polar daytime (PD), polar nighttime (PN), coastal daytime (CD), coastal nighttime (CN), desert daytime (DD) and desert nighttime (DN) (Ackerman et al., 2010).

Test	DO	NO	DL	NL	PD	PN	CD	CN	DD	DN
<i>BT</i> ₁₁	X	X								
<i>BT</i> _{13.9}	X	X	X	X	X	X	X	X		X
<i>BT</i> _{6.7}	X	X	X	X	X	X	X	X	X	
<i>R</i> _{1.38}	X		X		X		X		X	X
<i>BT</i> _{3.9} – <i>BT</i> ₁₂				X		X				X
(<i>BT</i> _{8.6} – <i>BT</i> ₁₁) & (<i>BT</i> ₁₁ – <i>BT</i> ₁₂)	X	X	X	X	X	X	X	X	X	X
<i>BT</i> ₁₁ – <i>BT</i> _{3.9}	X	X	X	X	X	X	X	X	X	
<i>R</i> _{0.66} <i>R</i> _{0.87}	X		X				X	X		
<i>R</i> _{0.87} / <i>R</i> _{0.66}	X		X							X
<i>BT</i> _{7.3} – <i>BT</i> ₁₁				X		X				
Surface Temperature test	X	X		X						
<i>BT</i> _{8.6} – <i>BT</i> _{7.3}		X								
<i>BT</i> ₁₁ variability test		X								

1.3.2. - MAIAC

MAIAC is a new land and inland water cloud mask algorithm developed as a part of the multi-angle implementation of the atmospheric correction algorithm for the MODIS sensor (Lyapustin et al., 2008). In contrast to the static MODIS cloud mask, this algorithm benefits from the use of temporal information, which is employed in the generation of a pre-built reference images used as a target comparison. Covariance analysis is used to build the reference images. This algorithm also possesses a dynamic land-water-snow mask which guides the surface and aerosol retrieval in rapid changing conditions, such as fires and flood (Lyapustin & Wang, 2007). The cloud mask is actually updated during these retrievals. In Figure 1.2, the general flowchart of the algorithm is shown.

The process is as follows. In a first place, a series of tests (snow, cirrus and clear-sky) are applied to the received tiles. If after these tests, the block is declared cloud-free then the reference cloud image (*refcm*) is updated and the algorithm proceeds to complete the land type classification (*confirm_LWSmask*). If the block has clouds, a further analysis of covariance is performed. In case, there is no available *refcm* the algorithm waits until new data arrives. At pixel level, clouds are identified by direct comparison with the *refcm* data, based on the fact that clouds are brighter and colder than the background. The reference surface pixel comes from the *refcm* and the estimates of brightness temperature comes from the clear land pixels detected by spectral tests for a given block or from the cloud-

free neighbor blocks identified by high covariance (Lyapustin et al., 2008). In case the covariance of the block is high, the algorithm first tries to initialize the *refcm*. *CM_highCov*, and *CM_lowCov* modules are responsible of providing the pixel level classification. Module *initRefcm* produces cloud mask only if initialization is successful.

The *MAIAC* cloud mask algorithm uses as an input five 500 m resolution MODIS bands B1, B2, B4, B5, B7, a 1 km band B26, and 1 km thermal bands B31, B32. As an output, it produces an integral cloud mask with values of *CM_CLEAR* for clear conditions and *CM_PLOUD* (possibly cloud) or *CM_CLOUD* for cloudy conditions.

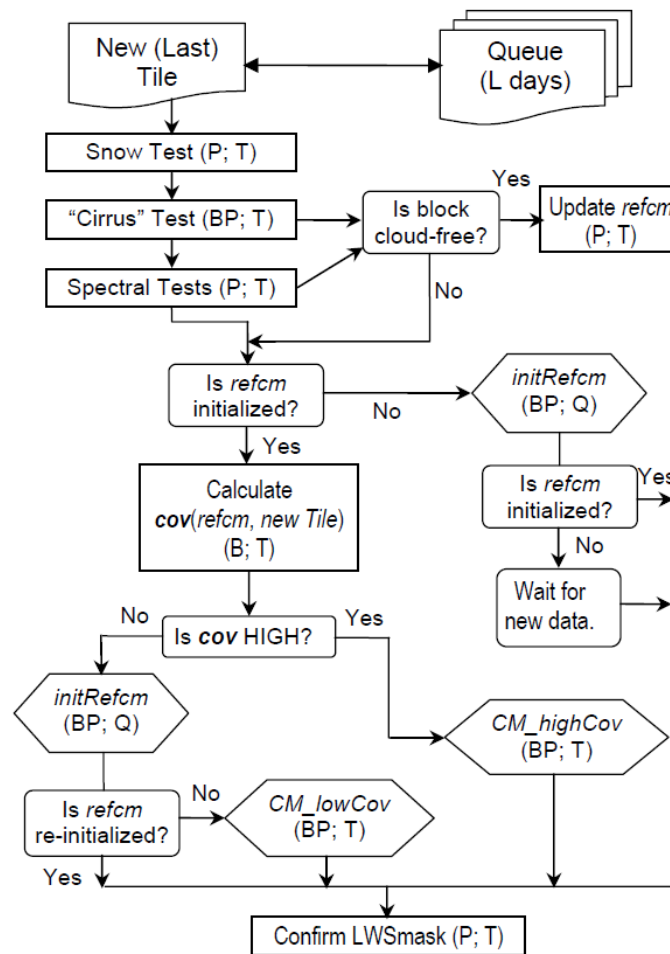


Figure 1.2. The general flowchart of *MAIAC* cloud mask algorithm. Here, rectangles represent separate functions, diamond shapes stand for the separate subroutines (algorithms), and round-corner rectangles indicate decision (branching) points. The letters in parentheses show spatial and temporal domains of operations at pixel- (P) and/or block- (B) level, and using the data of the last Tile (T) only or using the full time series of the Queue (Q) (Lyapustin & Wang, 2007). MODIS 1LB data granules are split into 600 km Tiles (T), which are further split into blocks (B) of 25 km x 25 km for the covariance analysis.

1.4. - Reference machine learning and statistical methods for cloud detection

Classification in the context of remote sensing can be understood as the process in which every pixel in the original image is assigned a label that corresponds to one of the pre-definite classes. A categorical map is obtained as a result. From a statistical point of view, a classifier can be defined as a function $f: \Phi \rightarrow \Omega$, where Φ refers to the observational space (all the possible values that an observation can take) and Ω to the classes space (the classes in which to classify the observations). Each observation is defined as $x = [x^1, x^2, \dots, x^D]$ where D is the total number of features. f is also called decision-function. In this learning of the mapping function a difference is made between the case we have labelled data (i.e. class labels and associated observations) or not. In the first case, it is called supervised learning, while in the second case it is called unsupervised learning. In this study, we have focused on supervised learning in order to accomplish the goal of detecting cloud using remote sensing data. In the following a brief description of the reference machine learning and statistical methods used is given. This review has been based on the bibliographic revision of the works of Hastie et al. (2005), Bishop (2006) and Mather & Tso (2016). We refer the reader to these works for a deeper description of the methods.

1.4.1.- Naïve Bayes

Bayes theorem is expressed in Equation 1.1. It states that the posterior probability $P(y_k|x)$ is the product of the prior probability $P(y_k)$ by the conditional probability $P(x|y_k)$ divided by the marginal probability $P(x)$. $P(y_k|x)$ is the probability that an object belongs to class y_k given the observation is x . $P(y_k)$ represents the knowledge that we have about the class before the observations are available. $P(x|y_k)$ represents the likelihood of an observation x given their class y_k . $P(x)$ is calculated as $\sum_i^k P(x|y_k)P(y_k)$.

$$P(y_k|x) = \frac{P(y_k)P(x|y_k)}{P(x)} \quad (1.1)$$

The pixel i will be allocated into the class k that has the largest $P(y_k|x)$ value (Equation 1.2). This classification criterion is called as Maximum a Posteriori (MAP).

$$y_k = \operatorname{argmax} \left(P(y_j|x) \right) \forall y_j \quad (1.2)$$

Since in general $P(x)$ is set to be uniform, Equation 1.2 can be rewritten as in Equation 1.3.

$$y_k = \operatorname{argmax} \left(P(y_j)P(x|y_j) \right) \forall y_j \quad (1.3)$$

The particularity of the naïve bayes classifier is that it assumes that features are conditionally independent (i.e. naïve assumption). In this case $P(x|y_k)$ can be calculated as $P(x|y_k) = \prod_i^D P(x_i|y_k)$, where $P(x_i|y)$ is assumed to be Gaussian (Equation 1.4), where μ_y and σ_y are the mean and covariance class values. In addition, $P(y_k)$ can be easily derived as the relative frequency of class y_k in the training dataset.

$$P(x_i|y) = \frac{1}{\sqrt{2\pi\sigma_y^2}} \exp\left(-\frac{(x_i - \mu_y)^2}{2\sigma_y^2}\right) \quad (1.4)$$

1.4.2. - Linear and Quadratic Discriminant Analysis

These algorithms also use Bayes Theorem in order to provide class predictions estimates. In this case however, $P(x|y_k)$ is modelled as a multivariate Gaussian distribution with density given by Equation 1.5, where Σ_y are the covariance matrixes and μ_y are the class means for the classes considered.

$$P(x|y_k) = \frac{1}{(2\pi)^{\frac{D}{2}} |\Sigma_{y_k}|^{\frac{1}{2}}} \exp\left(-\frac{1}{2}(x - \mu_{y_k})^T \Sigma_{y_k}^{-1} (x - \mu_{y_k})\right) \quad (1.5)$$

Introducing Equations 1.5 into 1.3 and taking logarithms in order to eliminate the exponent, we have the following expression (Equation 1.6).

$$\begin{aligned} y_k &= \operatorname{argmax} \left\{ -\frac{1}{2} \ln |\Sigma_{y_k}| + \ln P(y_k) - \frac{1}{2} (z - \mu_k)^T \Sigma_{y_k}^{-1} (z - \mu_k) \right\} \\ &= \operatorname{argmax} \left\{ -\ln |\Sigma_{y_k}| + 2 \ln P(y_k) - \mu_k^T \Sigma_{y_k}^{-1} \mu_k + 2z^T \Sigma_{y_k}^{-1} \mu_k - z^T \Sigma_{y_k}^{-1} z \right\} \end{aligned} \quad (1.6)$$

A classifier according to Equation 1.6 is called a quadratic classifier and the decision function is a quadratic decision function (quadratic dependence in z). The boundaries between the compartments of such a decision function are pieces of quadratic hypersurfaces in the N-dimensional space. This is the case of the quadratic discriminant analysis. Taking the special case when $\Sigma_{y_k} = \Sigma$ and after making the necessary calculation, leads to the situation of Equation 1.7.

$$y_k = \operatorname{argmax} \{ 2 \ln P(y_k) - \mu_k^T \Sigma^{-1} \mu_k + z^T 2 \Sigma^{-1} \mu_k \} \quad (1.7)$$

As we observe the quadratic dependence has disappeared and the decision function takes a form that is linear. This corresponding classifier is called a linear classifier and corresponds to the Linear Discriminant Analysis.

1.4.3.- Random Forests

Random Forests is an ensemble learning method used for combining predictions of multiple decisions trees. In order the trees to be de-correlated each tree is built from different training datasets derived by bagging (i.e. sample with replacement from the original dataset). In addition, random subsets of features are considered at each candidate splits. Trees are fully grown (i.e. without pruning). Briefly explaining the algorithm is as follows. For each of the trees considered draw a bootstrap sample from the training data. Then grow a random forest tree, by recursively repeating the following steps for each terminal node of the tree, until the tree is fully-grown (minimum node size is one): 1) select $p \leq D$ variables at random. The default value for p is \sqrt{D} although it depends on the problem and thus should be treated as a tuning parameter. 2) Pick the best variable/split point among the p features and 3) split the node into two daughter nodes. In step 2, at each node m considering the splitting variable j and the split-point s the candidate split $\theta = (j, t_m)$ partitions the data (Q) into two subsets $Q_{left}(\theta) = (x, y)|x_j \leq t_m$ and $Q_{right}(\theta) = (x, y)|x_j > t_m$. The best splitting point is selected as the one that minimises the impurity the node impurity given by Equation 1.8.

$$G(Q, \theta) = \frac{n_{left}}{N_m} H(Q_{left}(\theta)) + \frac{n_{right}}{N_m} H(Q_{right}(\theta)) \quad (1.8)$$

where N_m is the number of observations of the region given by the node m and n_{left} and n_{right} are the numbers of observations for the left and right regions respectively. As a measure of impurity Gini index is commonly used. It is given by Equation 1.9, where p_{mk} is the proportion of class k observations in node m .

$$H = \sum_{k=1}^K p_{mk}(1 - p_{mk}) \quad (1.9)$$

Random forest is grown up to a defined number of trees (n_{trees}). The final classification decision is taken as the majority vote between all the trees class predictions. The most important parameters to tune in random forests are the number of trees and the maximum depth of the tree (m_{depth}). n_{trees} corresponds in a monotonic decrease of the prediction error, while m_{depth} is related to the generalization ability of the forests.

1.4.4. - Support Vector Machines

Given N pairs of training data with $x_i \in \mathbb{R}^D$ and $y_i \in \{-1, 1\}$, and assuming the two classes are separable (i.e. no overlapping between classes Figure 1.3 (a)) the task of a support vector classifier is to find the hyperplane defined by $f(x) = x^T \beta + \beta_0 = 0$ (where β is the normal to the optimal decision hyperplane and β_0 represents the closest distance to the origin of the coordinate system) that maximizes the margin (M in Figure

1.3) between the training points for class +1 and -1. Defining $\|\beta\| = 1/M$, the optimization problem is given by Equation 1.10.

$$\begin{aligned} \min \frac{1}{2} \|\beta\| \quad \forall \beta, \beta_0 \\ \text{subject to } y_i(x_i^T \beta + \beta_0) \geq 1, i = 1, \dots, N \end{aligned} \quad (1.10)$$

In practice, however the constraints in Equation 1.10 cannot be satisfied as the classes can overlapped in the feature space (Figure 1.3 (b)). In order to relax these constraints we defined the slack variables, $\xi = (\xi_1, \xi_2, \xi_3, \dots, \xi_N)$ which are proportional to some measure of cost. With this, the optimization problem is given by Equation 1.11.

$$\begin{aligned} \min \frac{1}{2} \|\beta\| + C \sum_{i=1}^N \xi_i \quad \forall \beta, \beta_0 \\ \text{subject to } \xi_i \geq 0, y_i(x_i^T \beta + \beta_0) \geq 1 - \xi_i, i = 1, \dots, N \end{aligned} \quad (1.11)$$

The first part in Equation 1.11 aims to maximize the margin while the second part seeks to penalize the training sample located on the wrong side of the decision boundary. This is done by the parameter C .

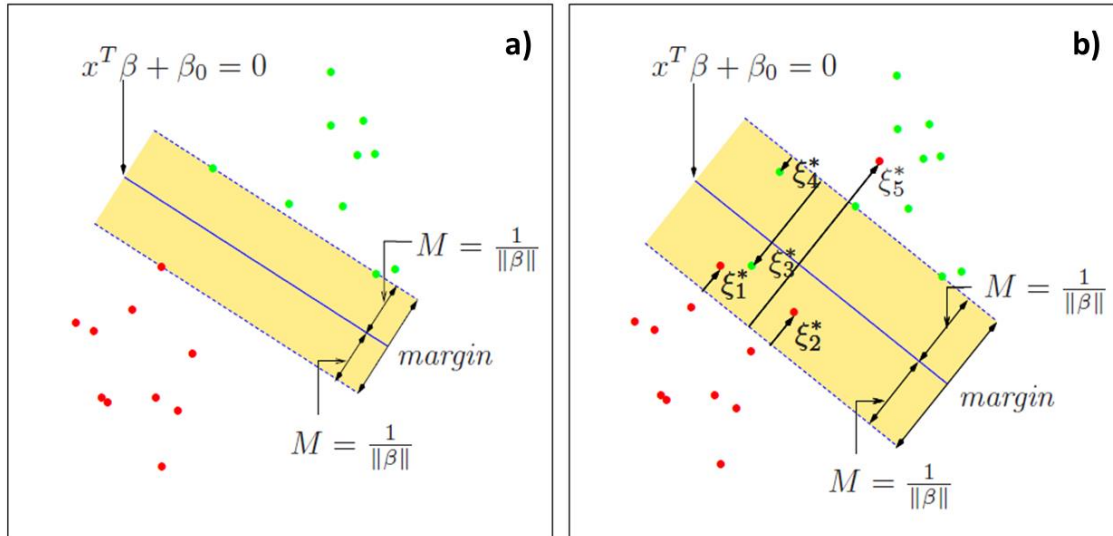


Figure 1.3. Support vector classifiers. Separable case is shown in panel a). The decision boundary is the solid line, while broken lines bound the shaded maximal margin of width $2M = 2/\|\beta\|$. Panel b) shows the non-separable (overlap) case. The points labeled ξ_j^* are on the wrong side of their margin by an amount $\xi_j^* = M\xi_j$; points on the correct side have $\xi_j^* = 0$. The margin is maximized subject to a total budget $\sum \xi_i \leq ct$. Hence $\sum \xi_j^*$ is the total distance of points on the wrong side of their margin (Hastie et al., 2005).

In order to solve the problem in Equation 1.11 we apply Lagrange multipliers. The Lagrangian (primal) function is given by Equation 1.12, where $\alpha_i \geq 0$ and $\mu_i \geq 0$ are the Lagrangian multipliers.

$$L_P = \frac{1}{2} \|\beta\|^2 + C \sum_{i=1}^N \xi_i - \sum_{i=1}^N \alpha_i [y_i(x_i^T \beta + \beta_0) - (1 - \xi_i)] - \sum_{i=1}^N \mu_i \xi_i \quad (1.12)$$

In addition, the corresponding Karush-Kuhn-Tucker conditions are: $\alpha_i \geq 0$, $\mu_i \geq 0$, $\xi_i \geq 0$, $\mu_i \xi_i = 0$, $\alpha_i [y_i(x_i^T \beta + \beta_0) - (1 - \xi_i)] = 0$ and $y_i(x_i^T \beta + \beta_0) - (1 - \xi_i) \geq 0, \forall i$. In order to solve the Equation 1.12 we want to minimize it with respect to β , β_0 and ξ_i . Setting the derivatives of L_P equal to 0 we obtain Equations 1.13 to 1.15

$$\frac{\partial L}{\partial \beta} = 0 \Rightarrow \beta = \sum_{i=1}^N \alpha_i y_i x_i \quad (1.13)$$

$$\frac{\partial L}{\partial \beta_0} = 0 \Rightarrow 0 = \sum_{i=1}^N \alpha_i y_i \quad (1.14)$$

$$\frac{\partial L}{\partial \xi_i} = 0 \Rightarrow \alpha_i = C - \mu_i \quad (1.15)$$

By substituting Equations 1.13-1.15 into Equation 1.12 we obtain the Lagrangian dual objective function. The problem in Equation 1.12 is thus transformed in maximizing Equation 1.16 with respect to the Lagrangian multipliers α_i .

$$L_D = \sum_{i=1}^N \alpha_i - \frac{1}{2} \sum_{i=1}^N \sum_{i'=1}^N \alpha_i \alpha_{i'} y_i y_{i'} x_i^T x_{i'} \quad (1.16)$$

subject to $0 \leq \alpha_i \leq C, \sum_{i=1}^N \alpha_i y_i = 0$

From Equation 1.16 we see that the solution for β has the form of $\beta = \sum_{i=1}^N \alpha_i y_i x_i$. In this expression only nonzero $\hat{\alpha}_i$ accounts for the solution. These observations are called the support vectors. Among these support vector points, some will lie in the edge of the margin ($\xi_i = 0$) and hence will be characterized by $0 < \alpha_i < C$. These can be used to solve for β_0 . Typically, an average of all the solutions is used for numerical stability. The remainder points ($\xi_i > 0$) have $\alpha_i = C$. Once the solutions of β and β_0 are known the decision function can be written as in Equation 1.17. The tuning parameters of this procedure is the cost parameter C .

$$f(x) = \text{sgn} \left(\sum_{i=1}^N y_i \alpha_i x_i^T x_j + \beta_0 \right) \quad (1.17)$$

There are some cases that a linear hyperplane is unable to separate the classes appropriately. In this situation, the training samples are projected into a higher dimensional space, \mathcal{H} , via a nonlinear vector mapping function $\Phi: \mathbb{R}^D \rightarrow \mathcal{H}$ (Figure 1.4). In this higher dimensional space, the separability between classes is increased. In order to account for this change, the feature vector x and training samples x_i must be changed by their mapped values (i.e. $\Phi(x)$ and $\Phi(x_i)$, respectively) in the previous equations. It is worth noting that in Equations 1.16 and 1.17 these mapping occurs in the form of inner products (i.e. $\langle \Phi(x_i), \Phi(x_j) \rangle$). Thus, we need not to specify the transformation Φ at all, but only the knowledge of the kernel function defined as in Equation 1.18 that computes inner products in the transformed space. This Kernel needs to satisfy Mercer's conditions (Mather, 2009).

$$K(x_i, x_j) = \langle \Phi(x_i), \Phi(x_j) \rangle \quad (1.18)$$

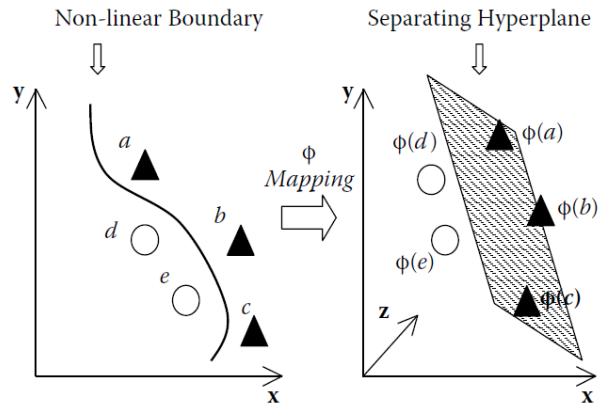


Figure 1.4. Sketch of the mapping of the Support vector machine into higher dimension. In the linearly non-separable case, Support Vector Machine maps the raw data into a higher dimension in order to increase the separability between classes (Mather, 2009).

1.4.5.- Multi-layer Perceptron

A multilayer perceptron is a class of feedforward artificial neural network. It consists of at least three layers: an input layer, a hidden layer and an output layer. In a first place, the input variables x_1, \dots, x_D (i.e. the same as features) are combined in a set of M linear combinations, where M corresponds to the number of hidden units (Figure 1.5). Equation 1.19 gives these combinations.

$$a_j = \sum_{i=1}^D w_{ji}^1 x_i + w_{j0}^1 \quad (1.19)$$

where $j = 1, \dots, M$, and the superscript 1 indicates that the corresponding parameters are in the first layer of the networks. The parameters w_{ji} and w_{j0} refer to the weights and biases respectively. a_j is known as activation. Each of them is then transformed using a differentiable, non-linear activation function $h()$ in order to give the so-called hidden units (i.e. $z_j = h(a_j)$). A general election is the logistic sigmoid function (i.e. $\sigma(a) = 1 / (1 + \exp(-a))$).

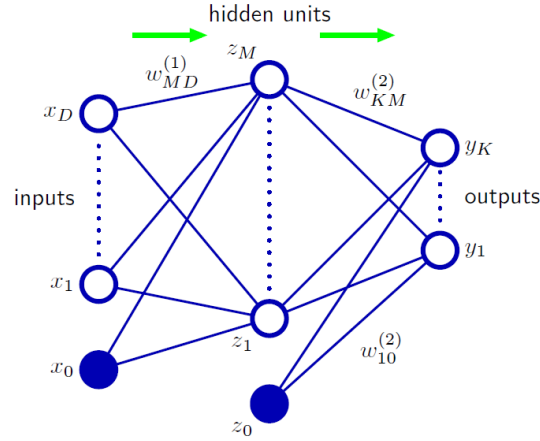


Figure 1.5. Network diagram for the two-layer neural network. The input, hidden and output variables are represented by nodes, and the weight parameters are represented by links between the nodes, in which the bias parameters are denoted by links coming from additional input and hidden variables x_0 and z_0 . Arrows denote the direction of information flow through the network during forward propagation (Bishop, 2006).

Values z_j are again linearly combined (Equation 1.20) in order to give the activation outputs, where the superscript 2 indicates that it is the second layer and $k = 1, \dots, K$ is the total number of output nodes.

$$a_k = \sum_{j=1}^M w_{kj}^2 z_j + w_{k0}^2 \quad (1.20)$$

Finally, the output activations a_k are transformed using an appropriate activation function depending on the nature of the data (i.e. binary classification uses a logistic sigmoid, multiclass classification a softmax activation and standard regression the identity function). The different stages can be combined and give Equation 1.21.

$$y_k(x, w) = \sigma\left(\sum_{j=1}^M w_{kj}^2 h\left(\sum_{i=1}^D w_{ji}^1 x_i + w_{j0}^1\right) + w_{k0}^2\right) \quad (1.21)$$

In order the MLP to fit the training data properly the weights parameters need to be adjusted (i.e. to train the MLP). This is done by minimizing a measure error of the fit. For classification problems, this is the standard cross-entropy loss function (Equation 1.22).

$$L(w) = - \sum_i^N y_i \ln \hat{y}_i - (1 - y_i) \ln(1 - \hat{y}_i) + \frac{1}{2} \alpha \|w\|^2 \quad (1.22)$$

where \hat{y}_i refer to the target vectors and y_i to the class predictions estimates. The term $(1/2) \alpha \|w\|^2$ is a L-2 regularization term that penalizes complex models. α controls the magnitude of the penalty.

The minimization of Equation 1.22 is obtained by the so-called back-propagation method. This consists in two main steps. In the first one, the current weights are fixed (initial random weights for first application) and then the MLP is feed forward (i.e. predictions estimates are obtained from Equation 1.21). In the second step, the loss error is back-propagated into the network and used in order to compute new values for the weights. This can be achieved by gradient descent (Equation 1.23).

$$w^{(\tau+1)} = w^\tau - \eta \nabla \text{Loss}_w^\tau \quad (1.23)$$

where $(\nabla \text{Loss}_w^\tau)$ is the gradient of the loss with respect to the weights, η is the learning rate with a value larger than 0 and τ refers to the iteration step. The algorithm stops when it reaches a maximum number of iterations or when the improvement in the loss is below a certain small threshold. Training of the MLP needs selecting a structure (number of hidden layers (n_{hlayers}) and nodes (n_{hnodes}) per layer), an activation function, a learning rate and alpha regularization parameter in order to prevent overfitting.

1.5. - Probability calibration

Most supervised learning methods produce classifiers that output score values which can be used to rank the examples in the test set from the most probable to the least probable member of a given class (Zadrozny & Elkan, 2002). Nevertheless, for several applications this ranking is not enough as what is needed is accurate and correctly calibrated estimates of the true probability that each class example is a member of the class of interest. In order to transform this model ranking into accurate probability estimates a calibration method needs to be applied. A classifier is said to be perfectly calibrated when for a sample or bin of examples with predicted probability p for the positive class, the expected proportion of positives is equal to p . Intuitively, if we consider all the examples to which a classifier assigns a score 0.8, then 80% of these examples should be members of the class in question. In the following, we focus on two common used methods: the Platt Scaling (Platt, 1999) and Isotonic regression (Zadrozny & Elkan, 2001-2002). These methods are applicable only to binary classifiers. For multiclass classification, the solution consists into decomposing the problem into many binary classifiers, calibrate them and then combine the results.

Following, Zadrozny & Elkan (2002) notation, the two classes considered are denoted as positive and negative class respectively, i.e. $y_k \in \{-1, +1\}$. The aim of the calibration is, given a scoring or membership value f provided by a classifier, to calculate the probability of the positive and negative classes (i.e. $P_{cal}(+1|f)$ and $P_{cal}(-1|f)$). Conditional probabilities for the negative class are usually estimated as the complement of the positive class. In the case of Platt's Scaling and Isotonic regression, this is accomplished via a mapping function. In Platt's method, the idea is to apply a sigmoid function to the values of $P_{cal}(+1|f)$ as given by Equation 1.24.

$$P_{cal}(+1|f) = \frac{1}{1 + \exp(A \cdot m + B)} \quad (1.24)$$

where parameters A and B are determined by minimising the negative log-likelihood of the training data (Equation 1.25).

$$\operatorname{argmin} \left\{ - \sum_i^N c_i \ln(P_{cal}(+1|f)) - (1 - c_i) \ln(1 - P_{cal}(+1|f)) \right\} \quad (1.25)$$

In order to avoid overfitting of the training data, this equation uses noisy class labels (c_i) such that for y_+ it takes the value of $c_i = (N_+ + 1)/(N_+ + 2)$ and for y_- the value of $c_i = 1/(N_- + 2)$. N_+ and N_- refer to the number of positive and negative samples in the training dataset.

In the case of the Isotonic regression method, the function is given by Equation 1.26, where s is an isotonic (monotonically increasing) function and ϵ_i is an individual error term.

$$P_{cal}(+1|f) = s(f_i) + \epsilon_i \quad (1.26)$$

Given the training dataset (f_i, y_i) , the Isotonic regression problem is finding an isotonic function \hat{s} such that (Equation 1.27):

$$\hat{s} = \operatorname{argmin} \sum (y_i - s(f_i))^2 \quad (1.27)$$

In order to constrain the function to $[0,1]$, true class binary labels are modified (i.e. $y_i \in \{0,1\}$). One algorithm that finds a stepwise constant solution for this problem is the pair-adjacent violators (PAV) (Ayer et al., 1955). Briefly explaining the algorithm is as follows. Suppose we have a set of examples $\{x_i\}_i^N$ for which we know the true labels. We first sort them according to their scores (descendant order). Then we assign true positive examples (i.e. one of the two classes considered) a calibrated probability ($P_{cal}(x_i)$) of 1 and true negative examples (i.e. the other class) a calibrated probability of 0. We thus have a calibrated probability (P_{cal}) succession of 1s and 0s following a score descendant order. The idea of PAV algorithm is that this probability sequence is isotonic (i.e. $P_{cal}(i + 1) \geq P_{cal}(i)$). If this is not the case, for each pair of consecutive probabilities such that $P_{cal}(i) \geq P_{cal}(i + 1)$ the PAV algorithm replaces both of them by their probability average $(P_{cal}(i) + P_{cal}(i + 1))/2$. This process is repeated (using the new values) until

an isotonic set is reached. At the end, PAV provides a set of intervals that accomplish the isotonic assumption and a probability estimate for each of them. To obtain an estimate for a test sample x_i , we find the interval i for which the score value of x_i is between the lowest and the highest scores in the interval and assign $P_{cal}(i)$ as the probability estimate for x_i . If the classifier scores the examples perfectly (one that scores all positives as 1 and negatives as 0) the estimated $P_{cal}(i)$ remains unchanged. Nevertheless, if the scores do not give any information about the ordering of the examples, $P_{cal}(i)$ will be a constant function whose value is the average of all $P_{cal}(x_i)$ values in the interval, which is the base rate of positive examples (i.e. it returns the fractions of positive examples in that interval).

2.- LAND SURFACE TEMPERATURE RETRIEVAL FROM SPACE

2.- Land surface temperature retrieval from space

2.1. Radiative Transfer Equation

A black body is a system in thermal equilibrium that absorbs all incident electromagnetic radiation and does not reflect any. In addition, it isotropically emits the greatest amount of energy (i.e. and ideal emitter) at a given temperature. The radiation emitted at a wavelength λ and temperature T is described by Planck's law (Equation 2.1).

$$B_{\lambda}(T) = \frac{c_1 \lambda^{-5}}{\exp\left(\frac{c_2}{\lambda T}\right) - 1} \quad (2.1)$$

where $B_{\lambda}(T)$ is the spectral radiance of a black-body ($\text{Wm}^{-2}\mu\text{m}^{-1}\text{sr}^{-1}$) at temperature T (K) and wavelength λ (μm). c_1 and c_2 are physical constants with values $c_1 = 1.191 \cdot 10^8 \text{ W}\mu\text{m}^{-4}\text{sr}^{-1}\text{m}^{-2}$, $c_2 = 1.439 \cdot 10^4 \mu\text{mK}$. Most of natural objects do not correspond to the definition of a black body, and their emissivity ε needs to be considered. Hemispheric spectral emissivity of a natural body is defined as in Equation 2.2.

$$\varepsilon(\lambda, T) = \frac{M(\lambda, T)}{M_b(\lambda, T)} \quad (2.2)$$

where $M(\lambda, T)$ is the object exitance in Wm^{-2} and $M_b(\lambda, T)$ is the isothermal blackbody exitance (Wm^{-2}). $\varepsilon(\lambda, T)$ depicts the object's capacity for emitting thermal radiation and it is determined by the object's composition and physical status. Depending on the value of ε , objects can be classified as perfect radiators (blackbodies) in which $\varepsilon(\lambda) = \varepsilon = 1$, grey bodies for which $0 < \varepsilon(\lambda) < 1$ being $\varepsilon(\lambda)$ constant and perfect reflectors when $\varepsilon(\lambda) = \varepsilon = 0$. Nevertheless, the most common case is having an object which emissivity as an λ dependence (i.e. $\varepsilon(\lambda) = f(\lambda)$) which is denoted as a selective radiator. In this case, the object can be characterized by its own spectral signature.

In order to define the radiance of natural body we need to introduce the notion of directional spectral emissivity which is given by Equation 2.3.

$$\varepsilon_{\lambda}(\theta, \varphi, T) = \frac{L_{\lambda}(\theta, \varphi, T)}{B_{\lambda}(T)} \quad (2.3)$$

where $L_{\lambda}(\theta, \varphi, T)$ is the radiance of the real object and $B_{\lambda}(T)$ is the radiance of the blackbody. As observed in Equation 2.3, the emission process presents directional effects, thus emissivity is dependent on the direction. In the case the emitting surface is Lambertian $\varepsilon_{\lambda}(\theta, \varphi, T) = \varepsilon_{\lambda}(T)$ in all directions. From Equation 2.3, the radiance of a natural body can be defined as in Equation 2.4.

$$L_{\lambda}(\theta, \varphi, T) = \varepsilon_{\lambda}(\theta, \varphi, T)B_{\lambda}(T) \quad (2.4)$$

In addition, from Equation 2.4 it is possible to define a brightness temperature (T_b) (or blackbody equivalent temperature) as the temperature of a blackbody that emits the same

radiance $L_\lambda(\theta, \varphi, T)$ of the natural body at temperature T , according to (Equation 2.5). T_b has the dimensions of temperature but lacks the physical meaning of temperature.

$$L_\lambda(\theta, \varphi, T) = \varepsilon_\lambda(\theta, \varphi, T)B_\lambda(T) = B_\lambda(T_b) \quad (2.5)$$

Radiation emitted by the surface suffers different processes when crossing the atmosphere. Assuming a cloud-free atmosphere in thermodynamic equilibrium (Figure 2.1), following Li et al. (2013) notation the channel infrared radiance (I_i), received by a sensor at the top of the atmosphere (TOA) is given by Equation 2.6:

$$I(\theta, \varphi) = R_i(\theta, \varphi)\tau_i(\theta, \varphi) + R_{at_i\uparrow}(\theta, \varphi) + R_{sl\uparrow}(\theta, \varphi) \quad (2.6)$$

where the measured I_i comes from the contribution of three terms: $R_i(\theta, \varphi)\tau_i(\theta, \varphi)$ which is the surface outgoing radiation attenuated by the atmosphere (path 1 in Figure 2.1). $R_i(\theta, \varphi)$ is the land leaving radiance and $\tau_i(\theta, \varphi)$ is the atmospheric transmissivity. $R_{at_i\uparrow}(\theta, \varphi)$ which is an atmospheric emission term represents the upward thermal radiance (path 2 in Figure 2.1), $R_{sl\uparrow}(\theta, \varphi)$ which is the atmospheric scattering term represents the upward solar radiance (path 3 in Figure 2.1). θ and φ represent the zenithal and azimuthal viewing angles. The channel radiance R_i observed in channel i at ground level is given by Equation 2.7.

$$R_i(\theta, \varphi) = \varepsilon_i(\theta, \varphi)B_i(T_s) + [1 - \varepsilon_i(\theta, \varphi)]R_{at_i\downarrow}(\theta, \varphi) + [1 - \varepsilon_i(\theta, \varphi)]R_{sl\downarrow}(\theta, \varphi) + \rho_{bi}(\theta, \varphi, \theta_s, \varphi_s)E_i \cos(\theta_s) \tau_i(\theta_s, \varphi_s) \quad (2.7)$$

$R_i(\theta, \varphi)$ comes from the contribution of four terms: $\varepsilon_i(\theta, \varphi)B_i(T_s)$ which represents the surface emission (path 4 in Figure 2.1). $\varepsilon_i(\theta, \varphi)$ and T_s are the effective surface emissivity and temperature. $[1 - \varepsilon_i(\theta, \varphi)]R_{at_i\downarrow}(\theta, \varphi)$ term represents the surface reflected down-welling atmospheric emission (path 5 in Figure 2.1). $R_{at_i\downarrow}(\theta, \varphi)$ is the downward atmospheric thermal radiance. $[1 - \varepsilon_i(\theta, \varphi)]R_{sl\downarrow}(\theta, \varphi)$ is the solar diffusion radiance reflected by the surface (path 6 in Figure 2.1). $R_{sl\downarrow}(\theta, \varphi)$ is the downward solar diffusion radiance. The fourth term is given by $\rho_{bi}(\theta, \varphi, \theta_s, \varphi_s)E_i \cos(\theta_s) \tau_i(\theta_s, \varphi_s)$ and represents the direct solar radiance reflected by the surface (path 7, in Figure 2.1). $\rho_{bi}(\theta, \varphi, \theta_s, \varphi_s)$ is the bi-directional reflectivity of the surface, E_i is the Top-of-Atmosphere (TOA) solar irradiance and θ_s, φ_s the solar zenith and solar azimuth, respectively.

In Equations 2.6 and 2.7, all variables and parameters are channel-effective values. The spectral quantities are averaged by the spectral response of the sensor according to Equation 2.8.

$$X_i = \frac{\int_{\lambda_1}^{\lambda_2} g_i(\lambda)X_\lambda d\lambda}{\int_{\lambda_1}^{\lambda_2} g_i(\lambda)d\lambda} \quad (2.8)$$

where $g_i(\lambda)$ is the spectral response function in channel i and λ_2 and λ_1 are the lower and upper boundaries of the wavelength in channel and X stands for the variables considered. Taking into account that the bandwidth of the channels is generally narrow and the various spectral quantities involved in Equations 2.6 and 2.7 should not offer rapid variations (i.e. atmospheric emissivity and transmissivity are not very variable in the spectral interval of the channels), the use of channel magnitudes in the radiative transfer equation (RTE) can be considered a good approximation of the RTE with monochromatic quantities.

It is worth noting here that in the thermal infrared domain (8-14 μm) the contribution of solar radiation at the TOA is negligible, the solar terms can be neglected and Equations 2.6 and 2.7 take the following form (Equations 2.9-2.10):

$$I(\theta, \varphi) = R_i(\theta, \varphi)\tau_i(\theta, \varphi) + R_{at_i\uparrow}(\theta, \varphi) \quad (2.9)$$

$$R_i(\theta, \varphi) = \varepsilon_i(\theta, \varphi)B_i(T_s) + [1 - \varepsilon_i(\theta, \varphi)]R_{at_i\downarrow}(\theta, \varphi) \quad (2.10)$$

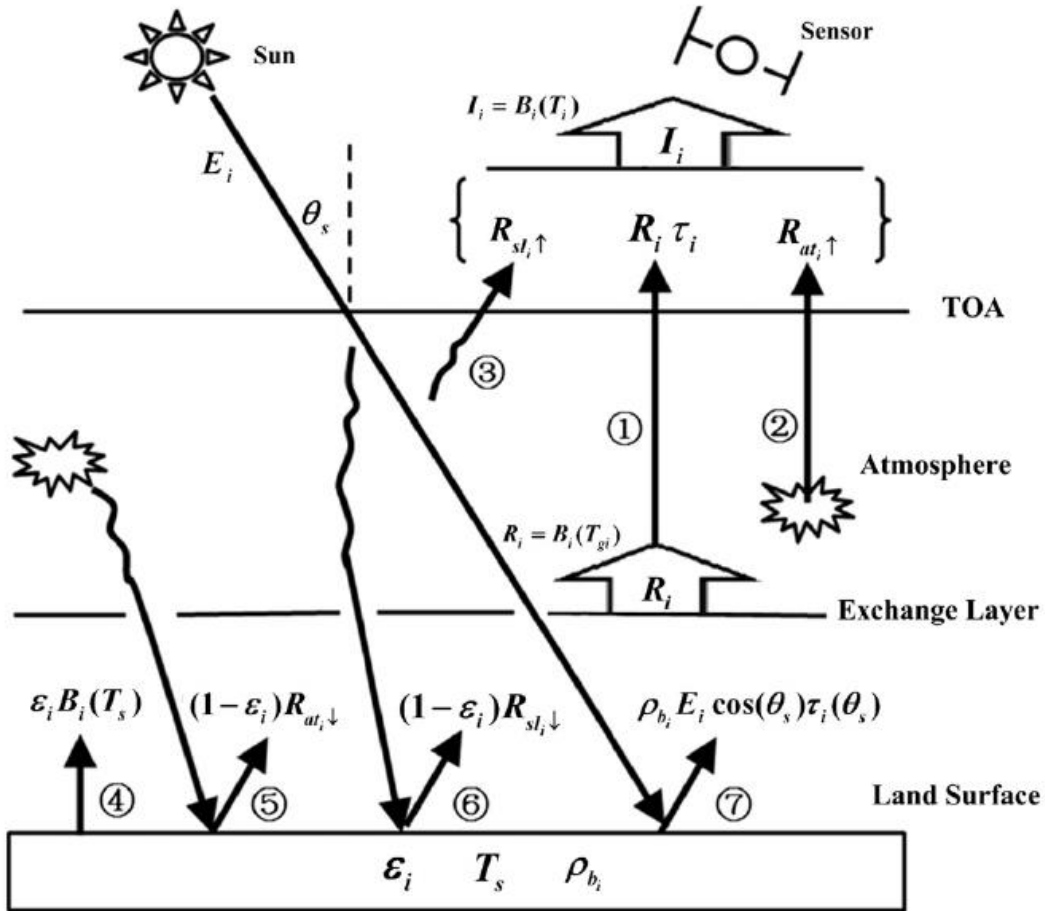


Figure 2.1. Illustration of radiative transfer equation in infrared domain. I_i and R_i are the radiance measured by the channel i at the TOA and ground level, respectively. These radiances can be expressed in terms of TOA (T_i) and ground level (T_g) brightness temperatures. Path 1 represents the radiance observed at ground level attenuated by the atmosphere. Path 2 and 3 represent the upward atmospheric thermal radiance and the upward solar diffusion radiance, respectively. Path 4 represents the radiance emitted directly by the surface. Path 5 and 6 represent the downward atmospheric thermal radiance and solar diffusion radiance reflected by the surface, respectively. Path 7 represents the direct solar radiance reflected by the surface (Li et al. (2013)).

As observed in Equations 2.9 and 2.10, the determination of the LST from space requires not only the knowledge of atmospheric information but also knowledge of the land surface emissivity (LSE). The implementation of atmospheric corrections is difficult because the need of accurate of vertical profiles of atmospheric water vapour and temperature, which both are highly variable (Perry & Morran, 1994). Nevertheless, even if these quantities are accurately estimated, the retrieval of LST from space is still an undetermined problem. For N channels measuring radiance, we have a system of N equations with $N+1$ unknowns (N emissivities + unknown LST). In order to solve this system, emissivity values must be known by a priori information or by assuming a constraint on emissivities values such as in TES model (Gillespie et al., 1996).

Apart from these previous difficulties, it is worth noting here the interpretation issue of these derived LST estimates. LST is a kinetic quantity that represents the thermodynamic temperature of the skin layer of a given surface (a few millimeters in the TIR region). This temperature definition differs from the definition of thermodynamic temperature (measured by a thermometer in a thermal equilibrium system). For homogeneous and isothermal surfaces, these two quantities are reported to be equivalent. However, most natural surfaces do not accomplish these conditions. In addition, taking into account the spatial resolution of the remote-sensing LST instruments (ground-based, airborne and spaceborne), the measured LST is the aggregated radiometric surface temperature of the ensemble of components within the sensor field of view (Norman & Becker, 1995). This fact complicates the physical interpretation of the satellite derived LST and its relation to other temperatures (aerodynamic and thermodynamic) used in estimating surface fluxes or other applications (Li et al., 2013).

2.2. Operative LST algorithms for medium resolution sensors

In order to determine the LST from space many algorithms which use different assumptions and approximations for solving the RTE and the LSE requirement have been proposed. In Li et al. (2013) a comprehensive revision of these algorithms is given. In the following, we focus on describing the LST algorithms employed in the retrieval of current LST products used in this work.

2.2.1.- MODIS

2.2.1.1- Split-window algorithm

NASA's current operational MODIS LST products are derived using the split-window algorithm developed by Wan & Dozier (1996) which has a similar formulation as the one proposed by Becker & Li (1990). It is given by Equation 2.11.

$$\text{LST} = b_0 + \left(b_1 + b_2 \frac{1 - \varepsilon}{\varepsilon} + b_3 \frac{\Delta\varepsilon}{\varepsilon^2} \right) \frac{T_{31} + T_{32}}{2} + \left(b_4 + b_5 \frac{1 - \varepsilon}{\varepsilon} + b_6 \frac{\Delta\varepsilon}{\varepsilon^2} \right) \frac{T_{31} - T_{32}}{2} \quad (2.11)$$

where T_{31} and T_{32} refers to the MODIS brightness temperatures of thermal bands 31 and 32 centered on 11.03 μm and 12.02 μm , respectively. ε and $\Delta\varepsilon$ are the mean and emissivity difference between bands 31 and 32 and b_i ($i = 0 - 6$) are the split-window coefficients which depend on surface emissivity, viewing zenith angle, surface air temperature (T_a) and atmospheric water vapour content. In the standard LST product, information about these last two variables is taken from the MODIS atmospheric profile product (MOD07) (Wan, 2008). Emissivity values in band 31 and 32 are defined as a combination of green and senescent components estimated from land cover types in each MODIS pixel through a look-up-table (LUT) based on TIR bidirectional reflectance distribution function (BRDF) an emissivity modelling (Snyder et al., 1998).

Instead of using fixed b_i coefficients a multi-dimensional lookup table (LUT) is used in order to cover a wide range of the variations of surface and atmospheric conditions. For each view zenith angle (VZA) (9 viewing angles are selected to cover the MODIS surface viewing angle range from nadir to 65.5 °, the atmospheric water vapour (WV), averaged emissivity ε , and T_a or LST are divided into several tractable sub-ranges. Considering these sub-ranges the coefficients are retrieved by minimizing Equation 2.11 using simulated radiative transfer calculations of T_{31} and T_{32} . Regarding the different parameters, the water vapour is divided into sub-ranges up to 6.5 g/cm^2 with an overlap of 0.5 g/cm^2 . The ε is separated into two groups, one varying from 0.90 to 0.96 and the other one varying from 0.94 to 1.0. The T_a sub-ranges are divided by 273, 281, 289, 295,

300, 305, and 310 K. The LST varies within $T_a \pm 16$ K and may be divided into four overlapped sub-ranges (Wan & Dozier, 1996). For a value of VZA not included in the LUT, the coefficients b_i can be linearly interpolated using the cosine of the VZA.

According to Wan & Dozier (1996), the LST is estimated in two steps. In the first step LST is estimated with coefficients b_i covering the entire LST range of $T_a \pm 16$ K. In the second step, the LST is refined by using the corresponding coefficients b_i associated with the difference between the approximate LST (first step) and T_a .

In order to improve the LST and emissivity retrieval for bare soil grids in hot and warm bare soil zones within latitude range from -38° to 49.5° , in Wan (2014) a new set of split-window coefficients (one set for daytime and one for nighttime) was derived. The ranges of the parameters employed in MODTRAN simulations are: the atmospheric surface temperature is set as 280–325 K for the daytime and 275–305 K for the nighttime. The atmospheric column water vapor varies from nearly zero to 5.5 cm. The variation in surface emissivity in bands 31 and 32 is around the averaged values for the soil and samples selected. The range of $(LST - T_a)$ is set as from 8–29K for daytime LSTs and from -10 –4K for nighttime LSTs.

2.2.1.2.- Day-Night algorithm

The day-night (DN) algorithm was developed in order to simultaneously retrieve LST and LSE using a combination of day/night pairs of Middle-Infrared-Radiation (MIR) and TIR data (Wan & Li, 1997). The DN method consists into setting Equations 2.6 and 2.7 for daytime and nighttime conditions considering three key assumptions. These are: 1) the LSE variations between day and night can be neglected, thus assuming equal emissivity values for day and night. In addition, a lambertian surface is considered. 2) The bidirectional reflectance factors in the mid-infrared thermal channels have very small variation (<2%) and is assumed identical for each mid-infrared channel used. 3) The MODIS atmospheric sounding channels and the corresponding retrieval algorithms provide the atmospheric temperature and humidity profiles. The profiles shapes are accurate and can be described with two parameters: the air temperature at the surface level, T_a , and the atmospheric water vapour (WV). With these assumptions, the atmospheric parameters in Equations 2.6 and 2.7 (i.e. $R_{at_i\uparrow}$, $R_{sl\uparrow}$, $R_{at_i\downarrow}$, $R_{sl\downarrow}$, E_i , $\tau_i(\theta_s, \varphi_s)$ and $\tau_i(\theta, \varphi)$) can be retrieved from T_a and WV values and atmospheric radiative transfer codes. Apart from these variables, we still have as unknowns the surface parameters ε_i , T_s and ρ_{bi} . Taking into account that the algorithm uses two observations (day and night), for N channels thus we have a total of $N+7$ unknowns (N channels LSEs, 2 LSTs, 2 T_a , 2 WV and 1 ρ_{bi} in the MIR channel). In order to make the equations deterministic, it is required that $N \geq 7$. MODIS seven selected bands selected are: 20, 22, 23, 29, 30, 31 and 32. These channels lie in the atmospheric windows of 3.5-4.2 μm and 8-13 μm respectively.

According to Li et al. (2013), this LST retrieval algorithm entails some strengths in comparison to other algorithms that use multiple observations, such as the day/night temperature independent spectral indices method and the Two-Temperature method. For example, the correlation amongst equations is decreased due to the contribution of solar terms in the MIR channels, thus making the solution more stable and accurate. In addition, the introduction of two additional variables T_a and WV help to account for the uncertainties in the initial atmospheric profiles. Moreover, as long as the surface emissivity does not change significantly, daytime and nighttime observations collected over several days is appropriated in order to run the algorithm. Nevertheless, this LST algorithm also suffers from some weaknesses. In particular, the problems of misregistration and variations in the satellite viewing conditions of the matched pair of observations (Wan, 2008). Some refinements in this algorithm were implemented for a better LST retrieval (Wan, 2008; Wan, 2014). These include: the combined use of TERRA and AQUA MODIS data, an increase in the number of sub-ranges of viewing angles, the use of temporal and viewing conditions constraints and the incorporation of the MODIS split-window method as a close component in the DN algorithm.

2.2.1.3.- Temperature Emissivity Separation (TES) method

The TES method comprises three mature modules: the normalization emissivity method (NEM) (Gillespie, 1995), the spectral ratio (SR), and the maximum–minimum apparent emissivity difference method (MMD) (Matsunaga, 1994). In Figure 2.2 the flow diagram of the process is presented. In the following, according to MOD21 algorithm theoretical basis document (Hulley et al., 2012) a brief description of the three modules is given.

The role of the NEM module is to compute the surface kinetic temperature T_{NEM} and a correct shape of the emissivity spectrum. Initially a first value of ϵ_{max} is set as 0.99 which is typical of vegetated surfaces, snow and water. For geologic materials such as rock and sands an initial value of 0.96 can be chosen. With this initial value, the ground radiance (R_i) is calculated. The NEM temperature (T_{NEM}) is estimated by inverting Planck function using ϵ_{max} and R_i and then taking the maximum of those temperatures. With this T_{NEM} a new emissivity spectrum is calculated. The process is then repeated (i.e. calculating a new R_i') until convergence (i.e. $R_{i+1} - R_i < t_2$, where t_2 is set as the radiance equivalent to $NE\Delta T$ of the sensor). The process is stopped if the number of iterations exceeds a limit $N = 12$ or if $|\Delta^2 R' / \Delta c^2 > t_1|$, where t_1 is also set to radiance equivalent of $NE\Delta T$ for the sensor. In this case, correction is not possible. After this process, the need of an ϵ_{max} reset is checked. This optimization is only useful for pixels with low emissivity contrast and therefore is only executed if the variance (v) for ϵ_{max} is less than an empirically determined threshold (V_1). In case $v > V_1$, the pixel is assumed to consist of either rock or soil and ϵ_{max} is reset to 0.96. In case $v < V_1$, then values for ϵ_{max} of 0.92, 0.95, 0.97, and 0.99 are used to compute the variance for each corresponding NEM emissivity spectrum. A plot of variance v versus each ϵ_{max} value results in an upward-facing parabola with the optimal ϵ_{max} value determined by the minimum of the

parabola curve in the range $0.9 < \epsilon_{max} < 1.0$. This minimum is set to a new ϵ_{max} value, and the NEM module is executed again to compute a new T_{NEM} . Further tests are used to see if a reliable solution can be found for the refined ϵ_{max} . If the parabola is too flat, or too steep, then refinement is aborted and the original ϵ_{max} value is used. Finally, if the minimum ϵ_{max} corresponds to a very low ν , then the spectrum is essentially flat (graybody) and the original $\epsilon_{max} = 0.99$ is used.

In the spectral ratio module, the NEM emissivities (ϵ_i) are rationed to their average value in order to calculate a β_i spectrum. In the MMD module, first the spectral contrast of β_i spectrum is calculated (MMD). This is related to the minimum emissivity ϵ_{min} in the spectrum using an empirical relation determined from laboratory measurements. In this expression, $\alpha_1 = 0.985$, $\alpha_2 = 0.7503$, and $\alpha_3 = 0.8321$. The TES emissivities are then calculated by re-scaling the β_i emissivities by a factor $\epsilon_{min}/\min(\beta_i)$. Finally the temperature can be refined, by inverting the Planck function using R_i' and the maximum of ϵ_{TES} . With this ϵ_{max} value the correction of reflected $L_\lambda \downarrow$.

The TES algorithm uses a radiative transfer model (typically MODTRAN) in order to correct the at-sensor radiances to surface radiances (i.e calculation of the transmissivity, path and downward thermal radiances). In this process, a water vapour scaling atmospheric correction method is used in order to adjust the retrieval during very warm and humid conditions (Tonooka, 2005). Numerical simulation and some field validations have demonstrated that the TES can retrieve the LST to within about ± 1.5 K and the LSEs to within about ± 0.015 when the atmospheric effects are accurately corrected (Gillespie et al., 1996, 1998). In addition, validation results have shown consistent accuracies at the 1 K level over all land surface types (Hulley et al., 2012).

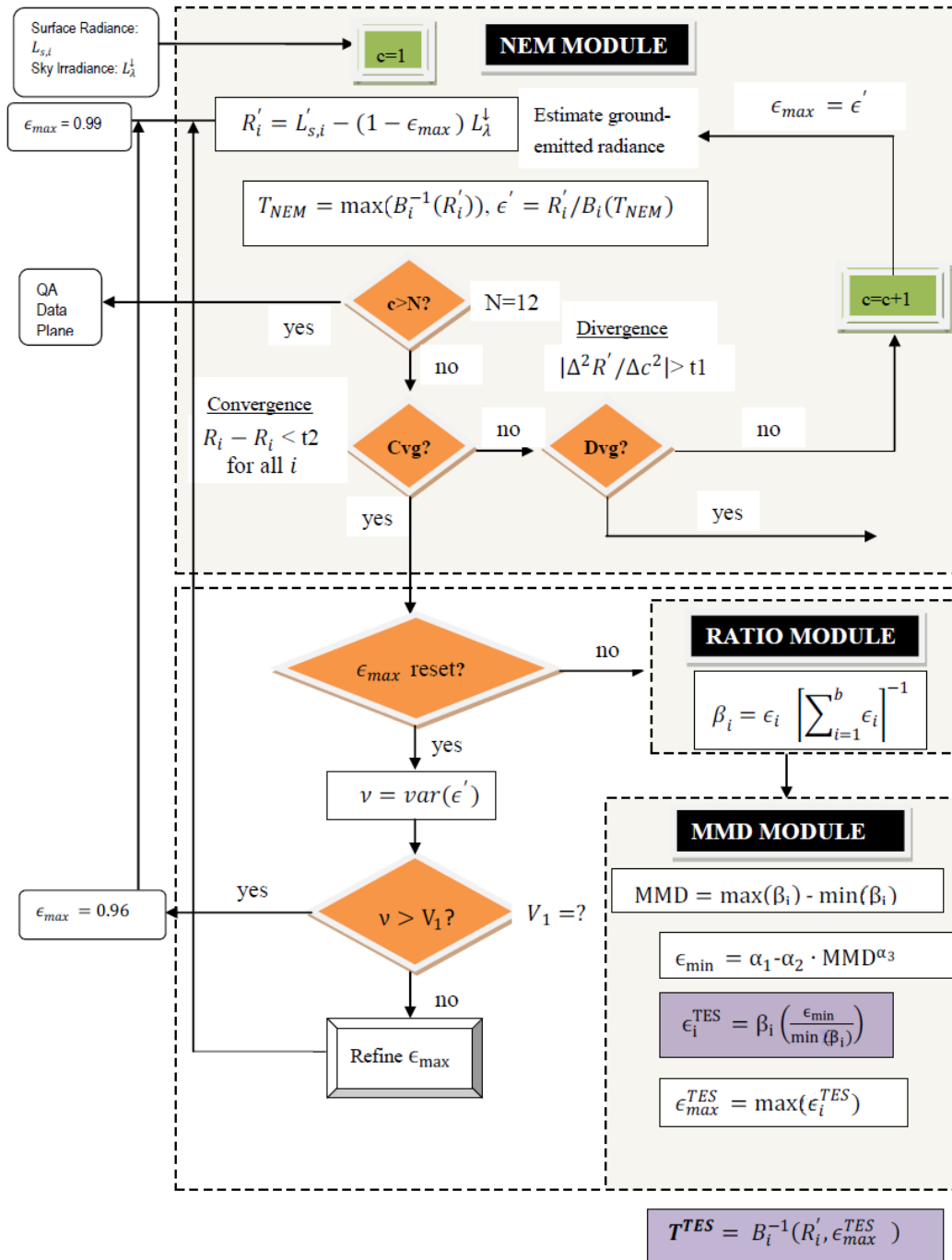


Figure 2.2. Flow diagram of the TES algorithm in its entirety, including the NEM, RATIO, and MMD modules. Details are included in the text, including information about the refinement of ϵ_{max} (extracted from Hulley et al., 2012).

2.2.2.- VIIRS

Since August 2012, the NOAA VIIRS Environmental Data Record (EDR) has been operationally produced using a single split window algorithm (Yu et al., 2005). It is given by Equation 2.12.

$$LST = a_0 + a_1T_{15} + a_2(T_{15} - T_{16}) + a_3(\sec\theta_v - 1) + a_4(T_{15} - T_{16})^2 \quad (2.12)$$

where T_{15} and T_{16} are the brightness temperatures measured in channels M15 and M16 centered on 10.76 μm and 12.01 μm respectively. θ_v is the satellite viewing zenith angle. a_i are algorithm coefficients derived from regression analyses of MODTRAN radiative transfer simulations over 17 different surface types as defined by the International Geosphere-Biosphere Program (IGBP). The algorithm regression coefficients were generated from an ensemble of MODTRAN radiative transfer simulations using a comprehensive set of geophysical parameters (VIIRS LST ATBD, 2011). In particular, surface temperatures and atmospheric temperature and water vapour profiles were derived from National Center for Environmental Prediction (NCEP) and band-averaged spectral emissivity values for each surface type were derived from the MOSART database. A different set of coefficients are derived for daytime and nighttime conditions. The bias and precision requirements specified by NOAA's Joint Polar Satellite System (JPSS) program for the VIIRS LST EDR are 1.5 K and 2.5 K, respectively for clear conditions (VIIRS LST ATBD, 2011).

In line with production of the new MOD21 LST & E product, NASA is currently in the processing of an equivalent TES-based product for VIIRS, termed VNP21. For a full detailed description of the algorithm and data inputs please see the VNP21 ATBD (https://viirsland.gsfc.nasa.gov/PDF/VNP21_LSTE_ATBD_v2.1.pdf). A brief description of TES algorithm is also provided in the previous MODIS LST algorithms section.

2.2.3.- SLSTR

The SLSTR algorithm (Equation 2.13) is developed as an evolution of the AATSR LST algorithm (Prata, 2002).

$$LST = a_{fiw} + b_{fi}(T_{11} - T_{12})^n + (b_{fi} + c_{fi})T_{12} \quad (2.13)$$

where T_{11} and T_{12} are the brightness temperature of SLSRT 11 μm and 12 μm bands and n , a_{fiw} , b_{fi} and c_{fi} parameters are given by Equations 2.14 to 2.17.

$$n = 1/\cos\left(\frac{\theta_v}{m}\right) \quad (2.14)$$

$$a_{fiw} = d(\sec\theta_v - 1)pw + a_{vif} + a_{si}(1 - f) \quad (2.15)$$

$$b_{fi} = b_{vif} + b_{si}(1 - f) \quad (2.16)$$

$$c_{fi} = c_{vif} + c_{si}(1 - f) \quad (2.17)$$

In these equations, θ_v is the satellite view zenith angle, f is the vegetation fraction, pw is the atmospheric water content (in cm). The parameters d and m are empirical parameters determined using radiative transfer simulations. The coefficients a_{fiw} , b_{fi} and c_{fi} are retrieved separately for each biome from the Globcover classification (denoted by the subscript i). They are obtained by weighting by the vegetation fraction f the regression coefficients obtained considering a 100% (v) and 0% (s) of vegetation fraction (i.e. a_{vi} , a_{si} , b_{vi} , b_{si} , c_{vi} and c_{si}). These coefficients are supplied separately for daytime and nighttime conditions. A full description of the retrieval algorithm can be found in the SLSTR Algorithm Theoretical Basis Document for Land Surface Temperature (Remedios, 2012).

2.3.- LST and LSE algorithms developed at the Global Change Unit

In the following, the split-window algorithm used for LST estimation in this thesis is presented. In addition, a brief introduction to the NDVI Thresholds method (NDVI^{THM}) for LSE retrieval is also provided.

2.3.1- Split-window algorithm (Sobrino and Raissouni (2000))

The basis of the technique is that the radiance attenuation for atmospheric absorption is proportional to the radiance difference of simultaneous measurements at two different wavelengths, each subject to different amounts of atmospheric absorption (McMillin, 1975). In particular, the bands located in the atmospheric window between 10 and 12 μm are used. The split-window is given by Equation 2.18, where T_i and T_j are the at-sensor brightness temperatures at the SW bands (in K), ε is the mean emissivity of channels i and j , $\Delta\varepsilon$ is the emissivity difference, w is the total atmospheric water vapour content (gcm^{-2}) and a_0 to a_6 are the split-window coefficients which are retrieved statistical regression of simulated data.

$$T_s = T_i + c_1(T_i - T_j) + c_2(T_i - T_j)^2 + c_0 + (c_3 + c_4W)(1 - \varepsilon) + (c_5 + c_6W)\Delta\varepsilon \quad (2.18)$$

The mathematical structure was firstly proposed by Sobrino et al. (1996) and later modified by Sobrino & Raissouni (2000). The main advantages of this algorithm are the following: 1) It is a physics-based algorithm, since it is obtained from the radiative transfer equation (RTE) applied to two different bands; 2) it takes into account both emissivity and water vapor effects; 3) it includes both LST and SST cases; and 4) it is totally operational. Simulated validation and in-situ validation results show that LST retrieved from this SW is typically below 2 K of RMSE.

2.3.2.- NDVI threshold method (Sobrino et al. (2008))

According to Sobrino et al. (2008), the emissivity retrieved by a sensor channel can be expressed as in Equation 2.19:

$$\varepsilon_{\lambda} = \begin{cases} a_{\lambda} + b_{\lambda}\rho_{red} & NDVI < NDVI_s \\ \varepsilon_{v\lambda}P_v + \varepsilon_{s\lambda}(1 - P_v) + C_{\lambda} & NDVI_s \leq NDVI \leq NDVI_v \\ \varepsilon_{v\lambda} & NDVI > NDVI_v \end{cases} \quad (2.19)$$

where $\varepsilon_{v\lambda}$ and $\varepsilon_{s\lambda}$ are the vegetation and soil emissivities. C_{λ} is a term which takes into account the cavity effect due to surface roughness ($C = 0$, for flat surfaces). P_v is the proportion of vegetation (i.e. vegetation fraction cover) that is obtained from the NDVI as in Equation 2.20:

$$P_v = \left(\frac{NDVI - NDVI_s}{NDVI_v - NDVI_s} \right)^2 \quad (2.20)$$

$NDVI_s$ and $NDVI_v$ are set as 0.2 and 0.5 in Sobrino et al. (2008), nevertheless they should be recalculated in order to adequate to specific conditions. When $NDVI < NDVI_s$, the pixel is considered to be bare soil and the emissivity is estimated from an empirical relationship with the red band of the sensor. When $NDVI > NDVI_v$, the pixel is assumed to be fully vegetated and a value of 0.99 is assumed. When $NDVI_s \leq NDVI \leq NDVI_v$, the pixel is considered mixed and the emissivity value results from a weighted mean between $\varepsilon_{v\lambda}$ and $\varepsilon_{s\lambda}$ taking also into account the cavity effect.

In Equation 2.19, there is a discontinuity at $NDVI_s$ and $NDVI_v$. In addition, for some soil specimens ε_{λ} and ρ_{red} have a poor relationship. These problems are formally solved by simplifying the $NDVI^{THM}$ as in Equation 2.21. Although this method contains several improvements in comparison to other emissivity classification methods, it still fails to indicate considerable changes in the LSE, especially for areas without vegetation cover.

$$\varepsilon_{\lambda} = \begin{cases} \varepsilon_{s\lambda} & NDVI < NDVI_s \\ \varepsilon_{v\lambda}P_v + \varepsilon_{s\lambda}(1 - P_v) + C_{\lambda} & NDVI_s \leq NDVI \leq NDVI_v \\ \varepsilon_{v\lambda} & NDVI > NDVI_v \end{cases} \quad (2.21)$$

3.- EVAPOTRANSPIRATION RETRIEVAL FROM SPACE

3.- Evapotranspiration retrieval from space

3.1.- Turbulent transport of heat and water in the atmosphere

Transport of heat and mass in the atmosphere is produced by turbulence. This latter can be visualized as consisting of irregular swirls of air motion called eddies (Figure 3.1). Superimposed on each other and having different sizes, these eddies are carried along with the wind bouncing with random motion. They are responsible of transport of heat, mass (water) and momentum in the atmosphere. These are generated by two ways: mechanical turbulence generated by friction between the moving air and land surface (i.e. the wind), and thermal turbulence, generated by buoyancy of the hot/cold air from the surface (i.e. gradient of temperature).

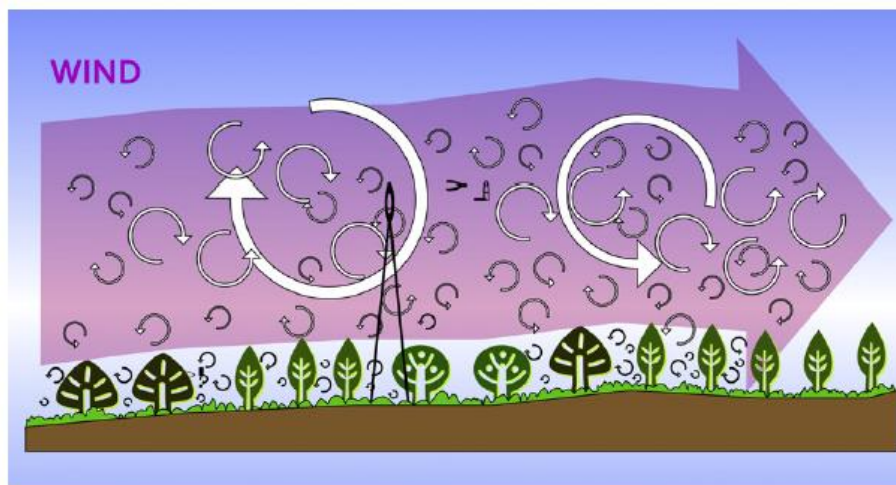


Figure 3.1 Airflow can be imagined as a horizontal flow of numerous rotating eddies, that is, turbulent vortices of various sizes, with each eddy having horizontal and vertical components (Wang & Dickinson, 2012).

The part of the atmosphere in which these turbulence (production and suppression) is noticeable is called the atmospheric boundary layer (ABL). It is the turbulent layer between the surface and the non-turbulent free troposphere. A main subdivision can be made between the outer region and atmospheric surface layer (ASL) (Figure 3.2 (a)). As indicated also by this Figure, the ABL has a strong diurnal variation due to the variation in insolation. At daytime under unstable conditions it reaches depths of 1 to 2 km. The ABL is heated from below and convection causes strong turbulence mixing leading to more or less uniform profiles (Figure 3.2 (b)). The outer region may be referred then as the mixed layer. At the top of the ABL an inversion layer (also called entrainment zone) separates the ABL from the free-troposphere. A strong inversion of the temperature profile causes the capping of the ABL (Figure 3.2 (b)). During nighttime, the ASL is in stable conditions due to the radiative cooling of the surface. The outer layer becomes uncoupled from the surface by the developing of the stable nocturnal layer. In this case, boundary layer can reach from tens of meters to approximately 500 m at sunrise (Brustaert, 2005). This weak nighttime turbulence the strong gradients in Figure 3.2 (b).

Although the entire ABL is influenced by the surface. In the following of the chapter, we are focusing on the description of processes occurring at the ASL. It represents roughly the 10% of the ABL. This region is characterized by large gradients in temperature and wind speed. In addition, the vertical turbulent fluxes do not change appreciably from their value at the surface.

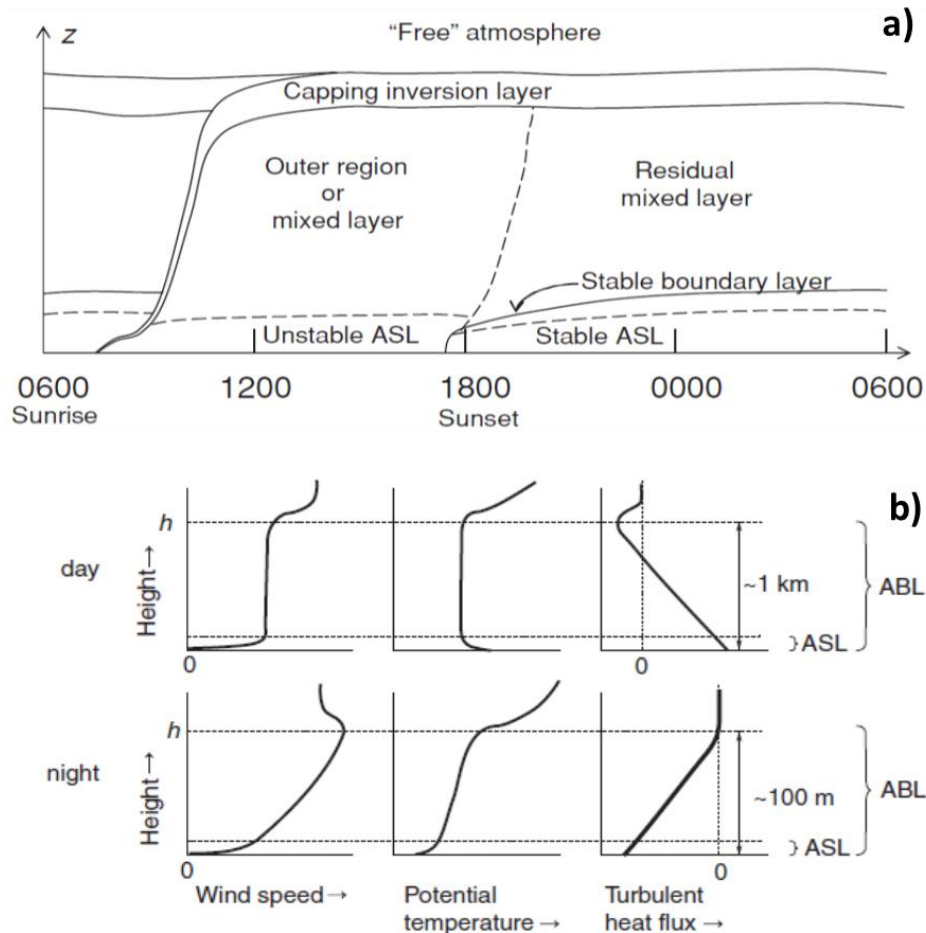


Figure 3.2. Temporal evolution of a fair weather boundary layer (ABL) over land under clear sky conditions (a). Sketch of the profiles of mean wind speed, mean potential temperature and the turbulent sensible heat flux in the ABL with depth h (b). Extracted from Brutsaert, 2005 and Moene & Van Dam 2014.

For modelling purposes, the transport of heat, water (mass) and momentum between different levels of the atmosphere due to motion of the eddies can be seen as an analog of the molecular diffusion processes in a gas. This is the basis of the K-theory (Brutsaert, 1982), that establishes that the fluxes of momentum, energy and mass (water) are given by Equations 3.1 to 3.3.

$$\tau = \rho K_m \frac{\partial \bar{u}}{\partial z} \quad (3.1)$$

$$H = -\rho c_p K_H \frac{\partial \bar{T}}{\partial z} \quad (3.2)$$

$$E = -\rho K_v \frac{\partial \bar{q}}{\partial z} \quad (3.3)$$

where τ ($\text{kgm}^{-1}\text{s}^{-2}$) is the shear stress term, H (Wm^{-2}) is the sensible heat flux, E is the mass flux ($\text{kgm}^{-2}\text{s}^{-1}$), latent heat flux is given by λE where λ (J kg^{-1}) is the latent heat of vaporization. K_m , K_H and K_v (m^2s^{-1}) are the turbulent transfer coefficients for horizontal momentum, sensible heat and water vapour, ρ (kgm^{-3}) is the air density, c_p ($\text{J kg}^{-1} \text{K}^{-1}$) the specific heat air at constant pressure, \bar{u} (ms^{-1}), \bar{T} (K) and \bar{q} (kgkg^{-1}) are the horizontal wind speed, air temperature at specific water concentration of the water in the air.

It is known that the turbulent transfer coefficients increase with height above the surface, wind speed, surface roughness and heating at the surface (Campbell & Norman, 2012). Assuming that they have some value characterized by surface properties at the exchange surface (i.e. where $z = d + z_{0m}$ or $z = d + z_{0h}$ or $z = d + z_{0v}$ respectively), they increase linearly with u_* (ms^{-1}) and z (m) according to Equations 3.4 to 3.6.

$$K_m = k u_* (z - d_0) / \phi_m \quad (3.4)$$

$$K_H = k u_* (z - d_0) / \phi_h \quad (3.5)$$

$$K_v = k u_* (z - d_0) / \phi_v \quad (3.6)$$

where k is the von Karman constant equal to 0.4, u_* is the friction velocity. It is defined as $u_* = (\tau/\rho)^{1/2}$. In this shear stress term (τ) it is included the effects of wind speed, surface roughness and surface heating (Campbell & Norman, 2012). z is the height above the surface (m) and d_0 is the zero displacement height (m), that corresponds to height of the surface that actually the flow experiences (i.e. the height where the drag acts on the canopy elements or null for bare soil). ϕ_m , ϕ_h and ϕ_v are dimensionless influence factors which equal one for pure mechanical turbulence. From these equations, the meaning of the so-called roughness lengths of momentum (z_{0m}), heat (z_{0h}) and water (z_{0v}) can be deduced. They represent the characteristic length (m) which makes the K coefficients equal to the values they have at the exchange surface. A common practice is to assume a correspondence between z_{0h} and z_{0v} . This approach presupposes that the drag of the surface is the same for all scalars. z_{0h} can be related to z_{0m} by Equation 3.7 (Garratt & Hicks, 1973).

$$kB^{-1} = \ln \left(\frac{z_{0m}}{z_{0h}} \right) \quad (3.7)$$

For the case of pure mechanical turbulence ($\phi_m = \phi_h = \phi_v = 1$), taking expressions 3.4-3.6 into equations 3.1.-3.3. and integrating between the exchange surface and a

generic height z , the following wind, temperature and water vapour concentration profiles are obtained (Equations 3.8 to 3.10).

$$u(z) = \frac{u_*}{k} \ln \left(\frac{z - d_0}{z_{0m}} \right) \quad (3.8)$$

$$T(z) = T_0 - \frac{H}{k\rho c_p u_*} \ln \left(\frac{z - d_0}{z_{0h}} \right) \quad (3.9)$$

$$q(z) = q_0 - \frac{E}{k\rho u_*} \ln \left(\frac{z - d_0}{z_{0v}} \right) \quad (3.10)$$

where T_0 (K) and q_0 (kgkg^{-1}) represent the temperature and specific water vapour concentration at the exchange height. Wind speed at this height is null. The values of roughness lengths can be derived from Equations 3.8 to 3.10 as the intercepted term of the linear regression of $\ln(z - d_0)$ against the mean profile difference (i.e. $T(z) - T_0$). These equations apply only for neutral conditions (i.e. adiabatic conditions).

The buoyancy of air can also play a role in the turbulent transport in the atmosphere. Strong heating of the air at the surface causes an increase of the turbulence and mixing, while strong cooling suppresses mixing and turbulence. This turbulence production (or suppression) is directly related to sensible heat flux at the surface. If H is positive (surface warmer than the air) the atmosphere is said to be unstable (i.e. mixing is enhanced), while if H is negative, the atmosphere is said to be stable (i.e. mixing is suppressed by thermal stratification). Unstable and stable conditions usually happen at daytime and nighttime respectively (Figure 3.2). In this situation Equations 3.8 to 3.10 need to be corrected. These diabatic corrections are made based on the Monin-Obukhov similarity theory (MOST) (Monin-Obukhov, 1954).

A measure of the atmospheric stability can be derived from the kinetic energy budget for a steady-state atmosphere (Lumley & Panofsky, 1964) given by Equation 3.11.

$$-\frac{u_*^3}{k(z-d)} + \frac{gH}{\rho c_p T} = \varepsilon_{vd} \quad (3.11)$$

where the first term represents the mechanical production of turbulent kinetic energy and the second term the convective production (i.e. buoyancy). Both terms equal the viscous dissipation of the energy (ε_{vd}). To characterize the role of buoyancy in the production of turbulence, often the ratio of convective to mechanical production is used. This provides a measure of atmospheric stability and it is given by Equation 3.12.

$$\zeta = -\frac{gHk(z-d)}{\rho c_p T u_*^3} \equiv \frac{(z-d)}{L} \quad (3.12)$$

where L refers to the Monin-Obukhov length (m). Although in many cases the effect of the water vapour on the density stratification can be neglected, it is still advisable to

include whenever possible. Therefore, the Monin-Obukhov length can be written as in Equation 3.13.

$$L = \frac{-\rho u_*^3}{kg \left(\frac{H}{c_p T} + 0.61E \right)} \quad (3.13)$$

where g is the acceleration gravity (ms^{-2}) and the rest of the parameters have been defined previously. In terms of this length, when L assumes negative values ($L < 0$), the atmospheric conditions are unstable (i.e. the actual thermal gradient is greater than the reference adiabatic one). When L assumes positive values ($L > 0$) the atmospheric conditions are stable (i.e. the thermal gradient is lower than the adiabatic one). When $|L|$ has high values (i.e. ζ is near zero), the atmosphere is adiabatic (neutral) conditions.

For this new situation, the same previous methodology is applied. Nevertheless, ϕ_m , ϕ_h , ϕ_v need to be taken into account. These functions depend on ζ , increasing from unity to positive ζ and decreasing with negative ζ . ϕ_h and ϕ_v are assumed to be equal. For a revision of the possible exact form of these functions we refer the reader to Brutsaert (1982) and Campbell & Norman (2012). For the models used in this work they have been provided when needed. Considering these corrections, Equations 3.8 to 3.10 take the following expressions (Equations 3.14 to 3.16), where $\psi(\zeta) = \int_0^\zeta [1 - \phi(x)] dx/x$.

$$u = \frac{u_*}{k} \left[\ln \left(\frac{z - d_0}{z_{0m}} \right) - \psi_m \left(\frac{z - d_0}{L} \right) + \psi_m \left(\frac{z_{0m}}{L} \right) \right] \quad (3.14)$$

$$\theta_s - \bar{\theta} = \frac{H}{k u_* \rho c_p} \left[\ln \left(\frac{z - d_0}{z_{0h}} \right) - \psi_h \left(\frac{z - d_0}{L} \right) + \psi_h \left(\frac{z_{0h}}{L} \right) \right] \quad (3.15)$$

$$q_s - \bar{q} = \frac{E}{k u_* \rho} \left[\ln \left(\frac{z - d_0}{z_{0v}} \right) - \psi_v \left(\frac{z - d_0}{L} \right) + \psi_v \left(\frac{z_{0v}}{L} \right) \right] \quad (3.16)$$

3.2. The energy budget constraint

Apart from the similarity relationships, the turbulent fluxes are also linked to the surface by the energy budget. Applying the conservation of energy at the surface the energy budget reads as follows (Equation 3.17). All terms have units of Wm^{-2} .

$$R_n = H + \lambda E + G + A_c + \Delta S \quad (3.17)$$

In this equation, R_n is the net radiation reaching the surface and it is defined as in Equation 3.18.

$$R_n = (1 - \alpha) S_\downarrow + \varepsilon L_\downarrow - \varepsilon \sigma T_s^4 \quad (3.18)$$

where S_{\downarrow} (Wm^{-2}) is the solar incoming radiation, α is the surface albedo, ε is the surface emissivity, L_{\downarrow} (Wm^{-2}) is the incoming longwave radiation and T_s (K) is the land surface temperature. σ is the Stephan-Boltzmann constant ($5.67 \cdot 10^8 \text{ Wm}^{-2}\text{K}^{-4}$). H and λE refer to the sensible and latent heat flux described in the previous section. G is the specific energy flux leaving the surface layer due to conduction processes. By neglecting horizontal exchanges, it can be expressed as in Equation 3.19.

$$G = -\lambda_g \left(\frac{\partial T(z)}{\partial z} \right)_{z=0} \quad (3.19)$$

where λ_g ($\text{Wm}^{-1}\text{K}^{-1}$) is the soil thermal conductivity, $T(z)$ is the soil temperature (K) and z (m) is the distance along vertical axis. The value assumed at the surface layer ($z=0$) is the same term which appears in the energy budget. The positive daytime values of G (warming) often tend to be compensated by negative nighttime values (cooling) and therefore daily values of G are often neglected in the surface energy budget. For practical applications the soil heat flux can also be assumed to be proportional to net radiation (i.e. $G = cR_n$, where c is an empirical constant) (Brutsaert, 2005). A_c refers to the photosynthesis which represents a small fraction of the R_n and also usually neglected. ΔS refers to the heat storage of the system. It is usually omitted when it is applied to a thin layer of water, soil or canopy. Nevertheless, in the case of tall vegetation, it may have to be considered (Moore & Fisch, 1986). Still, on a daily basis it can be safely neglected.

3.3- The process of transpiration

Stomata are the main path way for the exchange of both CO_2 and water vapour between the plant and the atmosphere. These are small opening that occur mainly on the plant leaves. In Figure 3.3, a representation of the water pathway through the leaf is given. Water is pulled from the xylem into the cell walls of the mesophyll, where it evaporates into the air spaces within the leaf. The water then exits the leaf through the stomatal pore. Along this pathway water moves predominantly by diffusion (difference in water vapour concentration). In the case of CO_2 , it diffuses in the opposite direction along its concentration gradient (low inside, higher outside). If this water loss is formulated in terms of potential difference and resistances, two resistances on this route can be identified: the leaf stomatal resistance (r_s) and the leaf boundary layer resistance (r_b). This latter provides the link between the air within the canopy and the conditions at the leaf surface.

As the outward diffusion of water and CO_2 is produced in a simultaneous way, all plants need to regulate the competing demands of taking up CO_2 while limiting water loss. The functional solution of this dilemma is the temporal regulation of stomatal apertures. On a sunny morning, when water is abundant and photosynthetic activity is favored due to the incoming solar radiation (i.e. the demand of CO_2 inside the leaf is large), the stomatal

pores are wide open. On contrary, at night as there is no demand for CO₂, the stomatal apertures are kept small in order to prevent water loss. When there are conditions of water stress the stomata will open less or even remain closed. This avoids dehydration.

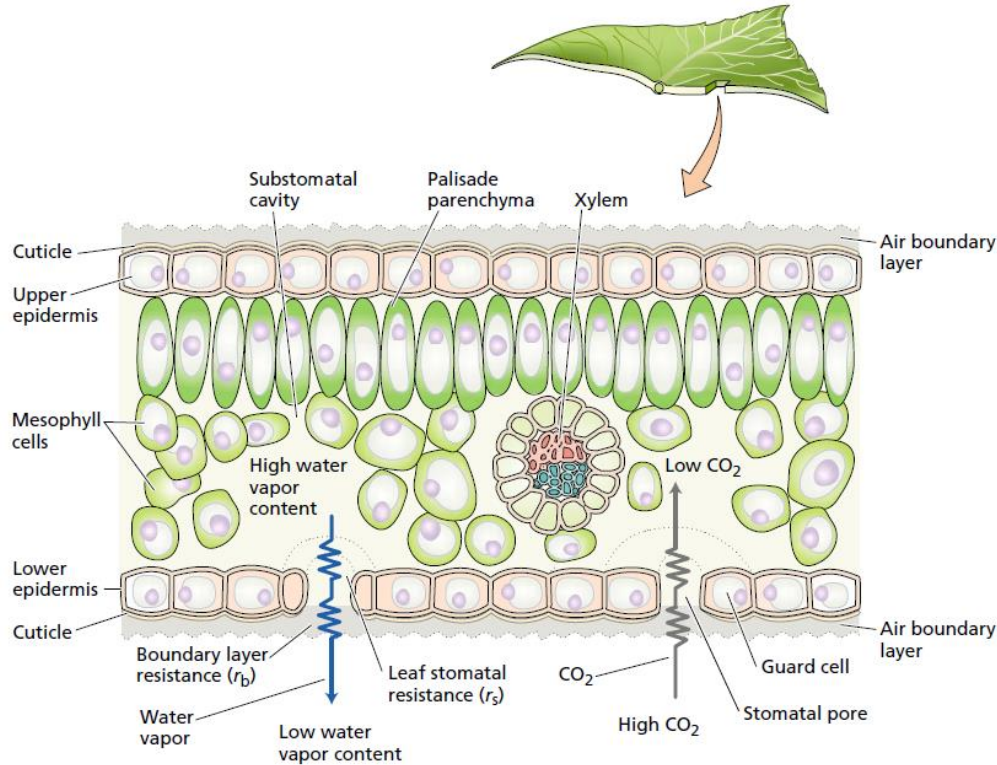


Figure 3.3. Water pathway through the leaf (Taiz et al., 2015).

3.4.- Evapotranspiration retrieval methods using remote sensing data

In Figure 3.4 a temporal revision of the state of art of evapotranspiration retrieval using remote-sensing data is provided. For further details, several literature reviews that expand this topic exist: Courault et al. (2005), Kalma et al. (2008), Li et al. (2009), Wang & Dickinson (2012) and Zhang et al. (2016).

Although it is difficult to establish a definitive classification of evapotranspiration algorithms, for this section we have adopted the classification proposed in Zhang et al. (2016) (Table 3.1). In this way, algorithms can be classified into models that calculate the λE as a residual of the energy budget (i.e. $\lambda E = R_n - H - G$). According to the description that they do of the surface they can be divided into one-source and two-source. In the latter, an explicit flux partition is obtained for soil and vegetation components. Amongst these models we can further consider a subdivision between single-pixel models such as SEBS or TSEB that do not require information from the other pixels and contextual models that require the specification of wet and dry points from the image such

as METRIC and SEBAL. In line with this need of contextual information, VI-T_s methods make use of the triangle space in order to determine the wet and dry edge. With some variations, pixel λE value is an interpolation of the λE values at these edges. Apart from these algorithms, there are physical-based models such as the ones based on Penman-Monteith and Priestley-Taylor logic. We can also mention the empirical methods, which are based on statistical relationships (or machine learning algorithms) between λE observations and remote sensing or meteorological magnitudes. Other methods make use of the water balance budget or its link with the carbon budget.

In Table 3.1 a bibliographic summary of the main advantages and disadvantages of each category is provided.

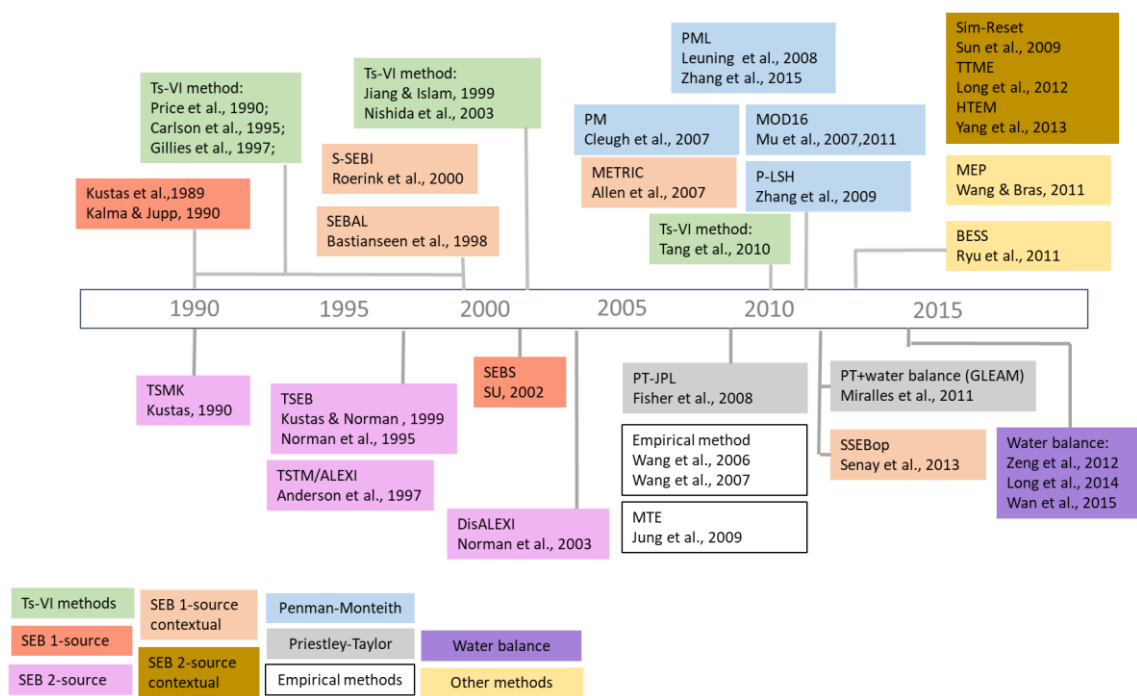


Figure 3.4. Chronological line of selected key publications in satellite remote-sensing evapotranspiration model development (adapted from Zhang et al., 2016).

Table 3.1. Summary of the existing major satellite-based evapotranspiration retrieval methods (adapted from Zhang et al., 2016).

Model	Advantages	Disadvantages	Minimum Forcing requirements
One-source SEB	- simple - low requirement for meteorological data	- only available for clear-sky - requires parametrization of excessive resistance and local calibration - susceptible to T_s and T_a errors - requires scaling of instantaneous to daily values	R_n, T_s, T_a, u and VI
Spatial variability	- simple - low requirement of meteorological data	- only available for clear-sky - requires parametrization of excessive resistance and local calibration - susceptible to T_s and T_a errors - requires scaling of instantaneous to daily values	R_n, T_s and α or VI
Two-source SEB	- low requirement for meteorological forcing	- only available for clear-sky -high sensitivity to surface temperature errors -requires scaling of instantaneous to daily values	R_n, T_s, T_a, u and VI
T_s -VI	- low sensitivity to T_s errors - low meteorological data requirement	- only available for clear-sky - relationship derived from T_s -VI space is oversimplified - requires scaling of instantaneous to daily values	R_n, T_s and VI
Penman-Monteith	- ET partition - process-based, - temporally continuous - flexible time step - low requirements for surface temperature	- high meteorological forcing requirements - simplified semi-empirical estimate of canopy conductance - models may require local calibration	R_n or radiation inputs, T_a , VPD and VI
Priestley-Taylor	- simple - moderate requirement for meteorological forcing -ET partition	- simplifications of physical processes - requirement of ground heat flux as input (or assumed negligible) - applied on a monthly time scale	R_n, T_a, α , VPD, P, θ and snow water equivalent for GLEAM
Water balance	- simple and easy to apply	- cannot directly derive gridded E - coarse spatiotemporal resolution - sensitive to precipitation data error	P, Q and ΔS
Water carbon linkage	- consideration of the linkage between carbon and water fluxes	- high requirements for forcing data - impacted by data gaps and errors - empirical carbon-water relationships	Varies for different models
Empirical	- simple, easy to apply	- requires calibration - degraded capability outside the calibration area - over-simplification of physical processes; - subject to weather condition if land surface temperature is required	Varies for different models but at least R_n and VI.

3.5 Reference remote sensing based evapotranspiration algorithms

After broadly reviewing the current evapotranspiration algorithms that make use of remote sensing data, in this section we focus on presenting the physical formulation of the four evapotranspiration algorithms considered in this work.

3.5.1 Priestley-Taylor Jet Propulsion Laboratory (PT-JPL)

In PT-JPL algorithm actual ET is derived by scaling the Priestley –Taylor potential evapotranspiration (Priestley & Taylor, 1972) considering different eco-physiological, atmospheric and soil constraints. Priestley-Taylor potential ET is given by Equation 3.20.

$$\lambda E = \alpha_{PT} \frac{\Delta}{\Delta + \gamma} (R_n - G) \quad (3.20)$$

where α_{PT} is the Priestley-Taylor constant (1.26), Δ is the slope of saturation-to-vapour pressure curve (kPa/K), γ is the psychrometric constant (kPa/K), R_n is the net radiation (Wm^{-2}) and G (Wm^{-2}) is the soil heat flux.

In PT-JPL model, λE is partitioned into three contributions: λE_I (interception evaporation), λE_c (canopy transpiration) and λE_s (bare soil evaporation). These contributions are given by Equations 3.21 to 3.23.

$$\lambda E_I = f_{wet} \alpha_{pt} \frac{\Delta}{\Delta + \gamma} R_{nc} \quad (3.21)$$

$$\lambda E_c = (1 - f_{wet}) f_g f_M f_T \alpha_{pt} \frac{\Delta}{\Delta + \gamma} R_{nc} \quad (3.22)$$

$$\lambda E_s = (f_{wet} + f_{SM}(1 - f_{wet})) \alpha_{pt} \frac{\Delta}{\Delta + \gamma} (R_{ns} - G) \quad (3.23)$$

where R_n is partitioned into a soil component (R_{ns}) and a canopy component (R_{nc}). These terms are calculated as $R_{ns} = R_n \exp(-k_{Rn} LAI)$ and $R_{nc} = R_n - R_{ns}$. The light extinction coefficient k_{Rn} assumes a value of 0.6 and LAI (m^2m^{-2}) is derived as: $LAI = (-\ln(1 - f_c)/k_{PAR})$ (Fisher et al., 2008). f_c is the fraction vegetation cover that in Fisher et al. (2008) is assumed equal to the fraction of photosynthesis active radiation (PAR) (Wm^{-2}) intercepted by total vegetation cover (f_{IPAR}) and k_{PAR} is equal to 0.5.

In Equations 3.21 to 3.23 the constraints used refer to: relative surface wetness (f_{wet}), green canopy fraction (f_g), plant temperature constraint (f_T), plant moisture constraint (f_M) and soil moisture constraint (f_{SM}). These terms are defined in Equations 3.24 to 3.28:

$$f_{wet} = RH^4 \quad (3.24)$$

$$f_g = f_{APAR}/f_{IPAR} \quad (3.25)$$

$$f_M = f_{APAR}/f_{APARmax} \quad (3.26)$$

$$f_T = \exp\left[-\left(\frac{T_a - T_{opt}}{T_{opt}}\right)^2\right] \quad (3.27)$$

$$f_{SM} = RH \frac{VPD}{\beta} \quad (3.28)$$

where RH is the relative humidity. f_{APAR} and f_{IPAR} are the fraction of PAR that is absorbed (APAR) and intercepted (IPAR) by green vegetation cover. According to Fisher et al. (2008), they are defined as: $f_{APAR} = 1.3632 \cdot SAVI - 0.048$ and $f_{IPAR} = NDVI - 0.05$, where SAVI and NDVI are the Soil Adjusted and Normalized Difference Vegetation Indexes, respectively. SAVI can be calculated as $SAVI = 0.45 \cdot NDVI + 0.132$ (Ershadi et al., 2014). Maximum yearly f_{APAR} value is used in the calculation of f_M . T_a refers to the maximum air temperature and T_{opt} ($^{\circ}C$) to the optimum plant growth temperature calculated as T_{max} ($^{\circ}C$) at $max\{PARf_{APAR}T_{max}/VPD\}$ and represents to the maximum air temperature at the time of the peak in canopy activity (i.e. maximum f_{APAR} and minimum VPD). VPD is the vapour pressure deficit ($e_s - e_a$) in kPa. β constant assumes a value equal to 1.0 kPa. The hypothesis behind f_{SM} is that surface moisture status is linked to and reflects the evaporative demand of the atmosphere (i.e. the soil moisture is reflected in the adjacent atmosphere). As the strongest link between atmospheric and soil moisture is at midday, the conditions at this time are used (RH_{min}, T_{max}) instead of daily averages for this calculation. In addition, for f_{wet} constraint it assumes to be zero for relative humidity (RH) values less than 0.7.

As observed, the model is driven with only five inputs: R_n , NDVI, SAVI, maximum air temperature (T_{max}), and water vapor pressure (e_a). In Fisher et al. (2008), estimated evapotranspiration was derived by using monthly means of tower-based meteorological measurements and also monthly AVHRR and ISLSCP-II (International Satellite Land-Surface Climatology Project, Initiative II) data. Nevertheless, some studies (Yuan et al., 2010; Garcia et al., 2013) have shown that it can be successfully applied considering daily forcing.

3.5.2 Penman Monteith-Mu (PM-Mu)

Mu et al. (2011) follows the Penman-Monteith logic (Monteith, 1965) in order to estimate λE . It is given in Equation 3.29.

$$\lambda E = \frac{\Delta(R_n - G) + \rho c_p VPD / r_a}{\Delta + \gamma(1 + \frac{r_s}{r_a})} \quad (3.29)$$

where ρ is the density of the air, c_p is the specific heat capacity of the air, r_a (sm^{-1}) is the aerodynamic resistance and r_s (sm^{-1}) is the surface resistance to evapotranspiration, which is an effective resistance to evaporation from land surface and transpiration from the plant canopy. Δ , γ , R_n , G and VPD have been defined previously in the PT-JPL model.

The PM-Mu model used in this study was firstly introduced in Cleugh et al. (2007), which used Equation 3.29 to estimate ET over Australia using MODIS data. Based on this model, Mu et al. (2007) developed a two-source ET model using remotely sensed data, suggesting its applicability for global ET estimation. Finally, in Mu et al. (2011) the version used in this study is provided. As in PT-JPL model, λE (Wm^{-2}) results from the contribution of three terms: evaporation from a wet canopy or interception term (λE_{wc}), transpiration from the canopy (λE_c) and evaporation from the soil (λE_s).

Evaporation from a wet canopy is calculated using Equation 3.30,

$$\lambda E_{wc} = f_{wet} f_c \frac{\Delta R_{nc} + \rho C_p VPD / r_a^{wc}}{\left(\Delta + \gamma \frac{r_s^{wc}}{r_a^{wc}} \right)} \quad (3.30)$$

where f_{wet} is calculated in the same form as in PT-JPL model, f_c represents the vegetation cover fraction (the fraction of PAR, f_{APAR} , is used as a surrogate for f_c), R_{nc} represents the canopy net radiation and resistances r_a^{wc} and r_s^{wc} represent the aerodynamic resistance and surface resistance for wet canopy, and are calculated following Equations 3.31 and 3.32.

$$r_a^{wc} = \frac{r_h^{wc} r_r^{wc}}{r_h^{wc} + r_r^{wc}} \quad (3.31)$$

$$r_s^{wc} = \frac{1}{f_{wet} g_e LAI} \quad (3.32)$$

where r_h^{wc} and r_r^{wc} are the wet canopy resistance to sensible heat flux and wet canopy resistance to radiative heat transfer, respectively. They are defined as in Equations 3.33 and 3.34.

$$r_h^{wc} = \frac{1}{f_{wet}g_hLAI} \quad (3.33)$$

$$r_r^{wc} = \frac{\rho c_p}{4\sigma(T_a + 273.15)^3} \quad (3.34)$$

In Equations 3.31 to 3.34, g_e and g_h (ms^{-1}) are the leaf conductance to evaporated water vapour and sensible heat per unit of LAI, respectively. σ is the Stephan-Boltzmann constant. T_a is the air temperature in $^{\circ}\text{C}$.

Regarding the available energy, R_{nc} is calculated as a function of R_n and f_c (i.e. $R_{nc} = f_c R_n$). In Mu et al. (2011) R_n is calculated as in Equation 3.35.

$$R_n = (1 - \alpha)R_s + (\varepsilon_a - \varepsilon_s)\sigma(T_a + 273.15)^4 \quad (3.35)$$

where α is the surface albedo, R_s is the shortwave incoming radiation, ε_a and ε_s are the atmospheric and surface emissivity respectively. ε_a is given by $\varepsilon_a = 1 - 0.26\exp(-7.77 \cdot 10^{-4} \cdot T_a^2)$ and ε_s is equal to 0.97.

The contribution from the canopy transpiration is calculated as in Equation 3.36.

$$\lambda E_c = (1 - f_{wet})f_c \frac{\Delta R_{nc} + \rho C_p VPD / r_a^t}{\left(\Delta + \gamma \frac{r_s^t}{r_a^t}\right)} \quad (3.36)$$

where r_a^t and r_s^t are the aerodynamic and surface resistances for transpiration respectively. r_a^t is calculated as in Equation 3.37.

$$r_a^t = \frac{r_h^t r_r^t}{r_h^t + r_r^t} \quad (3.37)$$

where the convective heat transfer resistance (r_h^t) is given by $r_h^t = 1/g_{bl}$ and the radiative transfer resistance (r_r^t) is calculated as $r_r^t = r_r^{wc}$ with g_{bl} (ms^{-1}) being the leaf-scale boundary layer conductance per unit LAI and assumed equal to that of the sensible heat (i.e. $g_{bl} = g_h$)

In the case of r_s^t it is calculated as the inverse of the bulk canopy conductance (C_c) (i.e. $r_s^t = 1/C_c$) where C_c (ms^{-1}) is calculated as in Equation 3.38.

$$C_c = \begin{cases} \frac{(1 - f_{wet})((G_s^{st} + G_s^{cu})G_s^b)}{G_s^{st} + G_s^{cu} + G_s^b} LAI & LAI > 0, (1 - f_{wet} > 0) \\ 0 & LAI = 0, (1 - f_w) = 0 \end{cases} \quad (3.38)$$

In this Equation 3.38, the canopy boundary-layer conductance G_s^b (ms^{-1}) is assumed equal to g_h (i.e. $G_s^b = g_h$), the cuticular conductance (G_s^{cu}) (ms^{-1}) is calculated as $G_s^{cu} = r_{corr}g_{cu}$ and the stomatal conductance (G_s^{st}) (ms^{-1}) is given by $G_s^{st} = C_L m(T_{min})m(VPD)r_{corr}$. The leaf cuticular conductance g_{cu} is per unit LAI and assumed equal to 0.00001 ms^{-1} . In addition, the mean potential stomatal conductance (C_L) (ms^{-1}) is per unit LAI and is assumed constant

for each biome. The r_{corr} is used to adjust the G_s^{st} based on the standard air temperature and pressure (Equation 3.39).

$$r_{corr} = \frac{1}{\frac{101300}{Pa} \left(\frac{T_a + 273.15}{293.15} \right)^{1.75}} \quad (3.39)$$

$m(T_{min})$ multiplier limits potential stomatal conductance by minimum air temperature (T_{min}) and $m(VPD)$ multiplier used to reduce the potential stomata conductance by VPD (Pa). They are given by Equations 3.40 to 3.41, where T_{min}^{open} , T_{min}^{close} , VPD^{open} and VPD^{close} depend on biome type.

$$m(T_{min}) = \begin{cases} 1 & T_{min} \geq T_{min}^{open} \\ \frac{T_{min} - T_{min}^{close}}{T_{min}^{open} - T_{min}^{close}} & T_{min}^{close} < T_{min} < T_{min}^{open} \\ 0 & T_{min} \leq T_{min}^{close} \end{cases} \quad (3.40)$$

$$m(VPD) = \begin{cases} 1 & VPD \leq VPD^{open} \\ \frac{VPD - VPD^{close}}{VPD^{open} - VPD^{close}} & VPD^{close} < VPD < VPD^{open} \\ 0 & VPD \geq VPD^{close} \end{cases} \quad (3.41)$$

The last contribution to total λE comes from the evaporation from the soil and is calculated as in Equation 3.42.

$$\lambda E_s = (f_{wet} + RH^{\frac{VPD}{\beta}} (1 - f_{wet})) \frac{\Delta (R_{ns} - G) + \rho c_p VPD / r_a^s}{\left(\Delta + \gamma \frac{r_s^s}{r_a^s} \right)} \quad (3.42)$$

where r_a^s and r_s^s are aerodynamic and surface resistances for the soil surface. The term $RH^{VPD/\beta}$ is based on the complementary hypothesis and describes the land-atmosphere interactions. β assumes a value of 200 Pa. R_{ns} is calculated as $R_{ns} = (1 - f_c)R_n$ and G is obtained from $G = G_{soil}(1 - f_c)$ and G_{soil} is given by Equation 3.43.

$$G_{soil} = \begin{cases} 4.73T_a - 20.87 & (T_{min}^{close} \leq T_{ann} < 25^\circ C) \text{ and } (T_{day} - T_{night} \geq 5^\circ C) \\ 0.0 & (T_{ann} \geq 25^\circ C) \text{ or } (T_{ann} < T_{min}^{close}) \text{ or } (T_{day} - T_{night} \geq 5^\circ C) \\ 0.39R_n & abs(G) > 0.39 \cdot abs(R_n) \end{cases} \quad (3.43)$$

r_a^s is calculated in a similar way to r_a^{wc} and r_a^t and is given by Equation 3.44.

$$r_a^s = \frac{r_h^s r_r^s}{r_h^s + r_r^s} \quad (3.44)$$

where the resistance to radiative transfer is equal to r_r^{wc} and the resistance to convective heat transfer (r_h^s) is assumed equal to r_s^s . This resistance is calculated as $r_s^s = r_{corr} r_{totc}$. r_{corr} is given in Equation 3.39 and r_{totc} is given by Equation 3.45.

$$r_{totc} = \begin{cases} r_{bl}^{max} & VPD \leq VPD^{open} \\ r_{bl}^{max} - \frac{r_{bl}^{max} - r_{bl}^{min}}{VPD^{close} - VPD^{open}} (VPD^{close} - VPD) & VPD^{close} < VPD < VPD^{open} \\ r_{bl}^{min} & VPD \geq VPD^{close} \end{cases} \quad (3.45)$$

r_{bl}^{max} , r_{bl}^{min} , VPD^{open} , VPD^{close} , T_{min}^{open} , T_{min}^{close} , g_h , g_e and C_L are parameters that depend on the biome type and need to be calibrated. In Table 3.2, the parameters values provided in Mu et al. (2011) are presented.

Table 3.2. Biome Properties Look-Up Table (BPLUT) for MODIS ET. ENF: evergreen needleleaf forest; EBF evergreen broadleaf forest; DNF deciduous needleleaf forest; DBF deciduous broadleaf forest; MF mixed forest; WL woody savannas; SV savannas; CSH closed shrubland; OSH open shrubland; Grass grassland, urban built-up or sparsely vegetated; Crop cropland (adapted from Mu et al. (2011)).

	T_{min}^{open} (°C)	T_{min}^{close} (°C)	VPD^{open} (Pa)	VPD^{close} (Pa)	g_h (ms ⁻¹)	g_e (ms ⁻¹)	C_L (ms ⁻¹)	r_{bl}^{min} (sm ⁻¹)	r_{bl}^{max} (sm ⁻¹)
ENF	8.31	-8	3000	650	0.04	0.04	0.0032	65	95
EBF	9.09	-8	4000	1000	0.01	0.01	0.0025	70	100
DNF	10.44	-8	3500	650	0.04	0.04	0.0032	65	95
DBF	9.94	-6	2900	650	0.01	0.01	0.0028	65	100
MF	9.5	-7	2900	650	0.04	0.04	0.0025	65	95
CSH	8.61	-8	4300	650	0.04	0.04	0.0065	20	55
OSH	8.8	-8	4400	650	0.04	0.04	0.0065	20	55
WL	11.39	-8	3500	650	0.08	0.08	0.0065	25	45
SV	11.39	-8	3600	650	0.08	0.08	0.0065	25	45
Grass	12.02	-8	4200	650	0.02	0.02	0.007	20	50
Crop	12.02	-8	4500	650	0.02	0.02	0.007	20	50

3.5.3. SEBS

In SEBS (Su, 2002), λE is obtained as a residual term of the surface energy balance (i.e. $\lambda E = R_n - H - G_0$). R_n and G_0 are defined as follows (Equations 3.46 to 3.47).

$$R_n = (1 - \alpha)S_{\downarrow} + \varepsilon L_{\downarrow} - \varepsilon \sigma LST^4 \quad (3.46)$$

$$G_0 = R_n[\Gamma_c + (1 - f_c)(\Gamma_s - \Gamma_c)] \quad (3.47)$$

where α is the surface albedo, S_{\downarrow} is the downward solar radiation, L_{\downarrow} is the downward longwave radiation, ε is the surface emissivity, σ is the Stephan-Boltzmann constant and LST is the land surface temperature. In Equation 3.46, R_n represents the net radiation, f_c the vegetation fraction cover and Γ_c and Γ_s represent the ratio of soil heat flux to net radiation and take values of $\Gamma_c = 0.05$ and $\Gamma_s = 0.315$.

In order to derive the sensible heat flux, the similarity theory is used. In Su (2002) a distinction is made between the Atmospheric Boundary Layer which uses the Bulk Atmospheric Boundary Layer Similarity (BAS) correction functions (Brutsaert, 1999) and the Atmospheric Surface Layer (ASL) which uses the Monin-Obukhov Similarity (MOS) functions also proposed by Brutsaert (1999). The ABL refers to the part that is directly influenced by the presence of the Earth's surface and responds to the surface forcings with a timescale of an hour or less, while ASL refers to the bottom 10% of ABL (Su, 2002). The selection of the similarity theory employed depends on the magnitude of the reference height (z_{ref}) and the height of the ASL (h_{st}). In order to derive this last quantity the height of the ABL (h_i) is required as input data to SEBS model. In case when no information is provided a default value of 1000 m can be used. In Su (2002), the h_{st} is calculated taking into account that it is proportional to h_i over moderated rough terrain and proportional to the surface roughness over very rough terrain (Brutsaert, 1999). This translates into Equation 3.48, in which default SEBS parameters were used.

$$h_{st} = \max(0.12h_i, 125z_{om}) \quad (3.48)$$

If $z_{ref} < h_{st}$, then MOS set of equations applies, otherwise BAS does. As it can be seen BAS only applies when we are dealing with atmospheric information at mid and upper levels of the atmosphere. Therefore, in the following only a brief explanation of retrieving H using MOS is provided. The set of established equations are given by Equation 3.13 to 3.16. In Equation 3.13, the contribution of E is not included. In these equations the stability corrections functions need to be specified for the unstable and stable conditions of the atmosphere. Unstable conditions are given by Equations 3.49 to 3.51, where where $y = -(z - d)/L$, $x = (y/a)^{1/3}$, $\Psi_0 = (-\ln a + 3^{1/2}ba^{1/3}\pi/6)$, and $a = 0.33$, $b = 0.41$, $c = 0.33$, $n = 0.78$, $d = 0.057$. Stable conditions are given by Equations 3.52 to 3.53, where $y_s = (z - d)/L$, $a_s = 1$, $b_s = 2/3$, $c_s = 5$ and $d_s = 1$. Unstable correction functions are given by Brutsaert (1999). Equation 3.49 apply for $y \leq b^{-3}$ and Equation 3.50 apply for $y >$

b^{-3} . For stable conditions, the expressions proposed by Beljaars & Holtslag (1991) and evaluated by van den Hurk & Holtslag (1997) were used.

Unstable conditions

$$\Psi_m(y) = \ln(a + y) - 3by^{\frac{1}{3}} + \frac{ba^{\frac{1}{3}}}{2} \ln \left[\frac{(1+x)^2}{1-x+x^2} \right] + 3^{\frac{1}{2}} ba^{\frac{1}{3}} \tan^{-1} \left[\frac{2x-1}{3^{\frac{1}{2}}} \right] + \Psi_0 \quad (3.49)$$

$$\Psi_m(y) = \Psi_m(b^{-3}) \quad (3.50)$$

$$\Psi_h(y) = \left[\frac{1-d_0}{n} \right] \ln \left[\frac{c+y^n}{c} \right] \quad (3.51)$$

Stable conditions

$$\Psi_m = -[a_s y_s + b_s \left(y_s - \frac{c_s}{d_s} \right) \exp(-d_s y_s) + b_s c_s / d_s] \quad (3.52)$$

$$\Psi_h = -\left[\left(1 + \frac{2a_s}{3} y_s \right)^{1.5} + b_s \left(y_s - \frac{c_s}{d_s} \right) \exp(-d_s y_s) + \left(\frac{b_s c_s}{d_s} - 1 \right) \right] \quad (3.53)$$

In SEBS, the roughness height for heat transfer is calculated as $z_{0h} = z_{0m} / \exp(kB^{-1})$. In order to estimate kB^{-1} , the model proposed by Su (2001) is used. kB^{-1} is thus given by Equation 3.54.

$$kB^{-1} = f_c^2 kB_c^{-1} + 2f_c f_s kB_m^{-1} + f_s^2 kB_s^{-1} \quad (3.54)$$

the first term in Equation 3.54 follows the full canopy model of Choudhury & Monteith (1988) and it is given by $kB_c^{-1} = kC_d / [4C_t \beta (1 - \exp(-\eta_{ec}/2))]$ with C_d is the drag coefficient of the leaves and takes a value of 0.2, C_t is the heat transfer coefficient of the leaf. For most canopies and environmental conditions C_t is bounded by $0.005 N \leq C_t \leq 0.075 N$, being N the number of sides of a leaf to participate in heat exchange. β is the ratio between the friction velocity and the wind speed at canopy height. It can be calculated from leaf area index (LAI) as $\beta = 0.32 - 0.264 \exp(-15.1 C_d LAI)$. η_{ec} is the within-canopy wind speed profile extinction coefficient calculated as $\eta_{ec} = C_d LAI / 2\beta^2$. The third term is that of Brutsaert (1982) for bare soil surface and it is calculated as $kB_s^{-1} = 2.46(Re_*)^{1/4} - \ln(7.4)$. Re_* is the roughness Reynolds number $Re_* = h_s u_* / \nu$. h_s is the roughness height of the soil equal to 0.009 m and ν is the viscosity of the air given by $\nu = 1.327 \cdot 10^{-5} (p_0/p) (T/T_0)^{1.81}$ with p and T being the ambient pressure and air temperature and $p_0 = 101.3 \text{ kPa}$ and $T_0 = 273.15 \text{ K}$. u_* is the friction velocity is given by $u_* = u_{zref} k / \ln[(z_{ref} - d_0) / z_{0m}]$ where u_{zref} is the wind speed at the reference height and d_0 is given by $0.667h$. h is the height of the canopy. The second term describes the interaction between vegetation and a bare soil surface and it is given by $kB_m^{-1} = \kappa \beta z_{0m} / C_t^* h$. h is the canopy height and $C_t^* = Pr^{-2/3} Re_*^{-1/2}$, where Pr is

the Prandtl number equal to 0.7. This term is weighted by f_c and f_s which are the canopy and soil fraction cover.

In order to determine the evaporative fraction, SEBS uses energy balance considerations at limiting cases (wet and dry limits). Under the assumption of dry-limit, the latent and sensible heat are given by Equations 3.55 and 3.56.

$$\lambda E_{dry} = R_n - G_0 - H_{dry} \equiv 0 \quad (3.55)$$

$$H_{dry} = R_n - G_0. \quad (3.56)$$

At the wet limit, λE reaches a maximum value and H_{wet} a minimum (but not zero). In addition, at this point λE coincides with potential evapotranspiration and its value could be derived from a Penman-Monteith type of equation (Equation 3.29). In this expression, the internal resistance (r_s is equal to 0) and then H_{wet} is evaluated as in Equation 3.57.

$$H_{wet} = \left((R_n - G_0) - \frac{\rho C_p e_s - e}{r_{ew} \gamma} \right) / \left(1 + \frac{\Delta}{\gamma} \right) \quad (3.57)$$

The external resistance r_{ew} can be expressed as in Equation 3.58.

$$r_{ew} = \frac{1}{ku_*} \left[\ln \left(z - \frac{d_0}{z_{0h}} \right) - \Psi_h \left(z - \frac{d_0}{L_w} \right) + \Psi_h \left(\frac{z_{0h}}{L_w} \right) \right] \quad (3.58)$$

where the Monin-Obukhov length at wet limit (L_w) (Equation 3.59).

$$L_w = - \frac{\rho u_*^3}{kg 0.61 (R_n - G_0) \lambda} \quad (3.59)$$

The relative evaporation is evaluated after the limiting cases as in Equation 3.60.

$$\Lambda_r = \frac{\lambda E}{\lambda E_{wet}} = 1 - \frac{\lambda E_{wet} - \lambda E}{\lambda E_{wet}} = 1 - \frac{H - H_{wet}}{H_{dry} - H_{wet}} \quad (3.60)$$

Then the evaporative fraction can be derived as in Equation 3.61.

$$\Lambda = \frac{\Lambda_r \lambda E_{wet}}{R_n - G} = \frac{\lambda E}{R_n - G} \quad (3.61)$$

In order to upscale the instantaneous fluxes to daily values, assuming that the evaporative fraction is conservative, the daily evapotranspiration value can be estimated as in Equation 3.62.

$$E_{daily} = 8.64 \cdot 10^7 \Lambda \frac{\overline{R_n}}{\lambda \rho_w} \quad (3.62)$$

3.5.4 LSA-SAF

The LSA-SAF model (Ghilain et al., 2011) can be described as a Soil Vegetation Atmosphere Transfer (SVAT) scheme modified to accept input data from external sources (Gellens-Meulenberghs et al., 2007). The parametrizations from TESSEL SVAT scheme (van den Hurk et al., 2000; Balsamo et al., 2009) are used as a baseline for model development, with a few variants in the formulations. These are: model runs decoupled from the atmospheric model and uses data from external sources like satellite remote sensing data, numerical weather prediction model output and recent information about land-cover characteristics.

In LSASAF model, the surface energy balance is solved independently for each of the so-called tiles. A tile is considered a smaller homogenous entity (vegetation, bare soil, snow etc). In practice, a maximum of four tiles (3 types of vegetation + bare soil) are allowed by pixel. The fluxes at pixel scale are then a weighted contribution of the fluxes of all the tiles composing the pixel.

The sensible (H_i) and latent (λE_i) are computed for each tile using Equations 3.63 and 3.64. This surface energy balance is computed in a conceptual layer called skin layer. This latter represents the coverage of the land surface as a flat layer, without description of the 3-D structure of the canopy.

$$H_i = \frac{\rho}{r_{ai}} [c_p (T_{ski} - T_a) - g z_a] \quad (3.63)$$

$$\lambda E_i = \frac{L_v \rho}{r_{ai} + r_{si}} [q_{sat}(T_{ski}) - q_a(T_a)] \quad (3.64)$$

where ρ is the air density, r_{ai} is the aerodynamic resistance, c_p is the heat capacity at constant pressure, T_{ski} is the surface skin temperature, T_a is the air temperature at level z_a above the surface, g is the acceleration due to gravity, L_v is the latent heat of vaporization, r_{si} is the stomatal resistance, $q_a(T_a)$ is the value of the surface specific humidity at height z_a and $q_{sat}(T_{ski})$ is the specific humidity at saturation. r_{ai} is calculated as function of the atmospheric stability following Monin-Obukhov similarity theory (Equation 3.65).

$$\frac{1}{r_{ai}} = \frac{ku_{*i}}{\ln\left(\frac{z_a - d_i}{z_{0hi}}\right) - \psi_h\left(\frac{z_a - d_i}{L_i}\right) + \psi_h\left(\frac{z_{0hi}}{L_i}\right)} \quad (3.65)$$

where L_i and u_{*i} are the friction velocity and Monin-Obukhov stability length defined as in Equations 3.13 and 3.14. The sensible heat and momentum stability functions (ψ_h and ψ_m) are defined as in Beljaars & Viterbo (1994). For the case of stable conditions, they agree with Equations 3.52 and 3.53 in the description of SEBS model, while for unstable conditions they take the following form (Equations 3.66 and 3.67), where $x = (1 - 16z/L)^{1/4}$.

$$\psi_m = \frac{\pi}{2} - 2 \operatorname{atan}(x) + \ln \frac{(1+x)^2(1+x^2)}{8} \quad (3.66)$$

$$\psi_h = 2 \ln \left(\frac{1+x^2}{2} \right) \quad (3.67)$$

The stomatal resistance is calculated following the same Jarvis approach (Jarvis, 1976) adopted in TESSEL SVAT scheme (Viterbo & Beljaars, 1995; van den Hurk et al., 2000). For vegetation, the general formulation is given by Equation 3.68.

$$r_{si} = \frac{r_{smini}}{LAI_i} f_1(S_{in}) f_2(\bar{\theta}) f_3(D_a) \quad (3.68)$$

For the particular case of bare ground, a simplified formulation is used (Equation 3.69).

$$r_{si} = r_{smini} f_2(\bar{\theta}_1) \quad (3.69)$$

where $f_1(S \downarrow)$, $f_2(\bar{\theta})$ and $f_3(D_a)$ functions are given by Equations 3.70 to 3.72 and taken from van den Hurk (2000).

$$f_1(S_{in})^{-1} = \min \left(1, \frac{0.004 S_{in} + 0.05}{0.81(0.004 S_{in} + 1)} \right) \quad (3.70)$$

$$f_2(\bar{\theta})^{-1} = \frac{(\bar{\theta} - \theta_{wp})}{(\theta_{fc} - \theta_{wp})} \quad (3.71)$$

$$f_3(D_a)^{-1} = \exp(-g_D D_a) \quad (3.72)$$

where S_{in} is the solar radiation incoming, $\bar{\theta}$ is the averaged water content in the root zone, θ_{wp} and θ_{fc} are the wilting point and field capacity of the soil assumed equal to 0.171 and 0.323 m³/m³. $\bar{\theta}$ is calculated according to Equation 3.73 and 3.74.

$$\bar{\theta} = \sum_{k=1}^4 R_k \max(f_{liqk} \theta_k, \theta_{wp}) \quad (3.73)$$

$$f_{liqk} = \begin{cases} 1 & T_k > T_{f1} \\ 1 - 0.5 \left(1 - \sin \left(\frac{\pi(T_k - 0.5T_{f1} - 0.5T_{f2})}{T_{f1} - T_{f2}} \right) \right) & T_{f2} \leq T_k \leq T_{f1} \\ 0 & T_k \leq T_{f2} \end{cases} \quad (3.74)$$

where T_{f1} and T_{f2} are two constant temperatures of 1°C (274.15 K) and -3° C (270.15 K). T_k and θ_k are the soil layer temperature and water content temperature of the NWP output (i.e. as derived from reanalysis) and R_k is the root distribution per vegetation type in % over the four soil layers (Table 3.3). In the case of the soil resistance, only the water content of the first soil layer ($\bar{\theta}_1$) is considered. D_a is the calculated as $e_{sat}(T_a) - e_a(T_a)$.

As in the case of r_{smin} , g_D is a vegetation type parameter. In Table 3.3, values are provided.

Table 3.3. Vegetation type considered in the LSASAF algorithm and associated parameters: minimum stomatal resistance (r_{smin}), coefficient for the dependency of canopy resistance on water vapour pressure deficit (g_D) and root distribution per vegetation type in % over the four soil layers (R_k). In the case of R_k , from left to right values correspond to increasing values of depth.

Vegetation type	r_{smin} (s/m)	g_D (hPa ⁻¹)	R_k
Bare soil	50	0	100-0-0-0
Snow	---	---	-----
Deciduous Broadleaved trees	300	0.03	24-38-31-7
Evergreen Needleleaved trees	250	0.03	26-39-29-6
Evergreen Broadleaved trees	250	0.03	25-34-27-14
Crops	180	0	24-41-31-4
Irrigated crops	180	0	24-41-31-4
Grass	110	0	35-38-23-4
Bogs and Marshes	250	0	25-34-27-11

At tile level i , the surface energy budget acts as a constraint and it is expressed by Equation 3.75.

$$R_{ni} - H_i - \lambda E_i - G_i = 0 \quad (3.75)$$

where R_{ni} and G_i are the net radiation and soil heat flux and are calculated as in Equations 3.76 and 3.77.

$$R_n = (1 - \alpha)S_{\downarrow} + \varepsilon(L_{\downarrow} - \sigma T_{ski}^4) \quad (3.76)$$

$$G_i = 0.5 \exp(-2.13(0.88 - 0.78 \exp(-0.6LAI))) R_{ni} \quad (3.77)$$

where T_{ski} is the model variable representing the surface temperature at tile level, σ is the Stephan-Boltzmann constant, α and ε are the surface and emissivity surface. S_{\downarrow} and L_{\downarrow} are the solar and longwave incoming radiation. All these values represent pixel values.

The surface energy balance is composed of four non-linear equations 3.63, 3.64, 3.65 and 3.13 and for unknowns ($H_i, \lambda E_i, T_{ski}, u_{*i}$). The rest of equations need to be taken into account through an iterative method. Neutral stability is assumed as initial condition. Iteration is stopped when pixel estimates of latent and heat fluxes are stabilized using a predefined precision. Heat fluxes for the whole pixel are calculated as a weighted contribution for each tile.

3.6.- Observations of Evapotranspiration

Retrieval of λE from estimations from satellite requires ground-based λE measurements in order to validate and also calibrate these methods. Currently, at landscape scale (i.e. meters to kilometers) the eddy covariance technique (EC), the energy balance Bowen ratio (BR) tower systems, lysimeters and scintillometers are able to provide these values. At even larger scale, such as that of a river basin, region or continent, λE can also be estimated from the surface water budget or atmospheric water balance. In Table 3.4, a summary of the λE observation and estimation methods is provided.

The EC technique measures H and λE fluxes from the statistical covariance of heat and moisture variations and vertical velocity using rapid response sensors at frequencies that are typically equal to or greater than 10 Hz (Wang & Dickinson, 2012). EC systems include a fast-response three-dimensional wind sensor (sonic anemometer) and an infrared gas analyzer. EC technique is a well-established method and deployed through global networks such as FLUXNET (Baldocchi et al., 2001). A typical error of about 5-20% or 20-50 W/m² has been reported (Foken, 2008). The main problematic aspect about this technique is the energy balance closure ratio (i.e. $R = (H + \lambda E)/(R_n - G)$) which report an imbalance of the 20% (Wilson et al., 2002). For further discussion on this issue we refer the reader to Foken et al. (2008) and Foken et al. (2011) works and references therein.

The Bowen Ratio method is also well established through U.S Atmospheric Radiation Measurement (ARM) system. It is based on simultaneous measurements of vertical gradients of air temperature and humidity that can be related using the Bowen Ratio (β) (Equation 3.78). Once β is known, λE and H can be estimated from the surface energy balance equation.

$$\beta = \frac{H}{\lambda E} = \frac{C_p(T_{a1} - T_{a2})}{\lambda(q_1 - q_2)} \quad (3.78)$$

Although this method presents some benefits, mainly that it requires less maintenance and is generally cheaper than the EC systems, it presents also several impediments: the difficulty in measuring small gradients over surfaces with efficient turbulent transfer. In addition, these measurements must lie within a constant-flux layer that becomes thin under high stable conditions. Besides, surface energy must be closed, which difficult the implementation for heterogeneous areas at short-time intervals. One of the main assumption is that turbulent transfer coefficients for heat and water are assumed to be identical.

Lysimeters are measuring devices introduced into the soil that can be used for measuring the amount of actual evapotranspiration. The measurement is directly obtained from the soil-water balance. These systems can be classified into non-weighting lysimeters and weighting-lysimeters. The first ones measure the amount of water percolating from the base of the lysimeter using a soil-water profile measurement method (such as neutron

probe). Precipitation can be measured with a rain gauge. Evapotranspiration can indirectly be retrieved from these measurements. In the case of weighing-lysimeters, precipitation, storage changes and drainage is measured directly (and in this way evapotranspiration) considering the mass change over time. Precision of lysimeters is about 0.05 mm to 0.1 mm equivalent water for hourly estimates (Holmes, 1984), thus commonly being used as reference for comparison with other methods. Nevertheless, it has a different scale (point measurement) than EC and BR methods. The main disadvantages of this technique include the difficulty in its construction and maintenance (Rana & Katerji, 2000) and the disturbance of the natural conditions by instrument itself (WMO, 2008).

Scintillometers are becoming a common alternative to EC and BR methods, because of its ability to quantify energy distributions at different scales (Lagouarde, 2002). This technique is based on the detection of intensity fluctuations caused by fluctuations of the refractive index of the air. These scintillations are indicators of the turbulent eddies in the scintillometer path. Generally, a scintillometer system consists of a transmitter and a receiver. Measurements at visible and radio (>1mm) wavelengths are performed in order to deduce the structure parameter of temperature and moisture from the structure parameter of refractive index of the air. From these structure parameters and making use of MOST similarity theory H and λE fluxes can be estimated (DeBruin, 2009), being λE calculated as a residual of the surface energy budget (Wang & Dickinson, 2012). The main inconvenient of this technique is the dependence on the MOST theory. It was reported that the overestimation of H flux (against EC H measurements) was related to the selection of the roughness parametrization and universal function of MOST (Zhang et al., 2010).

λE can also be estimated from the surface water balance and atmospheric water balance at basin or continental scale taking into account Equations 3.79 and 3.80.

$$ET = P - Q - dw/dt \quad (3.79)$$

where P is the precipitation, Q the river discharge and dw/dt the change of terrestrial water storage. Accuracy of the estimated ET comes from the accuracy of each input variable. Over well-maintained gauged networks accuracy of P should be less than 10% but this value can increase for satellite retrievals (Wang & Dickinson, 2012). In addition, errors in Q are far from negligible (Baldassare & Montanari, 2009). The last term can be derived from the Gravity Recovery and Climate Experiment (GRACE) satellite (Güntner, 2008).

$$ET = P + \overline{\nabla_H \bar{C}} + \partial W / \partial t \quad (3.80)$$

In Equation 3.80, W represents the column storage of atmospheric water vapor and \bar{C} the vertically integrated two-dimensional atmospheric water vapour flux. The operator ∇_H represents the horizontal divergence. This method requires reanalysis data in order to

estimate $\overline{\nabla_H C}$ and $\partial W/\partial t$, nevertheless it was shown that these data has substantial errors (Roads, 2003; Dominguez & Kumar, 2008). This method is only able to provide estimates at a monthly time scale and at low spatial resolution. This latter is determined by the fact that this balance can be applied only to areas large enough so that errors in estimates of atmospheric convergence are small (Lettenmaier & Famiglietti, 2006).

Table 3.4. Summary of the λE observation and estimation methods (extracted from Wang & Dickinson, 2012). * depend on measurement height above the canopy and wind speed

Method	Temporal scale	Spatial scale	Advantages	Disadvantages
Eddy covariance	Half hourly to yearly	Hundreds of meters*	Direct and independent measurement of λE and H	-Energy closure problem -Gap in bad weather and other conditions
Bowen Ratio	Half hourly to yearly	Hundreds of meters*	Energy is balanced	-Diffusivity for water and heat is assumed to be equal -Energy balance is assumed
Lysimeter	Half hourly to yearly	Point measurement	Direct observation of λE	- Environment is disturbed
Scintillometer	Half hourly to yearly	Meters to kilometers	Capture H and λE over large scale with known footprints	- Depends on MOST
Surface water balance	Monthly to yearly	Hundreds to thousands of kilometers	Direct estimate Regional and global estimation	- Accuracy guaranteed only for low temporal (multiyear average) and spatial resolution
Atmospheric water balance	Monthly to yearly	Hundreds to thousands of kilometers	Regional and global estimation	- Low accuracy

II. DATA AND METHODS

4. - DATA DESCRIPTION

4.1. - Sensors

4.1.1. - MODIS

The Moderate Resolution Imaging Spectroradiometer was launched into Earth orbit by NASA in 1999 on board the Terra platform satellite, and in 2002 on board the Aqua satellite (Figure 4.1). Together the instruments image the entire Earth every 1 to 2 days. They acquire data in 36 spectral bands (0.4 μm to 14.4 μm) and at varying spatial resolutions (250 m, 500 m and 1 km). They are able to provide measurements in large-scale global dynamics, including changes in Earth's cloud cover, radiation budget and processes occurring in the oceans, on land, and in the lower atmosphere. In Table 4.1, technical characteristics of MODIS sensor are provided.

Table 4.1. Technical characteristics of MODIS sensor. SNR refers to signal to noise ration and NET to noise-equivalent temperature difference.

Orbit	705 km, 10:30 descending node (Terra), 13:30 ascending node (Aqua), sun-synchronous, near-polar				
Swath dimensions	2330 km (cross track) by 10 km (along track at nadir)				
Scanning angle	$\pm 55^\circ$ (65° maximum vza)				
Temporal resolution	1-2 days (ground track cycle of 16 days)				
Radiometric resolution	12 bits				
Spatial resolution	250 m (bands 1–2) 500 m (bands 3–7) 1000 m (bands 8–36)				
Spectral resolution					
Band	Bandwidth (μm)	SNR/NET	Band	Bandwidth (μm)	SNR/NET
1	0.620-0.670	128	20	3.660-3.840	0.05
2	0.841-0.876	201	21	3.929-3.989	2.00
3	0.459-0.479	243	22	3.929-3.989	0.07
4	0.545-0.565	228	23	4.020-4.080	0.07
5	1.230-1.250	74	24	4.433-4.498	0.25
6	1.628-1.652	275	25	4.482-4.549	0.25
7	2.105-2.155	110	26	1.360-1.390	150 (SNR)
8	0.405-0.420	880	27	6.535-6.895	0.25
9	0.438-0.448	838	28	7.175-7.475	0.25
10	0.483-0.493	802	29	8.400-8.700	0.05
11	0.526-0.536	754	30	9.580-9.880	0.25
12	0.546-0.556	750	31	10.780-11.280	0.05
13	0.662-0.672	910	32	11.770-12.270	0.05
14	0.673-0.683	1087	33	13.185-13.485	0.25
15	0.743-0.753	586	34	13.485-13.785	0.25
16	0.862-0.877	516	35	13.785-14.085	0.25
17	0.890-0.920	167	36	14.085-14.835	0.25
18	0.931-0.941	57			
19	0.915-0.965	250			

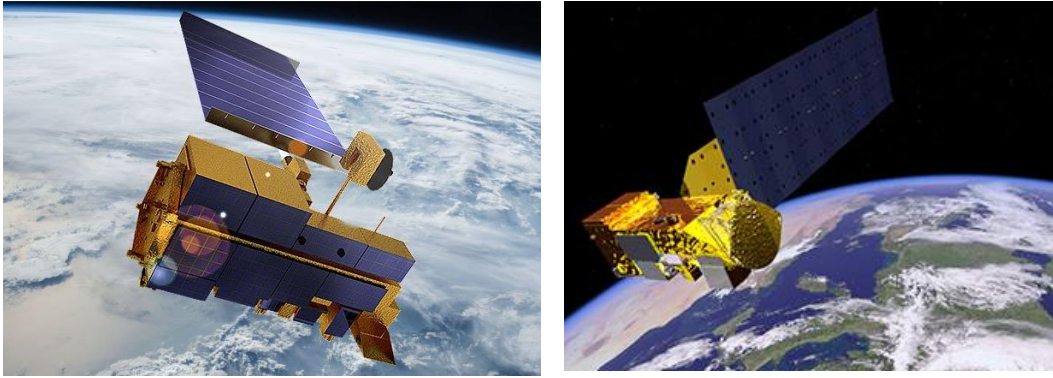


Figure 4.1. Artistic view of Terra (left) and Aqua (right) platforms

4.1.2. – VIIRS

Visible Infrared Imaging Radiometer Suite was launched into Earth orbit on board the Suomi NPP satellite in 2011 (Figure 4.2). The instrument is a whiskbroom scanning radiometer that collects visible and infrared imagery and radiometric measurements of the land, atmosphere, cryosphere and oceans. VIIRS extends and improves upon a series of measurements initiated by the Advanced High Resolution Radiometer (AVHRR) and the MODIS sensor. In Table 4.2, technical characteristics of VIIRS sensor are provided.

Table 4.2. Technical characterization of VIIRS sensor. SNR refers to signal to noise ration and NET to noise-equivalent temperature difference.

Orbit	824 km, 13:30 ascending node, sun-synchronous, near-polar				
Swath dimensions	3040 km (cross track) by 12 km (along track at nadir)				
Scanning angle	$\pm 56.28^\circ$ (70° maximum vza)				
Temporal resolution	1 day (ground track cycle of 16 days)				
Radiometric resolution	12 bits (M1-M4, M-7, M-13 High and Low gain)				
Spatial resolution	I-Imagery (375m), M-Moderate (750 m), DNB (750m)				
Spectral resolution					
Band	Bandwidth (μm)	SNR/NET	Band	Bandwidth (μm)	SNR/NET
I-1	0.6-0.68	214 (S)	M-6	0.739-0.754	368
I-2	0.85-0.88	264 (S)	M-7	0.846-0.885	457/631
I-3	1.58-1.64	149 (S)	M-8	1.23-1.25	221
I-4	3.55-3.93	0.4 (S)	M-9	1.371-1.386	227
I-5	10.5-12.4	0.4 (S)	M-10	1.58-1.64	586
DNB	0.5-0.9		M-11	2.23-2.28	22
M-1	0.402-0.422	588/1045	M-12	3.61-3.79	0.12
M-2	0.436-0.454	572/1010	M-13	3.97-4.13	0.04
M-3	0.478-0.488	628/988	M-14	8.4-8.7	0.06
M-4	0.545-0.565	534/586	M-15	10.26-11.26	0.03
M-5	0.662-0.682	336/631	M-16	11.54-12.49	0.03



Figure 4.2. Artistic view of the Suomi-NPP platform.

4.1.3. – SLSTR

Sea and Land Surface Temperature Radiometer is a dual scan view angle sensor (Figure 4.3). It was launched into Earth orbit onboard the Sentinel 3-A and Sentinel 3-B platforms in 2016 and 2018 respectively. The mission is aimed at maintaining the continuity with the (A) ATSR series of instruments. In Table 4.3, technical characteristics of SLSTR sensor are provided.

Table 4.3. Technical characterization of SLSTR sensor.

Orbit	814.5 km, 10:00 descending node, Sun-synchronous				
Swath dimensions	1400 km (nadir view), 740 km (dual view)				
Scanning angle	Almost nadir (nadir view), 55° (oblique view)				
Temporal resolution	0.5 to 1 day (nadir), 0.9-1.9 (dual) (ground track cycle 27 days)				
Spatial resolution	500 m (VIS-SWIR), 1000 m (IR-fire)				
Spectral resolution					
Band	Bandwidth (μm)	SNR/NET	Band	Bandwidth (μm)	SNR/NET
S1	0.535-0.574	>20	S7	3.074-4.140	< 80 mK
S2	0.640-0.679	>20	S8	10.078-11.630	< 50 mK
S3	0.847-0.889	>20	S9	11.118-12.928	< 50 mK
S4	1.354-1.396	>20	F1	3.344-4.410	< 1K
S5	1.553-1674	>20	F2	10.078-11.630	< 0.5 K
S6	2205.6-2305.9	>20			

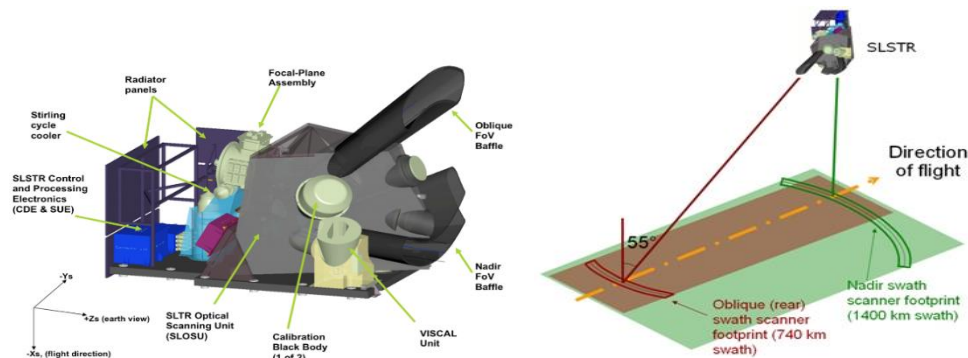


Figure 4.3. SLSTR instrument overview (left) and sketch of the instrument viewing geometry (right).

4.1.4. - CPR and CALIOP

The Cloud Profiling radar (CPR) is a 94 GHz nadir-looking radar and the Cloud-Aerosol Lidar with Orthogonal Polarization (CALIOP) is a lidar operating at 532 nm and 1064 nm. They were both launched in 2006 onboard the CloudSat and CALIPSO platforms respectively (Figure 4.4). Forming part of the A-Train constellation they flew along the same orbit close to each other (less than 2 minutes, Figure 4.5) so that footprints of both sensors overlapped, allowing to sense the same atmosphere volume. In Figure 4.5, the A-Train configuration over time is shown. In 2018, however due to technical issues both CloudSat and CALIPSO lowered their orbit out of the A-Train (16.5 km below). With this new configuration, simultaneity between A-Train and C-Train (CloudSat and CALIPSO) is obtained every 20 days.

CPR provides vertical profiles of the radar cross section and thus the refraction index, which is a measure for the concentration of cloud and precipitation particles. CALIOP provides information on the vertical distribution of aerosols and clouds and their optical and physical properties. CALIOP is built around a diode-pumped Nd:YAG laser producing linearly-polarized pulses of light at 1064 nm and 532 nm. Two-wavelength polarization measurements provide information on aerosol size and hydration. Combination of the data from both sensors (which work at different wavelengths and therefore sense different cloud occurrences) allows to obtain an almost complete characterization of the vertical cloud structure. In this way, CloudSat can penetrate the clouds that CALIPSO can't and CALIPSO can detect the thin, high cirrus clouds omitted by CloudSat. In Table 4.4, technical characteristics of CPR and CALIOP sensor are provided.

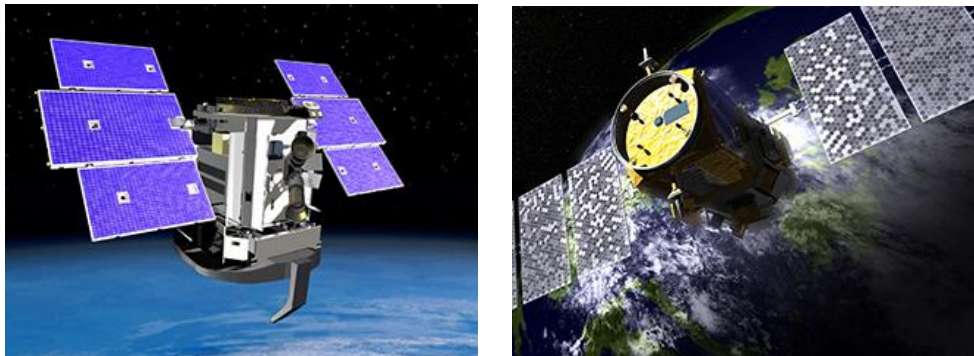


Figure 4.4. Artistic view of CloudSat and CALIPSO platforms.

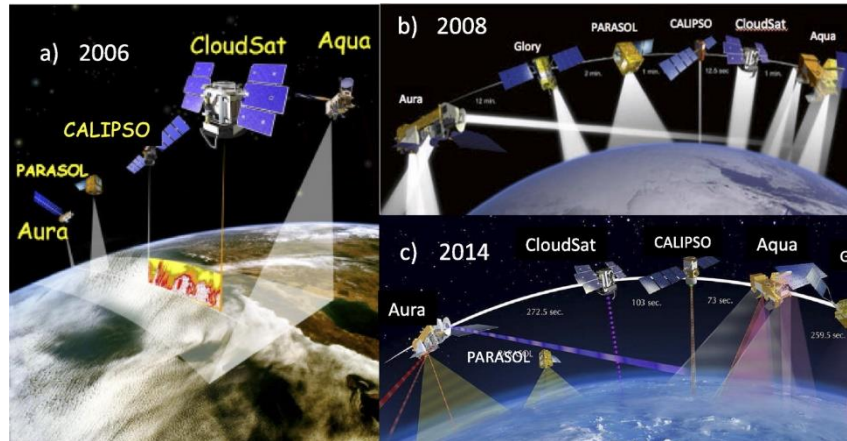


Figure 4.5. A-Train configuration over time

Table 4.4. Technical characterization of CPR and CALIOP sensors.

CPR		CALIOP	
Nominal Frequency	94 GHz	Wavelengths	532 nm, 1064 nm
Pulse Width	3.3 μ s	Pulse energy	110 mJoule/channel
PRF	4300 Hz	Repetition rate	20.25 Hz
Minimum Detectable Z	<-29 dBZ	Receiver telescope	1.0 m diameter
Data Window	0-25 km	Polarization	532 nm
Antenna Size	1.85 m	Footprint/FOV	100 m/ 130 μ rad
Dynamic Range	70 dB	Vertical resolution	30-60 m
Integration Time	0.16 s	Horizontal resolution	333 m
Vertical Resolution	500 m	Linear dynamic range	22 bits
Cross-track Resolution	1.4 km	Data rate	316 kbps
Along-track Resolution	1.7 km		
Repeat cycle	16 days		

4.2. - Reanalysis and land surface assimilation models

An atmospheric reanalysis is able to provide a description of the state of the atmosphere in a consistent four-dimensional way by combining a numerical weather prediction model with observations. The sources of data are: surface observations from land and ships, ocean buoys and upper air observations from radionsondes, aircraft and satellites (Barry & Carleton, 2001). A data assimilation system is used in order to incorporate these observations to the system and to constrain the reanalysis as close as possible to the observed atmospheric state. The assimilation scheme consists of the processing of observed data, interpolation, initialization, numerical forecast and post-processing (Kanamitsu, 1989). The forecast model has a crucial role in the data assimilation process. Making use of model equations it is possible to extrapolate information from locally observed parameters to unobserved parameters in a physically meaningful way, and also to propagate the atmospheric state in time (Dee et al., 2001). This propagated atmospheric

state (background) is updated, at regular time intervals, typically 6 or 12 hours, with observations, in order to form the analysis at that time. This update step typically uses variational data assimilation, whereby a cost function is minimized iteratively.

Reanalysis used in the present dissertation belong to the third-generation of global reanalysis. First generation of reanalysis were developed in 1990s. They were: NASA/DAO reanalysis (1980 - 1993), the NCEP/NCAR reanalysis (1948 - present), also called NCEP-1 reanalysis, and the ECMWF ReAnalysis (ERA) ERA-15 reanalysis (1979 - 1993). They were generated by optimal interpolation assimilation schemes. In the early 2000s several problems were resolved including the parametrization of physical processes in the same grid network (Kanamitsu et al., 2002). These new reanalysis belong to the second generation. They were: the JRA-25 reanalysis (1979 - 2004) from Japan, the NCEP-2 reanalysis (1979 - present), and the ERA-40 reanalysis (1958 - 2001). These reanalyses were based on three-dimensional variational (3DVAR) assimilation schemes. Third generation of reanalysis was developed in 2010s. They were generated by improved data assimilation schemes compared to 3DVAR. These reanalyses are: NASA/GMAO MERRA reanalysis (1979 – present), the NCEP CFSR reanalysis (1979 - 2008), the JRA-55 reanalysis (1958 – 2012), the 20CR reanalysis (1871 – present), and the ERA-Interim reanalysis (1979 – present).

In Table 4.5, a brief comparison of the MERRA-2 and ERA-Interim reanalysis is presented. In the following, a brief description of the reanalysis system is provided based on references in Table 4.5. MERRA-2 is an updated version of MERRA reanalysis (Rienecker et al., 2011). MERRA-2 is produced with 5.12.4 of the GEOS atmospheric data assimilation system. GEOS atmospheric model (Rienecker et al. 2008; Molod et al. 2015) and the Gridpoint Statistical Interpolation analysis scheme (Wu et al. 2002; Kleist et al. 2009) are the key components of the reanalysis system. . The model uses a cubed-sphere horizontal discretization at an approximate resolution of $0.5^\circ \times 0.625^\circ$ and 72 hybrid-eta levels from the surface to 0.01 hPa. The analysis is computed on a latitude–longitude grid at the same spatial resolution as the atmospheric model using a 3DVAR algorithm based on the Gridpoint Statistical Interpolation with a 6-h update cycle and the so-called First Guess at appropriate time procedure for computing temporally accurate observation-minus-background departures (Gelaro et al., 2017). Incremental analysis update procedure is used in order to correct the background state.

ERA-Interim is a global atmospheric reanalysis produced by the European Centre for Medium-Range Weather Forecasts (ECMWF), covering the data-rich period since 1979. It uses the ECMWF's Integrated Forecast System (IFS) cycle 31r2. The horizontal resolution of the data set is ~ 79 km (TL255 spectral grid) on 60 model levels from the surface up to 0.1 hPa (an altitude of about 65 km). The assimilation algorithm of the system is a four-dimensional variational analysis (4D-VAR) with a 12 h analysis window. Currently, ERA-Interim is being phased out and replaced by the next-generation ERA-5. This reanalysis is produced using the IFS cycle 41r2 with 4-D-Var data assimilation. ERA-5 benefits from a horizontal resolution of ~ 31 km (TL639 spectral grid) and a vertical resolution of 137 hybrid sigma–pressure levels, with the top level located at

0.01 hPa (an altitude of about 80 km). ERA-5 will eventually replace the ERA-Interim reanalysis. For a more detailed description of this reanalysis see Hersbach & Dee (2016).

Table 4.5. MERRA-2 and ERA-Interim comparison table.

	MERRA-2	ERA Interim
Source	NASA	ECMWF
Spatial domain	Global	Global
Period of record	1980-present	1979-present
Assimilation Algorithm	3D-VAR, with incremental update; aerosol data assimilation, observation corrected precipitation forcing for land surface and aerosol wet deposition	4D-VAR
Model Resolution	Native cube sphere grid output is interpolated to 5/8 lon x 1/2 lat deg; 72 sigma levels	T _L 255L60 and N128 reduced Gaussian
Dataset Resolution	5/8° lon x 1/2° lat 72 model levels	0.75°x0.75°x60 levels
Available timestep	Sub-daily, daily, monthly	Sub-daily, daily, monthly
Reference	Gelaro et al., 2017 Bosilovich et al., 2015	Dee et al., 2011 Berrisford et al., 2009

Apart from reanalysis, meteorological data were extracted from land assimilation systems. In particular, Global Land Assimilation system (GLDAS-2) (Rodell et al., 2004) was used. It integrates a large quantity of satellite-based, ground-based observations and model (re)analysis data in order to parameterize, force and constrain sophisticated numerical land surface models towards the goal of producing, physically consistent, high resolution fields of land surfaces states and fluxes. Datasets are available in a 3-hourly and monthly time resolution starting on January of 1948 to present with spatial resolutions of 0.25° and 1.00°. NASA GLDAS-2 has two components: one forced entirely with the Princeton meteorological forcing data (hereafter, GLDAS-2.0), and the other forced with a combination of model and observation based forcing datasets (hereafter, GLDAS-2.1). For further information on forcing datasets, please refer to <https://ldas.gsfc.nasa.gov/gldas/forcing-data>.

GLDAS products are retrieved from the Land Information System (LIS) , which is an open source flexible land-surface modeling and data assimilation software framework developed at NASA Goddard within the Hydrological Sciences Laboratory (Kumar et al., 2006). GLDAS is a specific use of this software. Enabled by this LIS system GLDAS drives four offline (not coupled to the atmosphere) land surface models. They are: Mosaic, Noah, Community Land Model (CLM) and the Variable Infiltration Capacity model (VIC). In the following a brief description of the models as extracted from the GLDAS Land Surface Model description (<https://disc.gsfs.nasa.gov/information/documents>, accessed the 3th of August 2019) is given.

- Mosaic (Koster & Suarez 1996) is a stand-alone, 1-D column model that can be run both uncoupled and coupled to the atmospheric column. Mosaic was the first to treat subgrid scale variability by dividing each model grid cell into a Mosaic of tiles (after Avissar & Pielke 1989) based on the distribution of vegetation types within the cell. Mosaic's physics and surface flux calculations are similar to the SiB LSM (Sellers et al., 1986).
- Noah (Chen et al., 1996) is the National Centers for Environmental Prediction/Oregon State University/Air Force/Hydrologic Research Lab (Noah) and has been used operationally in NCEP models since 1996. It is a stand-alone, 1-D column model which can be executed in either coupled or uncoupled mode. The model applies finite-difference spatial discretization methods and a Crank-Nicholson time-integration scheme to numerically integrate the governing equations of the physical processes of the soil-vegetation-snowpack medium
- VIC (Liang et al. 1994) is a stand-alone, 1-D column model that is run uncoupled. The model focuses on runoff processes that are represented by the variable infiltration curve, a parameterization of sub-grid variability in soil moisture holding capacity, and nonlinear baseflow. Various simulation modes are available including, water balance, energy balance, frozen soil, and other special cases.
- CLM (Dai et al., 2003) includes superior components from each of three contributing models: the NCAR Land Surface Model (Bonan, 1998), the Biosphere-Atmosphere Transfer Scheme (Dickinson et al. 1993), and the LSM of the Institute of Atmospheric Physics of the Chinese Academy of Sciences (Dai & Zeng 1997). The model applies finite-difference spatial discretization methods and a fully implicit time integration scheme to numerically integrate the governing equations. CLM can be run as a stand-alone, 1-D column model. It is also the land model for NCAR's coupled Community Climate System Model (CCSM).

4.3. - Study area and in-situ sites

4.3.1. - Amazonian region

In Figure 4.6, the Amazonian evergreen broadleaf forests as defined in this study are displayed. They were delineated from the intersection of pixels classified as “Evergreen Broadleaf Forests” in MCD12Q1 (1km) and MCD12C1 (5 km) MODIS land cover products and a geographical vector covering the political regions of Amazonia. This region encompasses the countries of Colombia, French Guiana, Suriname, Guyana, Venezuela, Ecuador, Perú, Bolivia and Brazil. This region is characterized by a flat topography (Figure 4.7(a)) (i.e. in exception of the Andes mountains the elevation of study region is less than 500 m) and is covered by dense tropical forest (mean annual NDVI value around 0.8 with 1- σ annual standard deviation of 0.02, Figure 4.7 (b)). The climate is hot and wet. Mean daily air temperature ranges between 298 K and 300 K (Figure 4.7(c)). Annual precipitation of the region range from approximately 1000 mm/year to values greater than 5000 mm/year at some locations (Figure 4.7 (d)), showing two maximum (3000 mm/year or more) located around the mouth of the Amazon River and over the northwestern part of the region (Espinoza et al., 2009). Rainfall is also abundant at the central area and close to the southeast due to the South Atlantic Convergence Zone (SACZ) established during the austral summer (Espinoza et al., 2009). The Andean region is characterized by a high spatial rainfall variability, registering the highest and lowest rainfall values in the region. In Figure 4.7(e), the soil classification of the region according to the Harmonized Soil World Database is provided.

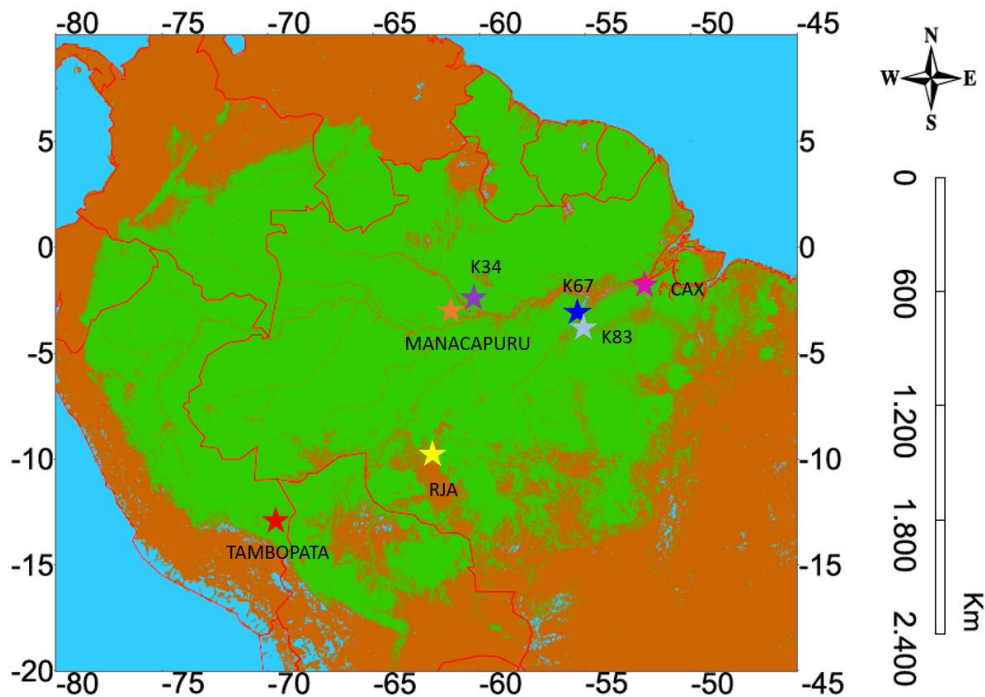


Figure 4.6. Map of the Amazonian evergreen broadleaf forests. The location of Tambopata (in-situ LST) station, together with LBA stations (K34, K67, K83, RJA and CAX) and Manacapuru station (in-situ cloud cover) is also displayed.

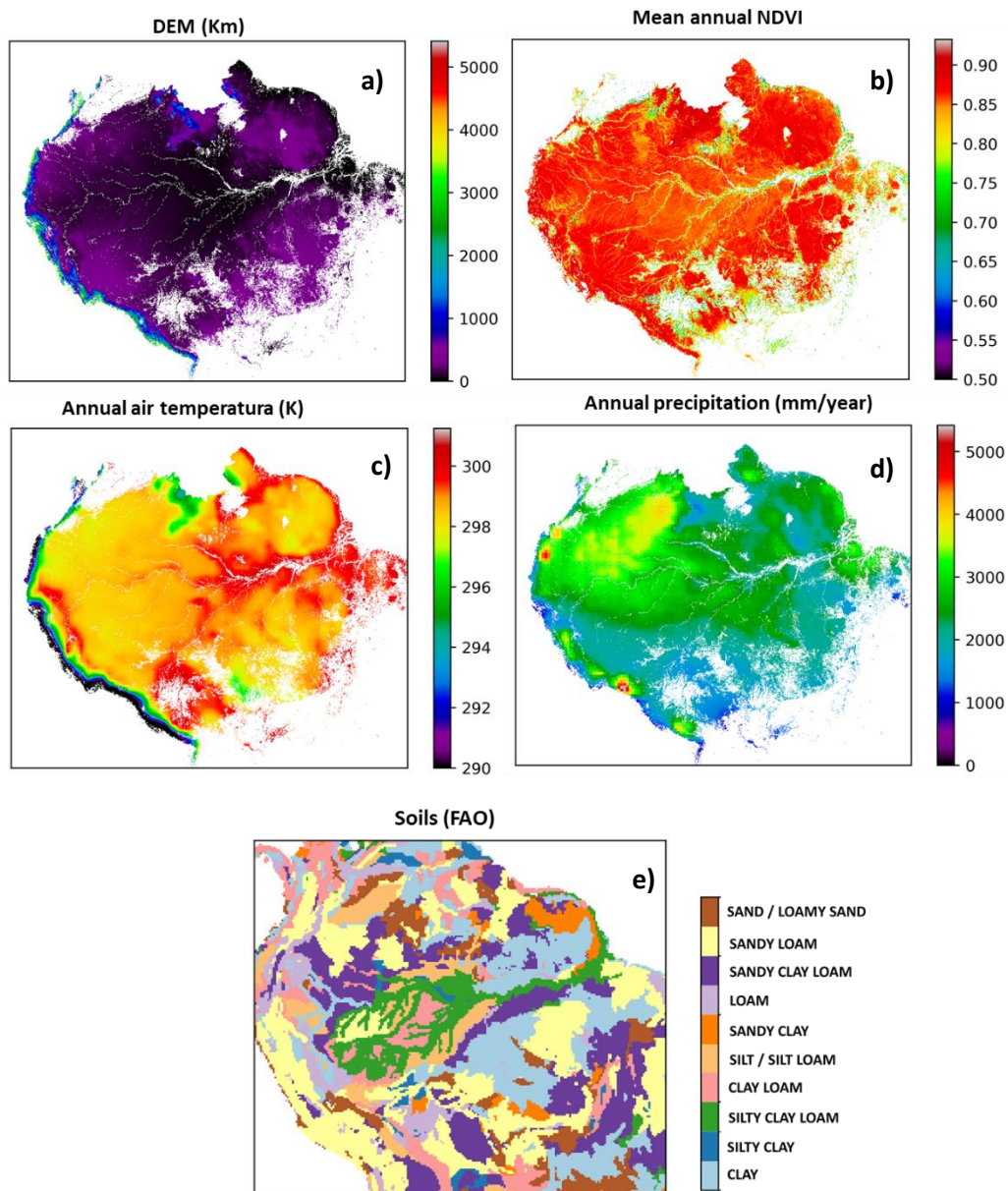


Figure 4.7. Topographic, vegetation, climate and soil conditions for the Amazon Evergreen Forests. Digital Elevation Model (DEM) was extracted from the Shuttle Radar Topography Mission (strm.csi.cgiar.org). Annual NDVI represents the mean NDVI derived from 2000-2014 MAIAC NDVI product. Air temperature (at 2m) was derived from MERRA-2 reanalysis over 2000-2006 years. Precipitation field was calculated from the Tropical Rainfall Measuring Mission (TRMM) data product from 1998-2018. Soil texture was extracted from the Harmonized Soil Word Database (FAO, 2012) according to USDA soil texture classification.

In the following, a brief description of the variability of the precipitation for the region is provided. This has been based on previous reviews of Amazonian climate (Fisch et al., 1998; Vera et al., 2006; Garreaud, 2007; Nobre et al., 2009; Garreaud et al., 2009; Espinoza et al., 2009). Tropical rainfall over the study region experiences a pronounced seasonal cycle, showing contrasting rainfall regimes between the northern and the southern Amazon (Nobre et al., 2009; Garreaud et al., 2009; Espinoza et al., 2009). These changes are controlled by the annual cycle of solar radiation (Nobre et al., 2009) and by complex interactions in low-level moisture transport (Fu, 1999). During the austral winter (June-July-August) the maximum continental rainfall is located to the north of the equator, almost in line with the oceanic ITCZ (Figure 4.8 (b)) while the central part of the continent (including southern Amazonia) experiences its dry season (Garreaud, 2007). During the austral spring (September-October-November), a rapid shift of the area of intense convection is produced between the northern extreme of the continent and latitudes south of the equator (Marengo et al., 2001). During the austral summer (December-January-February) the so-called South American Monsoon System is established. Associated with it, the southern parts of the region experiment a peak in rainfall and runoff. The SASM features the SACZ, which is a southeastward band of cloudiness and precipitation extending from southern Amazonia toward southeastern Brazil and the surrounding Atlantic Ocean (Vera et al., 2006). It is displayed in Figure 4.8(a). In addition, a deep continental low forms over the dry and hot Chaco region (approximately at 25°S) is formed as a regional response of the tropospheric circulation to the strong convective heating over the Amazon. It forces the trades that transport moisture from the Atlantic Ocean to turn south along the Andes towards the extra-tropics of South America (Garreaud et al., 2009). This northerly flow, organized in a low-level jet (South-American Low-Level jet) with its core at about 1km above the ground (Garreaud et al., 2007), is able to transport considerable amounts of moisture to between the Amazon and La Plata Basin (Vera et al., 2006). At upper levels of the atmosphere, the SASM features two distinctive characteristics: the well-defined anticyclone centered over Bolivia, the “Bolivian High” and a trough near the coast of northeast Brazil (Nobre et al., 2009). Their situation is also displayed in Figure 4.8(c). During the early fall, deep convection gradually diminishes over the subtropics and begins to shift northwards, with the demise of the South American Monsoon by the end of April (Garreaud, 2007).

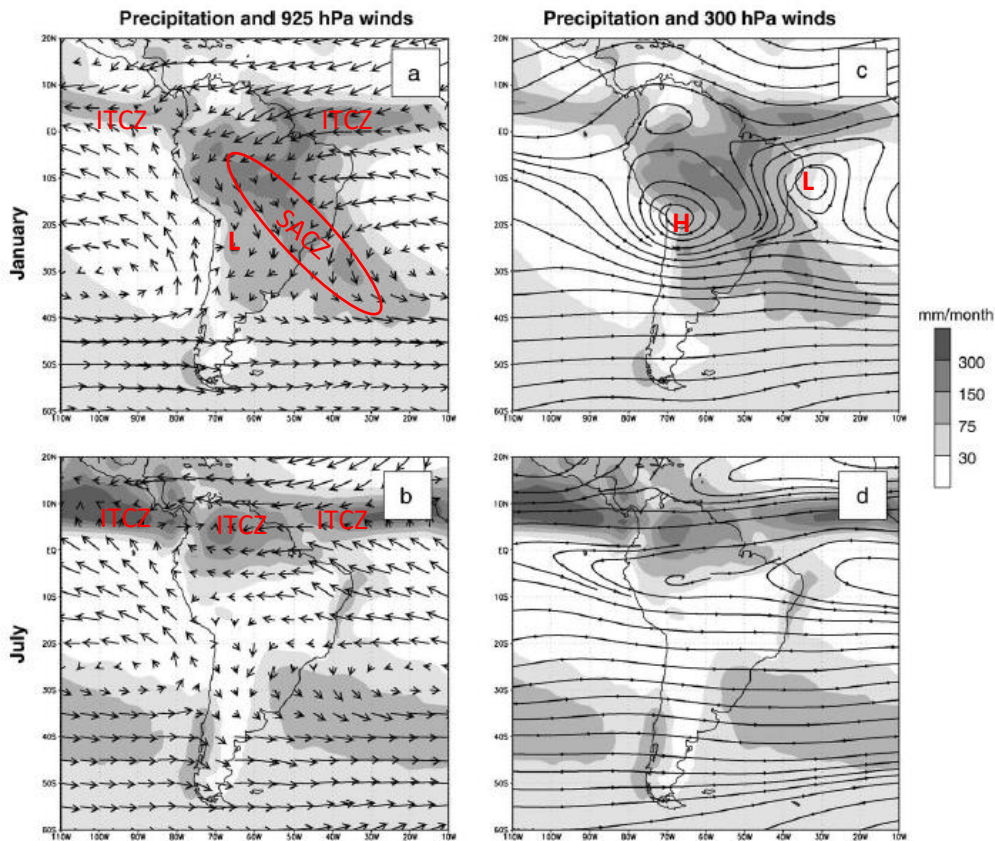


Figure 4.8. Long-term mean precipitation for January and July superimposed upon the low level (925 hPa) and upper levels (300 hPa) winds. The ITCZ in panels (a) and (b) represent the Intertropical Convergence Zone. In addition, in panel (a) the South American Convergence Zone (SACZ) together with the chaco low (L). In panel (c) Bolivian High and northeast Brazil trough are displayed by letters H and L respectively. (adapted from Garreaud et al., 2009).

The time evolution of rainfall conditions over the Amazon region exhibits non-regular fluctuations on a wide range of temporal scales (Garreaud et al., 2007). These fluctuations include the synoptic-scale variability on a sub monthly time-scale (2 to 10 days), the intraseasonal variability (from 10 to 90 days) and the low frequency variability, which involves changes between consecutive years (interannual) or in the scale of decades (interdecadal). Regarding the synoptic-scale variability, the fluctuations tends to exhibit a quasi-weekly periodicity associated with the passage of midlatitude disturbances that owe their existence to the baroclinic instability of the tropospheric flow (Garreaud et al., 2009). On intraseasonal scale, the 30- to 60-day oscillation is the principal mode of climatic fluctuations over tropical South America (Nobre et al., 2009). Interannual variability is linked to Atlantic and the Tropical Pacific Oceans. Evidences that the tropical Atlantic influences interannual climate variability of the Americas are provided by among others Marengo (1992), Liebman et al. (2001), Ronchail et al. (2002). The influence of the tropical Sea Surface Temperature (SST) over Amazonian rainfall is associated with Hadley-like cell perturbations. A positive rainfall anomaly can result from the northward displacement of the ITCZ due to one of the following reasons: anomalously

warm water in the tropical North Atlantic, cold surface waters in the equatorial South Atlantic or a weakening in the northeast trades (Nobre et al., 2009). In the case of the Tropical Pacific, the El-Niño-Southern-Oscillation (ENSO) phenomenon characterized by irregular fluctuations between its warm (El Niño) and cold (La Niña) is the major source of interannual variability over much of South America (Garreaud et al., 2009 and Nobre et al., 2009 and references therein). Episodes of el Niño are typically associated with a below normal rainfall and warmer than normal conditions in the northern part of South America, as well as anomalously wet conditions in the southeastern portion of the continent and central Chile. Opposite rainfall anomalies are typically observed in both regions during La Niña events (Garreaud, 2009). Regarding the variability at longer time-scales (i.e. decadal and inter-decadal) the “climate shift” around the mid 70s (the northern/southern part of Amazonia shows relatively less/more rainfall in comparison with the formed period) is consistent with the change in polarity in the Pacific Decadal Oscillation (PDO) (from cold to warm) (Garreaud et al., 2009). The PDO is an established phenomenon lasting 20-30 years in the Pacific. It is detected as warm or cool surface waters in the Pacific Ocean north of 20° (Mantua, 1997). When PDO is in positive phase water is colder in the central and western Pacific and warmer in the eastern Pacific. With a negative PDO the reverse is observed.

4.3.2. - Manacapuru site

In-situ cloud measurements used in the present dissertation belonged to the Green Ocean Amazon (GoAmazon2014/5) Experiment that was performed near the city of Manaus (central region of the Amazon basin) from January 2014 through 31 December 2015. The objective of this experiment was to understand and quantify the linked processes between vegetation and atmospheric chemistry on one hand and aerosol production and their connection to aerosols, clouds, precipitation on the other (Martin et al., 2016). To this end, the Manaus metropolis was used as a natural laboratory as it superimposes the background conditions of the central Amazon basin to the pollution plume from the city. Amongst the instrumented in-situ sites Manacapuru site (T3) was operated by the Atmospheric Radiation Measurement (ARM) Climate Research Facility of the United States Department of Energy. This facility included the ARM Mobile Facility One (AMF-1) and the ARM Mobile Aerosol Observing System (MAOS) (Mather & Voyles, 2013). The T3 site was located at 3.2130°S, 60.5981° W (70km of Manaus). It was a pasture site of 2.5km by 2km situated 2km to the north of a lightly travelled two-lane road (AM-070) that connects Manaus to Manacapuru (Martin et al., 2016).

Amongst the in-situ instrumentation a Total Sky Imager (TSI-880) was installed in order to detect cloud occurrences. This instrument is an automatic full-colour sky imager system that provides real-time processing and display of daytime sky conditions. It replaces the need for human observers under all weather conditions. Refer to Appendix A.1 for technical characterization of the TSI-880 instrument. Image acquisitions are

provided for solar elevations greater than 10 degrees with an interval of 30 s. The functioning of the instrument is as follows: 1) images from the sky are captured via a solid-state charge-coupled device looking downward onto a heated, rotating hemispherical mirror. A shadow band on the mirror blocks the intense direct-normal light from the sun, thereby protecting the imager optics. 2) An image processing program running on a user-provide PC workstation captures and displays the images at a user defined sampling rate. It saves the images to JPEG files for analysis. 3) Images are analyzed in order to infer both fractional sky cover and sunshine duration. The analysis step first masks out obstructions (the imager, its arm and the sun-blocking band). Fractional sky cover is determined by a processing algorithm that examines the colour relationships of the remaining image pixels to infer whether the pixel represents clear sky or thin or opaque clouds. In addition, the differential of brightness along the sun blocking band is analyzed to infer if the sun is blocked by cloud or not (i.e. a sunshine meter).

4.3.3.- Tambopata site

Tambopata test site (12.832 S, 69.282 W) is located in the Peruvian Amazon (Madre de Dios, Perú). This site is located at an elevation of 225 above the sea level. It has a yearly precipitation of 2580 mm/year. Annual mean temperature is about 299.2 K with a standard deviation of 2.8 K. Maximum and minimum temperature reach values of 308 K and 293 K, respectively. Dry season as defined by the number of month having less than 100 mm/month of precipitation extends from May to September (derived from TRMM precipitation product). The station is situated in a homogenous area characterized by dense tropical forest (mean NDVI of a 3x3 kernel of 0.83 with a standard deviation of 0.02). Canopy height reaches values of 30 m (Simard et al., 2011).

The equipment at Tambopata site consists of two infrared radiometers sensors (SI-111 and IR120) and a CNR4 net radiometer (Figure 4.9). Infrared radiometers determine the surface temperature of an object without physical contact. The CNR4 net radiometer consists of a pyranometer pair, one facing upward, the other facing downward, and a pyrgeometer pair in a similar configuration. The pyranometer pair measures the short-wave radiatio and the pyrgeometer pair measures long-wave radiation. All 4 sensors are integrated directly into the body of the instrument. For a detailed description of technical specifications of the sensor, please refer to Appendix A.1.



Figure 4.9. Tambopata test site tower site (perspective from below) together with images of CNR4 net radiometer (lower left) and infrared radiometers (lower right).

4.3.4.- LBA network

The Large-Biosphere-Atmosphere (LBA) program was created in 1993 with the purpose to develop the knowledge about the Amazon mainly in the fields of climate physics and biogeochemistry (Keller et al., 2004; Gonçalves et al., 2013). One of the achievements of this program was the establishment of a network of eddy covariance flux towers across the Brazilian Amazonia, providing important measures of energy, water and carbon fluxes (Saleska et al., 2013). In the present dissertation, we compiled original flux data from five LBA eddy covariance towers (Figure 4.6, Table 4.6): the Reserva Cuierias near Manaus city (K34 forest), the Tapajos National forest, near Santarem (K67 and K83 stations), the Caxiuana National forest near Belem (CAX station) and the Reserva Jaru forest (RJA station). In the following a brief description of the in-situ stations conditions as provided by the references in Table 4.6 is given. For a description of the instrumentation at each site, refer to Appendix A.1. In addition, in Figure 4.10 a description of the monthly meteorological and vegetation conditions for the sites is given.

- Manuas K34 is the most western of the central Amazonian sites and is located about 60 km north of Manaus, embedded in a vast area of pristine rainforest (Andreae et al., 2002). In contrast to Santarem sites (the nearest neighbouring LBA sites) it has a shorter dry season. Direct oceanic influence on the climate can be neglected (1600 km from the Atlantic). K34 tower was erected in 1999. It is a 1.5 m × 2.5 m-section aluminium tower, 50 m tall, on a medium sized plateau (60.209° W, 2.609° S 130 m asl). Near the centre of the reserve a selective logging experiment was conducted in 1987/99 and 1993 with 12 ha and 4 ha being investigated respectively. The extraction of trees represented approximately the 15% of average dry biomass for the area. Nevertheless, the resultant small disturbance is located about 8 km from the tower and hence represents only the 0.05% of the footprint of the tower (Araujo et al., 2002). Although there is a little large-scale relief in this region, at smaller scale the dense drainage network has formed a pattern of plateaus and valleys with a maximum height difference of about 60 m. In a 1km, 5km and 10km radius area of the site plateaus represented a 40%, 54% and 58% respectively (Araujo et al., 2002). Plateaus are covered mostly by clayey Oxisols and valleys by sandy Spodosols. The most frequent botanical families in the region are: Caesalpiniaceae, Vochysiaceae, Euphorbiaceae, Clusiaceae, Sapotaceae, Myristicaceae, Rutaceae, Malpighiaceae, and Anacardiaceae are most frequently found (Jardim & Hosokawa, 1987).
- Santarem K67 station is located at the Tapajos National Forest (54.959° W, 2.857° S Para Brazil). The forest is bounded by the Tapajos River to the west and the BR-163 highway on the east. The tower was located approximately at 6 km from both bounds, in an area of largely contiguous forest extending for tens of kilometres to the north and south (Hutyra et al., 2007). The soils are predominately nutrient-poor oxisols with pockets of sandy ultisols, both having low organic content and cation exchange capacity (Silver et al., 2000). The forest is on a flat terrain and has a closed canopy with a mean height of approximately 40-45 m and emergent trees reaching up to 55 m. Although this forest can be classified as 'primary' with abundant large logs, numerous epiphytes and uneven age distribution and emergent trees (Clark, 1996).
- Santarem K83 (54.971° W, 3.017°S) is situated also in the Tapajos National Forest about 50 km south of the city of Santarem, Para Brazil (da Rocha et al., 2004). The vegetation was closed tropical forest with emergent canopy (Hernandez Filho et al., 1993). The forest is semideciduous, with mostly evergreen and a few deciduous species. The site is situated on a flat plateau that extended many kilometres to the north, south and east. Forest extended 8/40 km to the south/north before reaching pasture and 5 km to the east before reaching pasture on the far side of the BR-163 highway. Forest continued 8 km west to the edge of the plateau before dropping to the Tapajos River (14 km from the tower). The total relief within 1-2 km of the tower was 10 m, with occasional 10-30 m deep stream

gulleys farther from the tower (Goulden et al., 2004). The soil was a yellow latosol clay (Haplic Acrorthox). About 15% of the trees with diameter at breast height greater than 35 cm were selectively logged over a 700-ha area during three months starting September 2001 (da Rocha et al., 2004).

- Caxiuana (CAX) station (51.454°W, 1.748°S) is situated approximately 350 km to the west of the city of Belem. The forest is extensive (33000 ha) and largely undisturbed, having been a reserve since the 1970 (Carswell et al., 2002). It is a dense lowland terra firme forest with a mean annual rainfall of 2500 mm, a canopy height of 35 m and aboveground dry biomass of 200 m³ha⁻¹ and a basal area of 30-35 m²ha⁻¹ (Carswell et al., 2002). The soil is largely a yellow latosol (oxisol in U.S. Department of Agriculture soil taxonomy), but has areas of iron sand approximately 3–5 m below the surface. The most frequent botanical families in the region are: Sapotaceae, Chrysobalanaceae and Lauraceae. The climate of the site is influenced by the river (Baía de Caxiuana, 6 km south-east). The tower was positioned on a plateau, the closest small river being 400 m to the south-west and another small river located 600 m to the east, but was thought to not substantially contribute to the north-easterly fetch (Carswell et al., 2002).
- Reserva Jaru (61.933° W, 10.078°S) is located inside the Reserva Jarú forest which is a terra firme forest area located about 100 km north of Ji-Paraná (Rondonia, Brazil). It consists of around 268000 ha of undisturbed tropical forest. Altitude is about 150 m above sea level. The canopy has a mean height of 35 m with higher trees reaching up to 45 m (Andreae et al., 2002). Understory vegetation of only a few meters consists mainly of palms. Forest reserve has been suffering some small scale slash and burn activities, especially close to north-western border. In addition, surface heterogeneity of the area is observed due to a few hills near the tower (closest hill is about 2 km northeast of the tower). Nevertheless, in spite of these heterogeneities fetch can be considered to be predominantly undisturbed forest (von Randow et al., 2004).

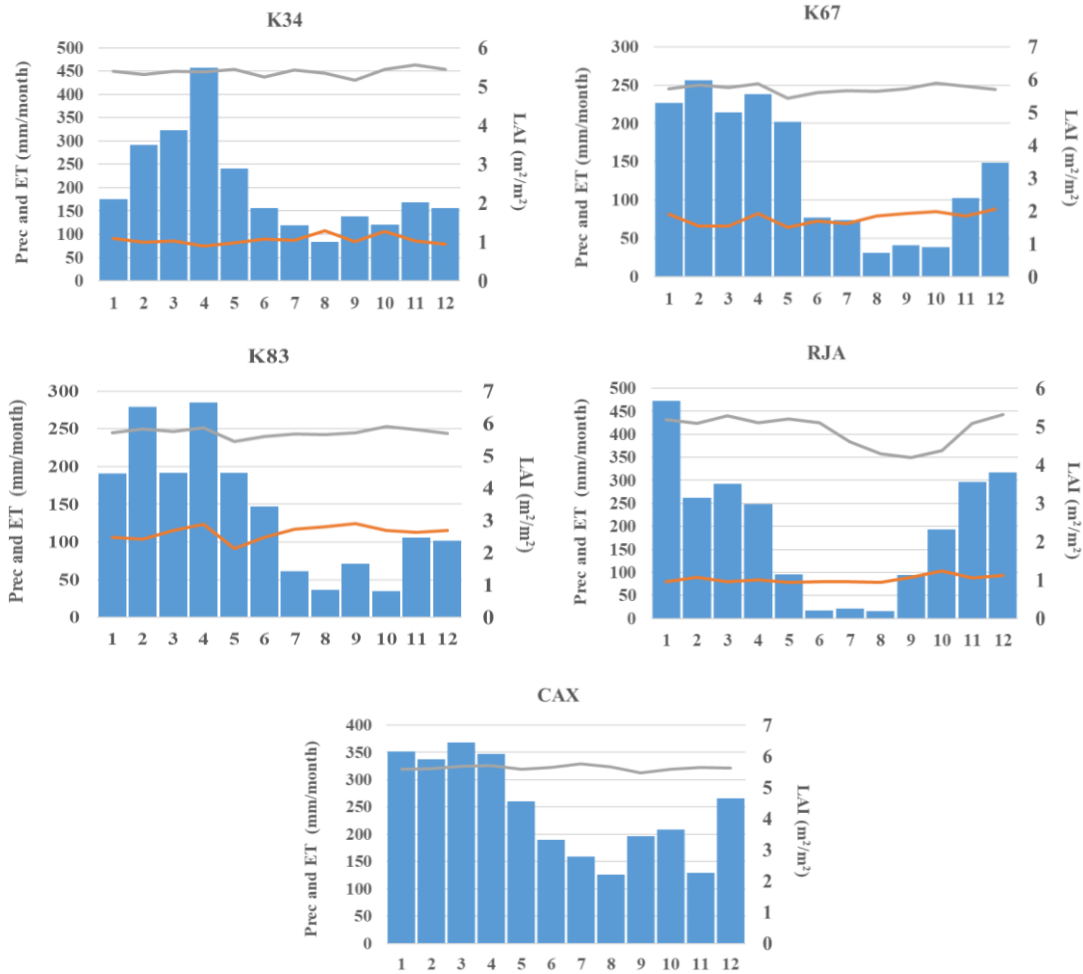


Figure 4.10. Monthly averages of the precipitation (blue bars), evapotranspiration (orange line) and Leaf Area Index (LAI). Precipitation and evapotranspiration were obtained from in-situ LBA observations and LAI from the MAIAC NDVI data using Fisher et al. (2008) formulation. In the case of CAX, only precipitation is displayed as there were not enough evapotranspiration observations available.

Table 4.6. Site descriptions. The table was adapted from Gonçalves et al. (2013), Restrepo-Coupe et al. (2013) and El-Masri et al. (2013). Soil texture was extracted from the Harmonized Soil World Database (FAO, 2012) according to USDA soil texture classification.

Site name	Lat (°)	Lon (°)	Elevation (m)	Measurement height (m)	Canopy height (m)	LAI	Soil texture	Annual rainfall (mm)	Dry season	Biome Type	Data availability
Manaus (K34)	-2.61	-60.21	130	50	35	4.7	clay	2329	July-September	Tropical rainforest	06-1999 to 09-2006
Tapajos (K67)	-2.86	-54.96	130	63	35	6.0	sandy clay loam	1597	July-November	Tropical rainforest	01-2002 to 01-2006
Tapajos (K83)	-3.02	-54.98	130	64	35	4.9	sandy clay loam	1656	July-November	(Logged) tropical rainforest	06-2000 to 12-2004
Caxiuana (CAX)	-1.75	-51.45	130	51.5	38	5.14	sandy clay loam	2500	September-December	Tropical rainforest	01-1999 to 06-2003
Reserva Jaru (RJA)	-10.08	-61.93	191	60	30	5.5	sandy loam	2354	June-August	Tropical wet and dry forest	03-1999 to 10-2002

Principle Investigators and data references (otherwise indicated at table):

- K34: Manzi, A., Nobre, A. (INPA, Brazil) (Araújo et al., 2002).
 K67: Wofsy, S. (Harvard, USA), Saleska, S. (U of A, USA), Camargo, A. (CENA/USP, Brazil) (Hutyra et al., 2007, Saleska et al., 2003).
 K83: Goulden M. (UC Irvine, USA), Miller, S. (SUNY, Albany, USA), da Rocha, H. (USP, Brazil) (da Rocha et al., 2004, Goulden et al., 2004, Miller et al., 2004).
 CAX: Sa, L. (Museo Goeldi), da Rocha, H. (USP, Brazil) (Carswell et al., 2002, Souza Filho et al., 2005).
 RJA: Manzi, A. (INPA, Brasil), Cardoso, F. (UFR, Brazil) (Kruijt et al., 2004, von Randow et al., 2004).

5. - DATA PROCESSING AND METHODOLOGY

5.1.- Cloud detection algorithm

In this section, we describe the different types of data employed in the proposed cloud detection scheme, as well as their preliminary processing. In particular, three types of data were used: 1) collocated MODIS and CPR/CALIOP orbits, 2) MODIS products and 3) in-situ ground cloud cover fraction derived from the Total Sky Imager. Six supervised classification algorithms were considered for cloud detection evaluation. They were: Gaussian Naïve Bayes (GNB), Linear Discriminant Analysis (LDA), Quadratic Discriminant Analysis (QDA), Random Forests (RF), Support Vector Machine (SVM) and Multilayer Perceptron (MLP). For a theoretical description of these models, please refer to section 1.4.

In front of global operative MODIS cloud masking algorithms (MYD35 and MAIAC) these algorithms benefit from the fact that they can be optimized to properly represent the local cloud conditions of the region. In addition, these algorithms are able to provide a continuous measure of cloud masking uncertainty (i.e. scores that can be converted to probability estimates or probability estimates) and therefore can be used for cloud masking under a probabilistic approach, which is the goal of this study.

5.1.1.-Collocated MODIS and CPR/CALIOP orbits

The purpose of collocated MODIS and CPR/CALIOP orbits was the creation of a truth reference database (i.e. clear and cloud labels and associated features) that served to train the machine learning models. Collocated satellite observations between different sensors were applied previously for this purpose with optimal results (Musial et al., 2014; Hollstein et al., 2014; Heidinger et al., 2012; Karlsson et al., 2015). In addition, MODIS sensor (on-board the AQUA platform) and CPR (on-board CloudSat) and CALIOP (on-board CALIPSO) were placed in the same orbit being able to sense the same atmospheric volume with a maximum time lag of 1-2 minutes (see section 4.1.4). Therefore, considering collocated MODIS and CPR/CALIOP observations can serve to provide high confident information of cloud occurrences.

Data used in the generation of the reference database were downloaded from CloudSat Data Processing Center (<http://www.cloudsat.cira.colostate.edu>). In particular, we used the 2B-CLDCLASS-LIDAR and MODIS-AUX products. Auxiliary information was extracted from 2B-GEOPROF and 2B-FLXHR-LIDAR. Below a brief description of the products is provided.

- ✓ 2B-CLDCLASS-LIDAR (Sassen & Wang, 2008) combines CloudSat and CALIPSO lidar measurements in order to classify clouds. As an ancillary field it also provides the combined CPR and CALIOP cloud detection results over the vertical profiles. As spatial domain (i.e. spatial and vertical resolution) of both instruments differ, the combined product is provided at CPR spatial domain (i.e. lidar observations are weighted in the CPR footprint).
- ✓ MODIS-AUX is an intermediate product that contains a subset of ancillary MODIS radiance and cloud mask data that overlaps and surrounds each CPR footprint. Using CPR geolocation data as reference, and a great-circle nearest neighbour scheme the closest MODIS pixel is located and a 3-pixel across-track by 5-pixel along-track grid of each MODIS parameter of interest is extracted and stored. If the CloudSat geolocation for a particular ray is missing or the closest MODIS pixel is more than 0.95 km from the CloudSat ray, the resulting MODIS geolocation data and the associated data vectors are filled with a missing value flag.
- ✓ 2B-GEOPROF (Marchand et al., 2008) product identifies those levels in the vertical column sampled by CloudSat that contain significant radar echo from hydrometeors. 2B-FLXHR-LIDAR (L'Ecuyer et al., 2008) product provides estimates of broadband fluxes and heating rates consistent with liquid and ice water content estimates from CPR, CALIPSO and MODIS. Ancillary data (i.e. land sea mask and land cover) were extracted from these products.

In Table 5.1, the layers selected from the products are presented. MODIS bands refer to top of atmosphere reflectance (TOA). For each product, a total of 1002 orbits covering the Amazonian tropical forests region (80°W-45°W,10°N-20°S) for the year 2007 were downloaded. Products used belong to product version 4. Main issue with this version is that uses MODIS collection 5.1 data as input, nevertheless at the time of performing the study version 5 of Cloudsat products (using MODIS collection 6.0) was not still released. Spatial resolution of 2B-CLDCLASS-LIDAR, 2B-GEOPROF, 2B-FLXHR-LIDAR products is determined by CPR resolution (1.7 along-track x 1.4 across-track). In the case of MODIS-AUX product, nearest MODIS 1km pixel to each footprint was selected.

Table 5.1. Products and layers used for reference database creation.

Products	Layers	Explanation
2B-CLDCLASS-LIDAR	Cloudlayer	Total cloud layers combining radar and lidar
2B-GEOPROF	Navigation_land_sea_flag	Land/Sea mask
2B-FLXHR-LIDAR	Land_Char	Land cover
MODIS-AUX	EV_250_RefSB	B1: 645 nm, B2: 859 nm
	EV_500_RefSB	B3: 469 nm, B4: 455 nm, B7: 2130 nm
	EV_1KM_RefSB	B26: 1375 nm
	Cloud_Mask	Modis cloud flags: Clear, Probably clear, Cloudy, Probably Cloudy

Collocated orbits were pre-processed in order to restrict the data to the tropical forest class and to screen non-valid pixels. Pre-processing steps consisted in: 1) screening sea pixels considering Land/Sea mask, 2) screening nighttime pixels and non-Evergreen Broadleaf forest (EBF) pixels and 3) screening non-valid pixels and non-valid class labels assignments. In particular, only pixels satisfying that Cloudlayer = 0 and MODIS cloud mask = Probably Clear / Clear and pixels satisfying that Cloudlayer > 0 and MODIS cloud mask = Probably Cloudy/Cloudy were selected. These points represent the clear and cloudy labels in the database. This consideration was assumed in order to take into account the overfitting risk of the models due to the superior cloud sensitivity of active (CPR/CALIOP) sensors in comparison to passive (MODIS) sensors. Using confident information from both types of sensors (i.e. a pixel is considered clear or cloudy when both sensors assign a clear or cloudy label) were not forcing the models to detect clouds that are theoretically impossible to detect using MODIS data. It is worth noting however, that this collocated dataset will inherit the cloud detection limitations of the sensors. For the Amazonian tropical forests, MODIS cloud detection (MYD35) fails in detecting the abundant small low clouds over the region (Hilker et al., 2012). CPR/CALIOP combination fails in detecting hydrometeors layers in a 1km range above the surface (Mace et al., 2014). Nevertheless, considering the temporal and spatial extent used for the generation of the dataset it is assumed that the samples considered encompass the totality of all possible cloud instances present in the region. Apart from these aspects, one important issue about the collocated database that needs to be considered is the agreement between the database (used to train the models) and the MODIS swath viewing conditions. CPR/CALIOP are near-nadir instruments while MODIS cover a wider view zenith angle range. This is a limitation that the current approach has (i.e. the collocation of both sensors observations will result in a database with only near-nadir measurements) and needs to be taken into account when analysing model results.

After initial pre-processing, definitive database used resulted in 477.415 data points. It consisted in binary labels (cloud and clear flags) obtained as explained previously and associated features for each label. A total of 7 features (derived from MODIS TOA reflectance) were selected: 5 MODIS spectral bands (top of atmosphere (TOA)): B1, B3,

B4, B7, B26 and 2 vegetation indexes (VI) the NDVI and the ratio vegetation index (RVI) which are given by $(B2-B1)/(B1+B2)$ and $B2/B1$. Although machine learning models are able to deal with a high number of features, for the classification problem proposed (i.e. discrimination between very green vegetation and clouds) the reduced set of features were considered sufficient. They cover the most important pieces of vegetation and cloud information provided by MODIS channels. Visible bands and vegetation indexes are commonly used for discriminating vegetation and cloudy pixels (Ackerman et al., 1998; Lyapustin et al., 2008). B7 is used in MAIAC algorithm (Lyapustin et al., 2008) and B26 is used in order to detect thin cirrus clouds (Ackerman et al., 1998). A reduced number of features (7 MODIS visible and near infrared bands) was also used in Chen et al. (2018) for cloud masking using neural networks with positive results in comparison to MYD35 cloud mask.

Last step of pre-processing consisted in scale features (converting to 0-1 range) in order to accommodate to machine learning models requirements. Scaling was done considering maximum and minimum values of the corresponding features. In addition, this reference database was randomly split into two datasets: train and test. A proportion of 2/3 (319868 data points) and 1/3 (157547 data points) was used in order to split the data. Models were trained on the train dataset and test dataset was reserved to test model performance over unseen data.

5.1.2-MODIS products

In Table 5.2 MODIS products at image level considered in the study are presented. Layers selected are also provided. They correspond to version 6.1 (v6.0 for MCD12Q1). MYD021KM products provide the MODIS TOA radiances from which features are derived, MYD03 product the geolocation files used for reprojection purposes and the Land/Sea Mask. Land cover is obtained from the MCD12Q1 product. In addition, MODIS cloud mask as derived from the MYD35 algorithm (MYD35_L2 product) and MAIAC algorithm (MAIACABRF product) were used for comparison with model results. MCD12Q1 data and MAIACABRF data were reprojected to swath projection in order to work on a common spatial framework. MYD021KM, MYD03, MYD35_L2 and MCD12Q1 were downloaded from ladsweb.nascom.nasa.gov while MAIACABRF product was obtained from dataportal.nccs.nasa.gov.

Table 5.2. MODIS products and layers selected used in the present study.

Products	Layers	Explanation
MYD021KM	EV_250_RefSB	B1: 645 nm, B2: 859 nm
	EV_500_RefSB	B3: 469 nm, B4: 455 nm, B7: 2130 nm
	EV_1KM_RefSB	B26: 1375 nm
MYD03	Land/Sea Mask	Land/Sea Mask
MCD12Q1	LC_Type1	Annual IGBP classification (EBF class)
MYD35_L2	Cloud_Mask	MYD35 cloud/clear flags
MAIACABRF	Status QA	MAIAC cloud/clear flags

These MODIS products were used for image and in-situ testing purposes (in section 5.1.5 model testing is explained). For image-testing only 20 images (i.e. 20 days) were considered. In order to take a period outside the training period, the year 2014 was selected. They are summarized in Table 5.3. They are identified by DOY.TIME. DOY refers to the day of the year (DOY) and time refers to the satellite passing time and it is given in Universal Time Coordinates (UTC). For in-situ testing, the time period considered expands from January to June 2015. For each of time period considered, MODIS products in Table 5.2 were downloaded and processed.

Table 5.3. Time period used for Image-testing and in-situ testing.

Testing	Time period
Image based	1) 001.1735, 2) 005.1710, 3) 025.1825, 4) 050.1820
	5) 075.1810, 6) 100.1805, 7) 100.1810, 8) 125.1800
	9) 150.1755, 10) 175.1745, 11) 175.1750, 12) 200.1740
	13) 200.1745, 14) 225.1735, 15) 250.1730, 16) 275.1725
	17) 300.1715, 18) 300.1720, 19) 300.1855, 20) 325.1710
In-situ based	01/01/2015 to 31/07/2015

The 20 MODIS swath images were aimed at generating an image-based reference database that could serve to validate cloud detection algorithm performance (models and MYD35/MAIAC). Reference database was created by manually classifying these images. In order to do so, for each swath image a 400x400 pixel region was extracted. Subsets were extracted in order to facilitate manual classification tasks. They were selected in order to properly represent cloud occurrence and satellite viewing conditions over the region. Manual classification was performed with ENVI software. It consisted in the following steps:

- 1) manually selecting distinctive regions of interest (vegetation and clouds) over RGB true colour images. For challenging regions additional features (same as in the database creation) were considered in order to better discriminate between both classes.
- 2) classifying the image using a maximum likelihood classifier. This was selected due to its relative high accuracy and speed. Previous selected regions served as a training dataset for the classification. Same 7 features as in previous section were used for classification.
- 3) for misclassified regions in the classified images repeat step 1 and 2 until classification visually agree with RGB true colour view. Adding labels from the difficult areas provides the classifier a better description of these problematic regions thus reducing the associated misclassification. In order to minimize the effect of the human error, a two-step approach was followed. Images were initially labelled and revisited some time later in order to re-evaluate past classifications.
- 4) as comparison is restricted to EBF pixels, last step consisted in screening non-EBF pixels using MCD12Q1 land cover layer.

For in-situ testing, processing of the MODIS products consisted in extracting a 3x3 kernel centered at the Manacapuru in-situ station. Definitive cloud labels, were assigned using the most common value in this kernel. After filtering non-valid data, a total of 110 data points (i.e. days with a measurement) were left for validation.

5.1.3- In-situ ground data

In-situ cloud occurrences were derived from the Total Sky Imager (TSI-880) at Manacapuru site. Data time availability is provided in Table 5.3. This site land cover is characterized by being “Natural Vegetation Mosaic”. Nevertheless, models were designed to “Evergreen Broadleaf Forests” pixels. In spite of this discrepancy, in-situ ground data was considered valid for model testing because among other factors the ground data scarcity of the region and that no different cloud distribution is expected for the pixel (the station effectively lies in the Amazon region and the most common land cover value in a 3x3 kernel is EBF).

We used the maotsiskycoverM1.b1 product. Amongst other layers, this product provides the percent of opaque and thin clouds that exists in the recorded images. A total cloud fraction was obtained by summing these two percentages. In order to account for the different spatial and temporal resolutions, in-situ cloud fraction measurements were averaged during the 5 minutes of time duration of MODIS satellite time overpass. For discriminating between clear and cloudy occurrences a threshold of 25% of cloud fraction

was considered (clear < 25% and cloud \geq 25%). This threshold value was selected in order to not completely restrict the clear-sky occurrences.

5.1.4. - Model training and probability calibration

As performing model training and model calibration on the same dataset will introduce an unwanted bias, train dataset was additionally split in two different datasets: train and calibration. A proportion of 2/3 for train and 1/3 for calibration was considered. Size databases resulted in 214311 for train and 105557 for calibration. Overall generated dataset consisted in train + calibration + test. The methodology employed for model training and probability calibration can be summarized in three major steps: 1) train models on the train set, 2) train the calibration models on the calibration set and 3) score the train models and calibration models on the test dataset. In order to follow a consistent notation, models trained on the train set (being their probability not calibrated) are named as pre-calibrated, and models trained on the train dataset and their probability calibrated dataset are named as post-calibrated.

Training for GNB, LDA and QDA models consisted in estimating the required parameters (covariance and class means) from the training dataset. For the case of RF, SVM and MLP training consisted in optimizing model parameters. For each model, different parameter combinations were tested and the best parameter combination was selected evaluating the averaged 5-fold cross validation Kappa coefficient (this statistic is described in model testing section). Parameters were allowed to vary over a pre-definite parameter space (5.4). In the case of RF model, m_{depth} and n_{trees} were allowed to vary. Default scikit-learn values were assumed for n_{leaf} , n_{feat} and n_{samp} (after initial testing variations in these parameters did not alter the results). In the case of MLP, logistic function was used as an activation function. Learning rate (η) was fixed constant (default scikit-learn value) to 0.001. n_{layers} was restricted to 1. n_{nodes} and α were optimized considering the parameter space in Table 5.4.

Calibration dataset was used in order to calibrate the probabilities estimates for each model. Probability calibration is a rescaling operation that allows to better calibrate the model probabilities or to add support for probability prediction (i.e. transform model scores into probability estimates). Main goal of calibration is to obtain well-calibrated classifiers. A non-parametric approach based on isotonic regression was used (Zadrozny & Elkan 2002–2001).

For methodology implementation, we used the Sklearn open source python package (Pedregosa et al., 2011). This package provides simple and efficient tools for data mining and data analysis. It provides tools for both model training and probability calibration. It is built on NumPy, SciPy and matplotlib packages.

Table 5.4. Parameter search space and optimal values for the parameters of the models that need to be optimized during the training process.

Model	Parameter	Parameter space	Optimal value
RF	n_{leaf}	----	2
	n_{samp}	----	2
	n_{feat}	----	4
	m_{depth}	[2-7]	7
	n_{trees}	[25-100]	100
	Split criterion	-----	Gini index
SVM	C	$[10^{-5}-10^5]$	1
	Activation function	-----	Logistic
	η	-----	0.001
MLP	n_{hlayers}	-----	1
	n_{hnodes}	[2-7]	2
	α	$[10^{-7}-10^{-1}]$	10^{-5}

5.1.5-Model testing

Evaluation of model performance was obtained using confusion matrices and derived statistics. In particular, we use overall accuracy (OA) and Cohen Kappa coefficient. They are presented in Table 5.5. For the confusion matrix, the diagonal elements represent the number of points for which the predicted label is equal to the true label, while off-diagonal elements are those that are mislabelled by the classifier. The higher the diagonal values of the confusion matrix the better, indicating many correct predictions. Overall accuracy provides the percentage of pixels being correctly classified. It has values between 0 to 1. Values closer to 1 indicates better performance. Kappa coefficient expresses the chance-corrected measure of agreement between two annotators. It is calculated taking into account the relative observed agreement (P_o) and the hypothetical probability of chance agreement (P_e). If there is a perfect agreement ($P_o = 1$) Kappa takes a value equal to 1. If there is no agreement other than what would be expected by chance ($P_o = P_e$) Kappa takes a value of 0. It is considered a more robust measure than OA. It is able to deal with models build from unbalanced data (i.e. class distributions not equivalent).

When evaluating the suitability of a classifier for satellite cloud masking retrieval, apart from its accuracy a quantitative measure of the computational cost associated is needed (i.e. an excessive computational cost will prevent the implementation of a classifier in an

operative processing chain). We considered the time employed in performing the calculations (i.e. time difference between the start and the end of the calculus) as the measure of computational cost. A computer with 8GB RAM and an Intel Core i3-6100 processor was used for doing so.

Table 5.5. Confusion matrix and derived metrics for comparison of model predictions and true label predictions.

Confusion matrix			
	Model clear	Model cloud	
Truth clear	a	b	$N_1 = a+b$
Truth cloud	c	d	$N_2 = c+d$
	$N_3 = a+c$	$N_4 = b+d$	$N_5 = a+b+c+d$
Statistics			
Overall accuracy (OA)	$(a+d)/(a+b+c+d)$		
Cohen Kappa coefficient	$(P_o - P_e)/(1 - P_e)$ $P_o = OA$ $P_e = (N_3 \cdot N_1 + N_4 \cdot N_2) / (N_5)^2$		

Goodness of the probability estimation for the models considered was performed using reliability curves. This curve plots the mean predicted probability (X axis) versus the fraction of positive real cases (Y axis). The processing is as follows. First, the prediction space is discretized into ten bins. Cases with predicted values between 0 and 0.1 fall in the first bin, between 0.1 and 0.2 in the second bin, etc. For each bin, the mean predicted value is plotted against the true fraction of positive cases. If the model is well calibrated the points will fall near the diagonal line. In addition, the Brier score loss was used as a measure of the accuracy of probabilistic predictions. Across the N items, this score measures the mean squared difference between the predicted probability assigned to the possible outcome for item (f_i) (i.e. probability estimation value) and the actual outcome (o_i) (i.e. 0 or 1). It is given by Equation 5.1. This formulation is mostly used for binary events. The lower the Brier score is for a set of predictions, the better the predictions are calibrated. It takes values between 0 and 1 (the maximum possible difference between the predicted probability and the actual outcome must be 1).

$$Brier\ score = \frac{1}{N} \sum_{i=1}^N (f_i - o_i)^2 \quad (5.1)$$

The methodology followed for model testing is summarized in Table 5.6. Briefly, it can be divided in three main blocks. In the first block, the performance of the selected models was validated on the reserved test dataset. Their probability estimates are evaluated in order to check if they provide well-calibrated estimates.

In the second block, testing is performed over the 20 manually classified images in order to test the validity of the supervised classification approach to other viewing angles. Only EBF pixels were used for comparison. As true label data provides binary values, and models provide probability estimates a threshold needs to be specified in order to assign clear or cloud flags respectively. Doing this, we were able to reassign model class predictions according to their uncertainty rather than using the default model class predictions. The threshold selection effect was evaluated by evaluating the agreement (Kappa coefficient) between models and truth reference images. For this purpose, discrimination between clear and cloudy occurrences was obtained by considering thresholds in the probability estimates as follows: clear \geq threshold and cloud $<$ threshold. Definitive threshold value is selected as the one that maximises the previous agreement. In addition, MYD35 and MAIAC cloud masks were also used for comparison purposes. For MYD35 a pixel was considered clear if associated flag was Clear or Probably Clear, and was considered cloudy when flag reported Cloudy or Probably Cloudy. For MAIAC case, Probably Cloudy and Cloudy labels were combined in order to flag cloudy pixels.

In the third block, the performance of the supervised classification and MYD35/MAIAC models was validated considering in-situ cloud data. Same methodology as image testing for model performance and model comparison is followed

Table 5.6. Testing strategy for model performance testing and comparison

Testing	Truth data	Methodology	Metrics
Database	Test dataset	- Evaluate model performance - Evaluate probability estimates - Probability calibration estimates	OA, Kappa, computational cost, reliability curves, brier score
Image	20 classified images	- Probability threshold estimation - Evaluate model performance - Comparison with MYD35 and MAIAC	OA, Kappa, computational cost, visual comparison
In-situ	Total Sky Imager	- Evaluate model performance - Comparison with MYD35 and MAIAC	OA, Kappa and confusion matrix

5.2. - LST retrieval

In this section, we describe the different types of data employed in the retrieval of the coefficients of the SW algorithms proposed and the comparison with operative LST products. In particular, we focused on the development and validation of LST algorithms for MODIS sensor on-board TERRA and AQUA platforms and VIIRS sensor. In addition, we provide an early assessment for SLSTR sensor on-board Sentinel-3. The data we used were: 1) Tambopata in-situ corrected LST derived from infrared radiometers SI-111 and IR-120, and net radiometer. 2) Atmospheric profiles and vegetation emissivity spectra employed in the database simulation, 3) sensor TOA radiances and operative LST products. LST retrieval algorithms proposed and current operative LST products were validated using three independent datasets: 1) simulated database, 2) in-situ LST (T-based approach) and 3) for MODIS sensor LST as derived from the R-based validation method.

5.2.1. - In-situ data and characterization of uncertainties

Land surface temperature can be obtained from radiometer measurements using the radiative transfer equation (Equations 2.9 and 2.10 in chapter 2). Generally, radiometers are collocated at a few meters above ground level (forest top in this case). With this configuration, it can be assumed that the atmospheric transmissivity for the atmospheric layer between the surface and the sensor equals 1, that is to say no significant atmospheric absorption exists. Thus, upward atmospheric radiance is approximately null. With these assumptions the measured radiance at the sensor is provided by Equation 5.2:

$$L_{g\lambda} = \varepsilon_{\lambda} B_{\lambda}(T_s) + (1 - \varepsilon_{\lambda}) L_{\lambda}^{\downarrow} \quad (5.2)$$

where $L_{g\lambda}$ refers to the ground leaving radiance ($\text{Wm}^{-2}\mu\text{m}^{-1}\text{sr}^{-1}$) (i.e. the same that arrives at the sensor), ε_{λ} is the surface emissivity, $B_{\lambda}(T_s)$ is the Planck radiance at surface temperature (T_s). L_{λ}^{\downarrow} is the downwards atmospheric radiance. In Equation 5.2, the term $(1 - \varepsilon_{\lambda}) L_{\lambda}^{\downarrow}$ refers to the reflected downwards radiance emitted by the atmosphere. The subscript λ refers to the spectral character of each parameter, that is each parameter is referred at an effective wavelength λ . This effective value is provided by Equation 5.3:

$$\lambda_{eff} = \int \lambda f(\lambda) d\lambda / \int f(\lambda) d\lambda \quad (5.3)$$

λ are the wavelengths included in the filter function (8-14 μm) and $f(\lambda)$ is the filter response function. In Figure 5.1, the response filters of the two radiometers considered SI-111 and IR-120 is displayed. Effective wavelength is also provided.

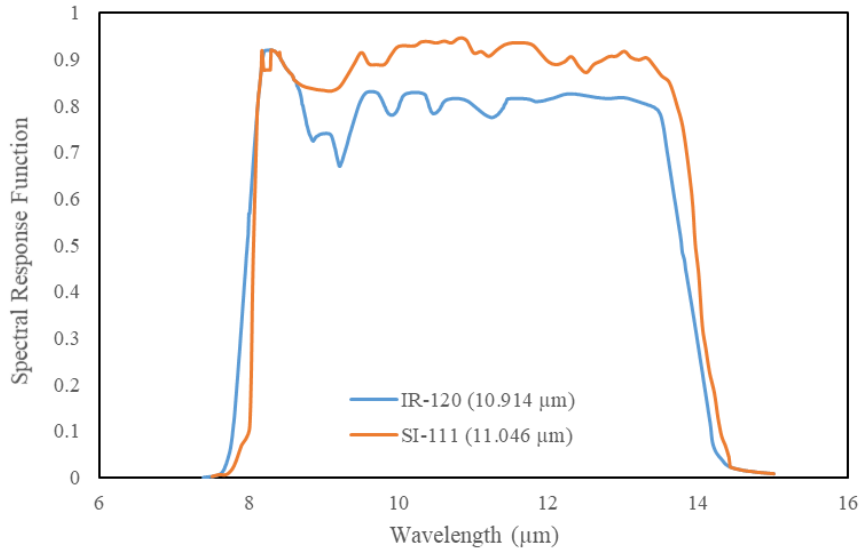


Figure 5.1. SI-111 and IR120 spectral normalized response.

Surface temperature can be retrieved by isolating (T_s) and inverting Planck law (Equation 2.1 in chapter 2) as follows (Equation 5.4):

$$T_s = \frac{c_2}{\lambda} \left\{ \ln \left[\frac{\varepsilon_\lambda c_1}{\lambda^5 (L_{g\lambda} - (1 - \varepsilon_\lambda) L_\lambda^\downarrow)} + 1 \right] \right\}^{-1} \quad (5.4)$$

where c_1 and c_2 are the Planck's radiation constants with respective values of $1.19104 \cdot 10^8 \text{ W}\mu\text{m}^4\text{m}^{-2}\text{sr}^{-1}$ and $14387.7 \mu\text{mK}$. λ refers to the effective wavelength. Note that retrieving LST from Equation 5.4 requires the knowledge ε_λ and L_λ^\downarrow . A fixed value of 0.99 was assumed for ε_λ as representative of dense green vegetation. L_λ^\downarrow can be derived using radiative transfers codes such as MODTRAN and atmospheric profiles as input (see next section for simulation procedure). Because L_λ^\downarrow is an hemispheric integrated down-welling radiance, it should be estimated for multiple angles (i.e. Gaussian angles: 11.6° , 26.1° , 40.3° and 53.7° plus 0° , 65° , 70° , 80° , 85° and 89° for a better description at large angles) (Galve et al., 2008). Nevertheless, this implies multiple simulations and typically a unique simulation at nadir of L_λ^\downarrow is performed. Nevertheless, this $L_\lambda^\downarrow(0^\circ)$ can be approximated to the hemispheric down-welling radiance by taking into account that L_λ^\downarrow at an angle of 53° represents well the hemispherically integrated L_λ^\downarrow value from the sky (Kondratyev, 1969). These two values are related by a factor of 1.3 (i.e. $L_\lambda^\downarrow(53^\circ) = 1.3L_\lambda^\downarrow(0^\circ)$) (Sobrino & Cuenca, 1999). In this study, we make use of this last relationship in order to retrieve the hemispheric L_λ^\downarrow .

The uncertainty of LST as derived by the IR-120 and SI-100 radiometers come from the contribution of several terms: uncertainty of the radiometers, emissivity, down-welling radiance, the pass band effect, and spatial variability of the in-situ stations (Skokovic, 2017). The uncertainty of a new radiometer is specific by the manufacturer (Tables A.1.1 and A.1.2 in appendix A.1) and is below 0.2 K. Nevertheless, this value increases with

time due to its use. From direct calibration with black body sources (Skokovic, 2017) it is known that these can reach maximum uncertainties of 0.4 K along the years. In the case of the emissivity, assuming a ε value of 0.990 and $\delta\varepsilon$ of 0.005 which can be assumed for vegetation (Skokovic, 2017) results in a contribution of 0.18 K. This value was calculated as the RMSE between unperturbed and emissivity perturbed LST values. The contribution from the down-welling radiance gives an error of 0.04 K. Assuming a representative profile of the atmospheric conditions of the region, the difference between the hemispheric integrated value using different MODTRAN runs and only one run using the previous relationship gives a difference of 0.6. Taking into account this value the resulting error in LST is of 0.04 K. In García-Santos et al. (2012), comparing different hemispherical radiance retrieval methods showed that difficult conditions gave a difference of $3 \text{ Wm}^{-2}\text{sr}^{-1}\mu\text{m}^{-1}$ between methods. Using this value as an upper threshold for the error we obtain a RMSE difference between perturbed and unperturbed values of 0.2 K. Regarding the pass-band effect, a maximum overestimation of -0.1 K can be obtained when using emissivity values of 0.99 (Skokovic, 2017). The last contribution left is the spatial variability and it is related with the assumption that the spatial point of the station is representative for all the satellite pixel. In order to calculate this contribution, one cloud-free LANDSAT-8 image was downloaded for 19th August 2014 and a homogeneity analysis was performed. Using the brightness temperature of band 10 (10.6-11.2 μm and at spatial resolution of 100 m), and for 3x3, 5x5, 10x10 and 15x15 it was found that 1- σ deviation between the values had a value of 0.08 K. Minimum and maximum observed values were 296.81-297.11 K. With all these contributions, the final uncertainty associated to in-situ LST as derived from radiometers is of 0.5 K. This value was calculated as the quadratic sum of the individual errors. As we can observe it is less than 1K. For validation purposes, both in-situ LST values were simply averaged. Doing this a more representative measure is provided as infrared radiometers do not exactly point to the same spatial point.

For pyrgeometer sensors LST was obtained by correcting the upwelling longwave radiation measured at the sensor (L^\uparrow) by the longwave down-welling (L^\downarrow) as in Equation 5.5.

$$LST = \left[\frac{L^\uparrow - (1 - \varepsilon)L^\downarrow}{\varepsilon\sigma} \right]^{\frac{1}{4}} \quad (5.5)$$

where σ represents the Stefan Boltzmann constant and has a value $5.67 \cdot 10^{-8} \text{ Wm}^{-2}\text{K}^{-4}$. L^\uparrow and L^\downarrow are in Wm^{-2} . As in the case of radiometers, ε was assumed a fixed value of 0.99. The uncertainty of LST as derived by the pyrgeometer can be obtained by error propagation (Equation 5.6).

$$\delta LST = \frac{1}{4\varepsilon\sigma LST^3} \sqrt{\left[(\delta L^\uparrow)^2 + \left(\frac{(L^\uparrow - L^\downarrow)}{\varepsilon} (\delta\varepsilon) \right)^2 + ((1 - \varepsilon)\delta L^\downarrow)^2 \right]} \quad (5.6)$$

As can be seen in Equation 5.6, the first term inside the square root is the one that contributes most to the total error. Assuming a ε value of 0.999 and $\delta\varepsilon$ of 0.005, the second term and third term contribute with a 0.5% and 1% respectively. The first term contributes with an uncertainty as indicated by the manufacturer which for the CNR4 sensor is of < 10%. A value of 5% is assumed for practical calculations. For representative values of L^\uparrow and L^\downarrow around 400 W/m² this typically results in uncertainties of 20 W/m². Assuming a $(L^\uparrow - L^\downarrow)$ difference of 40 W/m², the resulting error in LST is >3 K. This high uncertainty in comparison to the radiometer comes from the uncertainty provided by the sensor itself (an assumed 5%). Nevertheless, comparing the CNR4 derived in-situ LST against the LST derived from radiometers (i.e. average of both radiometers), an uncertainty of 0.8 K is derived (Figure 5.2). As a null bias is obtained the major contribution comes from the dispersion of the data. It is worth noting that the temporal resolution of both sensors is different (radiometers every 5 minutes while CNR4 every 10 minutes). Therefore, this 0.8 K value is assumed as representative of the pyrgeometer uncertainty. Adding the spatial variability term a resulting value of 0.83 is derived. As we can observed it is less than 1K.

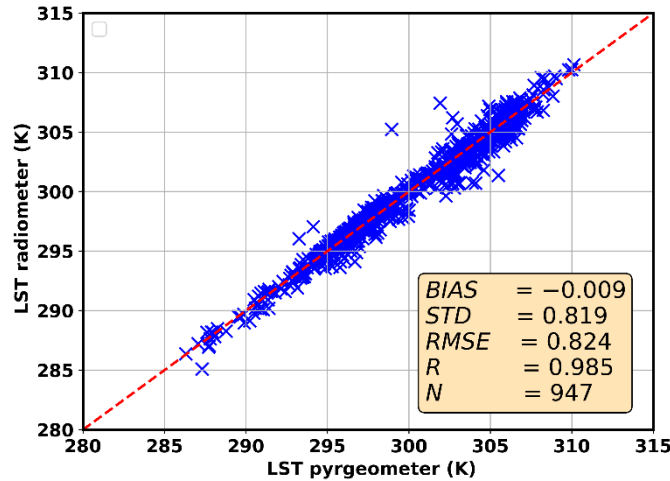


Figure 5.2. Comparison of in-situ pyrgeometer LST against in-situ radiometer LST. LST radiometer is taken as the average between the two sensors (SI-111 and IR120). Comparison was performed at satellites time overpass.

5.2.2. - Satellite data

In Table 5.7, the list of satellite products and layers selected together with an explanation of its purposes is provided. MODIS products were downloaded from <https://earthdata.nasa.gov/> and MAIAC products from <dataportal.nccs.nasa.gov>. MODIS products correspond to version 6. Sentinel data was downloaded from the Copernicus Open Access Hub. MODIS products are provided at 1km spatial resolution in exception of MXD11C1 and MCD12C1 which are given at 5km. VIIRS data is given at 750 m and SLSTR at 1km.

In order to validate MODIS and VIIRS LST retrieval algorithms at the station, for the time period December-2014 to March-2019 MX021KM, MXD03, MXD07_L2, MXD05_L2, MXD_35_L2, MXD11_L2, MXD21, MXD11C1, MAIACXBRF/MCD19A1, VNP03MOD, VNP02MOD and VNP21 products were downloaded for the in-situ station. In the case of the MXD21 product, only data corresponding to AQUA platform (i.e. MYD21KM) were used as MOD21 is still not available for the time-period of the in-situ station. Pre-processing consisted in applying respective scaling factors and extracting in-situ station pixel. In the case of MXD07_L2 atmospheric profiles were input to MODTRAN 5.2 radiative transfer code (explained in the next section) in order to derive the in-situ L_{λ}^{\downarrow} . In addition, this atmospheric profile product was also used in the retrieval of the Split-Window coefficients and for R-based validation method. MXDTBGA and MXD11A1 and MXD11C1 were used in order to retrieve the MODIS bands 31 and 32 and the MODIS LST values for the R-based validation approach. For implementation at basin scale the vegetation mask constructed as explained in section 4.3.1) was used in order to screen non-forest pixels.

Apart from MODIS and VIIRS validation (which the present study is mainly focused about) we provide an early assessment of the performance of the LST product from the SLSTR sensor. In addition, results were compared to the generalized Split-Window. Sentinel products were downloaded for the period July-August 2017. Data included Brightness Temperatures (L1 RBT) and the level 2 LST product (L2 LST). For each product test site values were extracted.

Table 5.7. List of satellite products and layers selected used in this section. X can take values of O or Y, referring to MOD (TERRA platform) or MYD (AQUA platform) respectively.

MODIS		
Product	Layer	Purpose
MXD021KM	EV_1KM_Emissive	MODIS B31 and B32 extraction
MXD03	Latitude, Longitude	In-situ station location
MXD07_L2	Retrieved_Temperature_Profile Retrieved_Moisture_Profile Retrieved_Height_Profile	Atmospheric profiles used for in-situ LST correction and algorithms coefficients retrieval
MXD05_L2	Water_Vapor_Infrared	Water vapour used in general SW
MXD35_L2	Cloud_Mask	Cloud mask flagging
MAIACXBRF MCD19A1	Status_QA	Cloud mask flagging
MXD11_L2	LST, QC, View_angle	MODIS LST retrieval
MXD21	LST, QC	MODIS LST retrieval
MXD11A1	LST_Day_1km, QC_Day	MODIS LST retrieval
MXD11C1	LST_Day_CMG, QC_Day	MODIS LST retrieval
MXDTBGA	Band 31, Band 32	MODIS B31 and B32 extraction R-based validation
MCD12Q1 MCD12C1	Land Cover Type 1 (IGBP)	Tropical forests delineation
VIIRS		
Product	Layer	Purpose
VNP03MOD	Latitude, longitude	In-situ station location
VNP02MOD	M15, M16	VIIRS M15, M16 extraction
VNP21	LST	VIIRS LST retrieval
SLSTR		
Product	Layer	Purpose
L1_RBT	S8, S9	SLSTR S8, S9 extraction
L2_LST	LST	SLSTR LST retrieval

5.2.3. - Simulations

At sensor brightness temperature can be simulated from forward simulations driven by the radiative transfer equation (Equations 2.9-2.10 in chapter 2), the combined used of atmospheric profiles and radiative transfer codes and emissivity spectra. Once we have a simulated dataset that accurately reproduces sensor measurements, the coefficients of the Split-Window LST retrieval algorithm can be derived by statistical minimization (i.e. linear regression) of this dataset. In the following, the data and methodology for the generation of this simulated database is presented.

5.2.3.1 Radiative Transfer codes

In order to retrieve the atmospheric parameters involved in the radiative transfer equation (atmospheric transmissivity and up-welling and down-welling radiances) we used the MODTRAN radiative transfer code. In particular, we use the version 5.2.0 (Berk et al., 2008). MODTRAN stands for MODerate spectral resolution atmospheric TRANSmittance algorithm and computer model. It was developed and continues to be maintained through a longstanding collaboration between Spectral Sciences, Inc. (SSI) and the Air Force Research Laboratory (AFRL). The spectroscopy of MODTRAN®5.2.0.0 is based on HITRAN2008 line compilation (Rothman et al., 1992; Rothman et al., 1998) with updates through January, 2007. In addition, this new version provides the ability to handle new species not already included in the built-in profile and molecular parameter files. A summary of the features included in this version is provided in Berk et al. (2008).

MODTRAN computes line-of-sight atmospheric spectral transmittances and radiances over the ultraviolet through long wavelength infrared spectral regime ($0 - 50,000 \text{ cm}^{-1}$; $> 0.2 \text{ }\mu\text{m}$). MODTRAN radiation transport physics is based on an atmospheric “narrow band model” algorithm with a resolution as fine as 0.2 cm^{-1} from its 0.1 cm^{-1} . In the solving of the radiative transfer equation MODTRAN includes the effects of molecular and particulate absorption/emission and scattering, surface reflections and emission, solar/lunar illumination, and spherical refraction. MODTRAN is able to provide accurate and fast modeling of stratified, horizontally homogenous atmospheres. The atmosphere is modelled via constituent vertical profiles, both molecular and particulate, which can be defined using built-in models or by user-specified radiosonde or climatology data.

5.2.3.2 Atmospheric soundings

Atmospheric vertical profiles were retrieved from the MXD07_L2 product (Table 5.7). Parameters provided by this product include the total column estimates of precipitable water vapour, ozone and atmospheric stability together with temperature and moisture profiles. Profiles are distributed in 20 atmospheric levels: 5,10,20,30,50,70,100,150,200,250,300,400,500,620,700,780,850,920,950 and 1000 hPa. The algorithm uses 11 infrared MODIS bands (bands 25 and from 27 to 36) in order to extract the vertical profiles with a statistical regression. All of these parameters are produced at day and night at 5x5 1-km MODIS pixel resolution when at least 9 observations are cloud free. For a detailed description of the product please refer to Borbas et al. (2011).

The atmospheric profiles used for the generation of the simulated database, were collected from 1118 spatial random points distributed in the study region (as defined by the vegetation mask) as in Figure 5.3. For each point, the cloud-free profiles were collected from the period 2014-2016. Atmospheric profiles were additionally averaged in a 5x5 pixel window. Therefore, each spatial point represented a spatial area of 25x25 km. Atmospheric profiles were input to MODTRAN code and we obtained the spectral atmospheric transmissivity and radiances (up-welling and down-welling). MODTRAN simulations were performed at the observed satellite view zenith angle. Spectral values were convolved considering the sensors spectral response in order to derive the channel values. In Figure 5.4, the spectral response of the sensors considered is presented.

Considering the spatial distribution and the temporal extent of the collected profiles, and taking into account that the profiles are observed by MODIS itself it is assumed that the simulated database is able to properly capture the observed distribution of the atmospheric parameters. It is worth mentioning that a simulated database was retrieved separately for TERRA and AQUA platforms at daytime and nighttime conditions. Therefore, it resulted in 4 different simulated databases. For the case of VIIRS and SLSTR sensors, AQUA and TERRA databases respectively were considered in order to derive the algorithms coefficients. In Figure 5.5, the description of the simulated databases for daytime and nighttime conditions in terms of water vapour and satellite view zenith angle is displayed. Although some overlapping between daytime and nighttime histograms is observed, hotter and wetter conditions are obtained for daytime in comparison to nighttime case. Regarding, satellite viewing conditions histograms are equivalent.

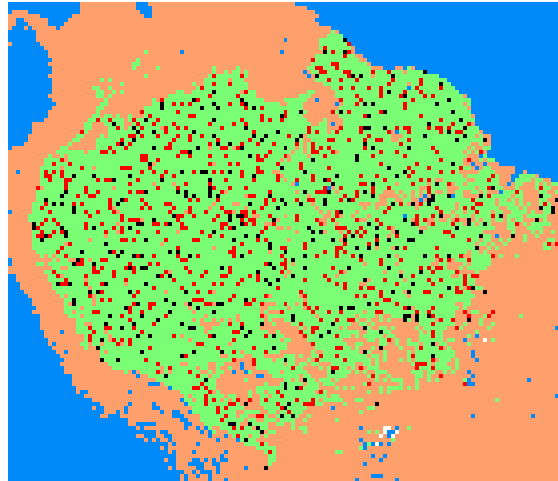


Figure 5.3. Spatial location of the atmospheric profiles. In green it is displayed the Amazon evergreen broadleaf forests. In red and black are displayed the train and test spatial points.

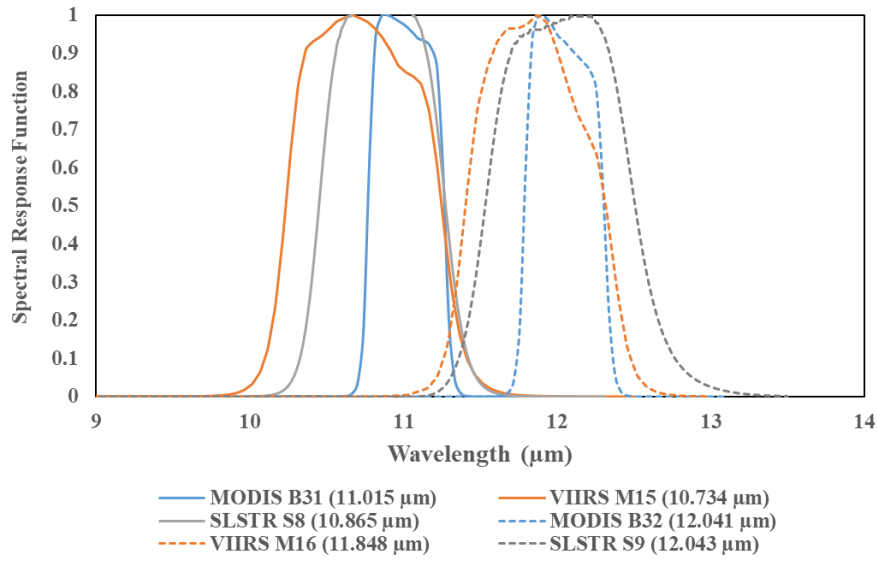


Figure 5.4. Spectral response functions for the thermal bands of the MODIS, VIIRS and SLSTR sensors in the 8-14 μm window.

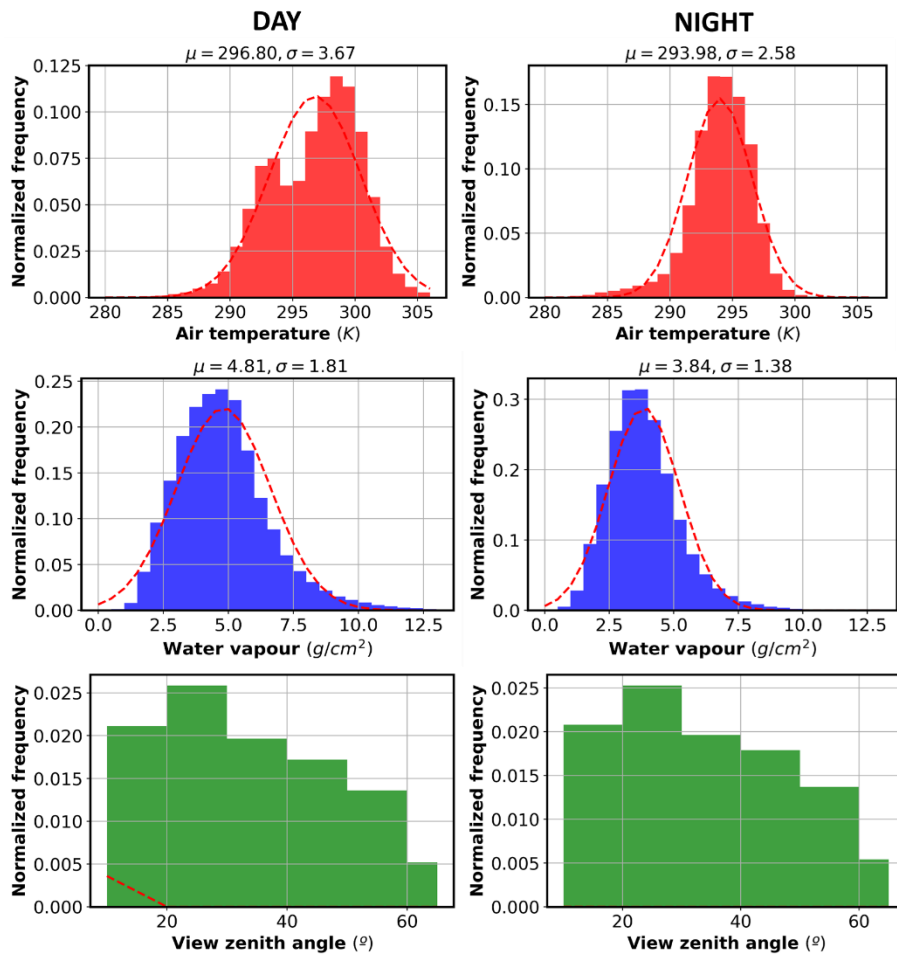


Figure 5.5. Simulated daytime and nighttime databases description. Histograms for air temperature, water vapour ($w/\cos\theta$) and view zenith angle are displayed.

5.2.3.3. Emissivity spectra

In order to obtain the at-sensor radiances emissivity values are required. Thus, in this simulation a series of emissivity spectrums extracted from the ASTER (Advanced Spaceborne Thermal Emission and Reflection Radiometer) spectral library (Baldrige et al., 2009). It is available at <http://speclib.jpl.nasa.gov>. This library is formed by three spectral libraries belonging to the JHU (Johns Hopkins University), JPL (Jet Propulsion Laboratory) and the USGS-Reston (United States Geological Survey) centers. It is a compilation of over 3400 spectra of natural and man-made materials. In February 2018, a new release which added over 1100 new vegetation and non-photosynthetic vegetation spectra.

For our case, we selected the available vegetation spectra. They correspond to grass, coniferous and deciduous. It is worth noting here, that these were the only vegetation spectra available at the time of performing the study (before February 2018). These three spectra were convolved using sensors spectral responses in Figure 5.4 and were employed in order to generate the simulated database.

Once we have the atmospheric transmissivity, up-welling, down-welling radiance and emissivity values at-sensor radiances and brightness temperatures are derived by simply applying the RTE. In these simulations, surface temperature was assumed equivalent to the first temperature in the given atmospheric profile. From a comparison between air temperature and the pyrgeometer LST an RMSE of 1.4 K was retrieved. Therefore, the previous assumption is considered valid for the simulation of at-sensor radiances.

5.2.4. - Algorithms coefficients and sensitivity analysis

Taking into account the three emissivity spectra and the total amount of atmospheric profiles the total amount of simulated data points for the cases considered: TERRA-day, AQUA-day, TERRA-night and AQUA-night were approximately 542000, 870000, 650000 and 680000 respectively. These datasets were split into a train dataset (70%) and a test dataset (30%). The train was used in order to retrieve the split-window coefficients by linear regression of these datasets. The test dataset was employed in order to validate the retrieved split-window algorithms over unseen data. Two versions of the split-window were derived. They are denoted by generalized and simplified. In the generalized version, a set of 6 coefficients were retrieved. In this case, all contributions (i.e. water vapour and emissivity terms) were included. For the particular case of the tropical forests, which have an emissivity value of 0.99 and spectral emissivity difference is negligible, the terms involving water vapour and emissivity can be omitted and the split-window reduces to a set of 3 coefficients. This case is denoted as the simplified version.

The uncertainty of the split-window is given by the quadratic sum of the different error sources (Equation 5.7).

$$e(T_s) = \sqrt{\delta_{sim}^2 + \delta_{NE\Delta T}^2 + \delta_\varepsilon^2 + \delta_w^2} \quad (5.7)$$

where δ_{sim} is the standard deviation of the algorithm obtained in the minimization (standard error of estimation), $\delta_{NE\Delta T}$ is the noise equivalent delta temperature (NE ΔT), δ_ε is the error due to the uncertainty of the surface emissivity, δ_w is the error due to the uncertainty of the atmospheric water vapour content. These contributions are given by Equations 5.8- 5.10:

$$\delta_{NE\Delta T} = \sqrt{\left(\frac{\partial T_s}{\partial T_i}\right)^2 e^2(T_i) + \left(\frac{\partial T_s}{\partial T_j}\right)^2 e^2(T_j)} \quad (5.8)$$

$$\delta_\varepsilon = \sqrt{\left(\frac{\partial T_s}{\partial \varepsilon}\right)^2 e^2(\varepsilon) + \left(\frac{\partial T_s}{\partial \Delta\varepsilon}\right)^2 e^2(\Delta\varepsilon)} \quad (5.9)$$

$$\delta_w = \left(\frac{\partial T_s}{\partial w}\right) e(w) \quad (5.10)$$

where $e(\Delta\varepsilon) = \sqrt{e^2(\varepsilon_i) + e^2(\varepsilon_j)}$ and $e(\varepsilon) = \frac{1}{2}\sqrt{e^2(\varepsilon_i) + e^2(\varepsilon_j)}$. Considering Equations 4.8-4.10 and performing the partial derivatives we obtain the following expressions (Equations 5.11-5.13):

$$\delta_{NE\Delta T} = \sqrt{[1 + 2c_2(T_i - T_j) + c_1]^2 e^2(T_i) + [-c_1 - 2c_2(T_i - T_j)]^2 e^2(T_j)} \quad (5.11)$$

$$\delta_\varepsilon = \sqrt{[-(c_3 + c_4w)]^2 e^2(\delta_\varepsilon) + (c_5 + c_6w)[e^2(\varepsilon_i) + e^2(\varepsilon_j)]} \quad (5.12)$$

$$\delta_w = [c_4(1 - \varepsilon) + c_6\Delta\varepsilon]e(w) \quad (5.13)$$

In order to calculate these expressions, the following typical errors are used: $e(T_i) = e(T_j) = 0.1$ K, $e(\varepsilon_i) = e(\varepsilon_j) = 0.01$ and $e(w) = 0.5$ g/cm². These reference values of uncertainties have been justified and considered in other simulations exercises (Jimenez-Muñoz & Sobrino, 2008). For the case of the generalized algorithm, we will have contributions from all the terms while for the simplified version only $\delta_{NE\Delta T}$ and δ_{sim} will be contributing.

5.2.5. - T-based validation

For this study, in-situ LST measurements were obtained from both the infrared radiometer (SI-100 and IR-120) and the CNR4 (net radiometer). As explained above, for the case of the radiometer the mean value of the two sensors was used for practical purposes. Validation was performed separately for daytime and nighttime conditions. In Table 5.8, the validation algorithms are summarized. For the case of the generalized SW, ε was assumed a fixed value of 0.99 and $\Delta\varepsilon$ a value of 0.005 for all the three sensors. Water vapour for all the three sensors was directly extracted from the MXD05_L2 product.

For practical purposes, LST daytime values were filtered for clouds using the MXD35_L2 and MAIAC cloud masks in the case of MODIS sensor at daytime. Nighttime LST values were filtered using MXD35_L2. For VIIRS sensor, both daytime and nighttime LST estimates were filtered using the VNP35_L2 cloud mask as embedded in the VNP21 product. In the case of SLSTR, possible LST cloud-contaminated values were screened by considering only values with a maximum difference of 6 K with in-situ LST values. In order to screen unseen clouds by sensors cloud masks this temperature difference filter was also applied for both MODIS and VIIRS. In order to analyze the possible effects of this restriction, results were also retrieved for a maximum difference of 15 K and 3 K (Appendix A.3). Other cloud screening procedures were tested such as the error LST values (<1K) provided by the LST products, nevertheless this provides similar results to the 3 K case with an important reduction of LST values.

Table 5.8. List of validated algorithms according to the scenarios considered.

Scenario	Validated algorithms
TERRA-day	SW-gen, SW-simpl, MODIS SW, MODIS day-night
TERRA-night	SW-gen, SW-simpl, MODIS SW, MODIS day-night
AQUA-day	SW-gen, SW-simpl, MODIS SW, MODIS day-night, MODIS TES
AQUA-night	SW-gen, SW-simpl, MODIS SW, MODIS day-night, MODIS TES
VIIRS-day	SW-gen, SW-simpl, VIIRS-TES
VIIRS-night	SW-gen, SW-simpl, VIIRS-TES
SLSTR-day	SW-gen, SW-simpl, LEVEL-2 LST

LST retrieval algorithms performance was evaluated using the following metrics: bias, standard deviation of the difference (σ), root mean square (RMSE), correlation coefficient (R) and the number of available points (N). The expressions are given by Equations 5.14-5.17, where x refers to LST estimates and y to in-situ LST values:

$$\bar{x} = \frac{1}{N} \sum_i^N x_i - y_i \quad (5.14)$$

$$\sigma = \sqrt{\frac{1}{N-1} \sum_i^N (x_i - y_i - \bar{x})^2} \quad (5.15)$$

$$\text{RMSE} = \sqrt{\frac{1}{N} \sum_i^N (x_i - y_i)^2} \quad (5.16)$$

$$R = \frac{\sum_i^N (x_i - \bar{x})(y_i - \bar{y})}{\sqrt{\sum_i^N (x_i - \bar{x})^2} \sqrt{\sum_i^N (y_i - \bar{y})^2}} \quad (5.17)$$

5.2.6.- R-based validation

As an alternative to the T-based validation method, R-based approach allows to validate LST values in points where we do not have any in-situ measurements. In this case, LST is obtained from the RTE using the at-sensor brightness temperature (TOA) and atmospheric profiles of temperature and water at the time of satellite observation. This method can be briefly summarized in two steps:

- 1) Inverse simulation: R-based in situ LST (T_R) is obtained from the 11 μm band using the RTE and at-sensor radiance, atmospheric profiles and surface emissivity data. The 11 μm band is used because it is less affected by variations in atmospheric water vapour and temperature.
- 2) Direct simulation: using derived R-based surface temperature (T_R), brightness temperature at bands 11 μm and 12 μm are calculated using the same coincident atmospheric profiles and emissivity data. The accuracy of the atmospheric is assessed with the test suggested by Wan & Li (2008). This test involves calculating the difference $\delta (T_{11} - T_{12}) = (T_{11} - T_{12})_{obs} - (T_{11} - T_{12})_{sim}$, that is the difference between the observed MODIS TOA radiance and simulated TOA radiances. Taking into account that T_{11} observed and simulated are equal, the difference reduces to $\delta (T_{11} - T_{12}) = (T_{12_{obs}} - T_{12_{sim}})$. This test is based on the fact that atmospheric effect is larger at 12 μm . When the atmospheric profile used for R-based LST calculation is over (under) correcting the atmospheric effect, then $\delta (T_{11} - T_{12}) < 0 (> 0)$ since the calculated profile based $T_{11} - T_{12}$ value is large (smaller) than the actual LST value. As validation should be restricted to cases in which the atmospheric effect is small, a maximum and minimum thresholds are applied to $\delta (T_{11} - T_{12})$. The optimal threshold value for this

difference is selected so that the difference between the simulated T_R and the in-situ LST lies within $\pm 1K$.

Due to the downloading and processing cost associated, this validation was restricted to the MODIS daytime case. In this case, MODIS-SW and MODIS day-night and SW-simpl were validated. We used 100 random points from the test simulated database. MODIS radiance values and MODIS LST values can be easily derived from reprojected MODIS products, thus reducing the downloading and computational cost associated. Cloud mask information was derived from MAIACXBRF product (i.e. MAIAC algorithm). The time period of this validation is December 2014- December 2016 period. This method requires a good knowledge of the spectral emissivity of the site. Taking into account that the selected spatial points correspond to evergreen broadleaf forests a value of 0.99 is assumed. In order to find the optimal threshold value for $\delta (T_{11} - T_{12})$ Tambopata test in-situ LST values were used.

5.2.7.- Spatial patterns

In order to complete the validation analysis, for the particular case of MODIS daytime a comparison between the spatial patterns of clear-sky days and LST obtained from MODIS standard product and the simplified SW algorithm was performed. In particular, seasonal mean LST values together with the number of clear sky days per season for the year 2014 were used for comparison. Results from MODIS operative algorithms were retrieved from the MOD11A1 and MYD11A1 products. Seasons included in the analysis were JFM (January-February-March), AMJ (April-May-June), JAS (July-August-September) and OND (October-November-December). Comparison was performed at three different levels of cloud masking: i) the MOD35 cloud mask as included in the MOD11 product without any additional QA discrimination (LST not produced due to clouds), ii) the MOD35 cloud mask as included in the MOD11 product and the additional filter based on the QC layer (LST not produced due to clouds + LST produced other quality) (Nishida et al., 2003; Williamson et al., 2013), and iii) the MAIAC cloud mask. For simplicity, we will refer to these three cases as MOD35, QC and MAIAC, respectively. Additionally, spatial pattern validation was extended repeating this same procedure using VIIRS data. Having satellite overpass time similar to AQUA and considered to be the successor of MODIS, VIIRS is presented as an add-on in order to validate the results derived from the LST presented here.

5.3. – Evapotranspiration retrieval

In this section, we described the different types of data employed in the comparison of evapotranspiration retrieval algorithms, as well as their preliminary processing and evaluation methodology. In particular, three types of data were used: 1) in-situ eddy covariance turbulent fluxes and meteorological data, 2) reanalysis meteorological data and 3) land surface variables derived from satellite data. Four evapotranspiration retrieval algorithms were considered for model evaluation. They were: Priestley-Taylor Jet Propulsion Laboratory (PT-JPL), Penman-Monteith MODIS operative parametrization (PM-Mu), Surface Energy Balance System (SEBS), and Satellite Application Facility on Land Surface Analysis (LSASAF) algorithm). In addition, the gap-filling technique used to provide evapotranspiration estimates for cloudy days in SEBS model is presented.

5.3.1.- In-situ data

The LBA experiment provides a high-quality in-situ dataset of hourly surface heat fluxes and meteorological data of the tropical forests of the Amazonian region, making them an appropriate source for model evaluation. A general description of the dataset can be found in Saleska et al. (2013). LBA data were available at ORNL Distributed Archive Active Centre (ftp://daac.ornl.gov/data/lba/carbon_dynamics/CD32_Brazil_Flux_Network/). Five stations were selected from this dataset based on two criteria: the availability of all required input data for simulation using the different models in this study and that stations must have an associated value of 2 in the International Geosphere-Biosphere Programme (IGBP) classification (i.e. representing Evergreen Broadleaf Forests). In this dataset, an initial quality control procedure was applied in order to flag non-valid data (refer to Saleska et al., 2013). For the study, only observed measurements were considered (i.e. no gap-filling procedure was used).

Eddy covariance (EC) method was used for obtaining in-situ flux estimates of evapotranspiration and sensible heat flux at the LBA stations. Hourly latent heat flux (LE) values were converted to mm/hour using $ET = LE/\lambda$, where λ is the latent heat of vaporization (Jkg^{-1}) and is given by $\lambda = (2.501 - 0.002361T_a) \cdot 10^6$ (Maidment, 1993). T_a refers to the hourly air temperature in Kelvins. Daily evapotranspiration values (mm/d) were obtained by summing hourly values (mm/hour). Daily values were excluded as missing data if less than 20 (out of 24) measurements were not available.

Model performance was evaluated mainly using these non-corrected ET values. Nevertheless, in order to take into account the observed non-closure issue two common non-closure techniques (Bowen Ratio and Energy Residual) were also considered. In Figure 5.6, the average energy balance closure at hourly scale for the stations considered is presented. This is in agreement with the closure values observed for most of the tropical sites within the LBA experiment (i.e. 70-80%) (Fisher et al., 2009).

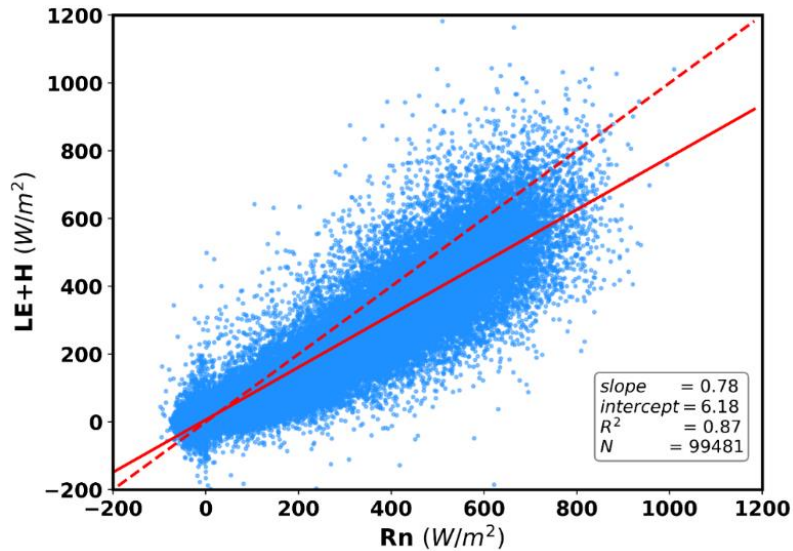


Figure 5.6. Hourly energy balance closure for the selected LBA-sites.

Following Twine et al., (2000), energy balance can be closed if turbulent heat flux measurements are distributed according to the Bowen Ratio $\beta = H/LE$. The Bowen Ratio correction is applied as: $LE_{BR} = R_n/(1 + \beta)$ and $H_{BR} = \beta R_n/(1 + \beta)$. Alternatively, the lack of closure can be approached by calculating the latent heat flux as a residual term in the energy balance equation $\lambda E_{ER} = R_n - H$ using the observed fluxes. This method is known as the Energy Residual method (ER). It is worth noting here, that both in Figure 5.6 and in the applied corrections the terms of soil heat flux and the heat storage of the system were not included due to the continuous discontinuity of the available data. Nevertheless, these values approach zero when integrated at daily scale, which is the case. Hourly corrected evapotranspiration values were corrected and summed to daily values. As in the non-corrected case, daily values were excluded as missing data if less than 20 (out of 24) measurements were not available. In the case of the Bowen Ratio method, as β approaches -1 it gives non-physical values. An absolute value of 1 mm/hour was used in order to reject non-valid ET measurements. In addition, in order to minimize this effect, we only consider as valid, pixels that accomplish the ratio of corrected/uncorrected values were greater than 0.5 or less than 2 as in Ershadi et al. (2014).

In the literature, several reasons were attributed to the lack of closure in eddy covariance method: instrument spatial representativeness, instrumental and methodological limitations and uncertainties, insufficient estimation of storage terms, unmeasured advective fluxes among others (Malhi et al., 2002; Wilson et al., 2002; Hasler & Avissar, 2007; Foken et al., 2011; Stoy et al., 2013). In spite of these reasons, the mechanism for this imbalance remains unclear. Likewise, the best way to handle it in terms of data correction is still a topic under discussion (Foken et al., 2012). In the present study, the three types of in-situ ET data were used in order to consider the impact of these methods in the evaluation metrics, and therefore provide bounds on the range in the probable model performance.

Apart from in-situ turbulent fluxes, in-situ surface radiation (R_n , SR_{in} , LR_{in}) and surface meteorology inputs (T_a , e_a , W_s , P) were used for forcing evapotranspiration models. Hourly inputs were averaged over daily, daytime/nighttime time intervals in order to accommodate to models requirements. A minimum SR_{in} threshold of 10 W/m^2 was used for separating daytime and nighttime conditions.

5.3.2.- Reanalysis data

Meteorological data at a coarser resolution were obtained by three different reanalyses: MERRA-2, ERA-Interim and GLDAS-2.1. MERRA-2 provides data at an hourly scale with a $0.5^\circ \times 0.65^\circ$ spatial resolution while ERA-Interim and GLDAS-2.1 provide data at a three hourly scale with a spatial resolution of $0.75^\circ \times 0.75^\circ$ and $0.25^\circ \times 0.25^\circ$ respectively. Table 5.9 presents the reanalysis variables from which model inputs are derived. MERRA-2 reanalysis variables were obtained from M2T1NXRAD, M2T1NXSLV and M2T1NXLND products. GLDAS-2.1 data were derived from GLDAS_NOAH025_3H product. In the case of ERA-Interim, variables were directly retrieved from the data-downloading platform.

The three reanalysis directly provide the incoming surface radiation (SR_{in} , LR_{in}), air temperature (T_a) and pressure (P). Net radiation is considered as the sum of the net shortwave radiation and net longwave radiation. Wind speed is obtained as the module of the wind components for MERRA-2 and ERA-Interim. Water vapour pressure is retrieved from specific humidity (MERRA-2 and GLDAS-2.1) or from dew point temperature (ERA-Interim) variables considering the relations expressed in Equations 5.18 to 5.20 (Ambaum, 2010).

$$q = \frac{e}{1.61(p - e) + e} \quad (5.18)$$

$$e_s(T_d) = e_a(T_d) \quad (5.19)$$

$$e_s(Pa) = 611.2 \exp\left(\frac{17.67 \cdot T(^{\circ}\text{C})}{T(^{\circ}\text{C}) + 243.5}\right) \quad (5.20)$$

$Root_{sm}$ (ERA-Interim and GLDAS-2.1) was derived by averaging the four-layered reanalysis soil water content taking into account a modulating soil temperature function, the root distribution and fixed values of w_{wp} ($0.171 \text{ m}^3/\text{m}^3$) and w_{fc} ($0.323 \text{ m}^3/\text{m}^3$) (Equation 3.73-3.74 in chapter 3). $Soil_{sm}$ is computed in a similar approach but considering only the first soil layer. $Root_{sm}$ and $Soil_{sm}$ (MERRA-2) were computed by inverting root-zone (GWETROOT) and soil (GWETTOP) wetness derived from MERRA-Land (Reiche et al., 2011) considering previous fixed w_{wp} and w_{fc} values.

Table 5.9. List of reanalysis variables according to model inputs.

Input	MERRA-2 variables	ERA-Interim variables	GLDAS-2 variables
SR _{in}	SWGDN	ssrd	SWdown_f_tavg
LR _{in}	LWGAB	strd	LWdown_f_tavg
Rn	LWGNT + SWGNT	ssr + str	SWnet_t_avg+ LWnet_t_avg
T _a	T2M	t2m	T_air_f_inst
e _a	Q2M	d2m	Q_air_f_inst
W _s	$(U2M^2 + V2M^2)^{1/2}$	$(u10^2 + v10^2)^{1/2}$	Wind_f_inst
P	PS	sp	Psurf_f_inst
Root _{sm} ,	GWETROOT	stl1-stl4	SoilMoix_xcm_inst
Soil _{sm}	GWETTOP	swvl1-swvl4	SoilTMPx_xcm_inst

Hourly and three hourly forcing inputs were averaged in order to obtain daily and daytime/nighttime values. Same in-situ SR_{in} threshold was considered for daytime and nighttime partition. For SEBS model, inputs at satellite time overpass were derived by linear interpolation between closest time acquisitions. Forcing inputs were spatially interpolated, considering a Gaussian interpolation between nearest neighbours, to a 1km scale for validation purposes and at 5 km for regional scale implementation.

5.3.3.- Satellite data

Table 5.10 presents the land surface variables derived from MODIS data. A reference of each product is provided. Spatial resolution of the products is 1km. Canopy height is available at <https://webmap.ornl.gov./ogcs/datasets>. In the case of vegetation fraction, we used the global product derived in Broxton et al. (2014). In this work, annual f_c was retrieved by scaling the annual maximum observed NDVI at each pixel (N_{max}) between the maximum soil (N_s) and vegetation (N_v) NDVI using the following relationship: $f_c = (N_{max} - N_s) / (N_v - N_s)$. Due to the characteristics of the region, assuming of a constant vegetation fraction for the entire year is plausible. In the case of emissivity, a simple linear mixing between the emissivity of vegetation (0.99) and the emissivity of the soil (0.96). LST employed in this study was retrieved from the LST products presented in Gomis-Cebolla et al. (2018) and section 5.2. LAI was calculated following the parametrization of PT-JPL model. f_{ipar} is obtained as NDVI-0.05 and k_{par} takes a value of 0.35. Albedo and NDVI were retrieved from the MAIAC suite products, available at dataportal.nccs.nasa.gov. MAIAC albedo corresponds to the combination of MOD43B3 black-sky and white-sky albedo weighted with respective relative direct and diffuse incident fluxes. For both NDVI and albedo in order avoid the lack of data due to continuous cloud coverage of the region monthly albedo and NDVI values were used to force the models. Missing monthly data was filled with the monthly climatological mean for the period 2000-2016.

For remote sensing data, same spatial resampling as reanalysis input data was considered. For regional scale implementation, tropical forests were delineated as explained in section 4.3.1.

Table 5.10. Land surface variables derived from MODIS remote sensing data.

Product	Explanation	Reference
Canopy height (h)	Global canopy height derived from spaceborne lidar	Simard et al. (2011)
Vegetation fraction (f_c)	Global green vegetation fraction derived from MODIS multitemporal analysis	Broxton et al. (2014)
Emissivity (ϵ)	$\epsilon_v f_c + (1 - f_c) \epsilon_s$	Sobrino et al. (2008)
LST	SW simplified algorithm	Gomis-Cebolla et al. (2018)
LAI	$-\ln(1 - f_{ipar})/k_{par}$	Fisher et al. (2008)
α	Surface albedo at a given solar zenith angle in ambient atmospheric condition	Lyapustin & Wang (2007)
NDVI	8-day angular corrected normalized difference vegetation index	Lyapustin & Wang (2007)

5.3.4.- Soil data and gap-filling technique

For gap-filling purposes (SEBS model), gridded soil properties (w_{wp} and w_{fc}) were obtained from Harmonized World Soil Database (HWSD) (FAO,2012). Following Anderson et al. (2007), they were indexed according to texture class (Table 5.11). The HWSD is based on soil mapping units with varying sizes. Thus, no fixed spatial resolution can be given.

Table 5.11. Soil moisture retention properties assigned to each HSWD texture class (extracted from Anderson et al., 2007).

Texture class	θ_{wp}	θ_{fc}	b
Sand	0.033	0.091	1.7
Loamy sand	0.055	0.125	2.1
Sandy loam	0.095	0.207	3.1
Silt loam	0.133	0.330	4.7
Silt	0.133	0.330	4.7
Loam	0.117	0.270	4.5
Sandy clay loam	0.148	0.255	4
Silty clay loam	0.208	0.366	6.6
Clay loam	0.197	0.318	5.2
Sandy clay	0.239	0.339	6
Silty clay	0.250	0.387	7.9
Clay	0.272	0.396	7.6

In the following a brief explanation of the gap-filling technique using an available water model as obtained from Anderson et al. (2007) is given. This method is based on the fact that the fraction potential evapotranspiration (f_{PET}) and the available water fraction (f_{AW}) can be related by a stress function as $f_{PET} = fn(f_{AW})$. The function considered is derived from physical principles, relating to soil and water potentials. These expressions are given by Equations 5.21 to 5.23.

$$f_{PET} = ET/PET \quad (5.21)$$

$$f_{AW} = \frac{AW}{AWC} = \frac{(\theta - \theta_{wp}) \cdot d}{(\theta_{fc} - \theta_{wp}) \cdot d} \quad (5.22)$$

$$fn = 1 - \frac{1}{(1 + 1.3f_{AW})^b} \quad (5.23)$$

ET is the actual evapotranspiration (mm/d) or plant water uptake and PET is the potential evapotranspiration (mm/d). For the case of SEBS it was calculated assuming the maximum evaporative fraction (i.e. $\Lambda = 1$) when upscaling from hourly to daily values. AW is the actual plant available water and AWC is the available water capacity of the soil. d is the thickness of the soil layer supplying water to transpiring vegetation. A soil-layer of 0-289 cm was assumed according to root distribution in evergreen broadleaf forests (van den Hurk et al., 2000). θ is the current soil moisture content (m^3/m^3) and θ_{wp} and θ_{fc} represent the soil water content at wilting point and field capacity (m^3/m^3). Wilting point is defined by convention as the water content at -1.5 kPa of suction pressure and represents the minimal amount of water in the soil that the plants requires not to wilt. At this stage, the soil still contains some water but it is too difficult for the roots to suck it from the soil. Field capacity is defined as the bulk water content retained in soil at -33

kPa of hydraulic head. It represents the amount of soil moisture held in the soil after excess water has drained away and the rate of downward movement has decreased. At this stage, the water and air contents of the soil are considered to be ideal for plant growth. θ_{wp} and θ_{fc} values were obtained from Table 5.11.

The gap-filling technique is accomplished by maintaining running pools of available water for the root zone (0-280 cm). In Table 5.12, the process is summarized. On clear days, the soil moisture conditions are inferred from the measured fluxes or evapotranspiration (steps 1 to 3). The available water for the next day will be therefore the calculated AW minus the water uptake by vegetation in that day. On cloudy days, the process is inverted. Evapotranspiration values are inferred from the soil moisture conditions (steps 1 to 3). The AW is updated for the next day by decrementing AW by the calculated ET.

Table 5.12. Gap-filling process for days with no ET estimate (extracted from Anderson et al., 2007).

Steps	Clear days	Cloudy days
1)	$f_{PET} = ET/PET$	$f_{AW} = AW/AWC$
2)	$f_{AW} = fn^{-1}(f_{PET})$	$f_{PET} = fn(f_{AW})$
3)	$AW = f_{AW}AWC$	$ET = f_{PET}PET$
4)	$AW_{next} = AW - ET$	$AW_{next} = AW_{rz} - ET$

5.3.5- Model configuration

In chapter 3, the theoretical formulation of the models is presented. Nevertheless, in this study some modifications were performed in order to estimate the ET. Below, they are explained:

PT-JPL:

- In Fisher et al. (2008), in the plant temperature constraint (f_T) the optimal plant growth temperature (T_{opt}) was estimated as the air temperature of the annual peak of canopy activity. Nevertheless, due to in-situ data scarcity for the present study T_{opt} was fixed at a constant value of 25°C. This value has been applied previously for global evapotranspiration modelling across different types of biomes (Yuan et al., 2010; García et al., 2013).
- For the calculation of the relative humidity, e_a and e_s were obtained at midday conditions (i.e. at T_{max} conditions). Preliminary analysis showed that using e_a at this time instead of daily e_a improved the results.
- Although PT-JPL model (Fisher et al., 2008) was originally developed for monthly time scale, previous studies showed that it can also be applied

successfully considering daily inputs (Yao et al., 2017; García et al., 2013). With this daily assumption, G was considered negligible in the present study.

PM-Mu:

- PM-Mu (Mu et al., 2007-2011) uses MODIS f_{apar} as a surrogate of f_c . In order to facilitate the implementation of the model f_c in this study was derived from the in-situ site information or from Broxton et al. (2014) product.
- In PM-Mu NDVI and albedo are derived from MODIS products, while in this study we have use NDVI and albedo from the MAIAC suite products.
- For the nighttime λE calculation, negative ET values were discarded. The stations considered generally provide a positive contribution to the ET at night. In addition, MODIS nighttime clearly underestimates R_n , thus introducing an important negative deviation that will be introduced in the calculation of daily ET estimates (see chapter 7). Preliminary analysis showed that when neglecting these values more accurate ET estimates and higher R values were obtained.

SEBS:

- Timmermans et al. (2013) parametrization for tall vegetation was used in order to retrieve H . This includes the use of the following update during the iterative process: $\ln\left(\frac{z_{om}}{z_{oh}}\right) = \frac{52\sqrt{u_*l}}{LAI} - 0.69$ where l is the length scale of leaves over viscous boundary layers occurs. It takes a value of 0.027. For the roughness parameter z_{om} , a value of 2.5 was assumed (Brutsaert, 2005). In addition, G flux is obtained as $G = 0.34R_n \exp(-0.46LAI)$.
- A constant evaporative fraction was assumed in order to upscale the hourly λE fluxes to daily ET values. In this daily step calculation G was considered negligible.
- SEBS estimates on cloudy days (no LST data) was accomplished by the gap-filled method explained in the previous section. In order to facilitate notation for the rest of the paper, not gap filled SEBS model (clear days only) is named as SEBS and gap-filled model (clear and cloudy days) is named as SEBS-GF.
- SEBS model was run independently at TERRA and AQUA time overpasses using TERRA and AQUA measured LST. The resulting daily used for validation was the average between the two daily values obtained from TERRA and AQUA.

LSASAF:

- In original formulation, λE is calculated at a hourly scale and aggregated at a daily scale. In this study, in order to reduce the computational time associated model was forced directly considering daily inputs. In particular, daytime forcing was considered as nighttime model λE values were negligible. At this daytime scale G was assumed to have a zero value. Preliminary analysis showed that calculating

G as in Ghilain et al.(2011) resulted in an overestimation of in-situ G . In addition, neglecting daytime G is also assumed in PM-Mu model for the study region conditions. In LSASAF algorithm, λE is calculated by iteratively solving the surface energy budget ($R_n - \lambda E - H = 0$).

- In this study, λE was calculated as $\lambda E_c f_c + \lambda E_s (1 - f_c)$. EBF and bare soil (Ghilain et al., 2011) were selected in order to derive λE_c and λE_s (i.e only two tiles were selected for λE calculation).
- For the roughness parameter z_{0m} , a value of 2.5 and 0.001 were considered for forests and bare soil (Brutsaert, 2005). z_{0h} was obtained as $0.1z_{0m}$ and d_0 as $\frac{2h}{3}$ (Brutsaert, 2013). For bare soil a height of 0.01 m was considered.

5.3.6- Model evaluation

In Table 5.13, the required inputs for the models considered are summarized. Evapotranspiration models differ in the required input data and the parametrization of λE employed. These differences arise from the logical approach considered in the ET estimation (scaling PET for PT-JPL, Penman-Monteih logic for PM-Mu, residual scheme for SEBS and SVAT scheme for LSASAF), the evapotranspiration components modelled (λE_j , λE_c and λE_s are considered for PT-JPL and PM-Mu, λE_c and λE_s are considered for LSASAF and λE is considered for SEBS) and the explicit model parametrization (R_n , R_n partition, r_a and r_s).

As seen in Table 5.13 the PT-JPL is the least-data demanding model. PM-Mu and LSASAF are the most complex and most demanding models because of aerodynamic and surface explicit description. In PM-Mu, however no soil moisture is required. SEBS being less complex than PM-Mu and LSASAF is dependent to LST observations. For this model, the gap-filling explained in the previous section was employed in order to provide ET estimates for the cloudy days. Due to the continuous cloud cover of the region, the number of available days for ET estimation is drastically reduced when using satellite LST. An issue which actually the other models do not suffer.

Table 5.13. List of required data and parameters for evapotranspiration models as used in the present study. Static fields are indicated with an asterisk (*). Models were forced considering the temporal resolution indicated.

Model	PT-JPL	PM-Mu	SEBS	LSASAF
Surface Radiation	Rn ₂₄	SR _{in}	SR _{in} , LR _{in} , Rn ₂₄	SR _{in} , LR _{in}
Surface Meteorology	T _{max} , e _{aTmax}	T _a , T _{min} , T _{ann} , e _a , P	T _a , e _a , W _s , P	T _a , e _a , W _s , P,
Land Surface Variables	NDVI, NDVI _{max}	α , LAI, h*, f _c *	LST, ϵ^* , α , LAI, h, f _c	ϵ , α , LAI, h, f _c
Soil Variables			Soil texture	Root _{sm} , Soil _{sm}
Roughness Parameters*			Z _{0m}	Z _{0m}
Biome parameters*		g _{lh} , g _{le} , C _L , rbl _{max} , rbl _{min} , T _{minclose} , T _{maxclose} , VPD _{minclose} , VPD _{maxclose}		r _{smin}
Temporal resolution	Daily	Daytime + Nighttime	Hourly +Rn ₂₄	Daytime

Model performance was validated under two scenarios (Table 5.14). In scenario I, models were forced using surface and meteorology inputs from in-situ station, land surface variables from remote sensing data and Root_{sm} and Soil_{sm} (LSASAF) from MERRA-2 reanalysis due to the lack of stations soil moisture measurements. For scenario II, surface and meteorology together with soil moisture inputs were retrieved from reanalysis (MERRA-2, ERA-Interim or GLDAS-2.1). Gridded soil properties (gap-filled SEBS) were derived from HWSO database and land surface variables were derived from remote sensing data. For each scenario, ET models estimates were validated using in-situ ET observations. In scenario I, due to SR_{in} input data scarcity, LSASAF could be only run for K34, K83 and RJA stations and PM-Mu used R_n for K67 station. SEBS also used station R_n (due to the continuous lack of SR_{in} and LR_{in} measurements at LST time observations). The small number of available LST observations also limited SEBS model for CAX station. In scenario II, SEBS was not considered for validation (instead, gap-filled SEBS was used). In both scenarios, models were forced considering the temporal resolution indicated in Table 5.13.

Table 5.14. List of data sources and variables used in the two forcing scenarios considered.

Forcing Scenario	Data source	Variables
I	FLUXNET	Surface Meteorology, Surface Radiation
	MERRA-2	Soil and root-zone soil moisture
	MODIS	Land Surface Variables
	HWSO	Soil texture
II	REANALYSIS	Surface Meteorology, Surface Radiation, Soil moisture
	MODIS	Land Surface Variables
	HWSO	Soil texture

Model performance was evaluated using the following metrics: bias, Root Mean Square (RMSE), correlation coefficient (R) and Taylor skill score (S) (Taylor, 2001). Taylor skill score is given by Equation 5.24. For the rest of the metrics refer to section 5.2.5 for their expression.

$$S = 4 \times \frac{1+R}{(\sigma_{model}/\sigma_{obs} + \sigma_{obs}/\sigma_{model})^2 \times (1+R_0)} \quad (5.24)$$

where R_0 represents the maximum theoretical correlation ($R_0=1$, in this study). σ_{model} and σ_{obs} refers to the standard deviation of modelled and observed values respectively. S varies from zero to one. Higher S value indicating better performance. In addition, Taylor diagrams were used in order to compare models results in a comprehensive way. Three statistics are summarized in a Taylor diagram: standard deviation (STD) (displayed as the radial distance), correlation coefficient (displayed as the angle in the polar plot) and centered root mean square difference (RMSD) (displayed as the distance to observation point which is given by $R=1$, $STD = 1$ and $CRMSD = 0$ coordinates).

5.3.7- Reanalysis quality assessment

Apart from evaluating model performance, evaluating the quality of the reanalysis data (used in Scenario II) is of special importance in order to understand the impact of reanalysis inputs in the quality of models results (i.e. if biases in model estimates can be explained by biases in reanalysis inputs). This assessment was obtained by directly comparing reanalysis forcing inputs against in-situ forcing inputs. Same metrics used for model validation were considered. In the case of surface meteorology inputs (T_a , e_a and W_s) this result in comparing variables values at different heights (i.e. in-situ and reanalysis measurements heights differ), nevertheless this discrepancy is not expected to lead comparison results. Main important factor to be considered is the spatial discrepancy between coarse resolution gridded reanalysis and in-situ data. In addition, the observed in-situ data are influenced by local environment conditions such as topography and land cover.

5.3.8- Sensitivity analysis

The effects of uncertainty of inputs parameters on evapotranspiration model output uncertainty can be evaluated using sensitivity analysis. Between, the different existent methods several variance-based Global Sensitivity Analysis such as Sobol' method (Sobol, 2001, Saltelli et al., 2010) were used recently to perform sensitivity analysis on PT-JPL (Garcia et al., 2013; Zhang et al., 2017). This method is based on ANOVA (analysis of variance) decomposition. Assuming that all model inputs are independent, output model uncertainty or variance (which results from propagating input variables uncertainty into the model) is decomposed into percentages that can be attributed to the independent contribution of input variables (Sobol first index) and interactions among inputs variables (Sobol second index). A total percentage can be computed gathering these two effects (Sobol total index). These percentages serve to identify the key input variables that drive model variance (i.e. the higher the percentage the higher the effect is). This technique can be used for non-linear models as no assumption between model input and output is required. Main drawback is the high computation intensity associated.

In the following a description according to Song et al. (2012) is provided. Formally, given a model $Y = f(X)$, where Y is the model output and $X = (X_1, X_2, \dots, X_k)$. A variance decomposition of f suggested by Sobol (1990) is given by Equation 5.25:

$$V(Y) = \sum_{i=1}^k V_i + \sum_{i=1}^k \sum_{j=i+1}^k V_{ij} \dots + V_{1 \dots k} \quad (5.25)$$

where X is rescaled to a k -dimensional unit hypercube $\Omega^k, \Omega^k = \{X | 0 \leq X_i \leq 1, i = 1 \dots k\}$. $V(Y)$ is the total unconditional variance. V_i is the partial variance or 'main effect' of X_i and X_j on the total variance minus their first-order effects.

Following Saltelli et al. (2008) the first-order sensitivity index S_i and total effect sensitivity index S_{Ti} are given by Equations 5.26 and 5.27:

$$S_i = \frac{V_i}{V(Y)} = \frac{V[E(Y|X_i)]}{V(Y)} \quad (5.26)$$

$$S_{Ti} = S_i + \sum_{j \neq i} S_{ij} + \dots = \frac{E[V(Y|X_{\sim i})]}{V(Y)} \quad (5.27)$$

where $X_{\sim i}$ denotes variation on all input parameters but X_i , S_{ij} is the contribution to the total variance by the interactions between parameters. In order to compute S_i and S_{Ti} two independent input parameter sampled matrices P and Q with dimensions (N, k) were created. N is the sample size and k is the number of input parameters. Each row in matrix P and Q represents a possible value of X . The variables ranges in the matrices are scaled between 0 and 1. The Monte Carlo approximations for $V(Y)$, S_i and S_{Ti} are defined as in Saltelli et al. (2010) and are given by Equations 5.28 to 5.31:

$$\hat{f}_0 = \frac{1}{N} \sum_{j=1}^N f(P)_j \quad (5.28)$$

$$\hat{V}(Y) = \frac{1}{N} \sum_{j=1}^N (f(P)_j)^2 - \hat{f}_0^2 \quad (5.29)$$

$$\hat{S}_i = \frac{1}{N} \sum_{j=1}^N \frac{f(Q)_j(P_Q^{(i)})_j - f(P)_j}{\hat{V}(Y)} \quad (5.30)$$

$$\hat{S}_{Ti} = \frac{1}{2N} \sum_{j=1}^N \frac{((f(P)_j) - f(Q)_j)(P_Q^{(i)})_j)^2}{\hat{V}(Y)} \quad (5.31)$$

Where superscript $\hat{\cdot}$ is the estimate, \hat{f}_0 is the estimated value of the model output, $P_Q^{(i)}$ represents all columns from P except the i -th column which is from Q using a radial sampling scheme (Saltelli and Annoni, 2010). To compute S_i and S_{Ti} simultaneously, a scheme suggested by Saltelli (2002) was used which reduced the models runs to $N(k + 2)$. To sample the P and Q matrices the Sobol' quasi-random sampling technique (Sobol', 1967) was used. The quasi-random sequence helps to distribute the sampling points as uniformly as possible in the variable space to avoid clustering and increases the convergence rate (Saltelli et al., 2008).

Implementation of Sobol sensitivity analysis consists in 4 main steps: 1) a pre-sobol analysis in which the parameters to be perturbed should be defined together with the lower and upper bounds. The distribution of these parameters needs to be specified. Generally, a constant distribution is chosen. 2) The generation of the parameter sets using the Sobol sequence, 3) Running of the model using the pre-definite parameter sets and 4) the calculation of the Sobol indices. This sensitivity analysis task can be performed using statistical toolboxes such as the Python SALib toolbox (Herman & Usher, 2017) which contains all the needed functions.

In Table 5.15, the parameters used in the pre-sobol analysis for each model are presented. A uniform distribution between the lower and upper bounds is assumed in order to perturb the models. Variables used in this analysis correspond to surface radiation, surface meteorology, land surface variables and soil variables. Surface pressure (P) and static variables such as ϵ , h , f_c and soil texture were not included in the analysis. In order to consider also the temporal variation of the sensitivity indices along the year, the analysis was performed on average monthly values. Each monthly variable (X) was perturbed within a range (X -range, X + range), where range corresponds to the calculated input uncertainties in the reanalysis quality assessment. A representative value for the three reanalysis considered was applied. These values are presented in Table 5.15. This is the case for surface radiation and meteorology inputs. For $Root_{sm}$ and $Soil_{sm}$ (no previous RMSE calculated) a 15 % of variation was considered (obtained from the discrepancy amongst reanalysis soil moisture estimates). Land surface variables (α and

NDVI) were perturbed a 10% and LST was perturbed in a ± 3 K range. In the case of SEBS and LSASAF, although the humidity variable refers to the specific humidity, the range is provided in e_a for similarity with other models.

For each analysis, $N(k + 2)$ model simulations were run. N is the sample size and equals 2500 and k is the number of inputs variables which depends on each model. This results in 17500 runs for PT-JPL model, 27500 runs for PM-Mu, SEBS and LSASAF models.

Table 5.15. List of data sources and variables used in the two forcing scenarios considered. Radiation inputs are given in W/m^2 , temperature inputs in K, humidity inputs in Pa and wind speed in m/s.

Model	Input	Range	Model	Input	Range
PT-JPL	NDVI	10%	PM-Mu	α	10%
	NDVI _{max}	10%		LAI	10%
	Rn ₂₄	[x-50, x+ 50]		SR _{inday}	[x-125, x+125]
	T _{max}	[x-3,x+3]		T _{aday} ,	[x-2, x+2]
	e_{aTmax}	[x-600, x +600]		T _{minday}	[x-2, x+2]
		e_{aday}		[x-600, x+ 600]	
		T _{anight} ,		[x-2, x+2]	
		T _{minnight}		[x-2, x+2]	
		e_{anight}		[x-600, x+600]	
SEBS	α	10%	LSASAF	α	10%
	LAI	10%		LAI	10%
	Rn ₂₄	[x-50, x+ 50]		SR _{inday}	[x-125, x+ 125]
	SR _{inhour}	[x-250, x+ 250]		LR _{inday}	[x-20, x+ 20]
	LR _{inhour}	[x-20, x+ 20]		T _{aday}	[x-2, x+ 2]
	T _{ahour}	[x-3, x+ 3]		e_{aday}	[x-600, x+ 600]
	e_{ahour}	[x-600, x+ 600]		W _{sday}	[x-1.5, x+ 1.5]
	W _{shour}	[x-2, x+ 2]		Root _{smday}	15%
LST	[x-3, x+ 3]	Soil _{smday}	15%		

5.3.9- Spatial patterns comparison

Apart from validating the model performance in scenario I and II, model ET estimates were compared at regional scale (Amazonian tropical forests only as defined by the vegetation mask) by assessing discrepancies in annual cumulative ET spatial patterns (year 2004) using difference maps and monthly zonal mean values. Spatial mean values were calculated considering only pixels from the vegetation mask described in section 4.3.1. Four additional models (apart from models considered) were included for the comparison. In particular, GLEAM (Miralles et al., 2011; Martens et al., 2017), MERRA-Land (Reiche et al., 2011), ERA-Interim and GLDAS-2.1. GLEAM calculates ET via a PT approach considering a soil moisture stress computation and a Gash analytical model of rainfall interception loss (Miralles et al., 2011). MERRA-Land is an offline replay of

MERRA with model-generated precipitation corrected using rain-gauge and with model parameter changes (Reiche et al., 2011). Surface fluxes in ERA-Interim are based on land surface model TESSEL forced by atmospheric analysis and short range forecasts (van den Hurk et al., 2000). GLDAS-2.1 consists of multiple off-line land surface models. For the study NOAH Land model was considered.

Benefiting from these estimates and in order to expand the sensitivity analysis and explore what are the variables that are driving ET at regional scale, model outputs were compared with model inputs (radiation, temperature, humidity, NDVI, wind speed and soil moisture inputs) by linear regression. R^2 was employed in order to quantify this contribution.

III. RESULTS

6. - MODIS PROBABILISTIC CLOUD MASKING

6.1. Database description

As the accuracy of the retrieved training dataset is a key factor that affects directly model results, in the following a brief description is presented. In Figure 6.1, histograms of the training database viewing conditions are shown. In Figure 6.2, histograms for the features considered as input for the statistical models are presented. In Table 6.1, the confusion matrix between CPR/CALIOP and MYD35 is presented for comparison of two reference cloud masks.

From Figure 6.1, the viewing condition issue can be observed. Satellite view zenith angle (Figure 6.1 (a)) is restricted to the range of 17-19°. Sun zenith angle (Figure 6.2 (b)) ranges from 23° to almost 50°. In order to ensure accuracy in the results, these database viewing conditions should agree with MODIS swath image conditions. Database sun view zenith angle almost covers the observed solar conditions at MODIS time overpass for the study region (10° to 55°), however database view zenith angle does not reproduce MODIS swath view zenith angle conditions (0° to 65°). This limitation is due to the fact that CPR/CALIOP are nadir-instruments. Although this fact does not preclude the study it has to be taken into account when analysing model results.

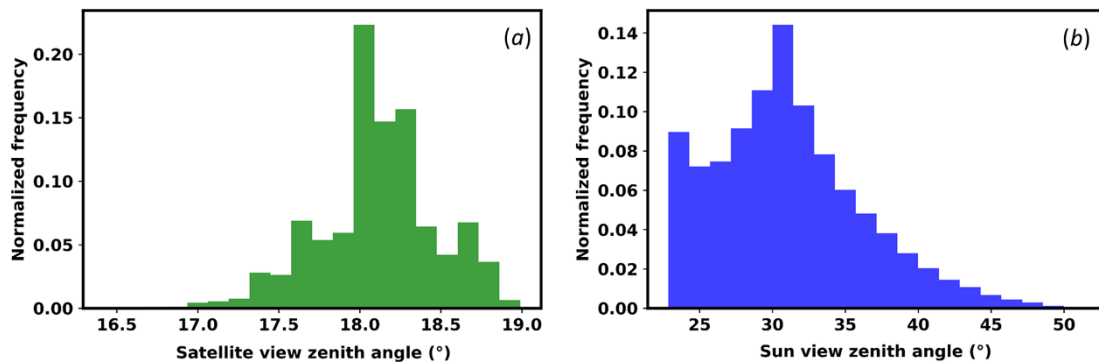


Figure 6.1. Histograms of the training dataset viewing conditions: (a) satellite zenith angle and (b) solar zenith angle.

Figure 6.2(a) and Figure 6.2(b) present the features values of the clear (tropical vegetation) and cloudy classes. Violon plots were used in order to plot the results. With these plots we are able to observe the full distribution of the data. Tropical class is characterized by reproducing vegetation spectral behaviour. Due to chlorophyll absorption in the blue (B1) and red (B4) band the green band (B3) presents a peak. In addition, B26 (1.375 μm) and B7 (2.13 μm) present small values due to their proximity to the absorption bands of water (1.4 μm and 1.9 μm). For NDVI and RVI high index values indicate green vegetation. Nevertheless, RVI present a higher intra-class variability than NDVI. Cloudy class present higher values of spectral reflectance (B1, B3, B4, B7 and B26) than the clear class. Spectral reflectance values additionally present a

higher intra-class variability than the vegetation counterparts. Amazonian tropical forests are characterized by a relative homogenous green cover in contrast to clouds which present high variability. In the visible range (B1, B3 and B4) the typical flat spectral behaviour of clouds is observed. In addition, for B26 and B7 the value decrease is also associated with the proximity of water absorption bands. NDVI and RVI, present the typical low values for non-vegetation class. In this case however, NDVI presents a higher intra-class variability than RVI. It is worth mentioning that due to angle bias in the dataset no angle features were considered as input for the models. Nevertheless, some angle dependence still exists in the features considered. This dependence is addressed in section 6.2.

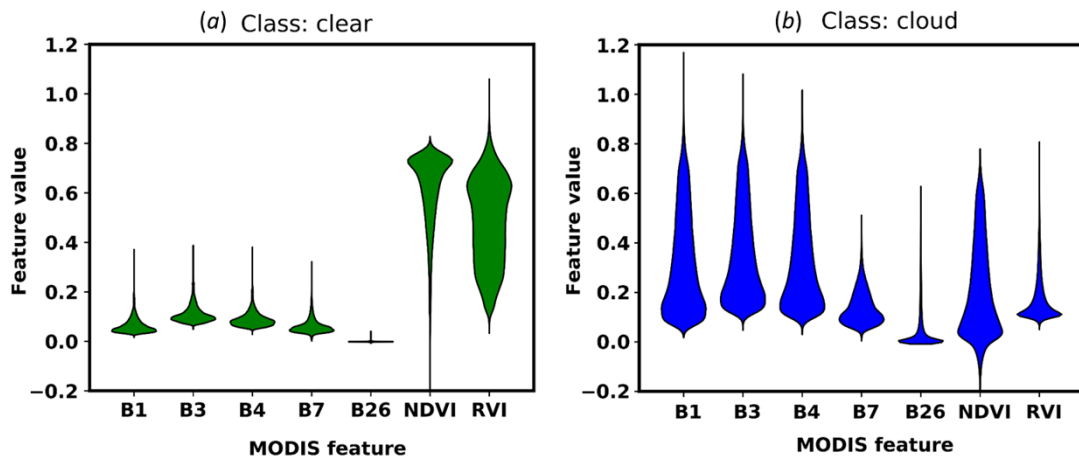


Figure 6.2. Violon plots of the features considered for classification: (a) clear class and (b) cloud class. Values were calculated over the training dataset.

Comparison of the two reference cloud masks was performed in order to observe the different cloud detection amongst the sensors considered. From Table 6.1, it is observed that both cloud masks equally classify a 78.3% (14.85% + 63.45%) of the total data points. Misclassifications represent the 21.7% (2.52% + 19.18%), mainly because 19.18% of MYD35 clear pixels are masked as clouds by CPR/CALIOP. Taking into account the superior sensitivity of active sensors for cloud masking in front of passive sensors such as MYD35, this result was expected. In fact, MYD35 clear and cloudy classes represent the 34.03% and 65.97% respectively while CPR/CALIOP clear and cloudy classes have values of 17.37% and 82.63%. For the generated database (created on the equally classified pixels) clear and cloudy classes represent the 19% and 81% respectively.

Table 6.1. Confusion matrix in percentage of CPR/CALIOP and MYD35 cloud masks. CPR/CALIOP is used as reference data. Results are calculated over the training dataset.

		MYD35	
		Clear	Cloud
CPR/CALIOP	Clear	14.85	2.50
	Cloud	19.18	63.45

6.2 Database validation

In Figure 6.3 and Table 6.2 the testing of the database is presented. In Figure 6.3, pre-calibrated and post-calibrated reliability curves are displayed. Probability of belonging to clear class is represented. As it can be observed MLP (Figure 6.3(f)) is the only model that provides well calibrated probabilities. For instance, considering MLP there are 50% of clear instances when predicted probability assumes a value of 0.5. Considering pre-calibrated results, GNB (Figure 6.3(a)), QDA (Figure 6.3(c)) and SVM (Figure 6.3(e)) probability predictions tend to be optimistic (fraction of positives higher than the mean predicted value). LDA (Figure 6.3(b)) presents a sigmoidal shape, for lower mean predicted values probability overestimate the observed distribution of positives while for higher mean predicted values the contrary is observed. RF (Figure 6.3(d)) additionally follows a sigmoidal shape, nevertheless it presents the opposite behaviour. It is worth noting that from all these models, RF is the one that shows a better probability estimation. For post-calibrated results it is observed that isotonic regression proved successful in retrieving well-calibrated probabilities. These results can also be observed with the Brier score values in Table 6.2. A decrease is obtained when comparing pre-calibrated and post-calibrated cases. MLP followed by RF show little to no-change after this process.

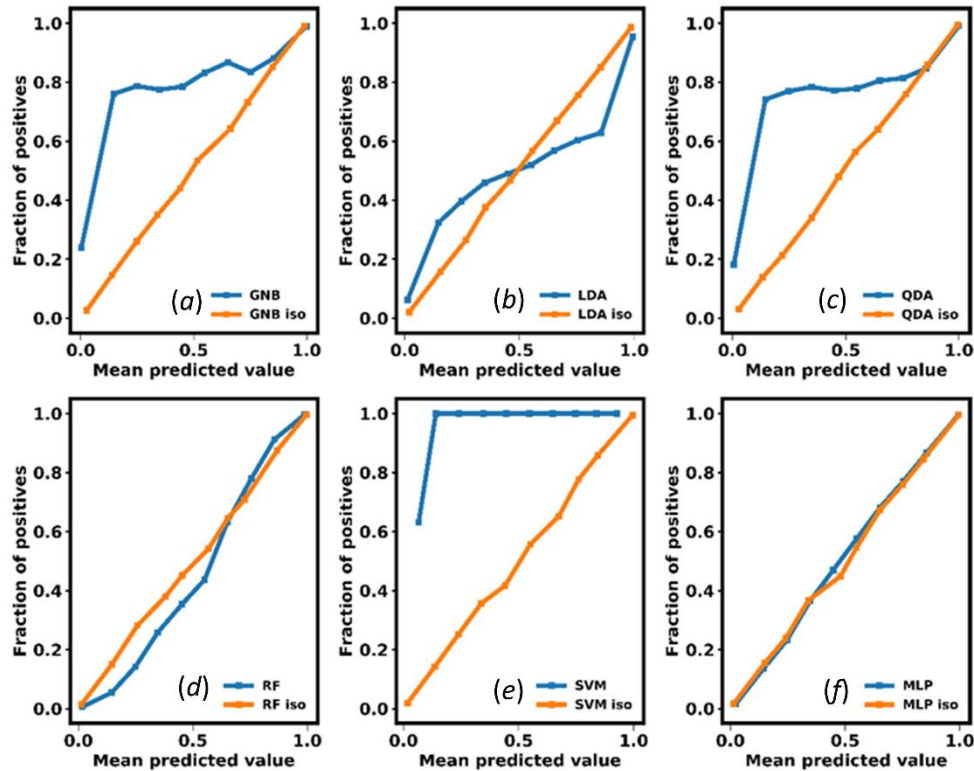


Figure 6.3. Reliability curves for model probability estimation testing: (a) GNB, (b) LDA, (c) QDA, (d) RF, (e) SVM and (f) MLP. For each model pre-calibrated results are displayed in blue and post-calibrated (denoted by iso of isotonic regression) are displayed in orange. Fraction of positives refers to the number of existent cloud instances given a probability threshold value (Mean predicted value).

In Table 6.2, OA, Kappa and brier score metrics for the test dataset are presented for both the pre-calibrated and post-calibrated scenarios. It is shown that in terms of OA and Kappa metrics, probability calibration is able to increase model performance (GNB, QDA and SVM) or keep it almost unaltered (LDA, RF and MLP models with maximum difference of 0.001 and 0.003 for OA and Kappa). Predictions estimates from the probability classifiers (post-calibrated) were obtained using a default value 0.5. Focusing on the post-calibrated scenario, it can be observed that all models are able to properly reproduce test dataset (minimum OA and Kappa value of 0.917 and 0.703 for LDA model). RF, SVM and MLP models however present a major level of agreement (higher OA and Kappa values) than GNB, LDA and QDA models. In particular, RF and LDA provide the best and worst agreement respectively. It is worth noting here that these results represent the level of agreement between model classification results and the test dataset (i.e. if models are able to properly reproduce test dataset class distributions). Nevertheless, this dataset is not completely reproducing MODIS conditions (restricted viewing angles), therefore a perfect adjustment of the models to these restricted data could result in a bad adaptation to other viewing conditions. A certain degree of flexibility thus needs to be allowed. These results show this situation, especially for the GNB, LDA and QDA models. Considering computational cost, all models considered are computationally efficient. Computational cost was calculated considering 214311 samples. GNB, LDA

and QDA benefit from a lower training time than RF, SVM and MLP. Training time was computed considering the best parameter combination obtained from cross-validation. For testing time RF presents the major cost associated, with MLP and SVM presenting better/equal cost than GNB, LDA and QDA models.

Table 6.2. Test overall accuracy and Kappa coefficient metrics for the classifiers considered. The training and testing computational cost is also presented.

	PRE-CALIBRATED					
Metrics	GNB	LDA	QDA	RF	SVM	MLP
OA	0.923	0.916	0.933	0.970	0.963	0.965
Kappa coefficient	0.718	0.706	0.802	0.900	0.878	0.884
Brier score loss	0.069	0.067	0.057	0.022	0.578	0.026
Training time (s)	0.318	0.422	0.451	37.152	37.148	57.262
Testing time (s)	0.113	0.011	0.129	1.083	0.012	0.032
	POST-CALIBRATED					
Metrics	GNB	LDA	QDA	RF	SVM	MLP
OA	0.942	0.917	0.952	0.971	0.963	0.965
Kappa coefficient	0.810	0.703	0.841	0.907	0.887	0.883
Brier score loss	0.040	0.058	0.036	0.021	0.028	0.026

6.3 Image validation

In Figure 6.4, an example of model probability estimates is presented (DOY 5 and 17:10 UTC crossing time). Location (Figure 6.4(a)), true color (Figure 6.4(b)) and manually classified image (Figure 6.4 (c)) are additionally shown. Clear probability is considered for display. Cloud probability can be derived as 1- clear probability. Considering the true color image, it can be observed the difficult situation classification algorithms have to deal with. Nevertheless, the statistical models considered are able to provide an accurate representation. Clouds present probabilities closer to 0 while tropical forests have values closer to 1. For this example, it can be observed that main existing differences between models arise between two groups (GNB-LDA-QDA (Figure 6.4(d)(e)(f)) and RF-SVM-MLP (Figure 6.4(g)(h)(i)). It is observed that for the range of intermediate clear probability values (corresponding mainly to cloud edges and small clouds) the second group tends to provide higher absolute values than the first group and thus tending to label these pixels as clear.

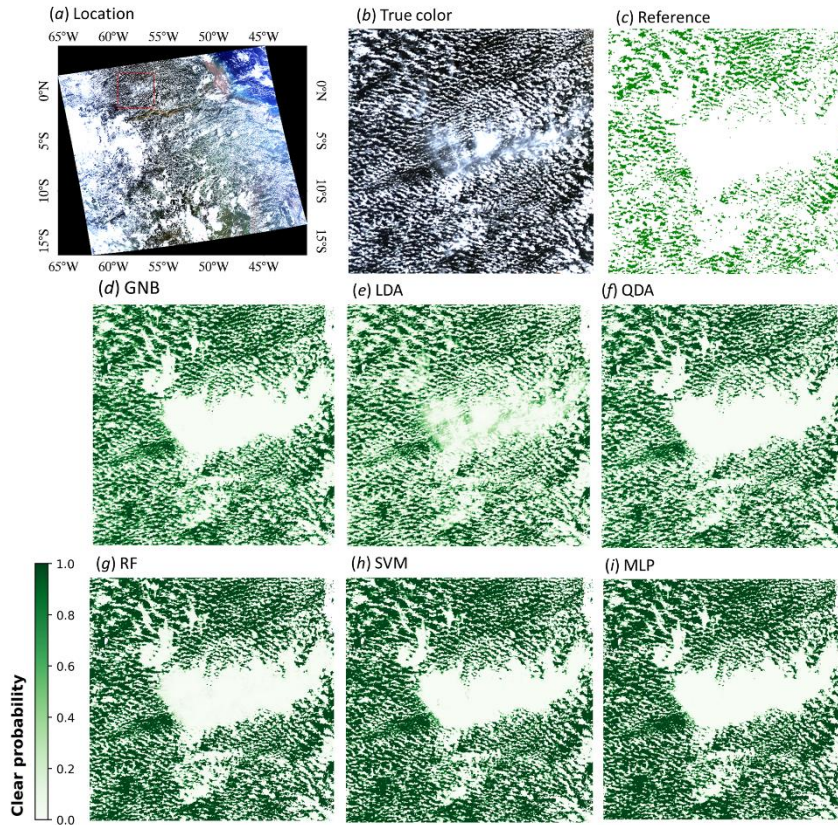


Figure 6.4. Clear probability estimates of DOY 5 (17:10 UTC time overpass) for the models considered: (d) GNB, (e) LDA, (f) QDA, (g) RF, (h) SVM and (i) MLP. True color image (b) and manually classified image (c) together with its location inside the swath image (a) are also displayed.

In Figure 6.5 the threshold selection process is shown. Kappa coefficient is calculated over the entire image dataset (20 images). MYD35 and MAIAC Kappa values are also displayed for comparison. In exception of RF, maximum Kappa values points mark the change between the ascendant and descendant behaviour. Starting from these point models start to overestimate cloud condition (assign more clear pixels to the cloudy class) and thus a decrease in the performance is obtained. For RF kappa maximum value is reached at the maximum threshold considered. In Table 6.3, model maximum Kappa values together with MYD35 and MAIAC Kappa values are shown. As it can be seen in Figure 6.5, GNB-LDA-QDA group provide higher values than RF-SVM-MLP group. In particular, LDA provides the best performance (0.722 of Kappa value) and MLP the worst performance (0.604 of Kappa value). With a Kappa value of 0.567 MAIAC cloud masking algorithm improves MYD35 performance (0.429) however lies below the worst performance Kappa value (0.604 for MLP) of the statistical models. Considering computational cost at image level (Table 6.3) all models are computationally efficient. RF and LDA stands out as having the highest and lowest cost associated respectively.

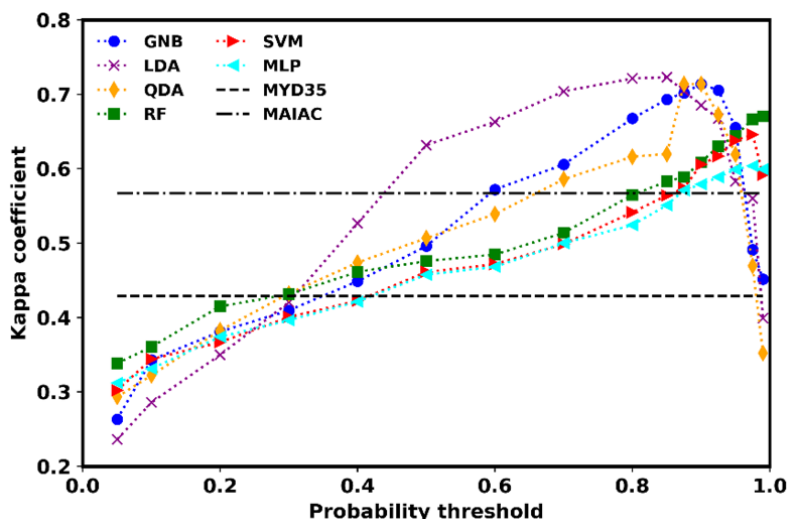


Figure 6.5. Probability threshold selection for label assigning. For each model considered Kappa coefficient is calculated considering different probability thresholds values in the range of 0 to 1. MYD35 and MAIAC Kappa values are also displayed.

Table 6.3. Probability threshold selected together with its associated Kappa value for the models considered. Computational cost at image level is also presented. MYD35 and MAIAC Kappa values are also provided.

Model	Threshold	Kappa coefficient	Computational cost (s)
MYD35	----	0.429	----
MAIAC	----	0.567	----
GNB	0.900	0.713	1.72
LDA	0.850	0.722	0.37
QDA	0.875	0.713	1.47
RF	0.990	0.670	9.49
SVM	0.975	0.646	0.42
MLP	0.975	0.604	1.00

Comparison of the performance for all the cloud masking algorithms under different satellite viewing conditions is presented in Table 6.4. Doing this, we are able to assess view zenith angle dependence in model performance. Three ranges ($vza \leq 20^\circ$, $20^\circ < vza < 40^\circ$ and $vza \geq 40^\circ$) were considered for comparison. Both Kappa and OA metrics are presented. Several results can be obtained from Table 6.4. Excepting MAIAC case, all cloud masking algorithms performance decrease with angle. In addition, as in overall results (Table 6.3), GNB-LDA-QDA group provides better performance than RF-SVM-MLP group. While in the first group all three models provide similar metrics values in the second group RF provides the best performance. All the statistical models considered are able to improve MYD35 performance, nevertheless only GNB-LDA-QDA are able to always outperform MAIAC performance. For RF model, although it does outperform MAIAC a minor discrepancy is obtained in comparison to the first group.

Table 6.4. Model performance (Kappa coefficient and OA metrics) under three different view zenith angle (vza) ranges.

Model	vza \leq 20°		20° < vza < 40°		vza \geq 40°	
	OA	Kappa coefficient	OA	Kappa coefficient	OA	Kappa coefficient
MYD35	0.760	0.474	0.723	0.411	0.740	0.377
MAIAC	0.861	0.516	0.723	0.564	0.910	0.625
GNB	0.904	0.734	0.901	0.698	0.923	0.710
LDA	0.908	0.741	0.908	0.715	0.925	0.709
QDA	0.904	0.738	0.900	0.700	0.920	0.700
RF	0.899	0.716	0.893	0.649	0.912	0.633
SVM	0.876	0.611	0.879	0.580	0.900	0.582
MLP	0.867	0.637	0.865	0.581	0.887	0.592

In Figure 6.6 model performance (Kappa coefficient) is evaluated at image level for each of the 20 images subsets manually classified. MYD35/MAIAC Kappa values are also displayed for comparison. For the models considered, GNB (Figure 6.6(a)) and LDA (Figure 6.6 (b)) provide the best performance. They have the highest Kappa values and provide the minimum number of intersections with MAIAC. RF (Figure 6.6(d)) provides similar Kappa values as GNB/LDA, nevertheless there are two cases in which model performance is below MYD35 performance (275_1725 and 300_1855 images). This is also observed for SVM (Figure 6.6(e)) in image 300_1720 and for MLP (Figure 6.6(f)) in 275_1725 and 300_1855 images. QDA (Figure 6.6(c)) although with lower Kappa values than GNB/LDA always outperform MYD35. In addition, it is worth mentioning that MYD35 generally provides the worse performance. MAIAC cloud masking generally outperforms MYD35 excepting for three cases (075_1810, 100_1805, 300_1720 images). For the models considered, GNB and LDA generally outperform both MYD35 and MAIAC. This result can also be observed in Figure 6.7 in which the cloud cover of these algorithms is shown. Results from manually classified images are also presented. Cloud cover was calculated as the ratio between cloudy pixels and the total number of pixels. GNB and LDA (Figure 6.7(a)(b)) closely reproduce reference cloud cover in comparison to the rest of the models. Reference cloud cover and model estimated cloud cover lies between MYD35 and MAIAC providing the minimum and maximum amount of clouds respectively.

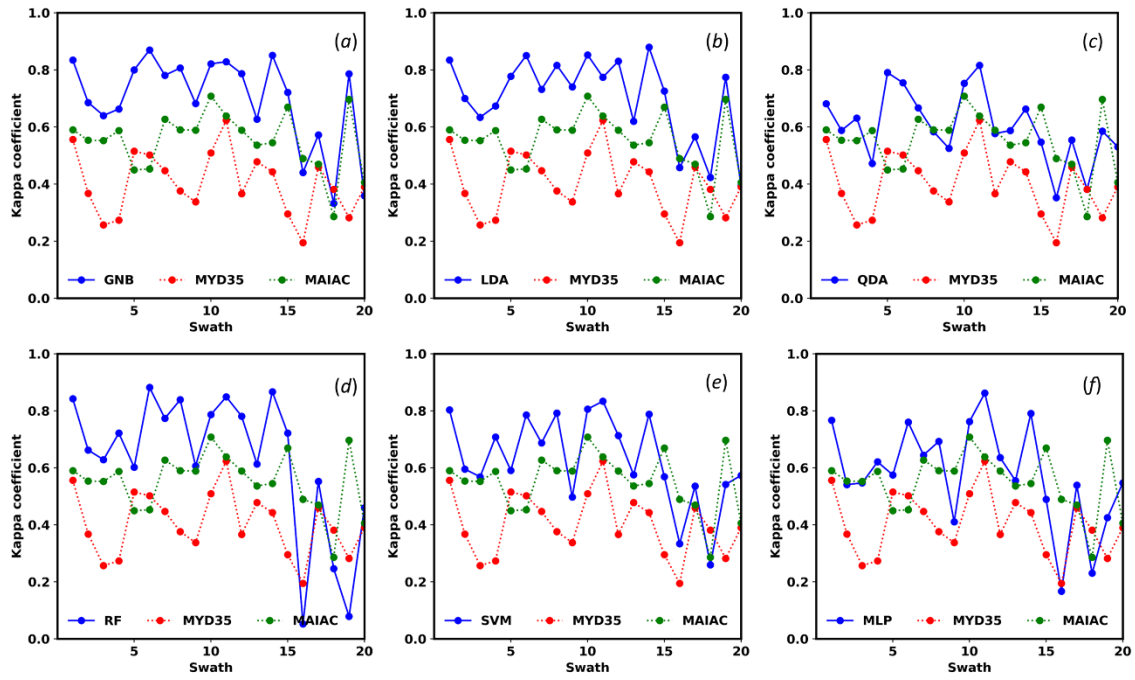


Figure 6.6. Model performance (Kappa value) over each of the manually classified images (image testing dataset). Results correspond to: (a) GNB, (b) LDA, (c) QDA, (d) RF, (e) SVM and (f) MLP models. In each model subplot, model results are displayed in blue and MYD35 and MAIAC in red and green respectively. Image identification is provided in Table 6.2.

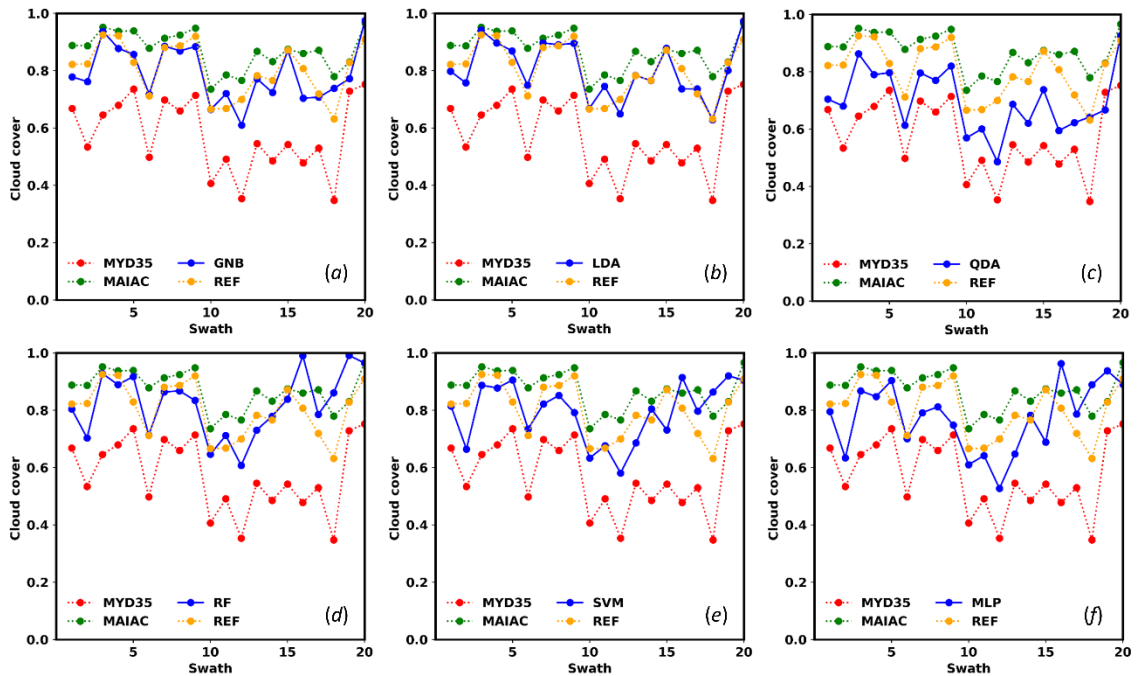


Figure 6.7. Image testing dataset derived cloud cover. Results are displayed for each model considered: (a) GNB, (b) LDA, (c) QDA, (d) RF, (e) SVM and (f) MLP. In each model subplot, cloud cover from the manually classification (REF) is displayed in orange and model, MYD35 and MAIAC in blue, red and green respectively.

In Figure 6.8, a visual comparison for DOYs 175_1745 (Figure 6.8(a)) and 275_1725 (Figure 6.8(b)) between MYD35/MAIAC and the models considered is shown. Additional images are presented in Supplementary Material. As observed in Figure 6.8(a) and Figure 6.8(b) MYD35 (Figure 6.8(a)(b)(iv)) provides an underestimation of the cloud cover (Figure 6.8(a)(b)(ii)). Although bigger and thicker clouds are correctly assigned MYD35 misses the great amount of small clouds in the images. MAIAC (Figure 6.8(a)(b)(v)) capturing the small cloud distribution provides a better detection of clouds. Nevertheless, it tends to overestimate the total cloud cover (Figure 6.8(b)(ii)). For the models considered, GNB and LDA followed by QDA provide the best agreement with reference data. RF, SVM and MLP provide a worse performance. In Figure 6.8(a) it can be observed that they do not reproduce as accurate as GNB/LDA the reference data. In addition, Figure 6.8(b) a complete overestimation of cloud cover is observed.

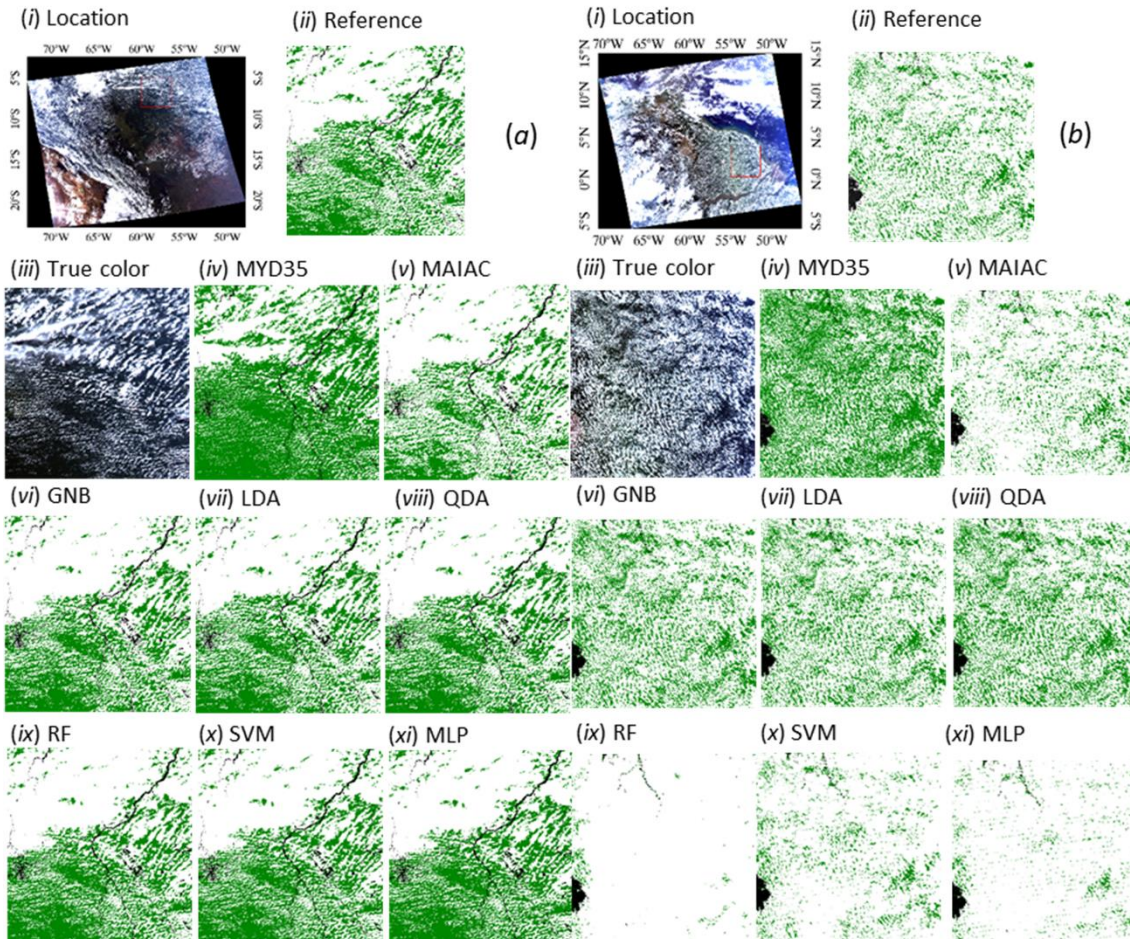


Figure 6.8. Visual intercomparison of models and MYD35/MAIAC cloud masking results for doys 175_1745 (a) and 275_1725 (b). For each doy, results are displayed as follows: (i) Location, (ii) Reference manually classified image, (iii) True color image, (iv) MYD35, (v) MAIAC, (vi) GNB, (vii) LDA, (viii) QDA, (ix) RF, (x) SVM and (xi) MLP results. Cloud and clear labels are displayed in white and green respectively. Non-EBF pixels are displayed in black.

6.4 In-situ validation

In Table 6.5, model and MYD35/MAIAC in-situ testing is shown. Results are presented using confusion matrices together with OA and Kappa coefficient metrics. Data points in confusion matrices represent days with a valid satellite measurement. In-situ testing dataset consisted in a total of 110 days (i.e. for each day a satellite measurement of the station). Cloudy and clear-sky days represent approximately the 95% (i.e. 104/110) and 5% (6/110) of the total amount of data. Although clear and cloudy classes are clearly imbalanced (with a major representation of the cloudy class) it is assumed that this distribution represent the cloud distribution of the station. MYD35 flags approximately a 15% (i.e. 16/110) of the data as clear-sky, while MAIAC flags the 2.7% (i.e. 3/110). Models tend to flag the 4% and the 5% as clear-sky. Taking into account the respective cloud underestimation and overestimation of MYD35 and MAIAC, it is expected that the observed in-situ cloud frequency lies between these two limits.

Table 6.5. In-situ testing results of MYD35, MAIAC, GNB, LDA, QDA, RF, SVM and MLP algorithms. Results are presented using confusion matrices together with OA and Kappa coefficient values. Samples in confusion matrices represent available days (i.e. for each day a prediction of clear/cloud in the station is obtained).

		Confusion matrix		OA	Kappa coefficient
		In-situ			
		Clear	Cloud		
MYD35	Clear	6	10	0.910	0.510
	Cloud	0	94		
MAIAC	Clear	3	0	0.972	0.653
	Cloud	3	103		
GNB	Clear	4	1	0.973	0.713
	Cloud	2	103		
LDA	Clear	4	0	0.982	0.791
	Cloud	2	104		
QDA	Clear	4	1	0.973	0.713
	Cloud	2	103		
RF	Clear	4	0	0.982	0.791
	Cloud	2	104		
SVM	Clear	4	0	0.982	0.791
	Cloud	2	104		
MLP	Clear	5	1	0.983	0.824
	Cloud	1	103		

It is observed (Table 6.5) that all models correctly classify the cloud class, major discrepancy in model performance derives from the ability of the models to properly classify the clear class. MYD35 properly flags the 6 clear-sky days, but it also misclassifies clouds samples as clear samples. MAIAC flags only 3 samples of the 6 clear samples. Its misclassification consists in flagging clear samples as cloud samples. Models are able to flag more clear samples than MAIAC (4 and 5 depending on the model) but also have misclassifications. Same MAIAC misclassification type is observed in LDA, RF and SVM. For GNB, QDA and MLP there are also cloud samples, which are misclassified as clear samples. In terms of the Kappa coefficients, models provide a better performance than MYD35 and MAIAC. Best performance amongst models is obtained for MLP, followed by LDA, SVM, RF, GNB and QDA. For OA metric, same results can be derived. Nevertheless, this metric does not take into account for the imbalanced problem in the dataset, thus the higher values observed (greater than 0.9).

6.5 Discussion

From database description, it was observed that considering the collocation of CPR/CALIOP and MODIS observations as training data entails one important deficiency. While MODIS swaths cover a range of 0-65° in view zenith angle, the database viewing conditions are restricted to lie between 17-19° (Figure 6.1(a)). Apart from this, it was observed that considering confident labels from both sensors when generating the reference database was able to correct the cloud underestimation in MYD35 (cloud percentage of approximately 65% in Table 6.1 and Figure 6.7) and provide a more robust reference database that it is able to properly represent the cloud distribution of the region. Clear and cloud classes represent the 19% and 81% for the reference database (Table 6.1) and the mean cloud cover of manually classified images (Figure 6.7) is approximately the 80%.

From database testing, it was observed that a probability calibration was needed in order to correct the probability estimates of the models. In exception of MLP (Figure 6.3(f)), rest of the models pre-calibrated probabilities lie apart of the diagonal line (Figure 6.3). These results agree with Niculescu-Mizil & Caruana (2005) in which a comparison of several machine learning methods (such as RF, SVM and Naïve Bayes) probability estimates was performed, pointing out that neural nets and bagged trees predicted well calibrated probabilities. In addition, it was observed that RF, SVM and MLP models were able to adjust better (higher OA and Kappa coefficients) to the test data than probabilistic models (GNB, LDA and QDA). This result was expected, as these are complex models (RF, SVM and MLP) that can be optimized in order to maximize classification results. It is worth noting here, that only a binary problem between green vegetation and clouds is being considered here. Other classes (such as bare soil or water), were discarded in order to not introduce additional misclassifications between these classes. Moreover, we are only interested in the tropical forests in Amazonia.

From image testing, it was observed that the models are able to improve MYD35 and MAIAC performance over the region of study. In Figure 6.5, it is observed that assuming the default 0.5 of well-calibrated classifiers (i.e. with no tuning of the probability threshold) all models are able to improve MYD35 performance. LDA model is able to outperform both MYD35 and MAIAC. After tuning of the probability threshold (Table 6.3), all model Kappa coefficient values surpass MYD35 and MAIAC Kappa values. In particular, a maximum and minimum increase of 0.293 and 0.175 is obtained for LDA and MLP models. Regarding MAIAC algorithm, a maximum and minimum increase of 0.155 and 0.037 is obtained also for LDA and MLP. This better performance is also observed in Figure 6.6. In exception of some images, models generally outperform MYD35 and MAIAC results (models provide higher Kappa values). Nevertheless, it is worth noting that some models perform better than others. Probabilistic models (GNB, LDA and QDA) outperform RF, SVM and MLP models (Table 6.3 and Figure 6.6). In particular, higher Kappa values were obtained for the first group. For the second group several misclassified images were observed (Figures 6.6 and 6.8(b)). In addition, GNB and LDA models better reproduce the cloud cover of the manually classified images than the rest of the models and MYD35 and MAIAC algorithms (Figure 6.7). Main reason behind this behaviour is that complex models (RF, SVM and MLP) adapted too well to the view angle biased training dataset, thus overfitting and not properly adapting to other viewing conditions. LDA is the less adapted to the training dataset (lowest Kappa value in Table 6.2) and the most adapted to the image testing dataset (highest Kappa value in Table 6.3). Considering the angle influence it was observed that models were able to adapt to other viewing conditions without a systematic bias (Table 6.4). Apart from these results, an underestimation and overestimation of cloud cover was reported for MYD35 and MAIAC algorithms (Figure 6.7 and Figure 6.8). MAIAC however always outperform MYD35 algorithm. MYD35 fails in properly classifying the abundant small clouds (and thus underestimating the cloud cover) over the study region, while MAIAC provides a more restrictive cloud masking (Figure 6.8). MAIAC using a temporal approach (i.e. using clear sky scenes as references) is shown to be more sensitive to small and difficult clouds. It is worth mentioning here, that the accuracy of previous results depends on the accuracy of the manually classified images. Manually classified image cloud sensitivity lies in the expected range between MYD35 (underestimation) and MAIAC (overestimation) (Figure 6.7). Thus, proving its validity for being used as a testing database. In addition, if human errors existed in the dataset they should have led to unexpected classification results.

Considering in-situ testing results, all models outperform MYD35 and MAIAC in terms of OA and Kappa metrics (Table 6.5). When analyzing these results, it is worth taking into account that we are dealing with a clear imbalanced distribution (95% of clouds and 5% of clear points). In addition, there is the spatial and temporal discrepancy issue between satellite and in-situ conditions together with the land cover discrepancy. A 3x3 kernel was used in order to alleviate the effects of the last issue. All algorithms properly label the cloud class and main classification issues arise in labelling clear cases. The models considered provide a clear-sky sensitivity between MYD35 and MAIAC (i.e.

flagging more clear cases than MAIAC but committing misclassifications). About the accuracy of the in-situ testing dataset, a higher cloud frequency than the observed in previous sections is obtained. Nevertheless, it absolutely agrees with the MAIAC and model cloud distribution observed. In addition, MYD35 reports a 15% but we have to take into account also the underestimation issue. In addition, increasing the representation of clear cases by raising the threshold value (to higher values than 25%) will also result in misclassified clear flags. Therefore, in spite of being imbalanced it properly represents the in-situ cloud distribution.

About the validity of the presented approach, it was found that the combination of collocated CPR/CALIOP and MODIS observations together with probabilistic models is proved suitable for MODIS cloud masking. Although machine learning algorithms were able to generally improve MYD35 and MAIAC performance, the current approach is limited to probabilistic models (especially LDA followed by GNB). These models were able to better deal with the issue in viewing conditions derived from the collocated training database. In addition, they were shown computationally efficient at image level (Table 6.4). In particular, LDA presents the lowest computational cost associated. A probability calibration however is needed in order to provide accurate probability estimates. The approach presented here accomplished study goals (cloud masking of Amazonian evergreen tropical forests) nevertheless it presents some limitations in order to be applied in a larger scale. The expansion to other types of surfaces can be easily solved by introducing additional classes and features in the training dataset. The viewing conditions issue can be alleviated by proper radiative simulations at different angles. Thus providing a more robust training dataset. In addition, although in the present study we focused only on individual model results, an ensemble of models can be applied in order to boost the cloud masking accuracy.

7. - LST RETRIEVAL ALGORITHM ADAPTED TO THE AMAZON EVERGREEN FORESTS

7. - LST retrieval algorithm adapted to the Amazon evergreen forests

7.1.- Simulated database validation

In Table 7.1, the coefficients of the split window and the results from the sensitivity analysis for MODIS, VIIRS and SLSTR cases are presented. Daytime and nighttime coefficients were derived from the TERRA-AQUA-daytime and TERRA-AQUA-nighttime simulated databases respectively.

For the simplified version of the SW algorithm, the total LST error ranges from 0.520 K to 0.896 K. Higher total contributions are obtained for daytime than nighttime. In particular, because a decrease in the standard error of the algorithm (δ_{alg}). A mean value of 0.36 K against a mean value of 0.53 K for the cases considered. For the generalized version of the SW algorithm, total LST ranges from 0.841 K to 1.695 K. This increase results from the consideration of additional contributions of emissivity and water vapour. As observed in Table 7.1, emissivity is the dominant contribution to the total LST error. Uncertainty in emissivity of about 1% lead to a contribution ranging from 0.732 K to 1.549 K. On the contrary, the uncertainty in water vapour has a minor contribution, with a maximum value of 0.184 K. As in the simplified case, higher total contributions are obtained for daytime than nighttime, mainly because of a decrease in δ_{alg} , δ_{ϵ} and δ_w .

In Table 7.2 and Figures 7.1 to 7.4, the validation of the split-window algorithms using the independent simulated database is presented. In Table 7.2, except in the case of VIIRS generalized SW for the nighttime case, all the SW algorithms provide a null bias and R values higher than 0.9. The RMSE is thus dominated by the standard deviation retrieved from the simulation. Values of σ range from 0.36 K to 1.0 K with also higher values at daytime. In addition, it is observed that the simplified versions for all the sensors considered tend to adjust better to the validation dataset and thus provide a lower σ value than the generalized version.

In Figures 7.1 to 7.4 validation results are analysed in terms of the water vapour content and viewing angle. In terms of water vapour (Figures 7.1 and 7.3) LST differences tend to mostly lie between ± 1 K, except for large values of water vapour ($w > 6$ g/cm²). This is especially observed at daytime, for nighttime however, a more stable behaviour is observed. Comparing the results from the simplified and the generalized versions, it is seen that data dispersion is higher in the case of the generalized version than in the simplified. This is particularly seen for the daytime case of AQUA and VIIRS, Figure 7.3 (c)(e) show a linear ascending behaviour while Figure 7.1 (c)(e) is more stable for the different w values. In terms of the viewing angle (Figures 7.2 and 7.4), although maximum/minimum LST differences can reach to absolute values up to 6 K, the boxplots interquartile tend to lie between ± 1 K for all the viewing angles considered. Generally, a slight increase with angle is observed for angles higher than 30°. Considering the comparison between the simplified and the generalized version same conclusion as for the case of water vapour are obtained. The deviation between validation temperature and SW temperature are higher for the generalized version than for the simplified (more separation between the extremes of the boxplot and wider interquartile range).

Table 7.1. Coefficients of the split-window for MODIS (TERRA and AQUA platforms), VIIRS and SLSTR cases. Both daytime and nighttime values are presented. In addition, individual contributions to the total uncertainty in LST are also given: standard error of the algorithm (δ_{alg}), uncertainty due to the Noise Equivalent Delta Temperature ($\delta_{NE\Delta T}$), contribution of the uncertainty in the emissivity (δ_ε) and contribution of the uncertainty in the total atmospheric water vapour (δ_w). Uncertainties of 0.1 K, 0.01 and 0.5 cm for brightness temperatures, emissivity and water vapour have been considered, respectively.

	C_0 (K)	C_1	C_2 (K ⁻¹)	C_3 (K)	C_4 (K·cm ² g ⁻¹)	C_5 (K)	C_6 (K·cm ² g ⁻¹)	δ_{alg} (K)	$\delta_{NE\Delta T}$ (K)	δ_ε (K)	δ_w (K)	e(LST) (K)	
Simplified	TERRA _{DAY}	1.461	2.208	0.629	---	---	---	0.481	0.559	---	---	0.734	
	AQUA _{DAY}	1.829	1.638	0.774	---	---	---	0.623	0.651	---	---	0.896	
	TERRA _{NIGHT}	1.578	1.918	0.883	---	---	---	0.334	0.510	---	---	0.607	
	AQUA _{NIGHT}	1.592	2.084	0.625	---	---	---	0.321	0.512	---	---	0.606	
	VIIRS _{DAY}	2.220	0.832	0.590	---	---	---	0.622	0.517	---	---	0.805	
	VIIRS _{NIGHT}	1.878	1.279	0.489	---	---	---	0.391	0.393	---	---	0.552	
	SLSTR _{DAY}	1.280	0.609	0.427	---	---	---	0.372	0.396	---	---	---	0.543
	SLSTR _{NIGHT}	1.389	0.616	0.485	---	---	---	0.384	0.352	---	---	---	0.520
	TERRA _{DAY}	1.425	1.504	0.670	-8.158	9.777	116.595	-40.533	0.361	0.473	1.107	0.133	1.264
	AQUA _{DAY}	2.691	0.707	0.794	-45.518	13.349	259.170	-55.516	0.400	0.530	1.549	0.184	1.695
General	TERRA _{NIGHT}	1.245	1.247	0.988	7.380	7.380	66.838	-33.285	0.204	0.439	0.975	0.104	1.093
	AQUA _{NIGHT}	1.348	1.518	0.659	2.678	7.150	78.323	-31.325	0.197	0.442	0.978	0.100	1.095
	VIIRS _{DAY}	3.040	0.135	0.583	-64.794	17.072	133.828	-30.657	0.379	0.419	0.930	0.190	1.104
	VIIRS _{NIGHT}	1.727	0.769	0.488	15.889	11.511	49.187	-21.189	0.253	0.324	0.723	0.129	0.841
	SLSTR _{DAY}	1.381	0.220	0.431	-7.413	8.906	84.197	-27.600	0.250	0.345	0.772	0.115	0.890
	SLSTR _{NIGHT}	1.230	0.200	0.508	5.139	7.778	59.908	-26.727	0.285	0.306	0.732	0.104	0.849

Table 7.2. Validation of the generalized and simplified split-window algorithms for the independent simulated dataset. Subscripts gen and simpl refers to the generalized and simplified versions of the algorithms.

	Daytime				Nighttime			
	Bias (K)	σ (K)	RMSE (K)	R	Bias (K)	σ (K)	RMSE (K)	R
TERRA_{SW-gen}	0.00	0.58	0.58	0.98	0.00	0.36	0.36	0.98
TERRA_{SW-simpl}	0.00	0.48	0.48	0.98	0.00	0.33	0.33	0.98
AQUA_{SW-gen}	-0.02	1.00	1.00	0.91	0.00	0.38	0.38	0.99
AQUA_{SW-simpl}	-0.03	0.57	0.57	0.97	0.00	0.33	0.33	0.99
VIIRS_{SW-gen}	0.02	0.98	0.98	0.91	0.47	0.48	0.67	0.98
VIIRS_{SW-simpl}	0.01	0.59	0.59	0.97	-0.06	0.38	0.38	0.99
SLSTR_{SW-gen}	0.00	0.43	0.43	0.98	0.00	0.41	0.41	0.98
SLSTR_{SW-simpl}	-0.06	0.36	0.36	0.99	0.00	0.38	0.38	0.99

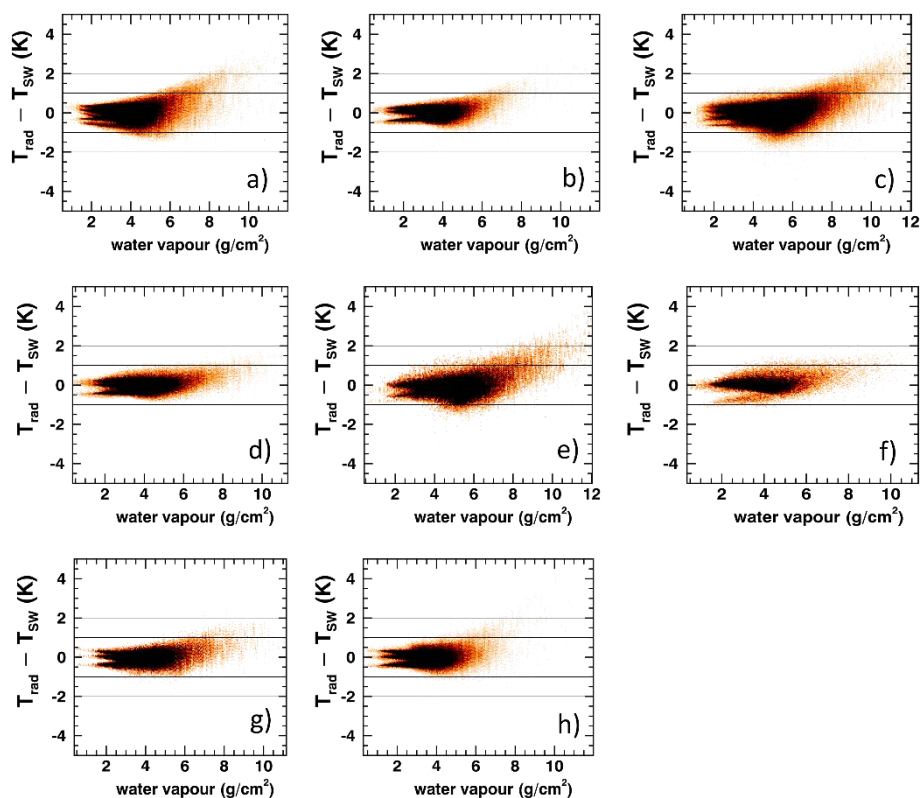


Figure 7.1. Difference between the temperature derived from the radio-sounding and the temperature estimated from the simplified version of the Split-window (T_{rad} and T_{SW}) against the atmospheric path water content ($w/\cos\theta$): a) TERRA_{DAY}, b) TERRA_{NIGHT}, c) AQUA_{DAY}, d) AQUA_{NIGHT}, e) VIIRS_{DAY}, f) VIIRS_{NIGHT}, g) SLSTR_{DAY} and h) SLSTR_{NIGHT}.

7. - LST retrieval algorithm adapted to the Amazon evergreen forests

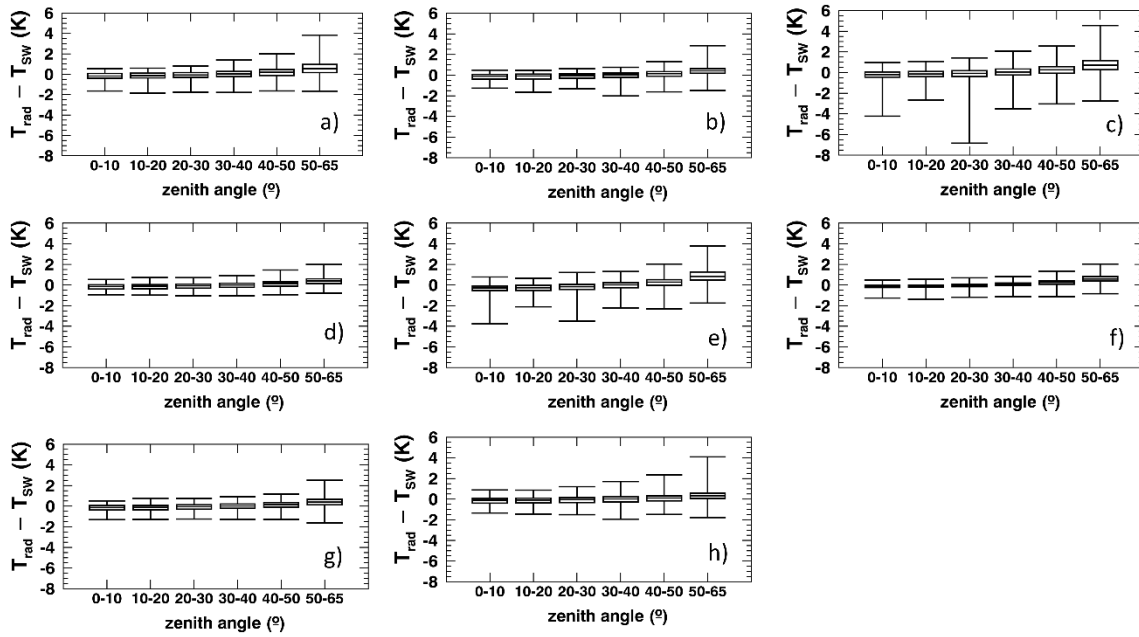


Figure 7.2. Difference between the temperature derived from the radio-sounding and the temperature estimated from the simplified version of the split-window (T_{rad} and T_{SW}) against the sensor view zenith angle a) $\text{TERRA}_{\text{DAY}}$, b) $\text{TERRA}_{\text{NIGHT}}$, c) AQUA_{DAY} , d) $\text{AQUA}_{\text{NIGHT}}$, e) $\text{VIIRS}_{\text{DAY}}$, f) $\text{VIIRS}_{\text{NIGHT}}$, g) $\text{SLSTR}_{\text{DAY}}$ and h) $\text{SLSTR}_{\text{NIGHT}}$.

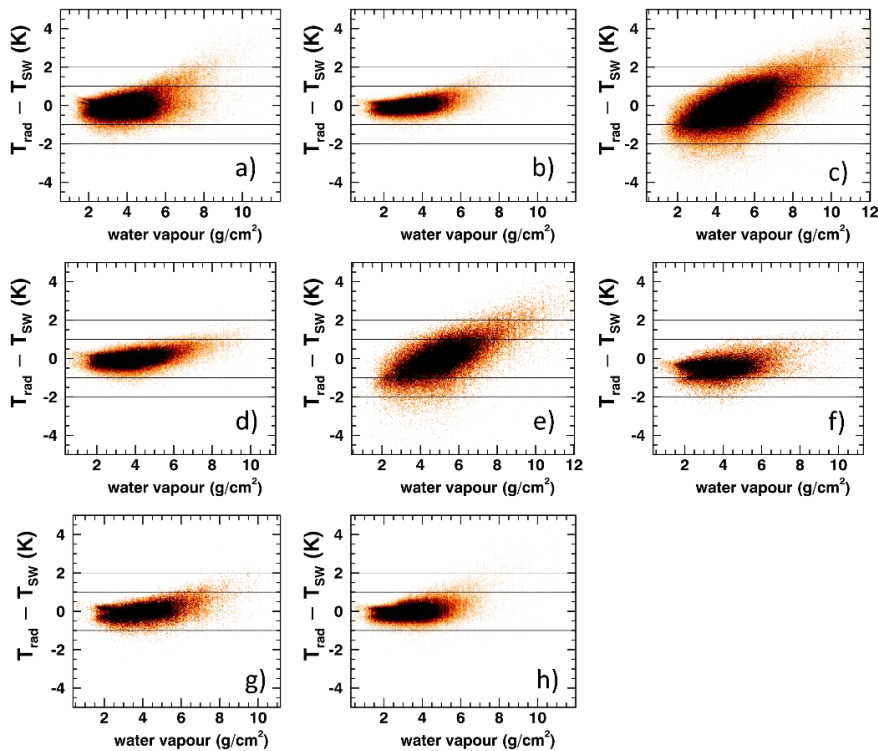


Figure 7.3. Difference between the temperature derived from the radio-sounding and the temperature estimated from the generalized version of the split-window (T_{rad} and T_{SW}) against the atmospheric path water content ($w/\cos\theta$): a) $\text{TERRA}_{\text{DAY}}$, b) $\text{TERRA}_{\text{NIGHT}}$, c) AQUA_{DAY} , d) $\text{AQUA}_{\text{NIGHT}}$, e) $\text{VIIRS}_{\text{DAY}}$, f) $\text{VIIRS}_{\text{NIGHT}}$, g) $\text{SLSTR}_{\text{DAY}}$ and h) $\text{SLSTR}_{\text{NIGHT}}$.

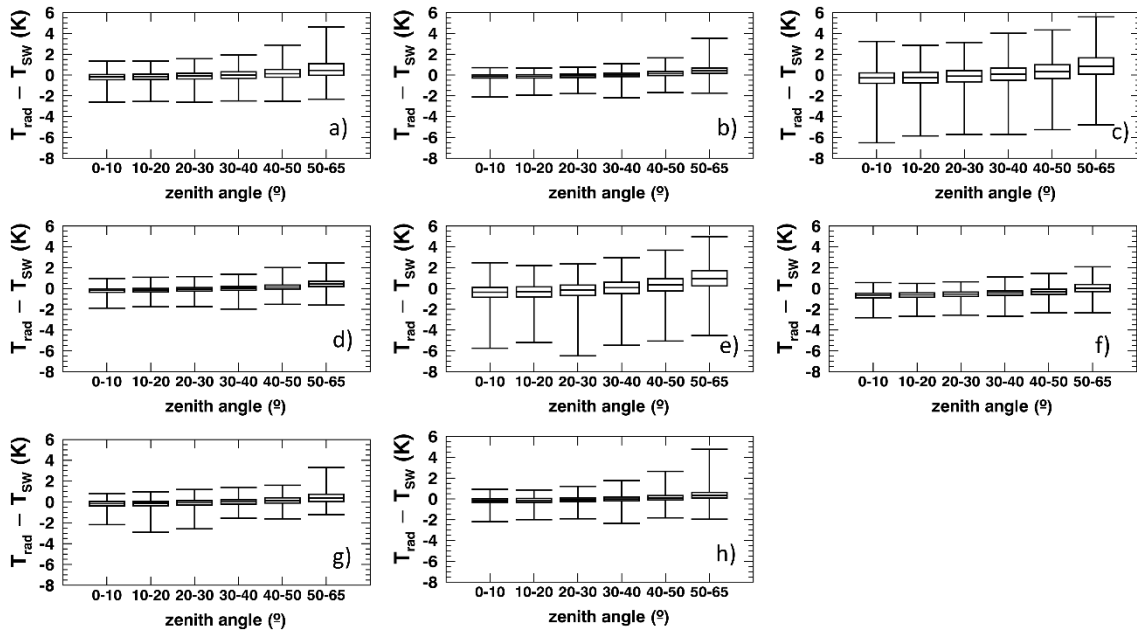


Figure 7.4. Difference between the temperature derived from the radio-sounding and the temperature estimated from the simplified version of the split-window (T_{rad} and T_{SW}) against the sensor view zenith angle a) TERRA_{DAY}, b) TERRA_{NIGHT}, c) AQUA_{DAY}, d) AQUA_{NIGHT}, e) VIIRS_{DAY}, f) VIIRS_{NIGHT}, g) SLSTR_{DAY} and h) SLSTR_{NIGHT}.

7.2.- T-based validation

LST algorithm validation using in-situ LST was performed separately for daytime and nighttime conditions. The screening procedure detailed in section 5.2.5 was applied for eliminating cloud contaminated values. Validation metrics are presented in Table 7.3 and Table 7.4, respectively. In Figures 7.5 to 7.8 scatterplots of in-situ LST against LST estimated from the algorithms validated are presented. It is worth noting that although some discrepancy in absolute values due to the number of available points may exist between the two sensors, in general a similar performance is observed (i.e. maximum differences in RMSE of 0.5 and 0.6 for nighttime and daytime cases respectively).

Starting with the daytime validation, for MODIS sensor operative MODIS LST algorithms (MODIS-SW and MODIS-DN) provide an uncertainty between 2 K and 3 K. For TERRA platform, no difference is observed between MODIS-SW and MODIS-DN algorithms with RMSE values between 2.7 K and 2.9 K. In this case, the major contribution to the uncertainty comes from the bias with values around 2.3 K in absolute value while the dispersion of the data contributes with 1.4 K to 1.6 K. It is observed that the use of the generalized SW proposed in this study does not provide an improvement of the validation metrics. On the contrary, the simplified version agrees better with the in-situ LST values than the rest of the algorithms. This is mainly because a reduction in the

bias with values ranging from -1.4 to approximately -1.7 K. In this case, the standard deviation has also decreased with a difference of 0.1 K -0.3 K.

For the case of AQUA, in terms of RMSE both the MODIS SW and TES have similar performance (values of 2.3 K for the radiometer and 2.9 K for the pyrgeometer). Nevertheless, TES tends to overestimate the in-situ LST values (bias value of 1.64/1.29 K for radiometer/pyrgeometer) while SW underestimates them (bias value of -1.69/-2.38 K for radiometer/pyrgeometer). In terms of data dispersion, a maximum difference of 0.15 K (pyrgeometer) is obtained for both algorithms. MODIS-DN underperform these algorithms with RMSE of 2.66 K and 3.05 K, mainly because an increase in the bias (absolute value) for both sensors. Considering the comparison of the SW proposed here, both the generalized and the simplified version are able to provide a better performance than MODIS operative LST algorithms (minimum RMSE value is obtained for the simplified SW followed by the generalized version). A reduction in the bias (absolute value) (from 1.4 K to approximately 1.9 K) is the responsible of this better agreement with the in-situ LST values.

For VIIRS sensor, the simplified SW is able to outperform the generalized version with an approximate reduction of 0.4 K-0.5 K in the RMSE. The bias is the main responsible of this fact (absolute reduction of about 1.0 K). It is worth noting that the higher values of standard deviation are obtained for this sensor. It should be said that cloud pixels were screened simply as indicated by MYD21 product and by considering values with an absolute difference of 6 K. In the case of MODIS, they were also filtered by MAIAC cloud mask. Regarding the VIIRS-TES product is providing best performance with a reduction in the RMSE of 0.2 K to around 0.3 K from the SW-simplified. As in the case of MYD21, it gives a positive bias.

For the case of the SLSTR sensor, simplified SW algorithm outperform the generalized split-window because a reduction in the RMSE of 0.6 K to 0.7 K, having the simplified case RMSE values around 2 K. In this case, operative L2 product provides a better agreement with in-situ LST values than the algorithms proposed here. Mainly also because of an absolute reduction in the bias. Nevertheless, it is worth noting that validation was performed over a small number of points (only 20).

Moving to the nighttime validation results, it is observed that RMSE values have generally decrease and range from approximately 0.7 K to 2 K. For TERRA platform, MODIS-SW provides a better performance than MODIS-DN (around 1.2 K-1.3 K of RMSE for SW against 1.6 K-1.7 K for DN). In the case of MODIS-DN, a higher data dispersion is obtained (1.2 K-1.3 K against 0.9 K-1 K of MODIS-SW). In the case of the generalized SW proposed in this study a similar performance to MODIS operative LST algorithms is obtained (a slight RMSE decrease of 0.12 K only for radiometer, for pyrgeometer similar values are obtained). In terms of the bias, an absolute difference of 0.1 K is obtained. In the case of the standard deviation, a slight decrease (around 0.1 K) is observed. The simplified version of the SW is able to outperform the above-mentioned algorithms with RMSE values of 0.7 K - 1.5 K (having MODIS operative algorithms

RMSE values of approximately 1.3 K - 1.7 K). As in the daytime counterpart, an absolute reduction of the bias is obtained.

For AQUA platform. MODIS TES provides the worst performance of all MODIS-SW and MODIS-DN (highest absolute value of bias and highest standard deviation for these three cases for both the radiometer and the pyrgeometer). MODIS-TES provides a 1.8 K (radiometer) and 2.0 K (pyrgeometer) of RMSE, while MODIS-SW has values of 1.2 K -1.3 K and DN values of around 1.3 K-1.7 K. In addition, MODIS-TES tends to overestimate in-situ LST values while MODIS-SW and MODIS-DN tend to underestimate them. Both the generalized and the simplified SW proposed are able to improve the validation metrics (RMSE decrease ranging from 0.3 K to 1.3 K). Although the simplified version still provides a better agreement with in-situ values the deviations from the generalized results in this case is lower than for the daytime case.

For the case of VIIRS sensor, same conclusions as in the daytime case can be observed. Simplified SW is able to outperform the generalized SW version with an approximate reduction of 0.2 K to 0.3 K in the RMSE because a reduction in the bias (absolute value) around 0.3 K. In this case, VIIRS-TES is not able to outperform both generalized and simplified split-window. A difference of 0.7 K to 0.8 K in RMSE is obtained regarding the simplified SW. In the case of the SLSTR sensor, the generalized SW provides the worst performance (RMSE of 1.8 K). In this case, L2 and SW tend to provide similar performance (maximum RMSE difference of 0.07 K). In this case, although the simplified SW reduces the standard deviation the bias of L2 is the lowest of both algorithms.

In Appendix A.3, same validation procedure is repeated in this case considering a maximum difference of 15 K and 3 K. For the case of 15 K, uncertainty increase to values of 2 K to almost 5 K, mainly because of the unscreened clouds (observed in the high standard deviations values retrieved). For the case of 3 K, RMSE decreases to values lower than 2 K. In this case, also the number of available points is reduced. Nevertheless, the same conclusions obtained from this analysis can be derived from the results in the Appendix A.3. A better performance is generally obtained for the simplified version of the SW in comparison to the generalized version of SW, and MODIS operative algorithms. For the case of VIIRS sensor, better daytime performance is still obtained for VIIRS-TES, nevertheless considering a difference of 3 K the discrepancy is reduced. For nighttime case, SW provide better performance than VIIRS-TES. For the case of SLSTR, L2 product still provides a better agreement with in-situ values. It is worth noting here the sensitivity of the algorithms proposed to the proper cloud filtering. The previous conclusions may not completely hold for the 15 K case due to the presence of unscreened clouds that difficult the proper comparison. In this case, MODIS operative algorithms can outperform the algorithms proposed.

Table 7.3. Daytime validation results of the LST algorithms considered in this study at Tambopata in-situ station. Metrics presented correspond to the bias, standard deviation and RMSE values together with the correlation coefficient and the number of points used to perform the validation. Validation is performed separately for the radiometer and pyrgeometer. In bold, it is highlighted the best performing algorithm for each sensor.

Daytime	Radiometer					Pyrgeometer				
	Bias (K)	σ (K)	RMSE (K)	R	N	Bias (K)	σ (K)	RMSE (K)	R	N
TERRA _{MODIS-SW}	-2.32	1.36	2.69	0.91	175	-2.28	1.44	2.70	0.87	135
TERRA _{SW-gen}	-2.31	1.40	2.70	0.91	175	-2.33	1.36	2.71	0.88	135
TERRA _{SW-simpl}	-1.41	1.25	1.88	0.92	175	-1.43	1.27	1.91	0.91	135
TERRA _{MODIS-DN}	-2.30	1.64	2.83	0.88	163	-2.25	1.41	2.65	0.89	122
TERRA _{SW-gen}	-2.54	1.46	2.93	0.90	163	-2.43	1.30	2.75	0.90	122
TERRA _{SW-simpl}	-1.66	1.36	2.15	0.92	163	-1.55	1.25	1.99	0.92	122
AQUA _{MODIS-SW}	-1.69	1.54	2.29	0.86	142	-2.38	1.54	2.84	0.81	112
AQUA _{MODIS-TES}	1.64	1.58	2.31	0.89	142	1.29	1.69	2.92	0.84	112
AQUA _{SW-gen}	-1.05	1.76	2.05	0.83	142	-1.82	1.66	2.46	0.80	112
AQUA _{SW-simpl}	-0.36	1.64	1.68	0.86	142	-1.00	1.61	1.90	0.83	112
AQUA _{MODIS-DN}	-2.00	1.75	2.66	0.85	114	-2.67	1.48	3.05	0.85	94
AQUA _{SW-gen}	-0.85	1.93	2.11	0.83	114	-1.66	1.89	2.52	0.79	94
AQUA _{SW-simpl}	-0.15	1.91	1.91	0.85	114	-0.85	1.91	2.09	0.81	94
VIIRS _{TES}	0.60	2.02	2.11	0.80	364	0.42	2.11	2.16	0.78	218
VIIRS _{SW-gen}	-1.70	2.15	2.74	0.77	364	-2.07	2.19	3.02	0.76	218
VIIRS _{SW-simpl}	-0.67	2.22	2.32	0.78	364	-1.04	2.27	2.50	0.76	218
SLSTR _{L2}	-0.29	1.44	1.47	0.88	20	-0.05	1.47	1.47	0.89	21
SLSTR _{SW-gen}	-2.65	1.10	2.87	0.93	20	-2.36	1.26	2.67	0.91	21
SLSTR _{SW-simpl}	-1.84	1.12	2.15	0.93	20	-1.56	1.32	2.04	0.92	21

Table 7.4. Nighttime validation results of the LST algorithms considered in this study at Tambopata in-situ station. Metrics presented correspond to the bias, standard deviation and RMSE values together with the correlation coefficient and the number of points used to perform the validation. Validation is performed separately for the radiometer and pyrgeometer. In bold, it is highlighted the best performing algorithm for each sensor

Nighttime	Radiometer					Pyrgeometer				
	Bias (K)	σ (K)	RMSE (K)	R	N	Bias (K)	σ (K)	RMSE (K)	R	N
TERRA _{MODIS-SW}	-0.77	0.98	1.25	0.94	210	-1.05	0.93	1.40	0.94	123
TERRA _{SW-gen}	-0.86	0.81	1.18	0.96	210	-1.12	0.79	1.37	0.95	123
TERRA _{SW-simpl}	-0.26	0.72	0.77	0.96	210	-0.50	0.72	0.88	0.96	123
TERRA _{MODIS-DN}	-0.92	1.33	1.61	0.87	239	-1.16	1.24	1.70	0.87	152
TERRA _{SW-gen}	-0.91	1.17	1.49	0.89	239	-1.23	1.15	1.68	0.89	152
TERRA _{SW-simpl}	-0.49	1.21	1.31	0.89	239	-0.81	1.25	1.49	0.88	152
AQUA _{MODIS-SW}	-0.34	1.16	1.21	0.91	191	-0.75	1.07	1.30	0.91	113
AQUA _{MODIS-TES}	1.25	1.79	1.83	0.85	191	0.86	1.86	2.00	0.83	113
AQUA _{SW-gen}	-0.17	0.94	0.96	0.95	191	-0.49	0.77	0.92	0.95	113
AQUA _{SW-simpl}	0.38	0.80	0.89	0.96	191	0.06	0.69	0.70	0.96	113
AQUA _{MODIS-DN}	-0.79	1.55	1.74	0.82	244	-0.77	1.08	1.33	0.90	117
AQUA _{SW-gen}	-0.55	1.46	1.56	0.85	244	-0.60	0.98	1.16	0.91	117
AQUA _{SW-simpl}	-0.06	1.41	1.41	0.86	244	0.00	0.93	0.93	0.93	117
VIIRS _{TES}	0.48	1.59	1.66	0.85	257	0.20	1.7	1.71	0.84	151
VIIRS _{SW-gen}	-0.59	0.96	1.12	0.94	257	-0.89	0.85	1.24	0.93	151
VIIRS _{SW-simpl}	-0.26	0.84	0.88	0.95	257	-0.55	0.81	0.98	0.94	151
SLSTR _{L2}	-0.08	1.33	1.34	0.88	21	-0.20	1.25	1.27	0.88	23
SLSTR _{SW-gen}	-1.18	1.34	1.79	0.88	21	-1.32	1.26	1.83	0.88	23
SLSTR _{SW-simpl}	-0.46	1.23	1.31	0.90	21	-0.60	1.19	1.34	0.90	23

7. - LST retrieval algorithm adapted to the Amazon evergreen forests

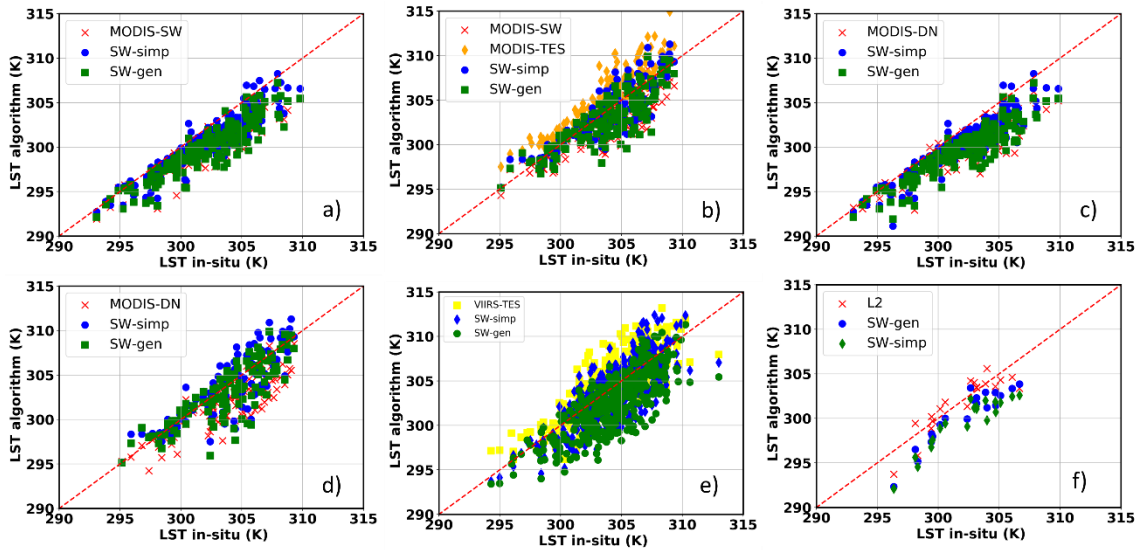


Figure 7.5. Scatterplots in in-situ radiometer LST against estimated LST for the daytime case. MODIS-SW, MODIS-TES and MODIS-DN refers to the LST as extracted from the MXD11_L2, MYD21_L2 product and MXD11C1 product. SW-simp and SW-gen refers to the simplified and generalized SW proposed. a) TERRA platform (1km) , b) AQUA platform (1km), c) TERRA platform (5km), d) AQUA platform (1km), e) VIIRS sensor and f) SLSTR sensor.

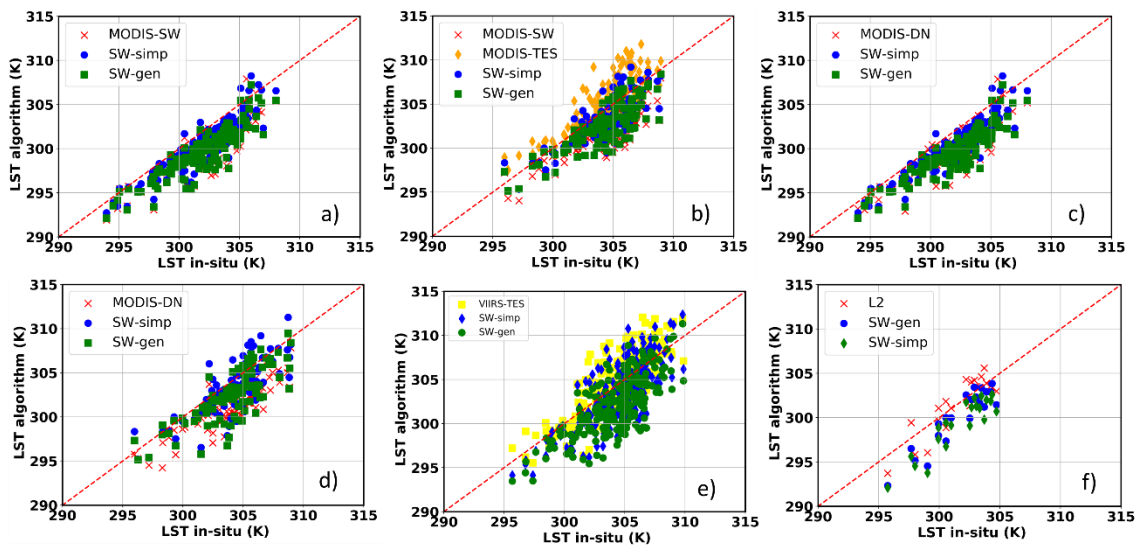


Figure 7.6. Scatterplots in in-situ pyrgeometer LST against estimated LST for the daytime case. MODIS-SW, MODIS-TES and MODIS-DN refers to the LST as extracted from the MXD11_L2, MYD21_L2 product and MXD11C1 product. SW-simp and SW-gen refers to the simplified and generalized SW proposed. a) TERRA platform (1km) , b) AQUA platform (1km), c) TERRA platform (5km), d) AQUA platform (1km), e) VIIRS sensor and f) SLSTR sensor.

7. - LST retrieval algorithm adapted to the Amazon evergreen forests

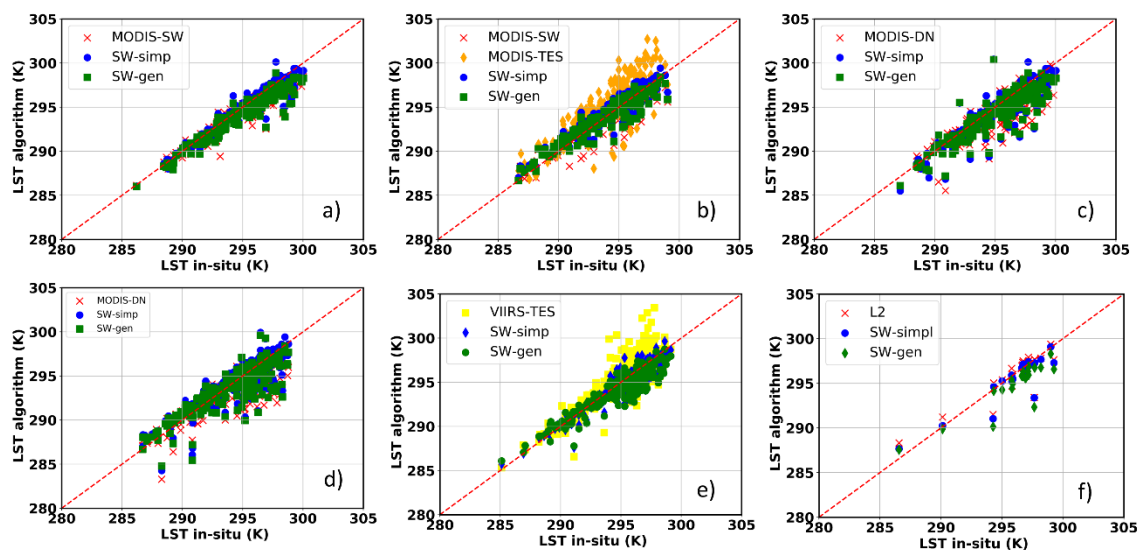


Figure 7.7. Scatterplots in in-situ radiometer LST against estimated LST for the nighttime case. MODIS-SW, MODIS-TES and MODIS-DN refers to the LST as extracted from the MXD11_L2, MYD21_L2 product and MXD11C1 product. SW-simp and SW-gen refers to the simplified and generalized SW proposed. a) TERRA platform (1km), b) AQUA platform (1km), c) TERRA platform (5km), d) AQUA platform (1km), e) VIIRS sensor and f) SLSTR sensor.

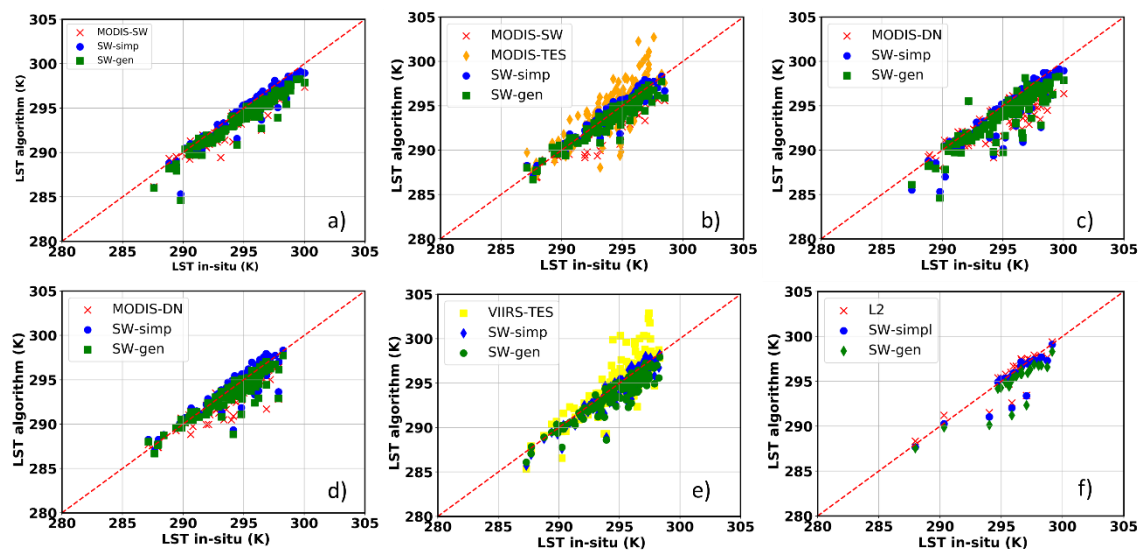


Figure 7.8. Scatterplots in in-situ radiometer LST against estimated LST for the nighttime case. MODIS-SW, MODIS-TES and MODIS-DN refers to the LST as extracted from the MXD11_L2, MYD21_L2 product and MXD11C1 product. SW-simp and SW-gen refers to the simplified and generalized SW proposed. a) TERRA platform (1km), b) AQUA platform (1km), c) TERRA platform (5km), d) AQUA platform (1km), e) VIIRS sensor and f) SLSTR sensor.

7.3. - R-based validation

For the particular case of MODIS sensor daytime case, validation was extended to a set of 100 pixels randomly selected within the study area. R-based validation method, which does not require in situ data (Wan & Li, 2008) was used for this purpose. This validation was limited to MODIS sensor because of the huge amount of data needed in order to extend to other points. The MODIS brightness temperature of bands 31 and 32 can be obtained from the MXDTBGA tile product, thus facilitating the associated processing. In addition MODIS-SW and MODIS-DN estimates can be obtained from the MXD11A1 (at 1km resolution) and MXD11C1 (at 5 km resolution). Validation was focused on the simplified SW, MODIS-SW and MODIS day-night algorithm.

The optimal threshold value for T_{b32} is selected so that the difference between the simulated LSTR and the actual LST lies within $\pm 1K$. Wan & Li (2008) proposed a threshold of $\pm 0.3 K$ for MODIS data and Hulley et al. (2012) showed that a threshold of $\pm 0.5 K$ resulted in a good balance between the number of profiles and the accepted accuracy. Nevertheless, taking into account that we dispose of in-situ LST measurement at Tambopata site, the threshold can be derived by direct comparison with these values. According to the results presented in Figure 7.9, the threshold values $-0.1K < (T_{12_{obs}} - T_{12_{sim}}) < 0.3K$ provides a difference of $\pm 1K$ in the difference between the R-based temperature and the LST in situ. However, taking into account the limitations in the number of clear-sky pixels imposed by the study region a final threshold of $-0.2K < (T_{12_{obs}} - T_{12_{sim}}) < 0.4K$ was considered in order to increase the number of points. This recalculated threshold values provide a difference of less than $\pm 2K$ (Figure 7.9).

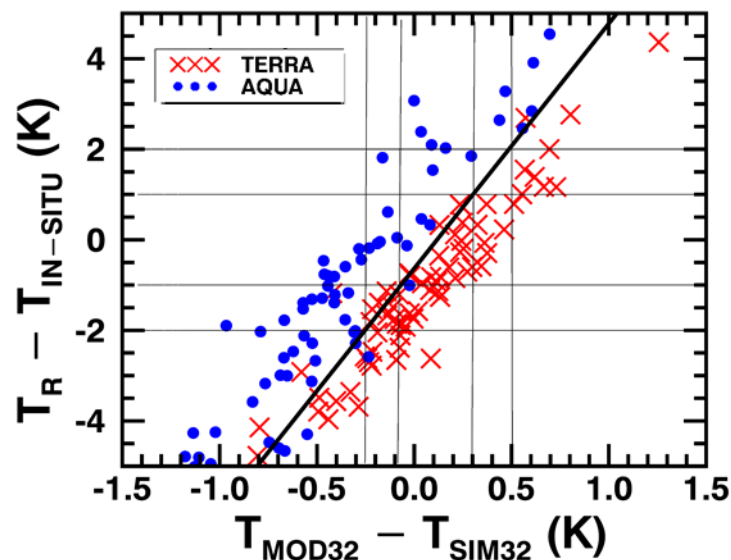


Figure 7.9. Determination of the optimal threshold value for ΔT_{b32} ($T_{MOD32} - T_{SIM32}$). ΔT_{b32} is represented against the difference between the T_R (derived from the R-based method) and $T_{IN-SITU}$ as derived in the section 5.1.

In addition, in Table 7.5, the comparison of in-situ LST as derived from the radiometers and as derived from the R-based method (i.e. by inverting the radiative transfer equation). As it can be seen, the bias metric together with standard deviation and the RMSE are within $\pm 2\text{K}$. LST as derived from the R-based method derived can be assumed as a source of in-situ data with a maximum uncertainty of 1.85 K.

Table 7.5. Error metrics derived from the comparison of in situ LST against reference LST obtained with the R-based method over the Tambopata test site considering a threshold of $-0.2\text{K} < \Delta T_{b32} < 0.4\text{K}$. RMSE: Root Mean Square Error, MAE: N: number of data points.

	Bias (K)	σ (K)	RMSE (K)	N
TERRA 1km	-1.08	1.16	1.58	44
AQUA 1km	0.99	1.18	1.54	15
TERRA 5 km	-1.37	1.23	1.85	38
AQUA 5 km	0.73	1.30	1.49	9

In Figure 7.10, R-based validation results are presented using scatterplots. In addition, bias $\pm \sigma$, together with the correlation coefficient (R) are displayed. The number of available points and the number of spatial points having data after applying the specified threshold are also provided. It is observed that the proposed LST algorithm shows lower values of bias and standard deviation in comparison to MODIS-SW (Figure 7.10 (a)(b)) and MODIS-DN (Figure 7.10 (c)(d)). The difference in terms of RMSE (MODIS operative algorithm minus proposed SW algorithm) is approximately of 0.9 K, 1.7 K, 0.7 K and 1.5 K for MODIS-SW TERRA, MODIS-SW AQUA, MODIS-DN TERRA and MODIS-DN AQUA cases. In spite the reduction of the initial spatial reference points, the number of values is still elevated in order to provide a reliable validation dataset.

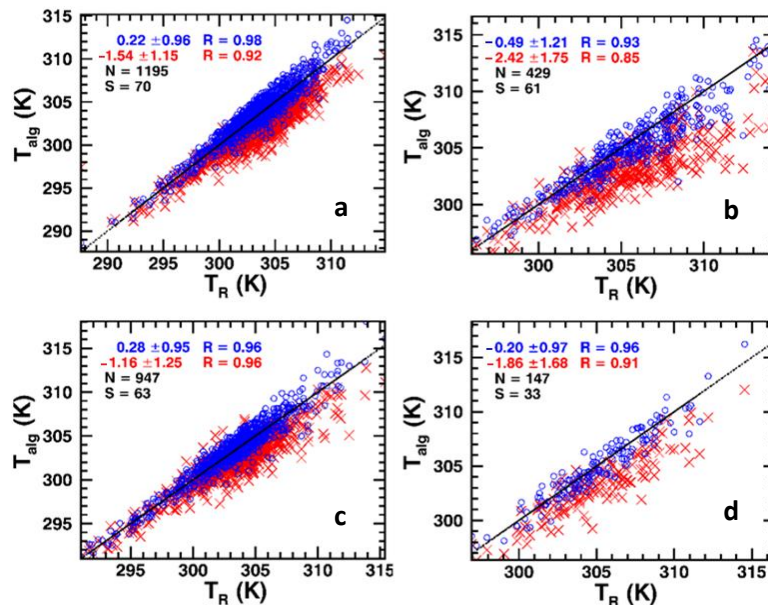


Figure 7.10. Simulated R-based (T_R) against estimated temperature (T_{alg}). Red cross refers to MODIS operative algorithms. Blue circle refers to the proposed SW algorithm. a) TERRA 1km, b) AQUA 1km, c) TERRA 5 km and d) AQUA 5 km. MODIS 1km algorithm is MODIS-SW and MODIS 5km algorithm is

MODIS-DN. Results include mean \pm bias, correlation coefficient, N: total number of points and S: number of spatial points with data. The line 1:1 is also represented.

7.4. - Spatial patterns

Considering the results presented in Figures 7.11 and 7.12, it can be seen that the difference revealed in LST patterns between MOD35 and QC/MAIAC arise from the correction of cloud-contamination effect. QC and MAIAC spatial patterns are enhanced after removing the alteration (colder-than-true) of temperature introduced by clouds. The use of an additional cloud filtering however considerably reduces the number of available clear-sky-days (Figures 7.11-7.12). This becomes especially evident for the northeast region for TERRA JFM/AJM, and AQUA QC JFM where after screening clouds it is produced a lack of available data. MOD35 provides more cloud-free pixels than QC/MAIAC (Figure 7.11). MAIAC however it is able to provide more cloud-free pixels than QC for AQUA (Figures 7.11-7.12) and also for TERRA (southeast region of AJM/JAS). These results agree well with previous studies (Hilker et al., 2012) in which MAIAC was shown to provide about 20-80% more cloud-free pixels depending on season than MYD09 surface reflectance product when applying all the quality control checks.

For the comparison of QC and MAIAC we see that MAIAC reproduces QC patterns. In this case, however the discrepancies due from an enhancement of some region by the LST product presented here cannot be properly addressed due to the low number of available points. However, when comparing TERRA (equatorial crossing time 10:30 am) and AQUA (equatorial crossing time 1:30 pm) results we see that MAIAC spatial patterns agree well. A spatial warming located in the northern region predominantly during JFM/AJM and a more widespread warming for JAS and OND is observed for both TERRA and AQUA.

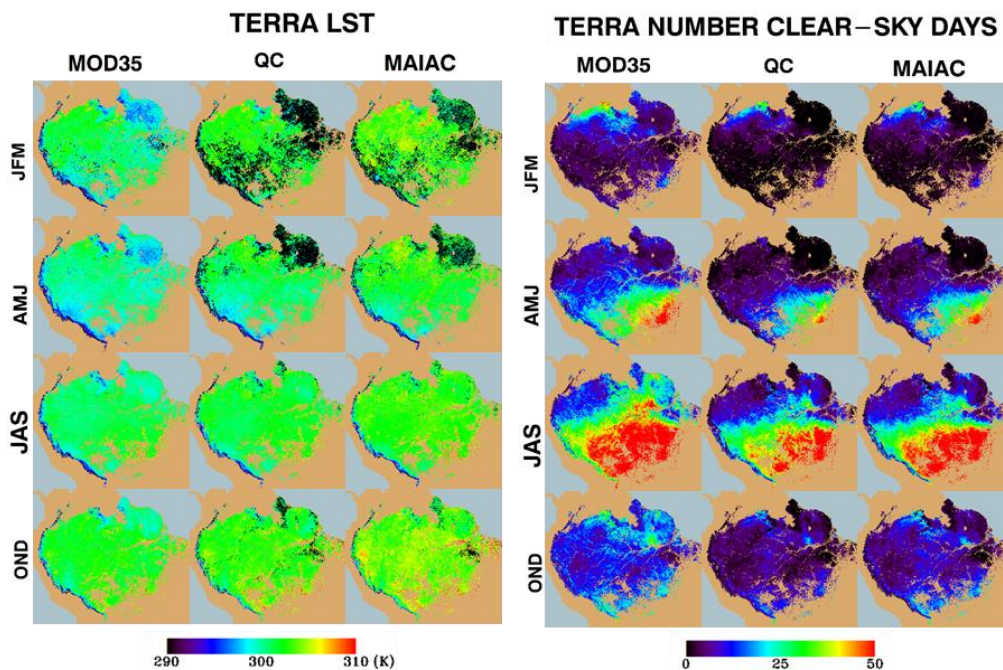


Figure 7.11. Spatial patterns of LST (left image) and Number of clear sky days (right image) for TERRA. For every panel the results are shown using rows as seasons (JFM, AMJ, JAS and OND) and columns as cloud masks filtering (MOD35, QC and MAIAC).

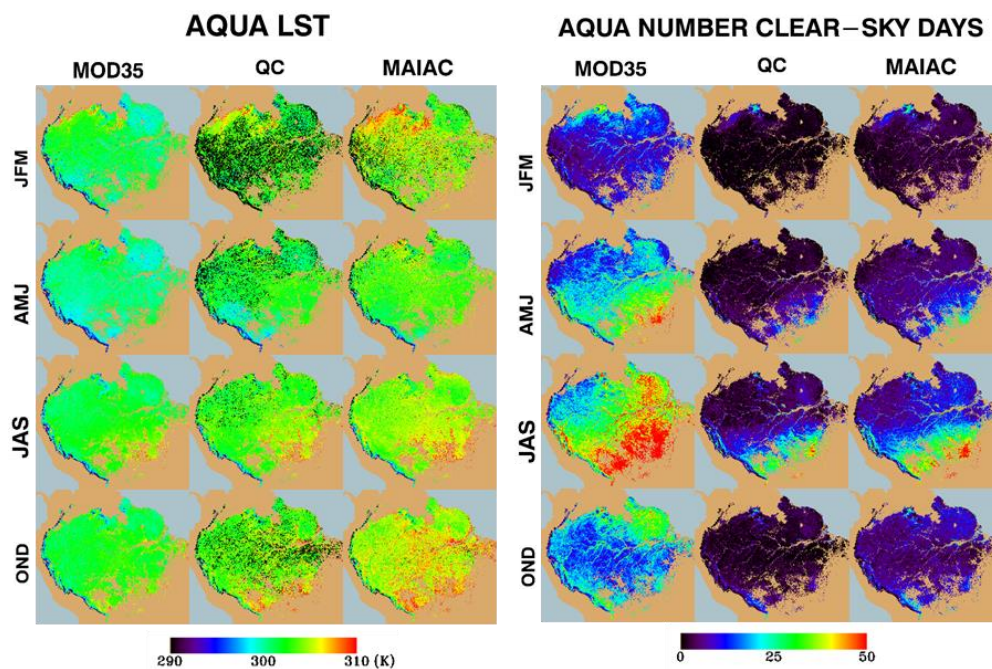


Figure 7.12. Spatial patterns of LST (left image) and Number of clear sky days (right image) for AQUA. For every panel the results are shown using rows as seasons (JFM, AMJ, JAS and OND) and columns as cloud masks filtering (MOD35, QC and MAIAC).

In Figure 7.13 seasonally LST and number of clear-sky days is presented for VIIRS. For the implementation of these comparison, brightness temperature of bands 15 and 16 were derived from the swath product NPP_VMAES_L1 (ladsweb.nascom.nasa.gov). Additionally, VNP35_L2 was considered for cloud masking. Obtained by heritage of MOD35_L2 product (MOD35 cloud mask) only pixels consider as confident clear were used for the LST retrieval. Considering VIIRS and MAIAC AQUA results having both an equatorial crossing time of 1:30 pm we see that VIIRS reproduces AQUA spatial patterns. Additionally, VIIRS number of clear-sky days' spatial pattern is similar to MOD35.

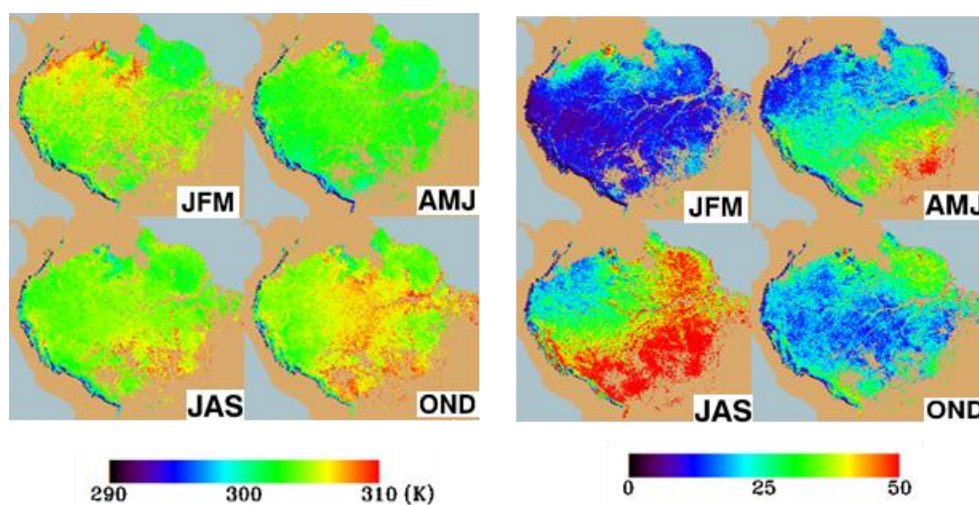


Figure 7.13. Spatial patterns of LST (left image) and Number of clear sky days (right image) for VIIRS sensor. Only confident clear pixels were considered for LST retrieval. For every panel the results are shown: JFM, AMJ, JAS and OND.

7.5. - Discussion

From the simulated database validation, it was observed that the inclusion of the emissivity and water vapour contributions in the SW (i.e. generalized SW) do not result in an improvement in the accuracy of the estimated LST. In fact, considering only contributions from the brightness temperature (i.e. the simplified SW) reduced the retrieved RMSE up to 0.4 K (Table 7.2). In addition, it shows more stability at large viewing angles and water vapour conditions than the generalized SW.

From the T-based validation, algorithms of three different sensors were validated: MODIS, VIIRS and SLSTR. For MODIS sensor, it was observed that amongst the MODIS algorithms considered DN algorithm provided the worst performance for daytime conditions (absolute deviations of the RMSE up to approximately 0.4 K). This was also true for the nighttime case but only for TERRA platform. For AQUA, MODIS-TES gives the highest RMSE values (up to 0.6 K of difference with the other MODIS algorithms). For daytime, it has a similar performance to MODIS-SW. Nevertheless, it

tends to tends to overestimate the in-situ LST values (positive bias) while MODIS-SW tends to underestimate them (negative bias). The in-situ location is characterized by being vegetation in an area of wet atmospheric conditions. Precisely, at surfaces with low spectral contrast emissivity (e.g water, snow, vegetation) and under hot and wet atmospheric conditions, some reports have exhibited that significant errors in the LST and LSE may arise for TES algorithm. (Coll et al., 2007; Hulley & Hook, 2009, 2011). Considering the SW algorithms proposed in this study, same conclusions obtained in the simulated database section can be applied to this section. The simplified version always outperforms the generalized version (at nighttime however, the difference is reduced). In addition, it also outperforms the rest of MODIS operative algorithms. For the case of the generalized version, there is not always an increase in the performance when comparing to MODIS algorithms. The best performance of the proposed simplified algorithm can be attributed to the fact that it was retrieved from a specific simulated database over the region. It is expected that this database is able to better represent the atmospheric conditions that a global database, such as the one used in MODIS LST retrieval.

For VIIRS sensor, it was show that the simplified SW algorithm is able to improve the generalized SW with differences up to 0.5 K in the RMSE. In addition, it outperforms VIIRS-TES nighttime case with a reduction of 0.7 K - 0.8 K in the RMSE. For daytime case, nevertheless VIIRS-TES agrees better with the in-situ LST observations. For the case of SLSTR sensor, L2 product provides a better agreement with in-situ observations that the algorithm proposed. Nevertheless, only a first assessment is presented with the validation being limited to a restricted number of points.

At this point, it is worth also mentioning the impact of a proper cloud screening in the LST validation. In MODIS and VIIRS sensors clouds were screened using operative cloud masks. Nevertheless, this could not completely eliminate the presence of unscreened clouds. In order to overcome this issue, only pixels that deviate a specified amount from in-situ LST measurements were used for validation. Three different quantities were considered: 3 K, 6 K and 15 K. In this section, 6K case validation results were presented. 3 K and 15 K are in the Appendix A.3. In the 15 K (Table A.3.1 and A.3.2), the presence of clouds is evident due to the high standard deviations observed (2.5 K to 4 K). Therefore, a more restrictive filtering is needed. A difference in 6 K is assumed to be valid. It represents a higher 3σ distance from the maximum LST error as derived from the sensitivity analysis ($1.695 \times 3 = 5.085$). In addition, only pixels deviating a maximum amount for all the algorithms considered are used. Therefore, the algorithms are compared over the same performance range. For the case of 3 K difference (Table A.3.3 and A.3.4) , results were retrieved in order to see the effect of a more restrictive filtering. For this case, same conclusions obtained for 6 K difference case hold true. For the case of 15 K, although generally same behaviour is observed there are cases where MODIS, VIIRS and SLSTR operative algorithms outperform the SW proposed. However, in these cases it is evident the presence of clouds (σ values of 3 and 4 K).

R-based method was shown to provide an alternative in-situ validation. Associated uncertainty was within the limits of 2 K. Same conclusions for MODIS sensor are

obtained using this method. The simplified SW proposed reduce the uncertainty in LST estimation (RMSE) in 0.7 to 1.7 K in comparison to MODIS operative algorithms.

From the spatial patterns comparison, it was seen that the difference revealed in LST patterns between MOD35 and QC/MAIAC arise from the correction of cloud-contamination effect. QC and MAIAC spatial patterns are enhanced after removing the alteration (colder-than-true) of temperature introduced by clouds. The cloud masking is especially important for the generation of monthly or seasonal means of LST, as usually considered in climate related studies. When cloud detection is relaxed more clear sky pixels are available within a month, but the monthly mean may be biased because of the consideration of LST values for cloudy pixels in the computation of the mean value. In contrast, a very restrictive cloud detection leads to a decrease in the number of clear sky pixels, which jeopardizes the computation of a monthly mean over areas with high cloud cover occurrence.

8.- INTERCOMPARISON OF REMOTE-SENSING BASED EVAPOTRANSPIRATION ALGORITHMS

8.- Intercomparison of remote-sensing based evapotranspiration algorithms

8.1. - Forcing scenario I

8.1.1. Algorithm validation

In scenario I, model performance for PT-JPL, PM-Mu, SEBS/SEBS-GF and LSASAF evapotranspiration algorithms was evaluated by comparing model estimates forced with in-situ data against in-situ ET observations. In Figure 8.1, the performance of the models for the totality of the stations is shown. Metrics used for validation are presented for both the uncorrected and corrected (Bowen Ratio and Energy residual) case. It is worth noting at this point that some discrepancy between metrics derived from these corrections is expected.

Models considered perform at R values ranging from 0.5 to 0.9. S values range from 0.7 to 0.9 and RMSE values lie between 0.55-1.25 mm/day. Models tend to provide a similar performance, nevertheless PT-JPL provides the highest R values range (0.65-0.88) in comparison to PM-Mu (0.56-0.74), SEBS (0.56-0.77), SEBS-GF (0.58-0.76) and LSASAF (0.53 - 0.69).

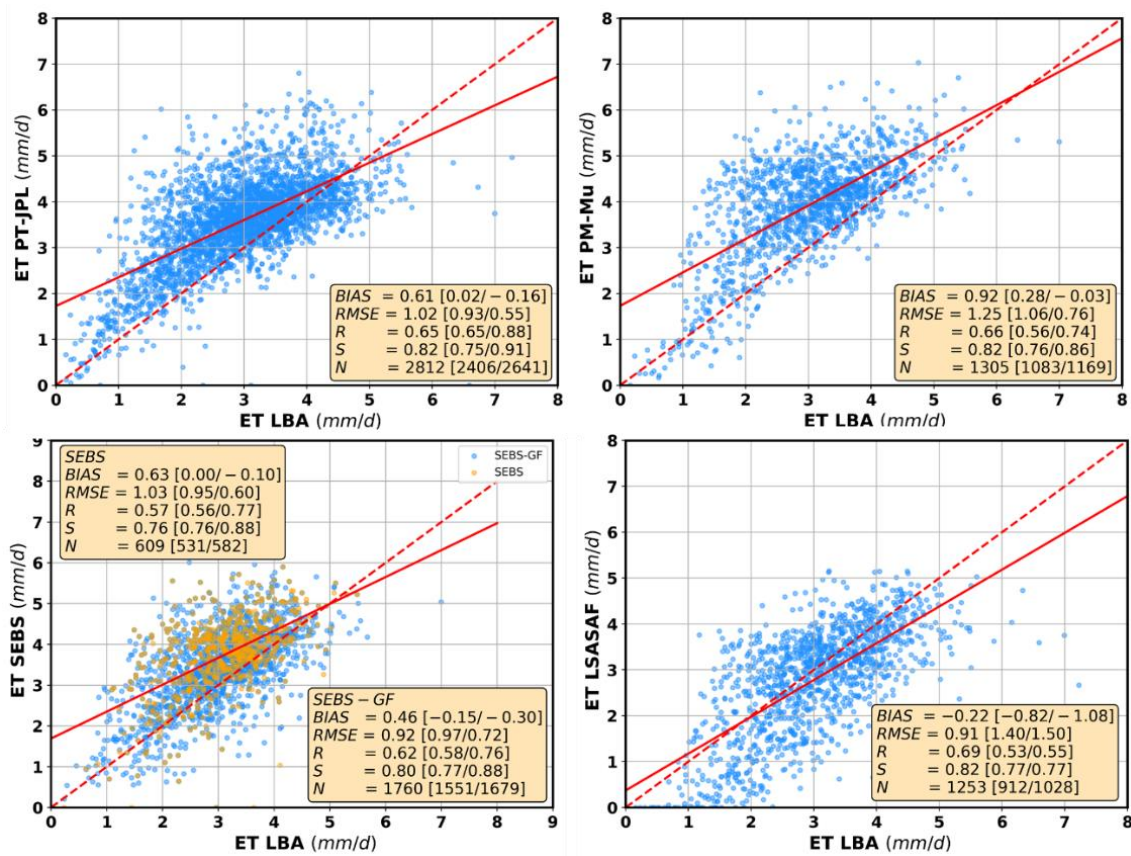


Figure 8.1. Scatterplots of model ET estimate against in-situ ET uncorrected observations. Bias, RMSE, R, and S metrics were calculated considering observations from all the stations. Metrics derived considering corrected ET values (Bowen Ratio/Energy Residual) are presented between parenthesis.

Best performance amongst models is obtained for PT-JPL (RMSE = 0.55 mm/day, R = 0.88 and S = 0.91) followed by SEBS (similar RMSE and S but lower R), SEBS-GF and PM-Mu. SEBS model especially suffers from the lack of input LST observations due to the continuous cloud cover of the region (minimum N value). On the contrary, PT-JPL being the least-data demanding is the less prone to suffer from the lack of input data issue (maximum N value). The gap-filling technique used is shown to alleviate in part this problem, nevertheless it is observed that SEBS-GF tends to underestimate SEBS values. Worst performance is obtained for LSASAF (RMSE = 1.50 mm/day, R = 0.55 and S = 0.77). In exception of LSASAF, best agreement between in-situ observations and models estimates is found when considering corrected ET measurements, especially for the Energy Residual correction (i.e. an increase in R and S values and a decrease in RMSE). For PT-JPL, PM-Mu, SEBS and SEBS-GF overestimation is generally observed for the uncorrected case. Bias values are decreased when considering ET corrected values. LSASAF generally tends to underestimate in-situ ET observations for both the uncorrected and corrected cases.

Apart from validating model ET estimates, additional fluxes provided by models themselves were also evaluated. This is the case of Rn for PM-Mu, Rn and H for LSASAF and H and λE for SEBS (Figure 8.2). For SEBS, due to data scarcity Rn was directed extracted from in-situ observations. The scatterplots for calculated net radiation (daytime and nighttime) for PM-Mu are shown (Figure 8.2 (a)(b)). For daytime conditions, PM-Mu tends to underestimate in-situ Rn, nevertheless a good agreement is found between the two datasets (R value of 0.95). For nighttime conditions, PM-Mu Rn estimates do not correlate with observed Rn. They are centered about a point of -60 W/m^2 while in-situ Rn range from -70 to 10 W/m^2 . It is worth noting here that considering these nighttime values in the calculation of ET estimates will introduce an important negative deviation, that is not physically justified. Therefore, for the nighttime values calculated ET values were discarded in the calculation.

For the case of LSASAF, the scatterplots of Rn and H are shown in Figure 8.2 (c)(d). It is worth remembering here that for running LSASAF model, G flux was discarded. Available in-situ daytime G flux data mean values lie within the range of -1 to 3 W/m^2 while calculated daytime LSASAF G flux provided values between 20 to 30 W/m^2 . From a preliminary analysis, it was concluded that neglecting these G flux values provide more accurate validation results than considering calculated G. In Figure 8.2(c)(d), it is observed that LSASAF tends to underestimate in-situ Rn and overestimate in-situ H. Rn has a small negative bias of approximately 8 W/m^2 , while for H a positive bias ranging from 50 to 70 W/m^2 is obtained. Taking into account that in this model the λE is derived as a residual from the energy balance, these biases (in particular H) will directly affect the accuracy of λE (and ET) estimates. In particular, a bias of 50 to 70 W/m^2 is equivalent to 0.9 - 1.2 mm/day .

Validation of instantaneous H and LE fluxes for both TERRA and AQUA are shown in Figure 8.2 (e)(f)(g)(h). SEBS tends to underestimate H flux for both TERRA and AQUA, and therefore tends to overestimate λE flux. Generally, (in exception of H flux for TERRA) a better agreement with in-situ results is obtained using corrected values than using non-corrected values. Considering a representative value of 350 W/m^2 and 500 W/m^2 for TERRA and AQUA hourly R_n values, and a representative value of 200 W/m^2 and 350 W/m^2 for LE flux and assuming a deviation of 50 W/m^2 (RMSE ET-corrected values) a maximum deviation of 0.15 and 0.1 is obtained in the evaporative fraction, which will be translated into the daily ET estimates.

Results from individual stations are shown in Table 8.1 and Figure 8.3. Metric values in Table 8.1 refer to the mean value \pm standard deviation of the metrics derived from the uncorrected case and Bowen Ratio and Energy Residual case. In the case of RMSE, mean value goes from 0.65 ± 0.14 (K67 PT-JPL) to 1.52 ± 0.41 (LSASAF RJA). For R metric mean values lie between 0.40 ± 0.15 (SEBS RJA) to 0.83 ± 0.09 (PT-JPL K34). In the case of the Taylor skill score S ranges from 0.64 ± 0.04 (PM-Mu K67) to 0.90 ± 0.03 (LSASAF K34). Generally, better model performance is obtained for K34, K67 and K83. In the case of RJA and CAX, each model provides the highest RMSE value and lowest R value (for the case of S metric no particular behaviour is observed). This observed discrepancy amongst stations is more accused for the PM-Mu, SEBS and LSASAF models. An additional aspect to consider when analyzing these values is the number of available points from which the metric was calculated. For the case of CAX station the lowest number of points (less than 50) is provided. For the bias metric, it is observed that the observed underestimation of LSASAF (Figure 8.2) mainly results from the negative bias in K34 and RJA station. In addition, for PM-Mu and SEBS a positive bias is obtained for all the stations. RJA and CAX stations have a higher variability between metrics (standard deviation of 0.6 and 1.1) than the rest of the stations.

Individual station validation results are also visualized using Taylor Diagrams in Figure 8.3. Models are represented by colors and evapotranspiration corrections by shapes (triangle – ET (uncorrected ET values), square– BR (Bowen Ratio) and circle – ER (Energy Residual)). Models generally perform at R values ranging from 0.5 to 0.9 and CRMSD less than 1. For CAX and RJA maximum R is obtained at 0.8. In addition, for RJA minimum R value is situated at 0.2 and CRMSD can be greater than 1. Considering corrected ET values PT-JPL outperform the rest of the models (i.e. the blue square and the blue circle are closer to the observation point than the rest of the squares and circles respectively). For the uncorrected case there is no model that provides a superior performance for all the stations.

8.- Intercomparison of remote-sensing based evapotranspiration algorithms

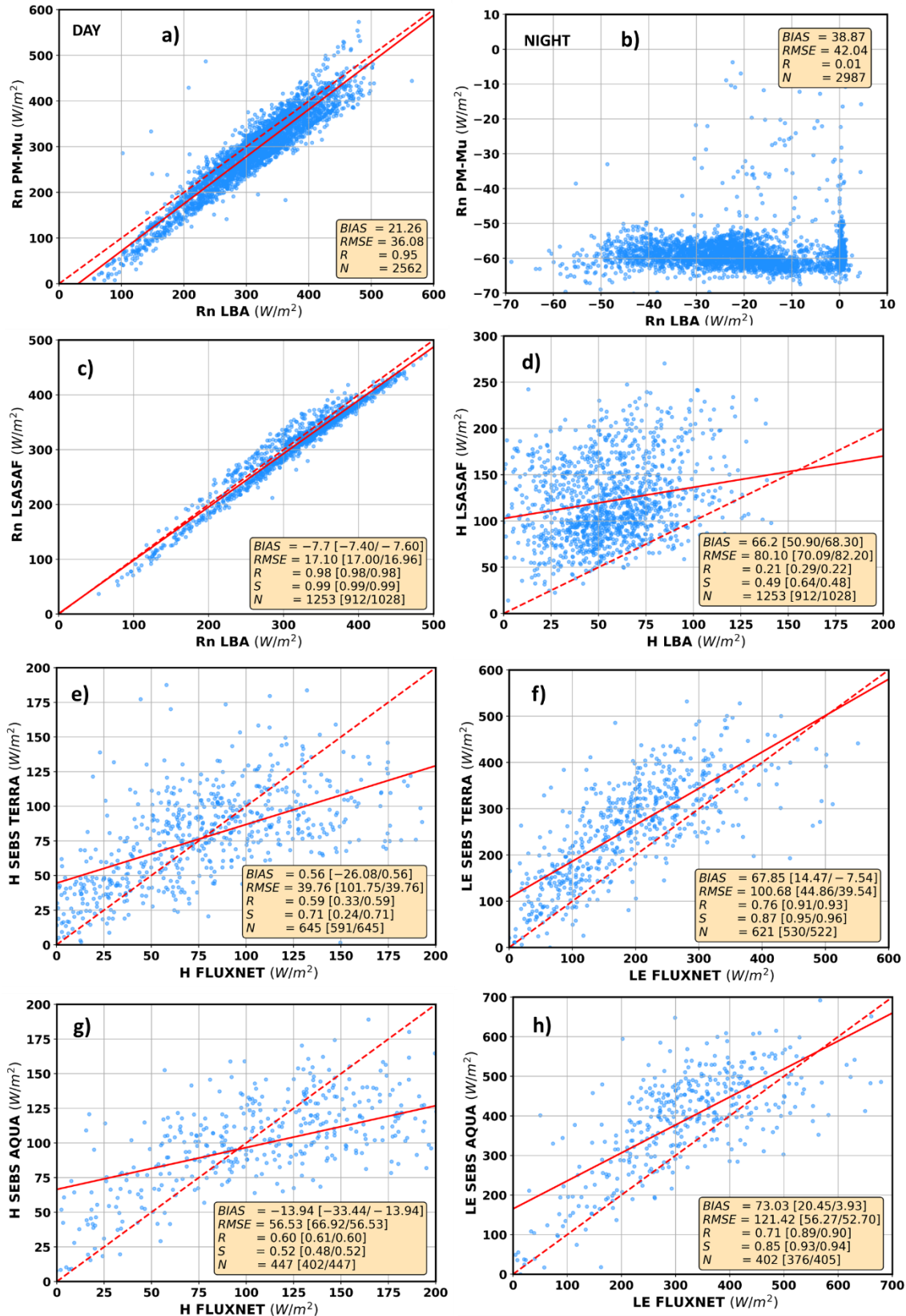


Figure 8.2. Validation of other fluxes provided by the ET models considered: a) daytime PM-Mu Rn b) nighttime PM-Mu Rn c) daytime LSASAF Rn, d) daytime LSASAF H e) SEBS H for TERRA platform, f) SEBS LE for TERRA platform, g) SEBS H for AQUA platform, h) SEBS LE for AQUA platform. Bias, RMSE, R, and S metrics were calculated considering observations from all the stations. Metrics derived considering corrected ET values (Bowen Ratio/Energy Residual) are presented between parenthesis.

8.- Intercomparison of remote-sensing based evapotranspiration algorithms

Table 8.1. Bias, RMSE, correlation coefficient (R), Taylor skill score (S) metrics together with the number of available points (N) for the individual station validation. Values refer to the mean value \pm standard deviation of the validation values from the uncorrected case and the Bowen Ratio and Energy Residual case.

BIAS (mm/d)					
	PT-JPL	PM-Mu	SEBS	SEBS-GF	LSASAF
K34	0.28 \pm 0.30	0.26 \pm 0.44	0.32 \pm 0.33	0.22 \pm 0.33	-1.00 \pm 0.42
K67	-0.02 \pm 0.41	0.11 \pm 0.45	0.00 \pm 0.41	-0.21 \pm 0.42	---
K83	-0.28 \pm 0.25	0.36 \pm 0.14	0.08 \pm 0.26	-0.11 \pm 0.25	-0.16 \pm 0.21
RJA	0.60 \pm 0.64	0.59 \pm 0.63	0.60 \pm 0.62	0.28 \pm 0.60	-0.98 \pm 0.62
CAX	0.33 \pm 1.18	0.10 \pm 1.16	---	---	---
RMSE (mm/d)					
	PT-JPL	PM-Mu	SEBS	SEBS-GF	LSASAF
K34	0.76 \pm 0.24	0.94 \pm 0.16	0.84 \pm 0.23	0.90 \pm 0.13	1.27 \pm 0.36
K67	0.65 \pm 0.14	0.69 \pm 0.22	0.68 \pm 0.18	0.77 \pm 0.10	---
K83	0.73 \pm 0.27	0.74 \pm 0.13	0.77 \pm 0.19	0.75 \pm 0.23	0.75 \pm 0.20
RJA	1.09 \pm 0.41	1.23 \pm 0.34	1.28 \pm 0.36	1.08 \pm 0.23	1.52 \pm 0.41
CAX	1.14 \pm 0.63	1.23 \pm 0.39	---	---	---
Correlation coefficient (R)					
	PT-JPL	PM-Mu	SEBS	SEBS-GF	LSASAF
K34	0.83 \pm 0.09	0.81 \pm 0.08	0.63 \pm 0.12	0.60 \pm 0.05	0.82 \pm 0.07
K67	0.80 \pm 0.10	0.59 \pm 0.19	0.79 \pm 0.12	0.76 \pm 0.09	---
K83	0.72 \pm 0.11	0.71 \pm 0.09	0.65 \pm 0.11	0.68 \pm 0.09	0.64 \pm 0.08
RJA	0.68 \pm 0.12	0.59 \pm 0.12	0.40 \pm 0.15	0.60 \pm 0.12	0.48 \pm 0.11
CAX	0.70 \pm 0.10	0.53 \pm 0.09	---	---	---
Taylor skill score (S)					
	PT-JPL	PM-Mu	SEBS	SEBS-GF	LSASAF
K34	0.89 \pm 0.06	0.89 \pm 0.03	0.78 \pm 0.07	0.77 \pm 0.04	0.90 \pm 0.03
K67	0.86 \pm 0.08	0.60 \pm 0.21	0.87 \pm 0.08	0.87 \pm 0.06	---
K83	0.73 \pm 0.16	0.76 \pm 0.11	0.80 \pm 0.08	0.79 \pm 0.11	0.73 \pm 0.12
RJA	0.82 \pm 0.07	0.78 \pm 0.06	0.69 \pm 0.08	0.79 \pm 0.07	0.73 \pm 0.05
CAX	0.74 \pm 0.01	0.64 \pm 0.04	---	---	---
Number of points (N)					
	PT-JPL	PM-Mu	SEBS	SEBS-GF	LSASAF
K34	733	200	91	295	164
K67	723	179	225	623	---
K83	439	214	130	319	300
RJA	453	426	85	314	448
CAX	41	44	---	---	---

8.- Intercomparison of remote-sensing based evapotranspiration algorithms

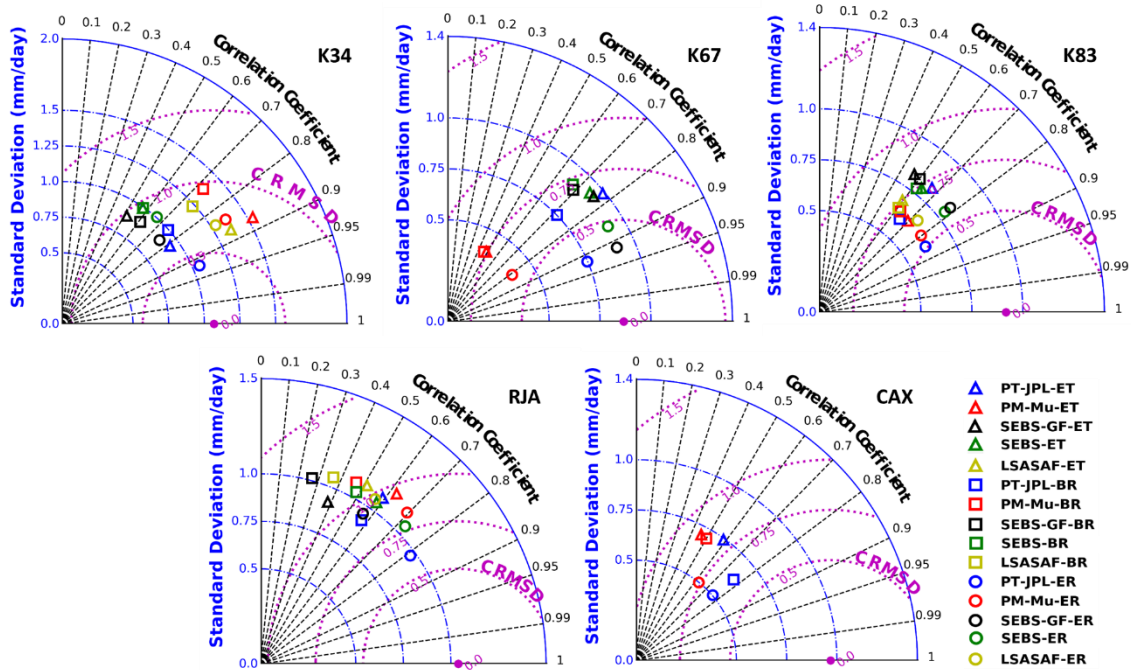


Figure 8.3. Taylor diagrams for the LBA in-situ stations. Models are represented by colors and evapotranspiration corrections by shapes (triangle – ET (uncorrected ET values), square – BR (Bowen Ratio) and circle – ER (Energy Residual)).

8.1.2. Temporal evolution

The temporal evolution of the models is compared considering time series of monthly mean values (Figure 8.4). Results using data from all the stations and individual station data are both displayed. Values were calculated considering at least 15 points for each month. Results for CAX station is not displayed as it didn't have the minimum number of available points. In-situ observations are also displayed. Variability in these measurements due to the energy balance closure issue is represented by the shadowed area. The lower, intermediate and upper limit indicate uncorrected, BR and ER correction ET observations respectively. Regarding the discrepancy between these values, it is observed that a greater deviation is observed between uncorrected and corrected values than between corrections.

Focusing on results from all the stations, models generally follow in-situ ET temporal pattern with maximum values in September. LSASAF peaks in August, nevertheless it is worth noting that K67 and CAX were not able to be included (contrary to the rest of the models). Along the year, PT-JPL, SEBS and SEBS-GF always lie in the determined range of in-situ ET. PT-JPL and SEBS being closer to the corrected rank than SEBS-GF which tends to underestimate SEBS estimates. LSASAF clearly underestimates in-situ ET values. From May to October the deviation is reduced to the increase in ET estimates. In this same period overestimation is found for PM-Mu. Amongst the models considered the major coincidence is found for PT-JPL and SEBS. Nevertheless, due to the lack of

8.- Intercomparison of remote-sensing based evapotranspiration algorithms

LST input data a complete year of estimates is not reached for SEBS (July-October providing the maximum number of observations).

Focusing on individual stations results, same previous conclusions for PT-JPL, SEBS and SEBS-GF can be derived. In addition, same overestimation and underestimation for PM-Mu and LSASAF is observed. Models generally follow in-situ temporal pattern. Nevertheless, for the RJA station PM-Mu and LSASAF are not able to reflect the decrease in the observed ET for the months of May-October. PT-JPL better reflects this pattern and thus it provides the best performance.

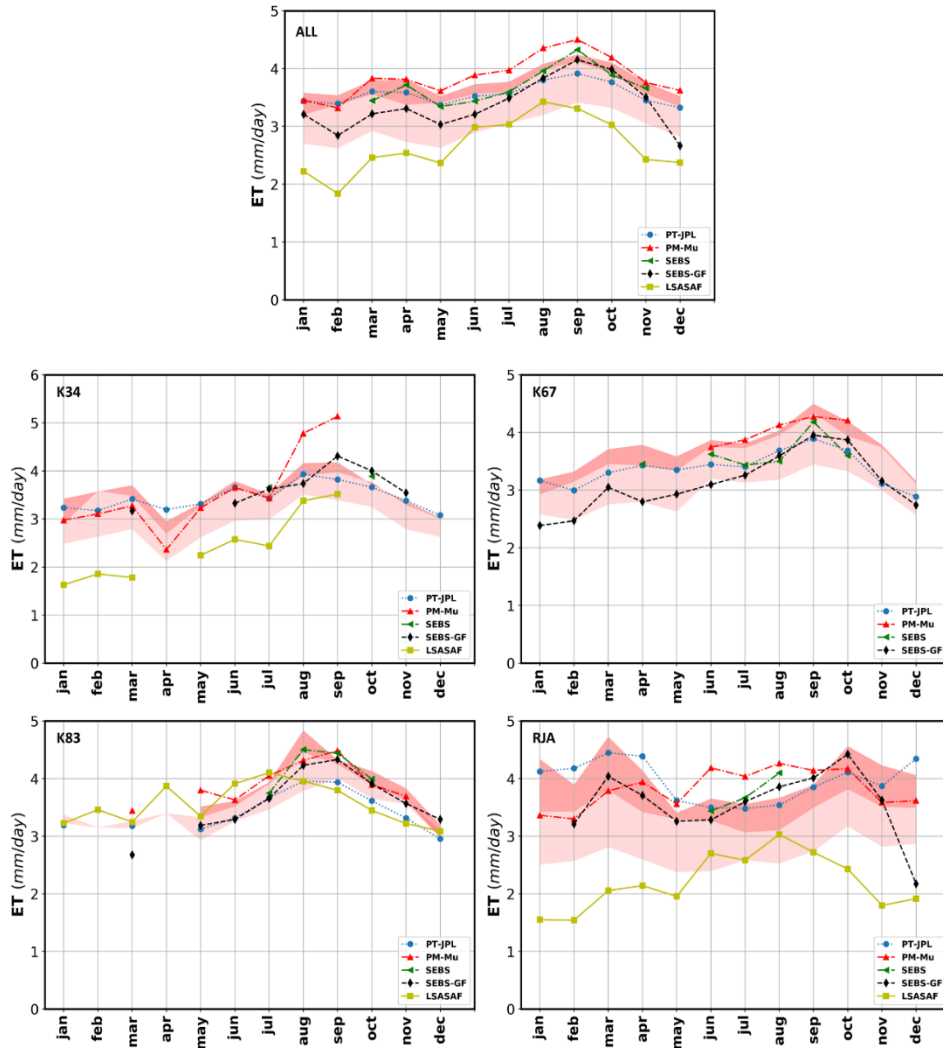


Figure 8.4. Time series of ET model monthly mean values. In-situ ET observations are represented by the shadowed area (lower, intermediate and upper limit indicating uncorrected, BR and ER ET observations respectively).

8.2.- Forcing Scenario II

8.2.1. Reanalysis quality assessment

Before proceeding to the validation of models, in order to assess the impact of the reanalysis meteorological data on model performance reanalysis inputs were compared against in-situ station meteorological inputs. An aspect to take into account when analysing the results is the spatial discrepancy between the in-situ point data and reanalysis data (minimum spatial resolution of 0.25°). In Table 8.2, calculated metrics (bias, RMSE and R) from the evaluation are shown. Metrics were calculated with a number of available points ranging from 500 to 4000 depending on model and forcing variable considered. In order to facilitate the notation for the rest of the section, MERRA, ERA and GLDAS are used as an abbreviation of MERRA-2, ERA-Interim, and GLDAS-2.1 reanalysis.

Several conclusions can be derived from Table 8.2. Generally, instantaneous values (at satellite time overpass) provide greater deviations from in-situ observations than averaged values (daytime, nighttime and daily). For radiation inputs, main difference amongst reanalysis is observed for the bias metric (similar RMSE and R values for the three reanalysis). MERRA tends to overestimate R_{n24} , SR_{inday} and SR_{inhour} while underestimating LR_{inday} and LR_{inhour} . Same behaviour is obtained for GLDAS although it tends to underestimate SR_{inday} . ERA tends to overestimate instantaneous values while underestimating daytime and daily values. For temperature inputs (in exception of T_{aday}) ERA provides the best agreement with in-situ observations amongst reanalysis. Overestimation is generally found for the three reanalysis (in exception of T_{aday} for ERA and T_{minday} for ERA and GLDAS) with maximum deviations for T_{max} and T_{ahour} . For humidity inputs, contrary to temperature inputs (in exception of e_{ahour}) ERA provides the worst performance for modelling humidity inputs (maximum R value of 0.21). Maximum R values are obtained for GLDAS however with also maximum RMSE values. In terms of bias, ERA and GLDAS overestimate e_{aTmax} while underestimate the rest of the inputs. MERRA only overestimates e_{anight} however with a R value of 0.02. Wind speed inputs are underestimated for the three analyses. R Best agreement is obtained for ERA (minimum RMSE and maximum R values).

It is worth noting at these point, that although larger absolute values are obtained for radiation and humidity inputs in comparison with temperature and wind speed (Table 5.15 in chapter 5). Generally, for the three reanalysis, wind speed is the most uncertain parameter with a greater than 60% of relative error, followed by radiation inputs (approximately 30% for solar radiation variables), humidity (15%) and temperature inputs (maximum relative error of 10%).

Table 8.2. Bias, RMSE and R values derived from the comparison of in-situ inputs against reanalysis inputs. The temporal resolution of the inputs is indicated by a subscript (day refers to daytime, night to nighttime and hour to hourly values at the time of satellite overpass).

	MERRA			ERA			GLDAS		
Radiation inputs (W/m²)									
	BIAS	RMSE	R	BIAS	RMSE	R	BIAS	RMSE	R
Rn₂₄	9.16	48.77	0.31	-10.36	44.07	0.37	8.65	43.53	0.39
SR_{inday}	10.7	124.17	0.26	-37.54	113.43	0.37	-28.56	109.08	0.37
LR_{inday}	-20.08	23.09	0.50	-15.38	18.60	0.68	-19.75	24.5	0.45
SR_{inhour}	141.80	241.47	0.33	94.8	216.05	0.34	126.66	224.54	0.39
LR_{inhour}	-16.04	23.55	0.57	1.39	15.55	0.67	-2.12	20.91	0.53
Temperature inputs (K)									
	BIAS	RMSE	R	BIAS	RMSE	R	BIAS	RMSE	R
T_{aday}	0.38	1.95	0.48	-1.24	2.07	0.61	0.31	1.99	0.58
T_{minday}	1.36	2.20	0.17	-0.62	1.46	0.55	-0.41	1.70	0.62
T_{anight}	0.75	1.85	0.34	0.10	1.31	0.62	0.60	1.73	0.48
T_{minnight}	1.28	2.16	0.17	0.08	1.30	0.56	0.26	1.70	0.38
T_{ahour}	0.62	2.94	0.44	0.18	2.30	0.49	1.24	3.32	0.50
T_{max}	2.0	2.81	0.50	0.80	2.30	0.41	3.18	4.28	0.38
Humidity inputs (Pa)									
	BIAS	RMSE	R	BIAS	RMSE	R	BIAS	RMSE	R
e_{aTmax}	-168.34	484.73	0.34	196.54	522.38	0.06	262.94	600.50	0.35
e_{aday}	-225.95	531.94	0.12	-135.59	539.65	0.05	-148.65	572.8	0.30
e_{anight}	56.32	453.85	0.02	-126.97	484.7	0.05	-179.60	607.9	0.14
e_{ahour}	-327.23	542.32	0.29	-249.13	533.60	0.21	-524.65	787.3	0.17
Wind speed (m/s)									
	BIAS	RMSE	R	BIAS	RMSE	R	BIAS	RMSE	R
W_{sday}	-1.29	1.38	0.53	-0.44	0.68	0.60	-0.96	1.06	0.51
W_{shour}	-1.92	2.18	0.34	-0.09	0.93	0.56	-0.77	1.19	0.55

8.2.2. Sensitivity analysis

Model sensitivity analysis results are displayed in Figure 8.5. It is observed that model output variability (uncertainty) can be explained by input radiation variability (uncertainty). For PT-JPL Rn₂₄ is able to completely explain model variability. For PM-Mu SR_{inday} (playing the major role) followed by e_{aday} and T_{aday} (especially from May to November) are the key variables driven model output uncertainty. For SEBS, W_{shour}, SR_{inhour} and LST contribute in a secondary way in comparison to Rn₂₄. This input sensitivity is also expected for SEBS estimates on cloudy days (SEBS-GF) (PET is directly estimated from Rn₂₄). For LSASAF, SR_{inday} followed by Root_{smday}, e_{aday} and T_{aday}, can explain model output variability. Taking into account the sensibility of the models to these variables, uncertainty in these inputs will be directly translated into model uncertainty. In Figure 8.6 we analyze the model deviations resulting from these uncertainties. For all the models, absolute deviations of approximately 2 mm/d are reached.

8.- Intercomparison of remote-sensing based evapotranspiration algorithms

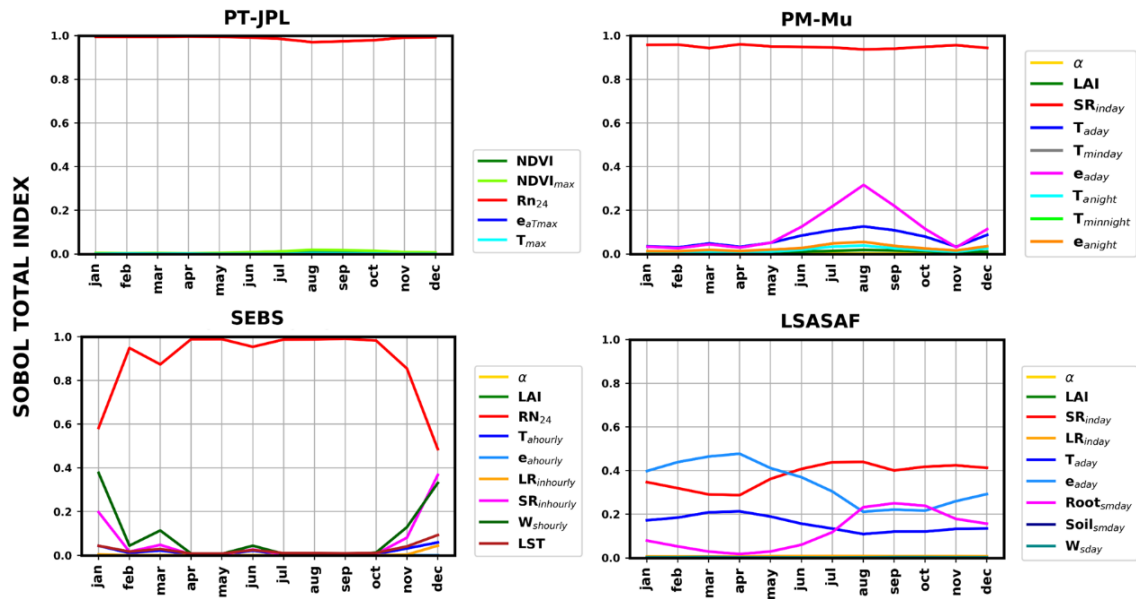


Figure 8.5. Sobol sensitivity analysis for the models considered. Temporal resolution of model inputs is indicated by a subscript (day refers to daytime, night to nighttime and hour to hourly values at the time of satellite overpass).

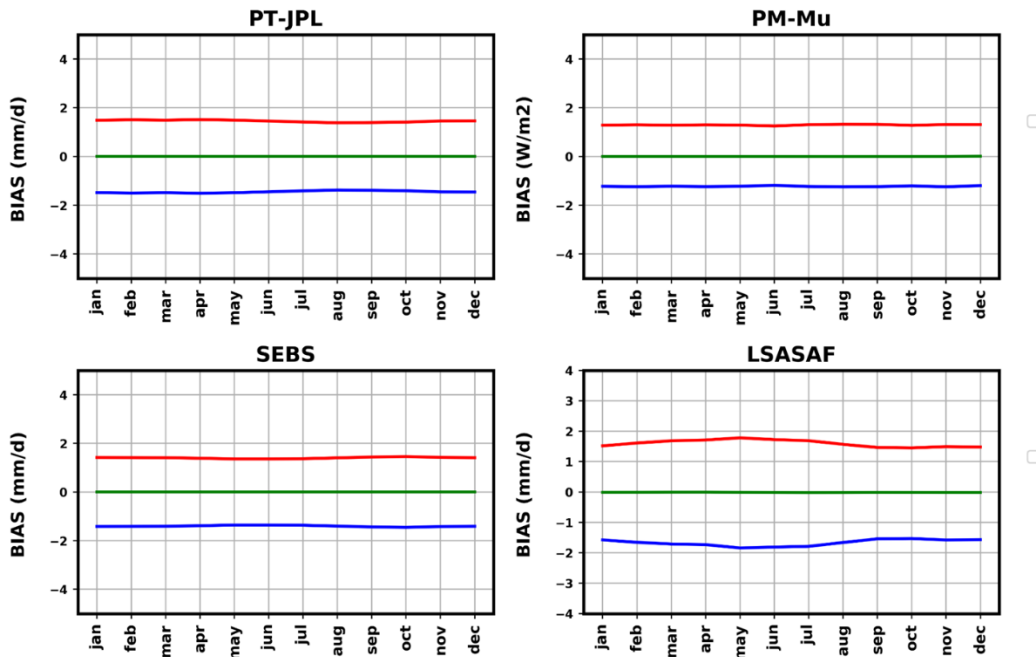


Figure 8.6. Bias analysis for the models considered. Bias was calculated as the difference between perturbed values and unperturbed values. Only radiation variables being responsible of the model variability were considered for perturbation. For SEBS, $SR_{in\,hour}$ was also included in the analysis.

8.2.3. Algorithm validation

In Figure 8.7, scenario II validation results are presented using scatterplots. A deterioration in model performance from Scenario I is observed (R and S metrics have decreased while RMSE has increased). Taking into account reanalysis input quality this result was expected. R metrics range from 0.2 to 0.3. S metrics range from approximately 0.5 to approximately 0.7 and RMSE values lie in the range of 1.1-1.7 mm/day. It is worth noting here the coincidence between the models R values range and the previous R values range derived for the radiation inputs. In addition, there is an agreement between overestimation/underestimation for the models and the positive/negative bias calculated from the reanalysis inputs (R_{n24} and SR_{in}). For PT-JPL and SEBS-GF which uses R_{n24} input, ERA forced results always tend to underestimate MERRA and GLDAS results (positive bias for MERRA/GLDAS and negative for ERA). Same conclusion is obtained considering SR_{in} and PM-Mu and LSASAF. In terms of R, S and RMSE metrics, there is no particular combination (model+reanalysis) that clearly outperform the rest of the combinations (PM-Mu-ERA and LSASAF-MERRA provide the best metrics but with little discrepancy from the rest)

8.- Intercomparison of remote-sensing based evapotranspiration algorithms

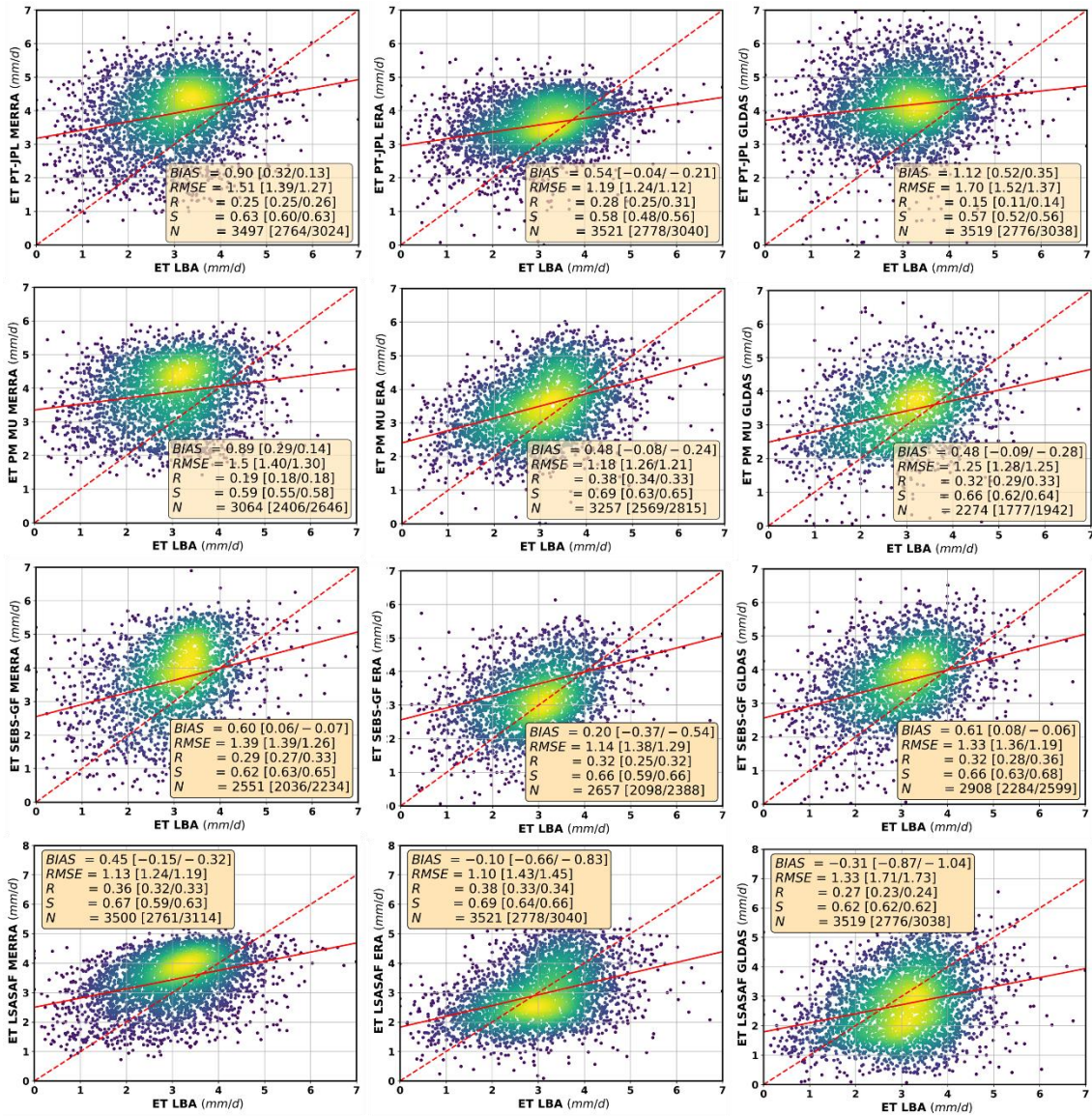


Figure 8.7. Scatterplots of ET derived from the selected models (scenario II) against in-situ measurements considering all stations. For each model, bias, RMSE, R and S, together with the number of points available for validation are shown. Metrics derived considering Bowen Ratio/Energy Residual method are presented between parenthesis.

Individual stations validation results are shown in Table 8.3 and Figure 8.8. As in scenario I, Table 8.3 values refer to the mean value of the metrics derived from the uncorrected case and Bowen Ration and Energy Residual case. Contrary to scenario I, no particular discrepancy emerges between the results from the different stations. Same conclusions as obtained from Figure 8.7 can be derived for individual stations. The negative Rn₂₄ ERA bias translate into a negative bias (or closer to zero bias) when comparing with MERRA and GLDAS results. The underestimation of LSASAF model (Figure 8.7) is observed in each of the stations for ERA and GLDAS. In terms of RMSE, models perform between 1 to 2 mm/day without a particular pattern. For R metric, values range between 0 to 0.4. The low R-values for PT-JPL-GLDAS and PM-Mu-MERRA in Figure 8.7 are also

8.- Intercomparison of remote-sensing based evapotranspiration algorithms

observed for each of the stations (in exception of K34). For S metric, values range between 0.4 to 0.7,

Table 8.3. Bias, RMSE, correlation coefficient (R), Taylor skill score (S) metrics together with the number of available points (N) for the individual station validation (scenario II). Values refer to the mean value of the validation values from the uncorrected case and the Bowen Ratio and Energy Residual case.

BIAS (mm/d)												
	PT-JPL			PM-Mu			SEBS-GF			LSASAF		
	M	E	G	M	E	G	M	E	G	M	E	G
K34	0.44	0.20	0.85	0.61	0.07	0.09	0.09	-0.21	0.20	-0.14	-0.51	-0.45
K67	0.52	-0.04	0.67	0.52	0.20	0.12	0.18	-0.35	0.20	0.08	-0.29	-1.04
K83	0.37	-0.02	0.40	0.26	0.11	0.10	0.31	-0.32	0.20	0.08	-0.56	-0.74
RJA	0.51	0.39	0.72	0.37	-0.22	-0.25	0.34	0.0	0.18	-0.05	-0.86	-0.66
CAX	-0.13	-0.77	-0.21	-0.57	-0.62	-0.03	---	---	---	-0.74	-1.14	-1.54
RMSE (mm/d)												
	PT-JPL			PM-Mu			SEBS-GF			LSASAF		
	M	E	G	M	E	G	M	E	G	M	E	G
K34	1.52	1.26	1.60	1.45	1.19	1.28	1.54	1.33	1.44	1.31	1.31	1.45
K67	1.29	1.01	1.54	1.35	1.12	1.20	1.25	1.21	1.21	1.02	1.16	1.81
K83	1.24	1.06	1.31	1.26	1.18	1.15	1.30	1.24	1.19	1.10	1.29	1.44
RJA	1.47	1.36	1.60	1.51	1.38	1.39	1.31	1.35	1.31	1.26	1.54	1.53
CAX	1.60	1.68	1.71	1.67	1.67	1.33	1.94	---	---	1.60	1.94	2.03
Correlation coefficient (R)												
	PT-JPL			PM-Mu			SEBS-GF			LSASAF		
	M	E	G	M	E	G	M	E	G	M	E	G
K34	0.24	0.32	0.30	0.30	0.43	0.39	0.26	0.34	0.35	0.31	0.43	0.39
K67	0.28	0.35	0.02	0.12	0.39	0.23	0.32	0.33	0.31	0.40	0.42	0.12
K83	0.14	0.20	0.07	0.17	0.28	0.15	0.19	0.22	0.25	0.21	0.27	0.30
RJA	0.25	0.18	0.02	0.02	0.07	0.14	0.20	0.14	0.23	0.25	0.08	0.05
CAX	0.19	-0.01	0.07	0.14	0.09	0.27	----	---	---	0.26	0.08	0.50
Taylor skill score (S)												
	PT-JPL			PM-Mu			SEBS-GF			LSASAF		
	M	E	G	M	E	G	M	E	G	M	E	G
K34	0.60	0.50	0.62	0.58	0.64	0.67	0.63	0.63	0.67	0.58	0.64	0.69
K67	0.63	0.63	0.50	0.55	0.68	0.61	0.63	0.65	0.64	0.69	0.69	0.51
K83	0.55	0.54	0.52	0.57	0.62	0.56	0.57	0.59	0.60	0.58	0.62	0.60
RJA	0.62	0.51	0.47	0.50	0.43	0.50	0.55	0.52	0.57	0.53	0.41	0.47
CAX	0.59	0.33	0.52	0.56	0.52	0.54	0.52	----	----	0.57	0.52	0.72

Taylor diagrams are displayed in Figure 8.8. In this case, only results derived from uncorrected ET observations are shown. For Bowen Ratio and Energy Residual, Taylor Diagrams are shown in the Appendix A.4. Nevertheless, same conclusions can be obtained. Shapes (triangle, square and circle) represent the reanalysis and colours represent models. Models generally perform at R values ranging from -0.1 to 0.5 and CRMSD greater than 1. On the contrary to scenario I, there is no combination (model + reanalysis) that provides the maximum agreement for all the stations. Nevertheless, in general, PT-JPL-ERA and LSASAF-MERRA tend to provide the minimum CRMSD values. In the case of K34 station, this value is provided by PM-Mu-ERA and LSASAF-ERA.

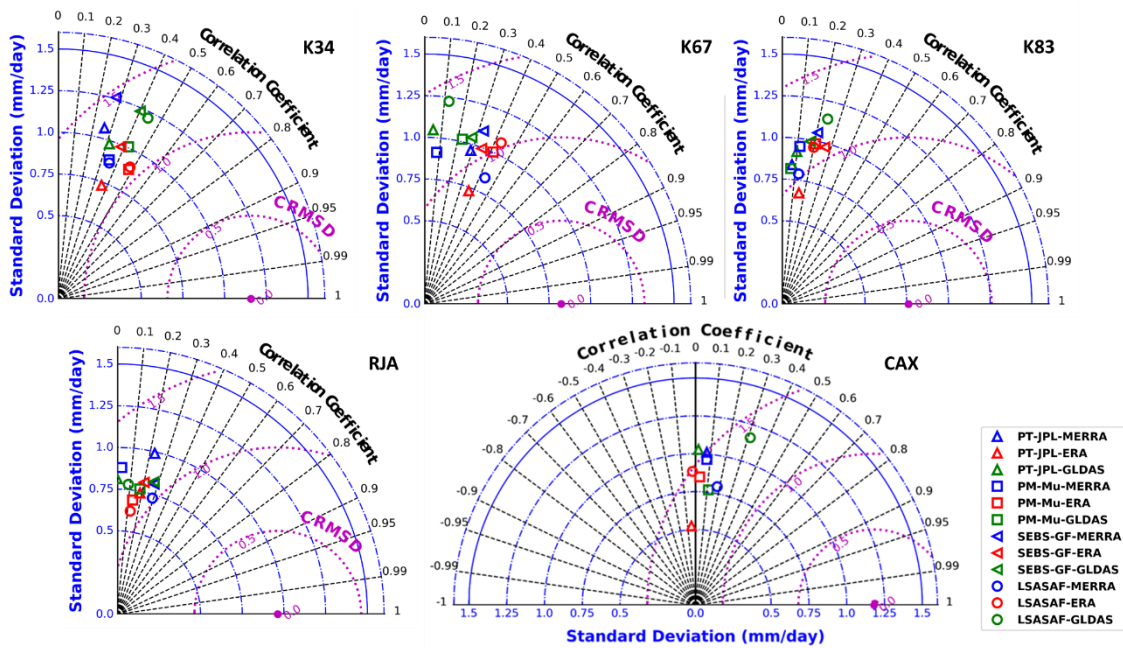


Figure 8.8. Taylor diagrams for individual station considering reanalysis forcing.

8.2.4. Temporal evolution

The temporal evolution of the monthly mean values (Figure 8.9) was used in order to compare in-situ forced and reanalysis forced ET estimates. In-situ ET observations were also included for comparison (same shadowed area as in Figure 8.4). For PT-JPL model, MERRA and GLDAS tend overestimate in-situ forced estimates while ERA tend underestimate these values. For MERRA and GLDAS this overestimation also results in an overestimation of in-situ observations for both uncorrected and corrected values. ERA is still within the range of ET observations values. For PM-Mu, MERRA provides the major coincidence with in-situ forced estimates. ERA and GLDAS on the contrary tend to underestimate these values. This fact however tends to alleviate PM-Mu overestimation issue and thus results in a better agreement with in-situ observations. For SEBS-GF

8.- Intercomparison of remote-sensing based evapotranspiration algorithms

scenario II estimates generally follow scenario I estimates. A positive deviation is found for MERRA and GLDAS. ERA provides the maximum (and negative) deviation. For LSASAF, maximum discrepancy among scenarios is obtained for MERRA. This deviation results in a better agreement with in-situ observations. ERA and GLDAS tend to follow scenario I estimates, maximum difference between reanalysis is found from September to October. Analyzing results by reanalysis, a strong seasonal behavior (similar temporal pattern for all the models) is found for ERA in contrast to MERRA and GLDAS (difference in temporal patterns between PT-JPL and PM-Mu/SEBS-GF/LSASAF).

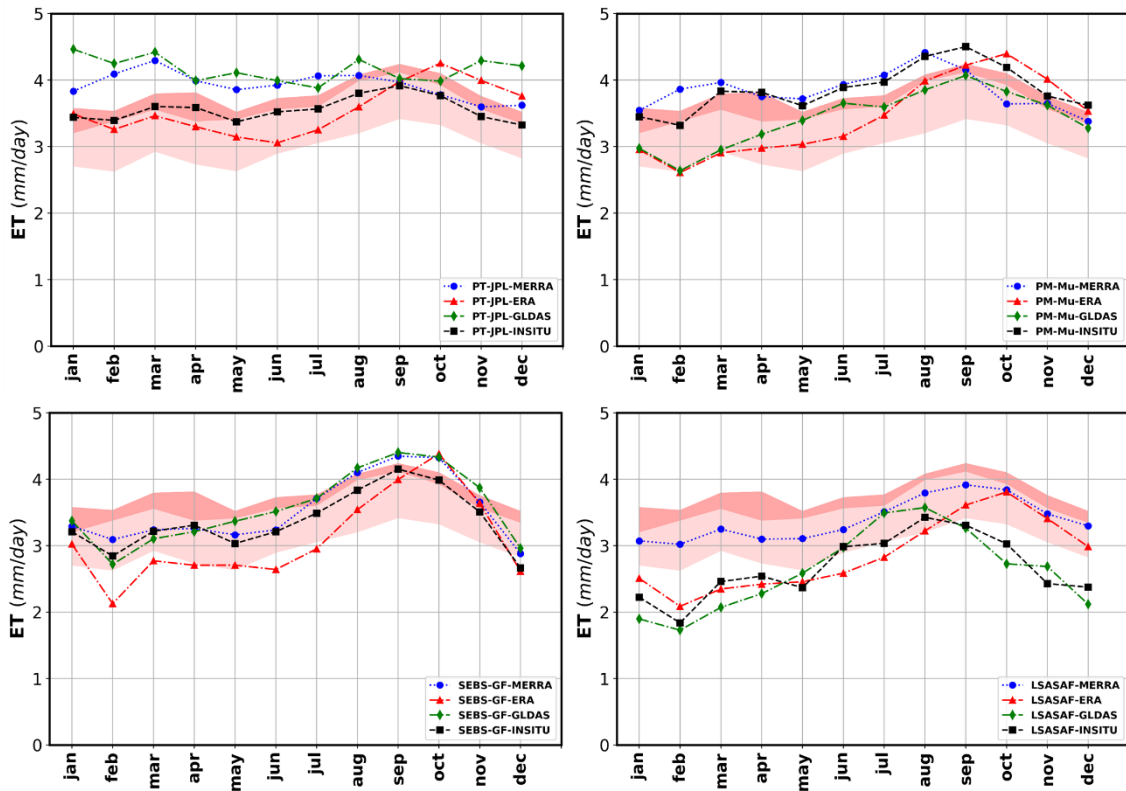


Figure 8.9. Time series of ET model monthly mean values for each combination (model + reanalysis) considered. In-situ ET observations are represented by the shadowed area (lower, intermediate and upper limit indicating uncorrected, BR and ER ET observations respectively).

8.2.5. Spatial patterns comparison

In Figure 8.10, the difference maps used for the comparison of model spatial patterns are shown. The ensemble (mean value) of all the models was considered as truth data. From Figure 8.10, it is observed that discrepancies amongst reanalysis can induced maximum absolute differences greater than 500 mm/year in annual cumulative ET values. Maximum negative deviations are obtained for LSASAF-ERA and LSASAF-GLDAS followed by LSASAF-MERRA and PM-Mu-ERA and PM-Mu-GLDAS. Maximum positive deviations are obtained for MERRA and GLDAS followed by PT-JPL-GLDAS and SEBS-GF-GLDAS. For the reference models major deviations from the ensemble model are obtained for GLEAM and MERRA.

Discrepancy amongst spatial patterns is also driven by differences in reanalysis inputs. Greater discrepancies are obtained when considering a fixed ET model forced with different reanalysis than when considering a fixed reanalysis and different models. In particular, it is observed that models driven by the same radiation input (PT-JPL/SEBS-GF for R_{n24} and PM-Mu/LSASAF for SR_{in}) tend to share similar spatial patterns (although some discrepancy may exist). This leads to the conclusion that differences in ET spatial patterns are generally explained by differences amongst reanalysis radiation inputs. In order to test, this hypothesis for the year 2004, model ET estimates were compared with model inputs (radiation, temperature, humidity, NDVI, wind speed and soil moisture inputs) by linear regression. These results are analysed in terms of R^2 -value (Figure 8.11). Only results for MERRA reanalysis are presented. ERA and GLDAS results are in Annex A.4. As it can be observed, independently of the model considered main contribution comes from the radiation inputs. Although some contribution also provides from other inputs. In particular, temperature and humidity for PM-Mu and temperature, humidity, wind speed and soil moisture for LSASAF model.

In Figure 8.12, the temporal evolution of the models is displayed using zonal mean values. Input net radiation is also displayed for comparison. Taking into account that growth and water use in tropical forests is radiation driven (Wagner et al., 2017) the comparison with radiation evolution can serve to indicate model performance. Discrepancies amongst model temporal evolution is also driven by reanalysis differences. For each reanalysis, models follow the same temporal pattern although differing in ET absolute values. Models are able to reproduce the temporal evolution of net radiation. Major deviation is obtained for PT-JPL-GLDAS. In particular, ERA follows a stronger seasonal net radiation evolution in comparison to GLDAS and MERRA. Considering the comparison of model temporal evolution between the reference models and the four models considered, the agreement with GLDAS and ERA is greater than with GLEAM and MERRA. In GLDAS and ERA the increase in ET values is observed for the period of May-December (with a peak in September/October) while for GLEAM and MERRA this behaviour is observed from January to September (with minimum values in September).

8.- Intercomparison of remote-sensing based evapotranspiration algorithms

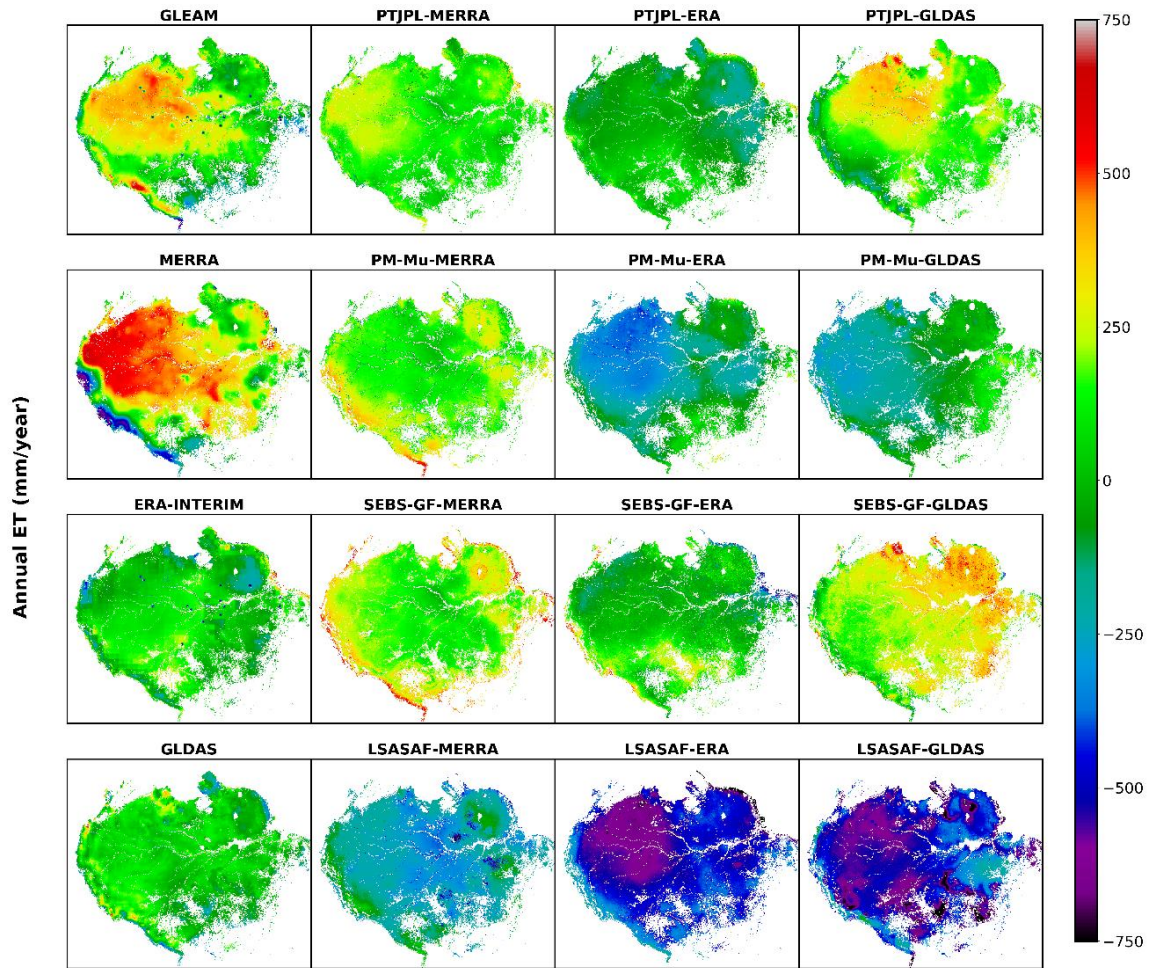


Figure 8.10. Annual cumulative ET (year 2004) spatial patterns (deviation from the ensemble mean).

8.- Intercomparison of remote-sensing based evapotranspiration algorithms

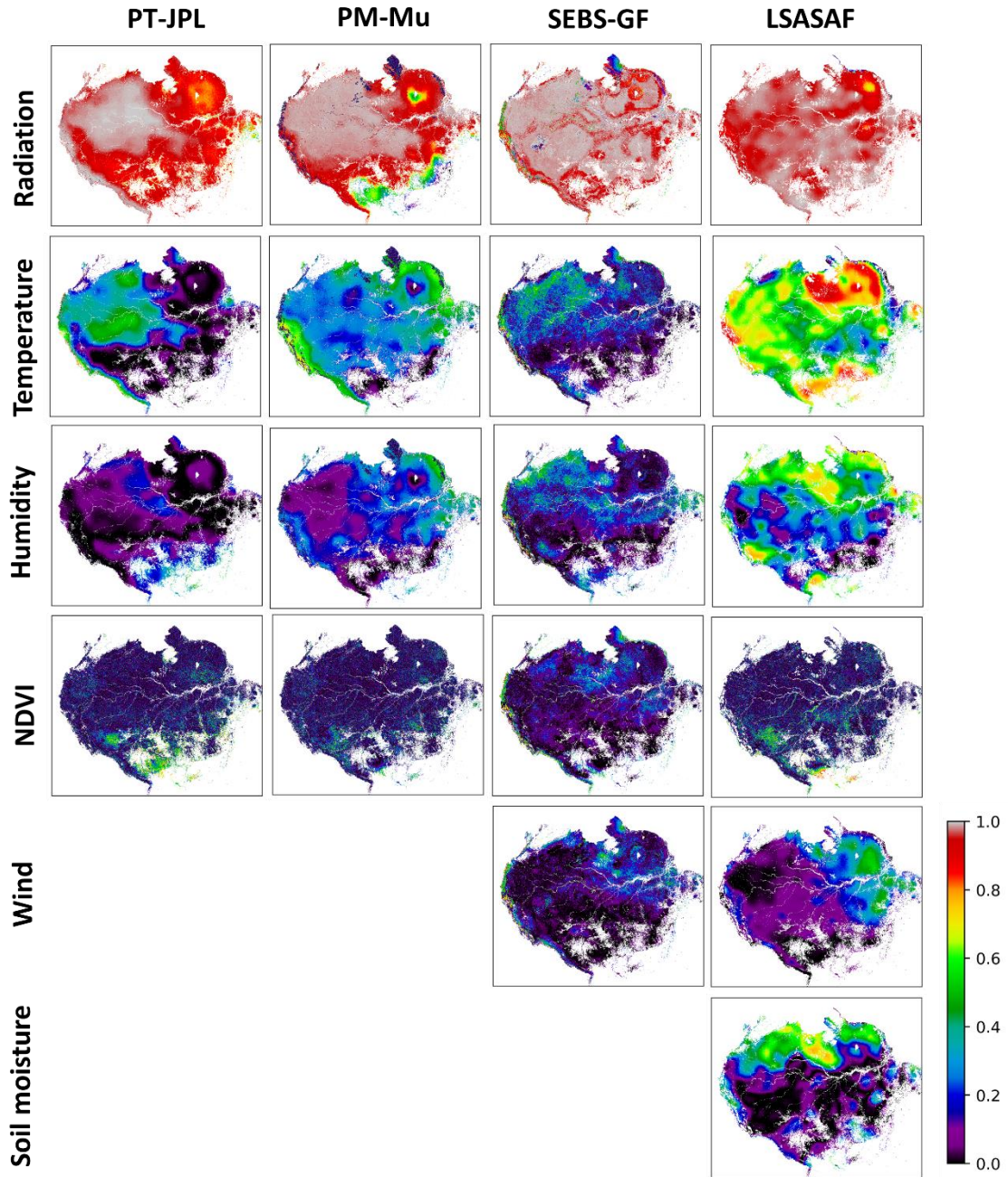


Figure 8.11. R^2 value derived from the linear regression of ET model estimates against model inputs (MERRA-forcing). Radiation inputs refer to Rn_{24} (PT-JPL and SEBS-GF) and SR_{in} (PM-Mu and LSASAF). Temperature and humidity inputs refer to T_a and e_a forced at the temporal scale indicated by the models. Soil moisture refers to the root zone soil moisture for LSASAF model. Non significant values ($p < 0.05$) are displayed in black.

8.- Intercomparison of remote-sensing based evapotranspiration algorithms

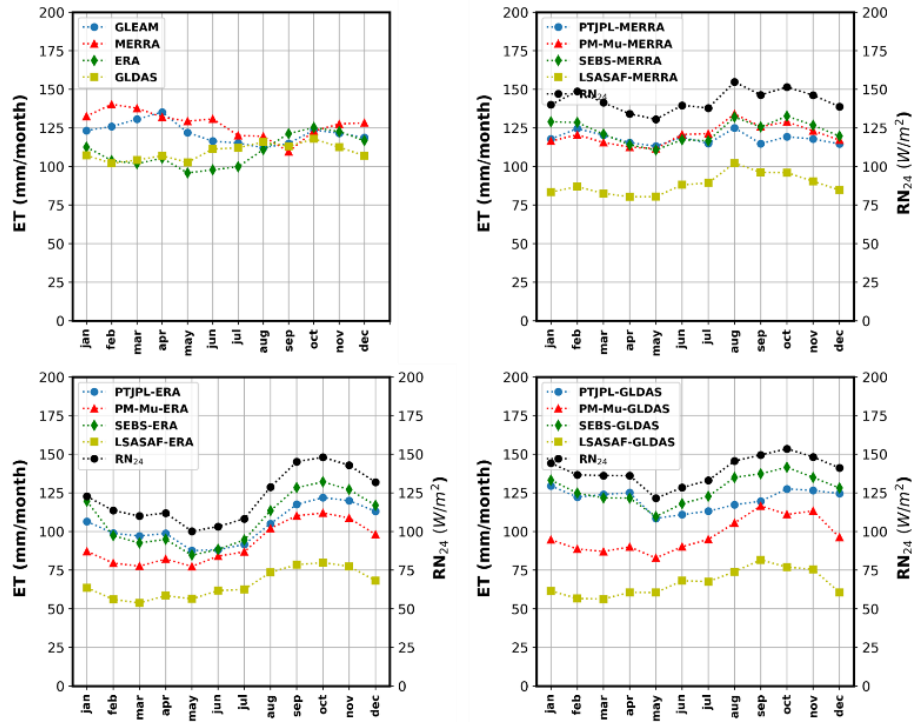


Figure 8.12. Temporal evolution of zonal mean values for the Amazonian region.

8.3.- Discussion

8.3.1.- Forcing scenario I

R_n was shown to control the seasonal variation of λE over the tropical forests in Amazonia (Fisher et al., 2009; da Rocha et al., 2009). The four models considered rely on radiation inputs for evapotranspiration estimation, hence their general agreement with in-situ observations (Figure 8.1). In addition, it was observed that the temporal evolution of model ET estimates follow closely the temporal evolution of in-situ ET measurements reaching maximum values around August-September (Figure 8.4). Nevertheless, the best performance was obtained for PT-JPL (minimum RMSE and maximum R values range) (Figure 8.1). Same conclusion is derived for each individual station (minimum RMSE and maximum R value in Table 8.1 and minimum distance to the observation point in Figure 8.3). These results could be attributed to the simplified approach used in estimating ET, which avoids the need of explicitly parametrizing the aerodynamic and surface resistance. As λE is mainly explained by R_n , the use of a more complex description (resistances) is not expected to contribute in a significant amount to λE explanation, instead additional noise is introduced by the use of additional parameters (Fisher et al., 2005). This is particular true for PM-Mu model. Considering the same λE partition as PT-JPL, the resistance formulation proposed does not result in an improved performance. These resistances are calculated using biome-specific physiological parameters. The most

arguably assumption about these values is that they do not change over space or time. For all the forests of the Amazon region same generic biome-specific properties are assumed, thus ignoring the high species diversity and the complex forest canopy structure. PM-Mu, however, succeeds in avoiding the need of soil moisture data, which for the region it is one of the most difficult parameter to model (Fisher et al., 2009). Main issue associated with PM-Mu is that it tends to overestimate in-situ ET observations (Figure 8.4). Mainly because of K34 and RJA stations. Because of the general reported underestimation for PM-Mu model (Michel 2016; Miralles et al., 2016) in comparison to other models, it is worth remembering here that we used f_c as obtained from the in-situ stations or the satellite data, while PM-Mu uses MODIS f_{apar} . The use of this value is thought to be driven the observed underestimation in MODIS algorithms (Talsma et al., 2018). For the region, MODIS f_{apar} takes values around 0.85 (Senna et al., 2005). With these new value, the overestimation observed is reduced. In appendix A.4 (Table A.4.1) the metrics and temporal evolution using all stations data are given. Although bias is reduced (0.06 for BR correction and -0.26 for ER correction), RMSE and R values are similar to the ones obtained previously. As observed in Figure 8.2, an underestimation of approximately 20 W/m² is derived for daytime PM-Mu R_n (daytime is the major contribution to daily ET). Even with this underestimation, PM-Mu still provides higher ET estimates than PT-JPL. PM-Mu relies on the use of biophysical parameters that have been calibrated. This calibration process is able to adjust the model to provide accurate ET estimates even if inputs values differ from their optimum values (underestimation in both R_n and f_c). It is worth noting here, that a calibration in order to meet the local conditions will also serve in order to increase the performance of the model.

SEBS model perform similar to PT-JPL, main discrepancy arises in R and S metrics. This similar performance could be attributed that both models heavily rely on daily R_n for ET estimation. In PT-JPL, PET (and therefore daily R_n) is scaled to ET values using biophysical constraints, for SEBS daily R_n is scaled using a pre-calculated evaporative fraction. As this fraction is calculated at the satellite time overpass, the variability introduced by using instantaneous values together with the assumption of constant value of evaporative fraction could help to explain the discrepancy for R and S metrics. In SEBS, the explicit parametrization of surface resistance (and the problematic parametrization associated) is avoided by calculating λE as a residual term. Accuracy in the results is thus determined by the accuracy in calculating r_a (and the derived H). Van der Kwast et al. (2009) pointed out to LST errors as a source of r_a uncertainty. In particular, the split-window algorithm used in this study was demonstrated to provide more accurate LST estimates than current MODIS LST operative products (Gomis-Cebolla et al., 2018). SEBS differ from the rest of the models in the fact that no λE partition is considered. Nevertheless, SEBS one-source approach can be assumed for the region (λE_s can be neglected, and the LST observations are expected to reflect the effect of intercepted water on the leaves and canopy for λE_l).

Main limitation of SEBS model is the lack of ET estimates for cloudy days. In order to deal with this problem, ET was derived from the f_{AW} in these days. This technique was

shown to overcome this issue nevertheless it tended to underestimate SEBS values. This fact may result from the simplification used (transpiration results only from the contribution of soil moisture). Although this assumption is generally true for water limited regions it may not offer a complete description for energy limited regions (evapotranspiration is mainly determined by the incoming radiation rather than the available water). In addition, this technique use default soil properties values that may not properly represent the local soil conditions of the in-situ stations. It also entails one additional aspect, the alteration in the ET estimates distribution. Due to the continuous cloud cover of the study region, f_{AW} ET estimates contribute more to the total distribution than SEBS estimates (i.e. from approximately 1600-1700 SEBS-GF estimates, only 500-600 are from SEBS).

LSASAF provides the worst performance amongst the models considered. ET estimates were clearly underestimated. In LSASAF, an explicit parametrization of r_s and r_a is used in order to estimate λE . r_s is calculated by upscaling r_{smin} using Jarvis functions. A constant value of r_{smin} is assumed for all the forests of the Amazonia. Apart from this issue, the soil moisture is considered in this calculation. The problematic description of this input together with the spatial mismatch between in-situ point station and reanalysis data negatively affect model performance. Apart from this, LSASAF (and also SEBS-GF) use default soil properties values that may not properly represent the soil conditions of the in-situ stations. In addition, as in SEBS, there is a dependency on roughness parameters for r_a calculation. Therefore, uncertainty in this parametrization could also affect model performance. An additional reason behind the underestimation of LSASAF model is the not inclusion of an interception term in the λE partition. In order to test this hypothesis, λE_I was calculated assuming r_s equal to 0 (as in open waters). Same vegetation roughness lengths driving r_a . λE components were weighted as in PM-Mu by a f_{wet} factor. Results are presented in Table A.4.2 (Appendix A.4). They indicate that the inclusion of this new term help to overcome the underestimation issue. Although some variability in validation metrics is expected because of this fact, same model comparison conclusions can be derived in terms of R and S metrics. Therefore, stressing the importance of the previously commented issues (reanalysis soil moisture). It is worth mentioning here that in the new launch of LSASAF ET products the lack of λE_I is explicitly addressed by modulating the vegetation r_s by a wet fraction term.

Apart from the above mentioned model limitations, it has to be taken into account that the resulting deviations between in-situ ET observations and modelled ET estimates result also from the contribution of other causes. In particular, it is worth noting the extra uncertainty introduced by the spatial mismatch between ground measurements and remote sensing data. Footprints for eddy covariance range from 0.1 to 0.5 km² (Kljun et al., 2004) depending on the reference height. This scale is much smaller than the MODIS (or MERRA) pixel 1km² resolution. In addition, uncertainty in these remote sensing data will also introduce uncertainty in the modelled ET estimates. This uncertainty may be derived from an imperfect cloud masking and atmospheric correction of these data (Hilker et al., 2012; Gomis-Cebolla et al., 2018). Another cause of deviation to take into account is the uncertainty derived from the in-situ eddy-covariance measurements. At nighttime

eddy covariance measurements are generally unreliable because of low turbulence (Fisher et al., 2007). In addition, there is the issue of the lack of energy closure and the possible deviations introduced by the selection of a specific correction method. As it was observed validation metrics (and therefore the final conclusions) were dependent on the type of in-situ data (uncorrected or corrected) and the type of correction considered (BR or ER). Nevertheless, it is worth noting that same model comparison conclusions were derived from BR and ER (although with different validation metrics values).

8.3.2.- Forcing scenario II

With respect to scenario I, scenario II differs in the use of reanalysis meteorological data for forcing the models. It is therefore necessary to quantify the existing errors in these input data in order to address their impact on model performance. Uncertainty in these data results from reanalysis inherent errors and the spatial mismatch between ground measurements. Reanalysis quality was addressed by comparison of reanalysis inputs against in-situ stations inputs. From Table 8.2, the poor quality of these data can be deduced. Wind speed with a relative error greater than 60%, followed by radiation inputs (30%), humidity (15%) and temperature inputs (10%). In addition, R values range from 0.3 to 0.7 for radiation, temperature and wind variables while for humidity variables a maximum value of 0.35 is obtained. The impact of these inputs uncertainty on model output was assessed using the Sobol global sensitivity analysis. From Figure 8.5, it can be deduced that radiation inputs are the key variables driven model output, and therefore model uncertainty will result mainly from radiation input uncertainty. This fact, is clearly in agreement with the fact that the tropical forests of Amazonia are energy driven (Fisher et al., 2009; da Rocha et al., 2009). In particular, for PT-JPL and SEBS model R_{n24} is the key variable. A bias in these input will be therefore directly translated into a bias in the estimates, which can reach up to 2 mm/d (Figure 8.6). Considering the scaling logic of PET for PT-JPL and the assumption of constant evaporative fraction this result could be expected. In addition, this fact also explained the similarity in PT-JPL and SEBS results in scenario I. In the case of PM-Mu, model variability is mainly driven by SR_{in} variability. A bias in SR_{in} translates into a direct bias in R_n and therefore in the estimates (up to 2 mm/d, Figure 8.6). It is worth mentioning the role played by T_a and e_a variables (especially from May to November). These inputs are involved in the calculation of VPD (e_s is derived from T_a). During these months, VPD generally increases (due to a decrease in RH) therefore contributing more to λE . In addition, T_a is also involved in the calculation of R_n . For LSASAF, SR_{in} explains most of the model variance causing a maximum deviation of 2 mm/d. Nevertheless, e_a , T_a and $Root_{sm}$ additionally play an important role. Taking into account model parametrization these results were expected. e_a is involved in the λE calculation, explicitly (specific humidity) and implicitly (in the calculation of r_s). The same holds true for T_a but for the sensible heat flux. $Root_{sm}$ is used in r_s calculation. Therefore, the effect of reanalysis inputs on model estimates is not as direct as in the other

models. It is worth noting here, that model is almost insensitive to wind speed (even if it is the most uncertain input).

From Figure 8.7 and 8.8, it is observed the negative impact these inputs have on model performance. It is observed that for some models (PM-Mu-ERA and LSASAF-MERRA) the biases introduced by model parametrization tend to cancel out when considering input forcing data with an opposite bias (i.e. the overestimation of in-situ ET values for PM-Mu is alleviated when considering a SR_{in} that has a negative bias). This fact could explain the slight improvement observed for these models. Nevertheless, no particular combination stood out as the best performing one (Figure 8.7 and 8.8). Taking into account the similarity in reanalysis radiation inputs, this result was somehow expected.

The effect of reanalysis biases in ET estimates is clearly deduced in Figure 8.9. These biases are mainly explained by the biases in reanalysis radiation inputs. For PT-JPL, the positive bias in MERRA and GLDAS reanalysis explains the overestimation of in-situ forced results. The contrary is observed for ERA. For PM-Mu, the ERA and GLDAS underestimation observed correlates with the negative bias in SR_{in} . The best agreement provided by MERRA could be explained because the biophysical constants used in the model were calibrated considering this reanalysis data as input (Mu et al., 2011). For future developments this specific model parameter calibration could be a solution in order to avoid the issue of reanalysis inputs. For SEBS-GF the bias in Rn_{24} is directly translated into model estimates. For LSASAF, the biases observed in ET estimates could be explained mainly by the SR_{in} bias. Amongst reanalysis it was found that ERA provides a stronger seasonal behaviour than MERRA and GLDAS (Figure 8.9 and Figure 8.12). This fact is directly translated into ET temporal patterns. This results helps to confirm the suspicion that input data quality is more important than model quality in order to explain the results. This can also be deduced considering spatial patterns comparison (Figure 8.10). Spatial discrepancy amongst different reanalysis is greater than amongst models that use the same reanalysis. In addition, the selection of a specific reanalysis explains the temporal variability (models differ in the absolute values provided). In agreement, with previous results it was observed that ET spatial patterns and temporal behaviour was leaded by radiation inputs (Figure 8.11). Biases in these inputs translated directly into biases in ET estimates (same explanation of Figure 8.9 applied here) and were able to explain maximum negative deviations greater than 500 mm/year for LSASAF using ERA and GLDAS reanalysis (the underestimation effect of LSASAF is increased by the negative bias of these reanalysis) and deviations ranging between ± 500 mm/year for the rest of the models.

8.- Intercomparison of remote-sensing based evapotranspiration algorithms

CONCLUSIONS

In this section, we present the main conclusions derived from this study. They have been organized according to the three research lines followed. In order to be self-contained a brief summary of the work done is provided before the conclusions.

I. MODIS probabilistic cloud masking

MODIS sensor on-board TERRA and AQUA platforms is amongst major tools for studying the Amazonian tropical forests. Nevertheless, MODIS operative surface variable retrieval was reported to be impacted by cloud contamination effects (Hilker et al., 2012; Gomis-Cebolla et al., 2018). A proper cloud masking is a major consideration in order to ensure accuracy when analysing Amazonian tropical forests current and future status. In this study, we investigated the feasibility of using supervised machine-learning algorithms for Amazonian tropical forests cloud masking using MODIS data. The main drawback of these techniques is the need of high quality datasets in order to train the models. In order to overcome this issue, we used collocated observations of MODIS and CPR/CALIOP. This approach was successfully applied previously for AVHRR cloud masking in Heidinger et al. (2012) and Karlsson et al. (2015). Six different supervised algorithms were considered: GNB, LDA, QDA, RF, SVM and MLP. These classifiers are able to provide score values that can be transform to probability estimates (i.e. for each class example, the probability of membership of the class of interest), and therefore can be used for probability cloud masking. Model performance was tested using three independent datasets: 1) collocated CPR/CALIOP and MODIS data, 2) MODIS manually classified images and 3) in-situ ground data. For satellite image and in-situ testing results were additionally compared to current operative MYD35 (version 6.1) and MAIAC cloud masking algorithms.

Major conclusions of the present study are:

- The use of collocated CPR/CALIOP and MODIS observations can be used as training data for machine learning algorithms, nevertheless the resulting database is restricted to a certain viewing conditions range. This issue will be inherited by the models that are train on this dataset.
- In order to facilitate the generalization of the models to other viewing conditions a probabilistic approach can be considered. Instead of focusing on predictions, we focused on obtaining a measure of cloud masking uncertainty (i.e. probability estimates) that can be tuned to adapt to other conditions.
- Amongst the algorithms considered, GNB, LDA, QDA and SVM presented a distort probability estimation. RF and MLP were shown to provide more well-calibrated probabilities. Isotonic regression was proved successful in order to solve this issue.

- From the satellite and in-situ testing results it was shown that under the approach followed, probabilistic methods (LDA, GNB and in a less extent QDA) provided better performance than other machine learning algorithms such as RF, SVM and MLP. This fact results from inheriting the deficiencies of the generated database. Although, RF, SVM and MLP are able to adapt better to more complex situations than GNB, LDA and QDA the viewing conditions limitation tend to bias the RF/SVM/MLP estimations. GNB/LDA/QDA less adapted to the train dataset are therefore more capable to better generalize to other viewing conditions.
- The proposed approach improves MODIS cloud masking methodologies because it is able to correct the deficiencies observed in MYD35 and MAIAC cloud masks. A cloud cover underestimation and overestimation over the study region was reported by MYD35 and MAIAC respectively.
- Models have a good trade-off between accuracy and computational cost. In particular, LDA stands out from the rest of the models obtaining the maximum accuracy and lowest computational cost.
- The proposed approach provides a refinement of MODIS cloud mask products by using a ready-to-use implementation. Collocated CPR/CALIOP and MODIS orbits are directly provided by the CloudSat datateam. And the methodology can therefore be applied for other regions. Apart from this, it can be easily expanded to other sensors such as VIIRS onboard the SUOMI-NPP, which is considered as the continuity of MODIS mission.
- Nevertheless, the dependence on the collocated dataset and the viewing conditions and surface type restrictions arise as the main weaknesses in order to extend the proposed approach to other regions. Surface type issue can be solved by introducing additional classes and features. Viewing conditions issue can be alleviated by proper radiative simulations at different angles.

II. LST retrieval algorithm adapted to the Amazon evergreen forests

The use of thermal satellite imagery has been proven as a valuable tool to monitor tropical forests (Jiménez-Muñoz, 2013, 2015, 2016a, 2016b, 2018). In particular, some studies showed the relationship between this variable and the CO₂ absorption capacity and biomass loss of these tropical forests proving the potential use of vegetation temperature in the monitoring of the vegetation status (Toomey et al, 2011). Nevertheless, the use of these type of data over tropical forests still has some limitations being of special importance the atmospheric correction under very humid conditions and the possible high occurrence of cloudy pixels. In addition, the performance of these land surface

temperature products is poorly evaluated due to the restrictions imposed by the availability of in-situ data. The aim of this study was to generate specific LST products for the Amazonian tropical forests. This goal was accomplished by using a tuned split-window equation. The performance of this algorithm was compared to operative LST products. The study was mainly focused on MODIS sensor, nevertheless it has been expanded to include other sensors such as VIIRS and SLSTR. Validation of the LST products was obtained by direct comparison between LST estimates as derived from the algorithms and two types of different LST observations: in-situ LST (T-based validation) and LST derived from the R-based method. In addition, LST algorithms were validated using independent simulated data. In-situ LST was retrieved from two infrared radiometers (SI-100 and IR-120) and a CNR4 net radiometer, situated at Tambopata test site (12.832 S, 62.282 W) in the Peruvian Amazon.

Major conclusions derived from this study are:

- Uncertainty from in-situ SI-100 and IR-120 infrared radiometers was less than 1 K, thus meeting the requirements for LST validation tests sites. In addition, LST as derived from CNR4 sensor in comparison to the infrared derived LST show a null bias and a RMSE of 0.8 K. Thus also proving the validity of the CNR4 data for LST validation.
- In order to generate the tune-split window equation a simulated database was employed. This database was derived using MODTRAN radiative transfer code, ASTER emissivity spectra and MODIS atmospheric profiles gathered from more than 1000 spatial points over the region for 3 years.
- Two version of the tune split-window were considered. One generalized equation with contributions including emissivity and water vapour terms, and one simplified equation in which these previous terms were neglected.
- From the simulated database validation, it was observed that for the particular case of the region which features a dense green vegetation the inclusion of the emissivity and water vapour contributions in the SW (i.e. generalized SW) do not result in an improvement in the accuracy of the estimated LST. In fact, the simplified version reduces the RMSE by 0.1K to 0.4 K. In addition, it is more stable at larger viewing angles and higher water content.
- From the T-based validation it was concluded that:
 - o For MODIS sensor on-board TERRA platform, MODIS operative LST algorithms (MODIS-SW and MODIS-DN) provide an RMSE up to 2.70 K and 2.83 K at daytime and up to 1.40 K to 1.70 K at nighttime. For daytime case, the generalized SW did not provide an improvement in validation metrics. At nighttime a decrease up to 0.1 K in RMSE is obtained. The simplified SW proposed was able to improve MODIS LST

algorithms (daytime and nighttime) with a decrease of 0.2 K to 0.8 K of RMSE.

- For MODIS sensor on-board AQUA platform, at daytime the MODIS-SW and MODIS-TES have similar performance (RMSE values around 2.3 K for the radiometer and 2.9 K for the CNR4 net radiometer). MODIS-DN underperform these algorithms with RMSE of 2.66 K and 3.05 K respectively. At nighttime, MODIS-TES provide the worst performance of all MODIS operative LST algorithms, with a difference in RMSE ranging from 0.1 K to 0.7 K. MODIS-TES tends to overestimate in-situ LST values while MODIS-SW and MODIS-DN tend to underestimate them. Both the generalized and the simplified SW proposed are able to improve the validation metrics (RMSE maximum decrease up to approximately 1.3 K). The simplified version provides a better agreement than the generalized version (a decrease in RMSE up to approximately 0.6 K).

- For VIIRS sensor, it was show that the simplified SW algorithm is able to improve the generalized SW algorithm with differences of approximately 0.2 K to 0.5 K in the RMSE. For daytime conditions, VIIRS-TES provide the best performance with a difference of 0.2 K to around 0.3 K in RMSE regarding the simplified split window algorithm. At nighttime however, VIIRS-TES is not able to outperform both generalized and simplified split-window. A difference of 0.7 K to 0.8 K in RMSE is obtained regarding the simplified SW.

- For the case of SLSTR sensor, L2 product provides a better agreement with in-situ observations that the simplified SW algorithm proposed (difference of around 0.6 K in daytime RMSE and a difference up to 0.07 K in nighttime RMSE). In the case of the SLSTR sensor, the generalized SW provides the worst performance. Nevertheless, only a first assessment is presented with the validation being limited to a restricted number of points.

- In MODIS and VIIRS sensors clouds were screened using operative cloud masks. Nevertheless, this could not completely eliminate the presence of unscreened clouds. In order to overcome this issue, only pixels that deviate a specified amount from in-situ LST measurements were used for validation. A difference in 6 K was assumed to be valid. An additional threshold of 3 K was used in order to see the effect of a more restrictive filtering. In this case, a maximum reduction of 1.1 K in RMSE could be obtained regarding metrics derived from the 6 K threshold.

- R-based method was shown to provide an alternative in-situ validation. Associated uncertainty was within the limits of 2 K. Due to practical limitations, this method was applied only to MODIS daytime case validation. MODIS-SW, MODIS-DN and the simplified SW were compared. The simplified SW proposed reduce the uncertainty in LST estimation (RMSE) in 0.7 to 1.7 K in comparison to MODIS operative algorithms.
- From the spatial patterns comparison, it was seen that the difference revealed in LST patterns between MOD35 and QC/MAIAC arise from the correction of cloud-contamination effect. QC and MAIAC spatial patterns are enhanced after removing the alteration (colder-than-true) of temperature introduced by clouds.

III. Intercomparison of remote-sensing based evapotranspiration algorithms over Amazonian forests

Evapotranspiration is a key variable in the understanding of the Amazonian tropical forests and their response to climate change (Cox et al., 2000). Remote-sensing based evapotranspiration models are presented as a feasible means in order to provide accurate spatially-distributed ET estimates over this region. In this work, the performance of four commonly used ET remote sensing models was evaluated over Amazonian tropical forests using MODIS data. Remote sensing models included were: i) PT-JPL, ii) PM-Mu, iii) SEBS, and iv) LSASAF operative algorithm. These models were forced using two ancillary meteorological data sources: i) in-situ data extracted from LBA stations (scenario I), and ii) three reanalysis datasets (scenario II), MERRA-2, ERA-Interim, and GLDAS-2.1.

Major conclusions derived from this study are:

- When using accurate inputs (scenario I), ET retrieved using remote-sensing data can reach an uncertainty less than 1 mm/day. Therefore, proving the capability of MODIS data in order to estimate ET in the region.
- Models considered performed at a bias range of -1.08 to 0.92 mm/day, at a RMSE range of 0.55 to 1.50 mm/day and with R-values ranging from 0.55 to 0.88. Amongst these models, PT-JPL provided the higher R value range (0.65-0.88) and the best performing point considering Energy Residual balance closure correction (RMSE = 0.55 mm/day and R = 0.88). In addition, it gave the closest point to the observational point in Taylor Diagrams.
- Amongst the models, LSASAF provides the most discrepant performance. In particular, a clear underestimation was found in comparison to the rest of the models. Reasons behind this fact are reanalysis soil moisture was used in order to force the model. The problematic description of this input in the region together

with the spatial mismatch between in-situ point station and reanalysis data negatively affect model performance. In addition, this issue is alleviated when considering the inclusion of an interception term.

- PM-Mu shows similar performance to PT-JPL (i.e. a difference in RMSE of approximately 0.2 mm/day and a maximum deviation of 0.1 in R-value). Nevertheless, it was shown that inputs values differ from their optimal values (f_c and R_n).
- SEBS performance was similar to that of PT-JPL. Nevertheless, being dependent on LST observations, SEBS estimates are limited by the continuous cloud cover of the region. A drastically decrease in the number of available estimations of a factor 4 in comparison to PT-JPL model was obtained.
- A gap-filling procedure based on inferring ET from soil moisture status using a function stress (Anderson et al., 2007) was employed in order to provide estimates on cloudy days. This technique was proved to alleviate this issue, nevertheless it resulted in an underestimation of SEBS values.
- When using reanalysis data in order to force the remote-sensing models, ET retrieved accuracy increased to values greater than 1 mm/day. In addition, a poor correlation (maximum R-value around 0.3) is obtained.
- This poor performance is mainly explained by the poor accuracy of the reanalysis data. Validation of these inputs was performed by direct comparison with in-situ surface radiation, meteorological inputs. Wind speed is the most uncertain variable modelled by the reanalysis with a relative error greater than 60%, followed by radiation inputs (30%), humidity (15%) and temperature inputs (10%).
- In order to analyse the impact of reanalysis uncertainty on model uncertainty Sobol sensitivity analysis was used. From this analysis, it was found that model uncertainty was mainly driven by reanalysis radiation uncertainty.
- About the reanalysis radiation inputs, MERRA-2 tends to overestimate daily net radiation and incoming solar radiation. ERA-Interim tends to underestimate both variables, and GLDAS-2.1 tends to overestimate daily radiation while underestimating incoming solar radiation. Biases in these variables are directly translated into biases in the ET estimates. In addition, discrepancies amongst these inputs explain discrepancies between models ET estimates.
- From the comparison of all possible combinations of model + reanalysis, no particular combination outperform the rest. As all the reanalysis considered perform poorly, no clear distinction is derived. This fact, thus serve to emphasize

the need to improve the accuracy of reanalysis estimates in order to improve the accuracy in ET estimates.

APPENDICES

APPENDIX A.1

Table A.1.1.- Technical characterization of SI-111 sensor.

Parameter	Value
Input Power	2.5 V excitation (for thermistor)
Response Time	< 1 s (to changes in target temperature)
Target Temperature Output Signal	60 μ V per $^{\circ}$ C difference from sensor body
Body Temperature Output Signal	0 to 2500 mV
Optics	Germanium lens
Wavelength Range	8 to 14 μ m (corresponds to atmospheric window)
Field of View (FOV)	22 $^{\circ}$ half angle
Operating Temperature Range	-55 $^{\circ}$ to +80 $^{\circ}$ C
Operating Relative Humidity Range	0 to 100% RH
Cable Description	4.5 m (14.76 ft) twisted, shielded 4-conductor wire with Santoprene casing, ending in pigtails
Absolute Accuracy	$\pm 0.2^{\circ}$ C (-10 $^{\circ}$ to +65 $^{\circ}$ C)/ $\pm 0.5^{\circ}$ C (-40 $^{\circ}$ to +70 $^{\circ}$ C)
Uniformity	$\pm 0.1^{\circ}$ C (-10 $^{\circ}$ to +65 $^{\circ}$ C)/ $\pm 0.3^{\circ}$ C (-40 $^{\circ}$ to +70 $^{\circ}$ C)
Repeatability	$\pm 0.05^{\circ}$ C (-10 $^{\circ}$ to +65 $^{\circ}$ C)/ $\pm 0.1^{\circ}$ C (-40 $^{\circ}$ to +70 $^{\circ}$ C)
Diameter	2.3 cm (0.9 in.)
Length	6 cm (2.4 in.)
Weight	190 g (6.7 oz)

Table A.1.2.- Technical characterization of IR120 sensor.

Parameter	Value
Field of View (FOV)	20 $^{\circ}$ (half angle)
Dimensions	92 mm long by 28 mm diameter
Response Time	<1 second to changes in target temperature
Target Output Signal	20 mV per $^{\circ}$ C (difference from sensor body)
Signal Offset	removed by calibration (supplied)
Typical noise level	IR120 0.05 $^{\circ}$ C RMS (as measured by a CS datalogger)
Wavelength Range	IR100: effective bandwidth: 8 to 14 μ m (some sensitivity from 2-6 μ m)
Calibrated Range	-25 $^{\circ}$ C below body temperature to +25 $^{\circ}$ C above body temperature
Operating Range	-25 $^{\circ}$ C to +60 $^{\circ}$ C
Accuracy over Calibrated Range	$\pm 0.2^{\circ}$ C (against a blackbody source over a 50 $^{\circ}$ C temperature span under laboratory conditions)
Current Consumption	0.4 mA when excitation applied, 0 mA quiescent
Sensor output impedance	320 Ω
Thermopile Excitation Voltage	+2 to +3.5V
Thermistor Excitation Voltage	-2.5V or +400 mV

Table A.1.3.- Technical characterization of CNR4 sensor.

Parameter	Value
Spectral range (50% points)	0.3 to 2.8 μm = 300 to 2800 (short wave) nm
Spectral range (50% points)	4.5 to 42 μm = 4500 to 42000 (long wave) nm
Sensitivity	5 to 20 $\mu\text{V}/\text{W}/\text{m}^2$
Temperature dependence of sensitivity (-10 °C to +40 °C)	< 4 %
Response time	< 18 s
Non-linearity	< 1 %
Operating temperature	-40 to +80 °C for CNR4, -40 to +70 °C for CNF4
Power supply	12 VDC, 1.25 A (with heater on) for the optional CNF4 ventilation unit
Ventilation power	5 W continuously
Heating power	10 W externally switched

Table A.1.4.- List of measurements, instruments and measurements heights for the Automatic Weathers Station and for Eddy Correlation Instrument at the K34 tower (extracted from Araujo et al., 2002).

Measurement	Instrument Used	Height, m/Depth, m
Shortwave in and out	Kipp & Zonen Pyranometer CM 21	44.60
Longwave in and out	Kipp & Zonen Pyrgeometer CG 1	44.60
PAR	LI-COR LI-190SZ quantum sensor	51.6
Relative humidity	Vaisala HMP35A	51.1
Soil heat flux	Hukseflux SH1	0.01
Wind direction	Vector W200P	51.45
Wind speed vertical profile	Vector A100R	51.9; 42.5; 35.3; 28.0
Rainfall	EM ARG-100	51.35
Surface temperature	Heimann KT15 infrared sensor	50.40
Air pressure	Vaisala PTB100A	32.45
Longwave in and out temperature	PT100	44.60
Air temperature vertical profile	PT100	51.1; 42.5; 35.5; 28.0; 15.6;
CO ₂ concentration vertical profile	PP Systems CIRAS SC IRGA	53.1; 35.3; 28.0; 15.6; 5.2;
H ₂ O concentration vertical profile	PP Systems CIRAS SC IRGA	53.1; 35.3; 28.0; 15.6; 5.2;
Soil temperature profile	IMAG-DLO MCM101	0.01; 0.05; 0.2; 0.4; 1.0
Soil moisture profile	IMAG-DLO MCM101	0.01; 0.05; 0.2; 0.4; 1.0
CO ₂ concentration	IRGA LI-COR 6262 closed-path	53,1
H ₂ O concentration	IRGA LI-COR 6262 closed-path	53,1
U, V and W wind vectors speed	solent three-axis ultrasonic	53,1

Table A.1.5. List of Environmental Measurements, Instruments, and Measurement Heights on the K67 Tower (extracted from Hutyra et al., 2007)

Measurement	Instrument	Height on Tower
Eddy flux measurement	IRGA, LI-6262, Licor, Lincoln, NE	57.8 m
Net radiation	Rebs Q7.1 with RV2 ventilation	64.1 m
Photosynthetically active radiation (PAR)	Licor 190-SA	63.6 m and 15.1 m
Aspirated air temperature	Met One 076B-4 aspirations with YSI 44032 thermistors	61.9, 49.8, 39.1, 28.4, 18.3, 10.1, 2.8, and 0.6 m
Atmospheric pressure	MKS 627A Baratron pressure transducer	Ground-level
Dew point hygrometers	EdgeTech 200M	57.9 m
Wind speed	Spinning cup anemometer, Met One 010C	64.1, 52, 38.2, and 30.7 m
Wind direction	Met One 020C	64.1 m
Precipitation	Texas Electronics 076B-4	42.6 m

Table A.1.6. List of Environmental Measurements, Instruments, and Measurement Heights on the K83 Tower (extracted from da Rocha et al., 2004).

Measurement	Instrument	Height on Tower
CO ₂ and H ₂ O densities	Li-Cor 7500 open-path Li-Cor 6262 close path	64 m
Air temperature and wind	sonic anemometer (Campbell Scientific)	64 m
Precipitation	TE525 rain gauge; Texas Electronics	64 m
incoming short-wave radiation	CM6B pyranometer; Kipp & Zonen	64 m
net radiation	Q*7.1 ventilated net radiometer	64 m
soil moisture	Campbell Scientific CS615 water content reflectometers	5- to 250-cm depth
soil heat flux	REBS HFT3.1 heat flux plates	at 2 cm

Table A.1.7. List of Environmental Measurements, Instruments, and Measurement Heights on the CAX Tower (extracted from Carswell et al., 2002).

Measurement	Instrument	Height on Tower
Wind velocity	three-dimensional sonic anemometer	53 m
H ₂ O concentration	Li-6262 infrared gas analyzer	53 m
solar and longwave radiation	CNR1, Kipp & Zonen,	45.5 m
Air temperature	shielded thermistors	16 m and 32 m
soil temperature	Thermocouple probes	at 5 cm depth
Saturation deficit	aspirated Delta T psychrometer	53
Wind direction	WP1-UM2, Delta-T Devices, Cambridge, UK wind vane (Campbell Scientific)	53

Table A.1.8. List of Environmental Measurements, Instruments, and Measurement Heights on the RJA Tower (extracted from von Randow et al., 2004).

Meteorological variables	Used instrument, manufacturer (model)	Heights
Incident and reflected short wave radiation	Pyranometers Kipp & Zonen (CM21)	19.3 m
Incident and emitted long wave radiation	Pyrgeometers Kipp & Zonen (CG1)	19.3 m
Photosynthetically Active Radiation (PAR)	Quantum sensor LI-COR (LI-190SZ)	25.6 m
Air temperature	Vaisala thermohygrometer (HMP35A), PT100 resistors	60.0;45.2;35.0;25.3;15.3;5.3 m
Relative humidity	Vaisala thermohygrometer (HMP35A)	60 m
Wind speed	Cup anemometers Vector A100R	61.1;45.2;34.7;25.3
Wind direction	Wind vane Vector (W200P)	60.7 m
Rainfall	Rain gauge EM ARG-100	60.3 m
Surface radiative temperature	Infrared sensor Heimann (KT15)	59.1 m
Atmospheric pressure	Barometer Vaisala (PTB100A)	40 m
Temperature of pyrgeometers	PT100 resistors	54.3 m
Vertical profile of CO ₂ and water vapour concentration **	Infrared gas analyser PP Systems (CIRAS SC)	62.7;45.0;35.0;25.0;2.7;0.05 m
Soil heat flux	Flux plates Hukseflux (SH1)	1 and 10 cm (depth)
Soil temperature profile	Soil thermometers IMAG-DLO (MCM101)	0.05;0.15;0.3;0.6;1.0m (depth)
Soil moisture profile	FDR sensors IMAG-DLO (MCM101)	0.05;0.15;0.3;0.6;1.0m (depth)
Soil moisture profile with Neutron probe	Neutron probe	Every 20 cm down to 3.6 m (depth)
High frequency measurements of 3-D wind speed, temperature, H ₂ O and CO ₂ concentration (10.4 Hz)	Eddy correlation system (Gill Sonic Anemometer and LI-COR 6262 IRGA)	62.7 m

Table A.1.9 . Technical characterization of TSI-880 instrument.

Parameter	Value
Image resolution	352 x 288 colour, 24-bit JPEG format
Sampling rate	Variable, with maximum of one image every 30 s
Operating temperature	-40°C to +44°C
Weight/Size	32 kg / 20.83”x18.78” x 34.19”
Power requirements	115/230 VAC; mirror heater duty cycle varies with air temperature; 560 W with heater on/ 60 W off
Software	Image application supports MS-Windows
Data storage	Local workstation disk
Communication	10BaseT/RJ45 (15m)

APPENDIX A.2

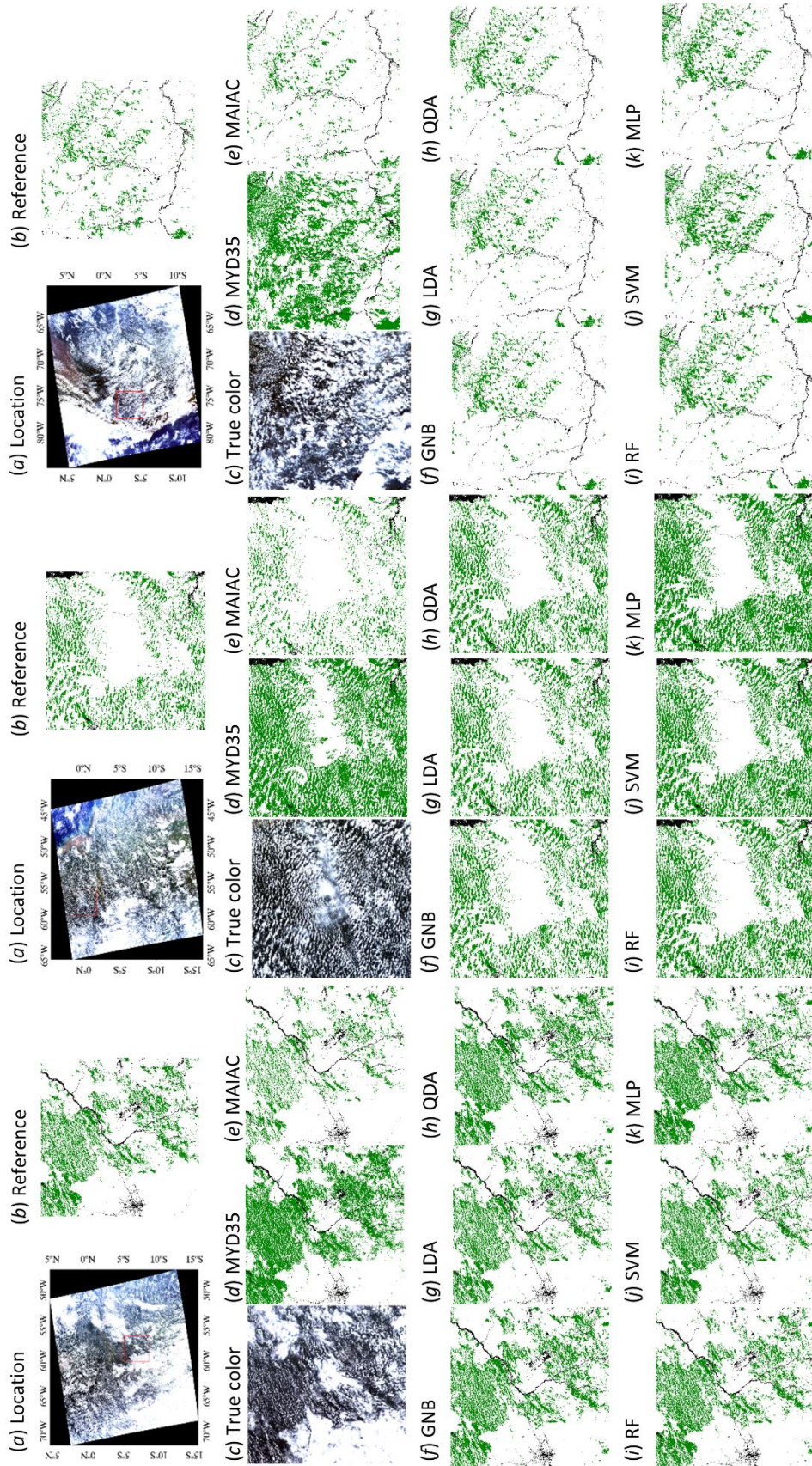


Figure A.2.1. Visual intercomparison of models and MYD35/MAIAC cloud masking results for day 001_1735 (left), day 005_1710 (center) and day 025_1825 (right). Results are displayed as follows: (a) Location, (b) Reference manually classified image, (c) True color image, (d) MYD35, (e) MAIAC, (f) GNB, (g) LDA, (h) QDA, (i) RF, (j) SVM and (k) MLP results. Cloud and clear labels are displayed in white and green respectively. Non-EBF pixels are displayed in black.

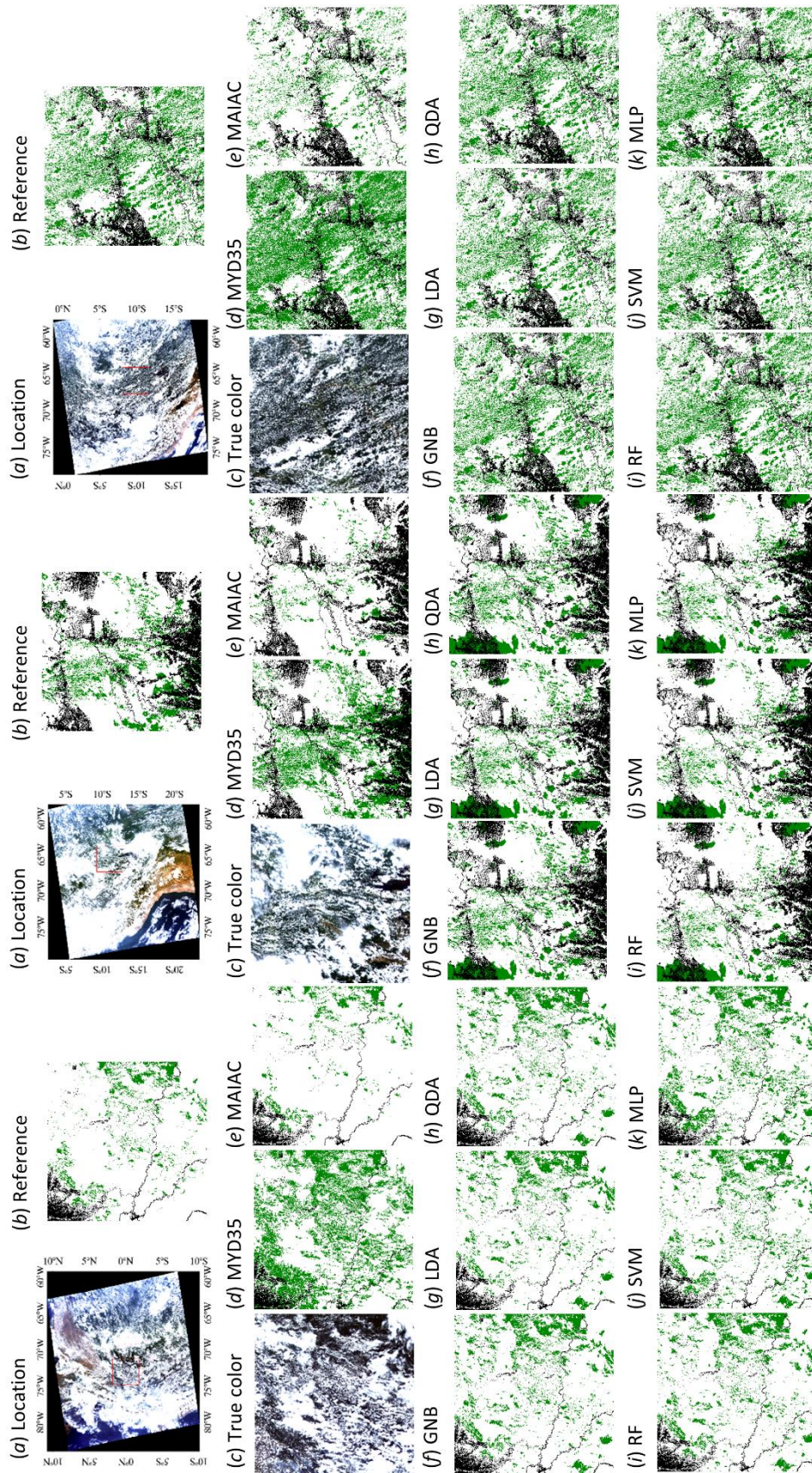


Figure A.2.2. Visual intercomparison of models and MYD35/MAIAC cloud masking results for doy 005_1820 (left), doy 075_1810 (center) and doy 100_1805 (right). Results are displayed as follows: (a) Location, (b) Reference manually classified image, (c) True color image, (d) MYD35, (e) MAIAC, (f) GNB, (g) LDA, (h) QDA, (i) RF, (j) SVM and (k) MLP results. Cloud and clear labels are displayed in white and green respectively. Non-EBF pixels are displayed in black.

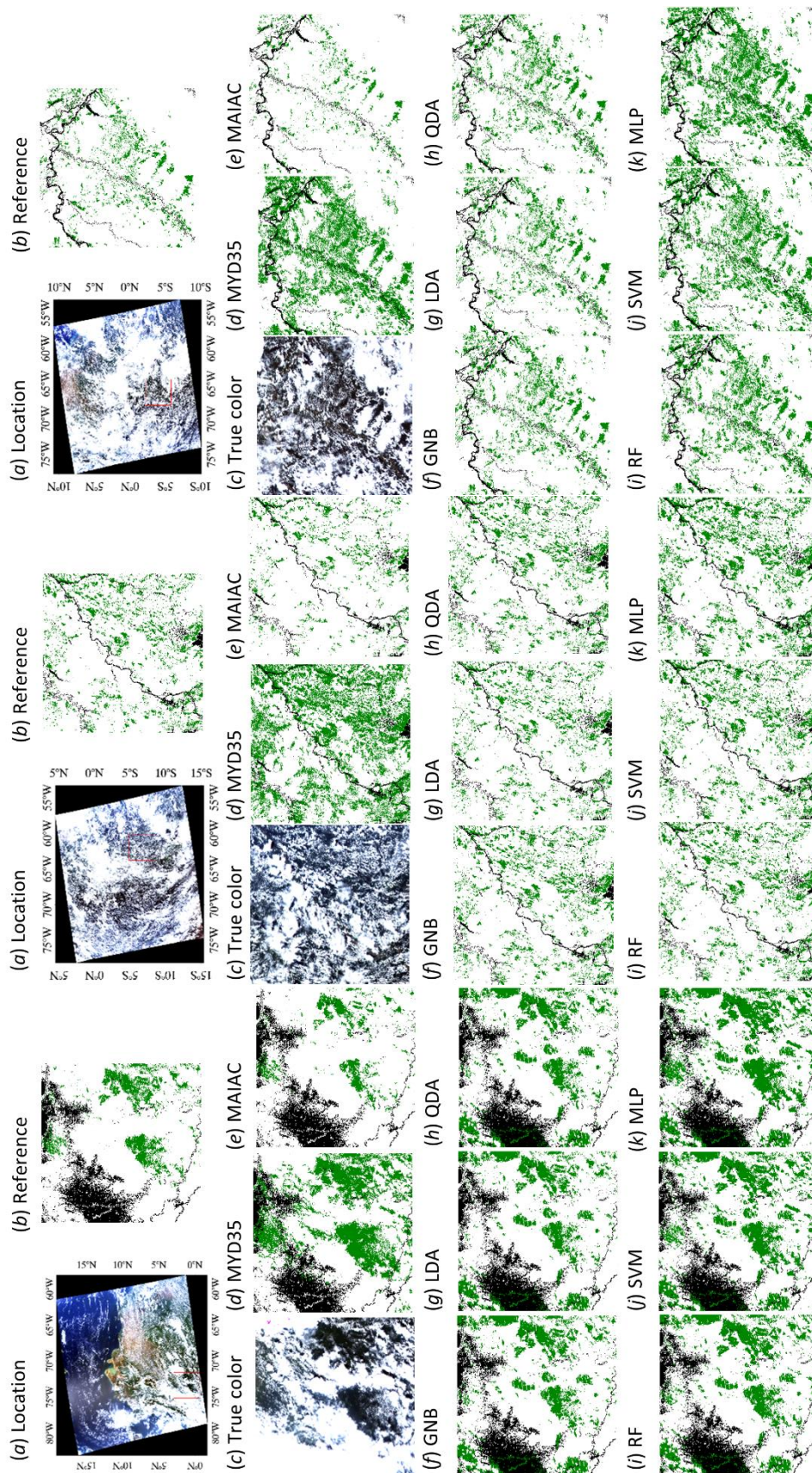


Figure A.2.3. Visual intercomparison of models and MYD35/MAIAC cloud masking results for day 100_1810 (left), day 125_1800 (center) and day 150_1755 (right). Results are displayed as follows: (a) Location, (b) Reference manually classified image, (c) True color image, (d) MYD35, (e) MAIAC, (f) GNB, (g) LDA, (h) QDA, (i) RF, (j) SVM and (k) MLP results. Cloud and clear labels are displayed in white and green respectively. Non-EBF pixels are displayed in black.

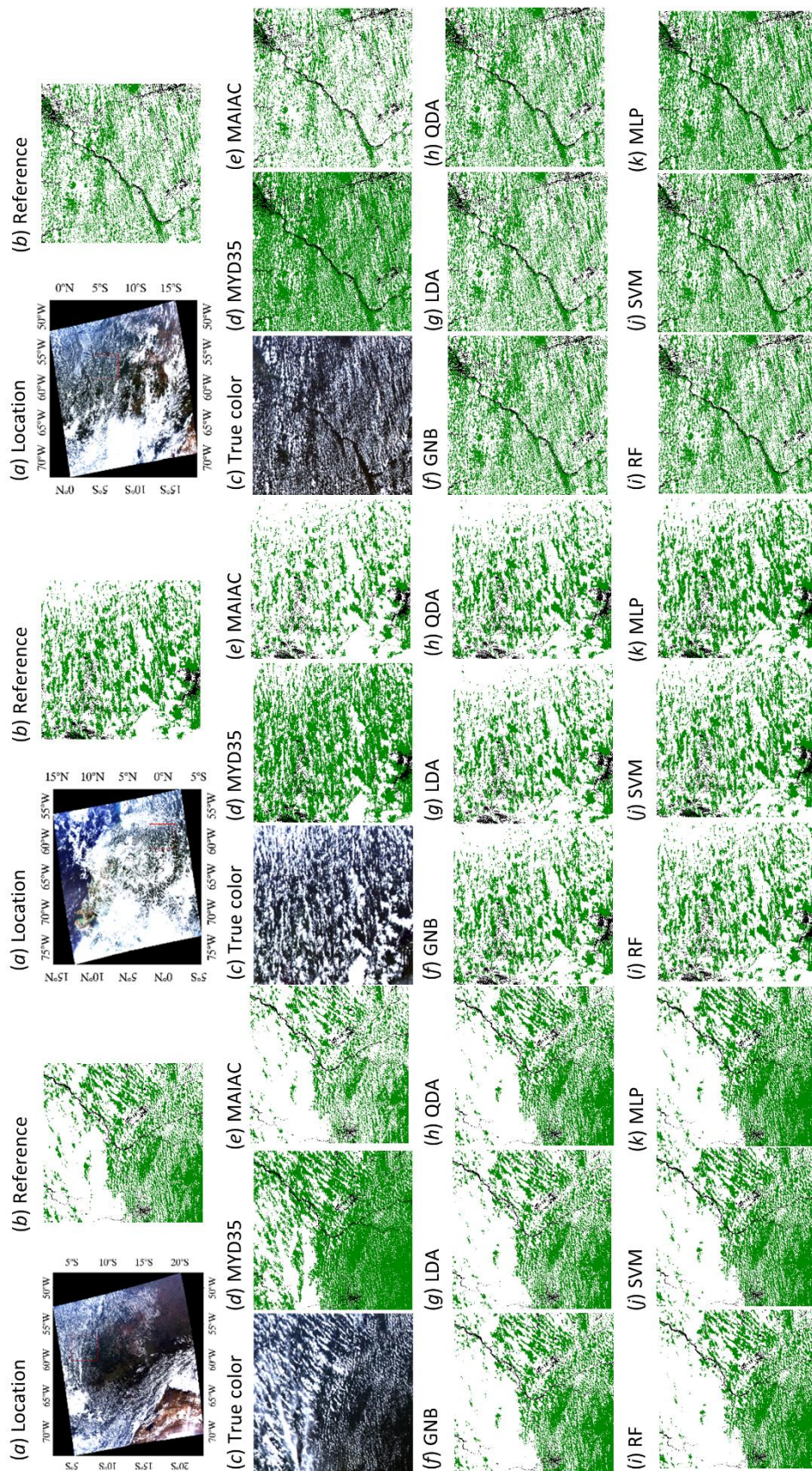


Figure A.2.4. Visual intercomparison of models and MYD35/MAIAC cloud masking results for day 175_1745 (left), day 175_1750 (center) and day 200_1740 (right). Results are displayed as follows: (a) Location, (b) Reference manually classified image, (c) True color image, (d) MYD35, (e) MAIAC, (f) GNB, (g) LDA, (h) QDA, (i) RF, (j) SVM and (k) MLP results. Cloud and clear labels are displayed in white and green respectively. Non-EBF pixels are displayed in black.

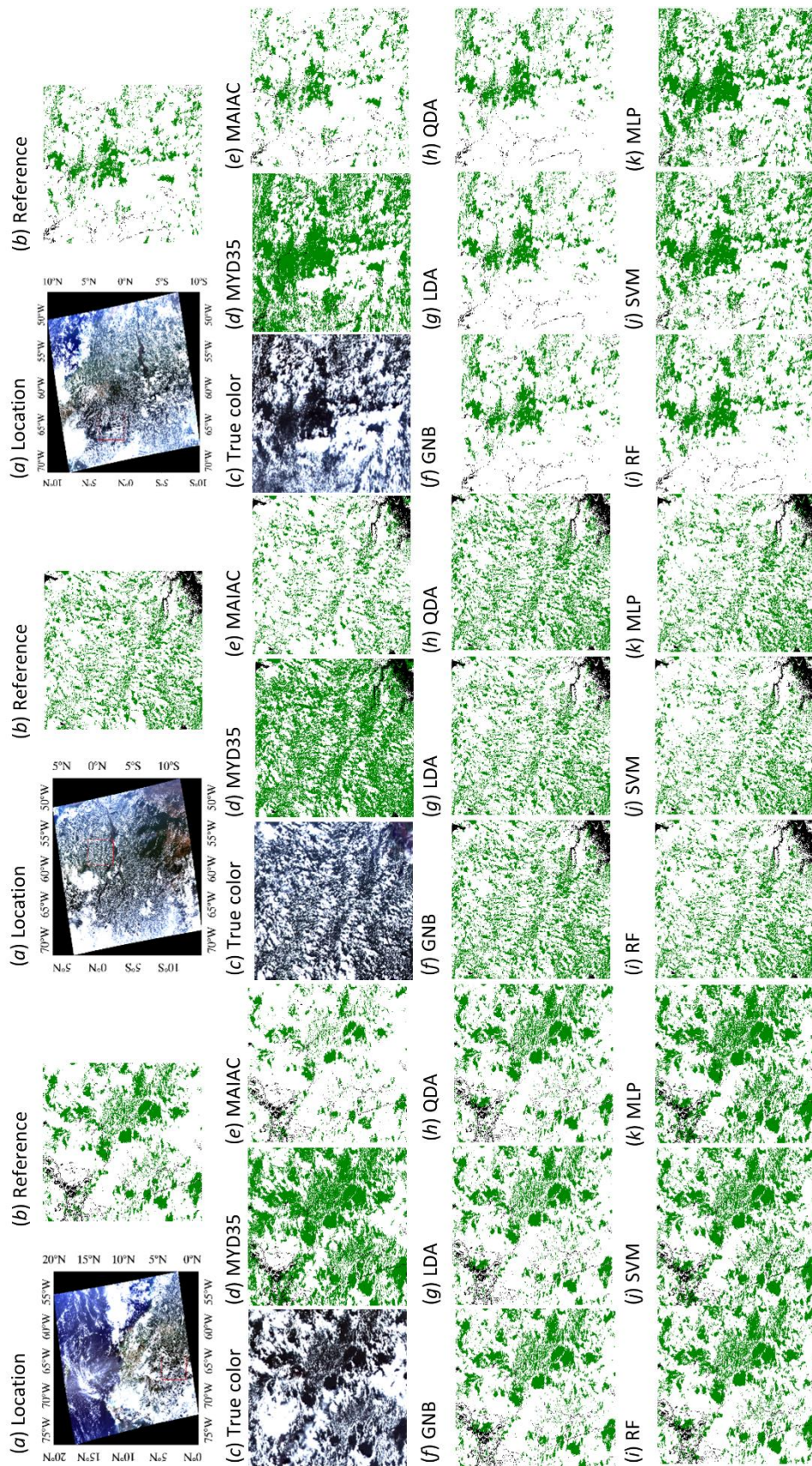


Figure A.2.5. Visual intercomparison of models and MYD35/MAIAC cloud masking results for doy 200_1745 (left), doy 225_1735 (center) and doy 250_1730 (right). Results are displayed as follows: (a) Location, (b) Reference manually classified image, (c) True color image, (d) MYD35, (e) MAIAC, (f) GNB, (g) LDA, (h) QDA, (i) RF, (j) SVM and (k) MLP results. Cloud and clear labels are displayed in white and green respectively. Non-EBF pixels are displayed in black.

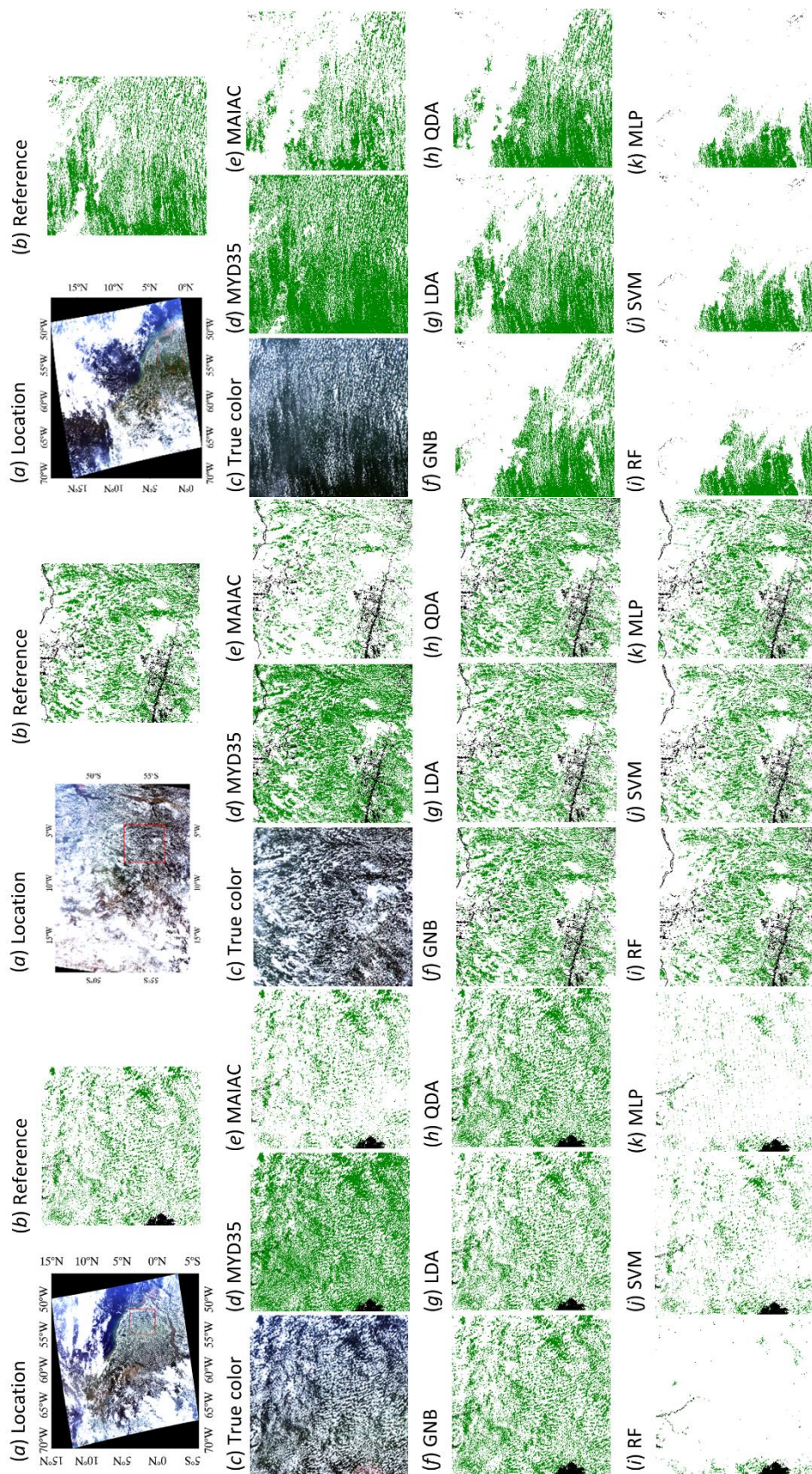


Figure A.2.6. Visual intercomparison of models and MYD35/MAIAC cloud masking results for day 275_1725 (left), day 300_1755 (center) and day 300_1720 (right). Results are displayed as follows: (a) Location, (b) Reference manually classified image, (c) True color image, (d) MYD35, (e) MAIAC, (f) GNB, (g) LDA, (h) QDA, (i) RF, (j) SVM and (k) MLP results. Cloud and clear labels are displayed in white and green respectively. Non-EBF pixels are displayed in black.

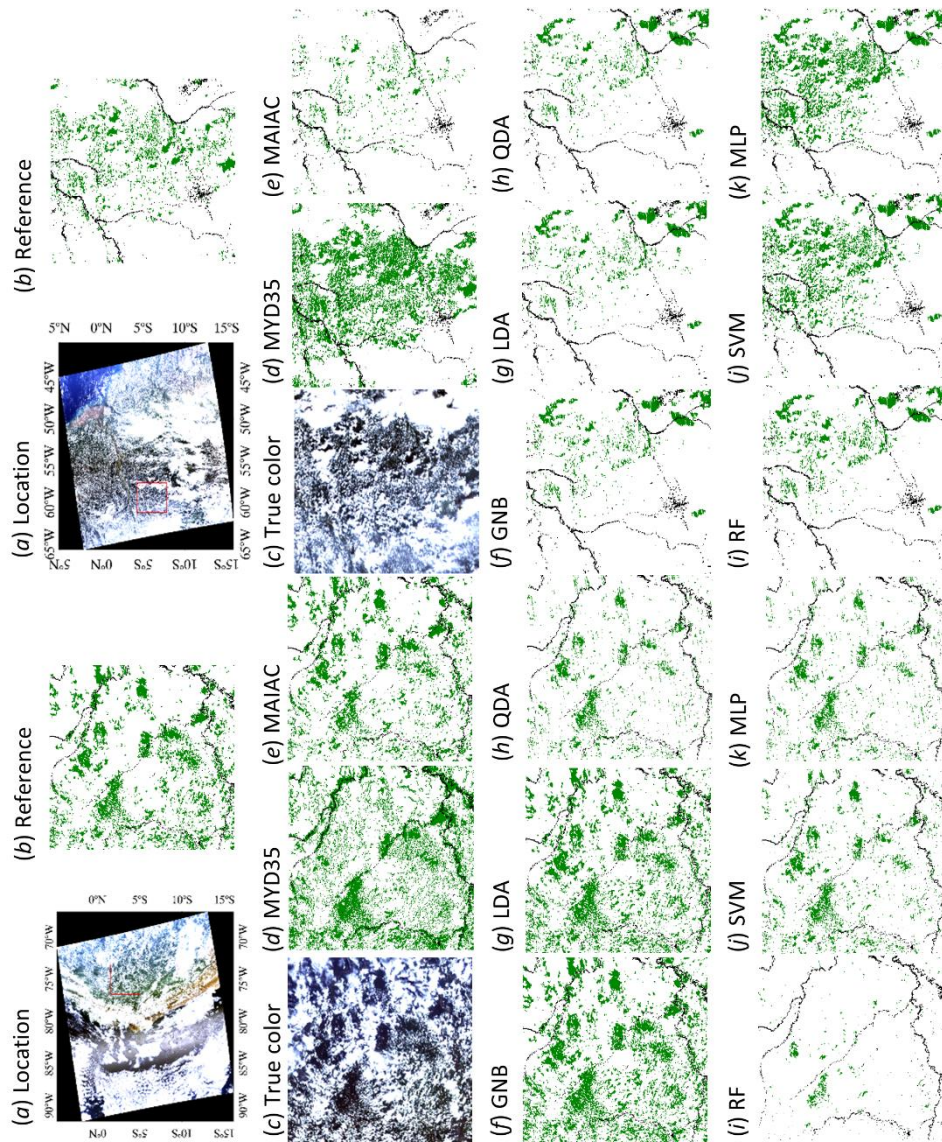


Figure A.2.7. Visual intercomparison of models and MYD35/MAIAC cloud masking results for doy 300_1855 (left), and doy 325_1710 (right). Results are displayed as follows: (a) Location, (b) Reference manually classified image, (c) True color image, (d) MYD35, (e) MAIAC, (f) GNB, (g) LDA, (h) QDA, (i) RF, (j) SVM and (k) MLP results. Cloud and clear labels are displayed in white and green respectively. Non-EBF pixels are displayed in black.

APPENDIX A.3

Table A.3.1 . Daytime validation results of the LST algorithms considered in this study at Tambopata in-situ station. Metrics presented correspond to the bias, standard deviation and RMSE value together with the correlation coefficient and the number of points used to perform the validation. Validation is performed separately for the radiometer and pyrgeometer. In bold, it is highlighted the best performing algorithm for each sensor. An absolute difference of 15 K between LST estimate and LST-insitu was used in order to screen clouds.

Daytime	Radiometer					Pyrgeometer				
	Bias (K)	σ (K)	RMSE (K)	R	N	Bias (K)	σ (K)	RMSE (K)	R	N
TERRA _{MODIS-SW}	-2.63	1.84	3.20	0.84	185	-2.45	1.72	2.98	0.83	139
TERRA _{SW-gen}	-2.56	1.77	3.11	0.85	185	-2.47	1.56	2.92	0.86	139
TERRA _{SW-simpl}	-1.65	1.60	2.30	0.88	185	-1.53	1.44	2.10	0.88	139
TERRA _{MODIS-DN}	-2.72	2.25	3.53	0.78	180	-2.63	2.08	3.35	0.78	131
TERRA _{SW-gen}	-3.04	2.40	3.86	0.76	180	-2.83	2.04	3.49	0.78	131
TERRA _{SW-simpl}	-2.18	2.46	3.28	0.77	180	-1.96	2.13	2.90	0.79	131
AQUA _{MODIS-SW}	-1.92	2.00	2.77	0.77	154	-2.66	2.09	3.39	0.70	123
AQUA _{MODIS-TES}	1.54	2.33	3.02	0.78	154	1.25	2.19	3.45	0.77	123
AQUA _{SW-gen}	-1.22	1.99	2.34	0.78	154	-1.98	1.93	2.76	0.74	123
AQUA _{SW-simpl}	-0.48	1.88	1.94	0.82	154	-1.12	1.87	2.18	0.78	123
AQUA _{MODIS-DN}	-2.63	2.46	3.60	0.69	135	-3.18	2.16	3.85	0.67	109
AQUA _{SW-gen}	-1.82	3.36	3.83	0.59	135	-2.32	2.94	3.75	0.60	109
AQUA _{SW-simpl}	-1.09	3.37	3.54	0.63	135	-1.51	3.04	3.39	0.63	109
VIIRS _{TES}	0.59	3.07	3.12	0.64	406	0.39	3.00	3.03	0.64	245
VIIRS _{SW-gen}	-2.05	2.75	3.44	0.65	406	-2.38	2.68	3.59	0.65	245
VIIRS _{SW-simpl}	-1.02	2.85	3.02	0.66	406	-1.36	2.80	3.11	0.67	245
SLSTR _{L2}	-1.64	4.06	4.38	0.61	23	-1.93	4.60	4.98	0.77	25
SLSTR _{SW-gen}	-3.65	3.02	4.74	0.75	23	-2.92	3.58	4.62	0.85	25
SLSTR _{SW-simpl}	-2.83	3.02	4.14	0.78	23	-3.73	3.55	5.14	0.83	25

Table A.3.2 . Nighttime validation results of the LST algorithms considered in this study at Tambopata in-situ station. Metrics presented correspond to the bias, standard deviation and RMSE value together with the correlation coefficient and the number of points used to perform the validation. Validation is performed separately for the radiometer and pyrgeometer. In bold, it is highlighted the best performing algorithm for each sensor. An absolute difference of 15 K between LST estimate and LST-insitu was used in order to screen clouds.

Nighttime	Radiometer					Pyrgeometer				
	Bias (K)	σ (K)	RMSE (K)	R	N	Bias (K)	σ (K)	RMSE (K)	R	N
TERRA _{MODIS-SW}	-0.79	1.07	1.34	0.92	211	-1.05	0.93	1.39	0.94	123
TERRA _{SW-gen}	-0.89	0.90	1.26	0.95	211	-1.12	0.79	1.37	0.95	123
TERRA_{SW-simpl}	-0.29	0.85	0.90	0.95	211	-0.50	0.72	0.87	0.97	123
TERRA _{MODIS-DN}	-1.32	1.98	2.38	0.71	262	-1.56	1.90	2.45	0.71	166
TERRA _{SW-gen}	-1.62	2.70	3.14	0.55	262	-1.53	2.89	3.27	0.57	166
TERRA _{SW-simpl}	-1.24	2.91	3.16	0.54	262	-1.88	2.67	3.27	0.57	166
AQUA _{MODIS-SW}	-0.51	1.44	1.54	0.86	200	-0.98	1.47	1.77	0.82	119
AQUA _{MODIS-TES}	0.82	2.67	2.73	0.70	200	0.37	2.79	2.96	0.63	119
AQUA _{SW-gen}	-0.35	1.27	1.32	0.89	200	-0.72	1.27	1.46	0.87	119
AQUA_{SW-simpl}	0.21	1.12	1.5	0.92	200	-0.15	1.17	1.18	0.89	119
AQUA _{MODIS-DN}	-1.49	2.59	2.99	0.58	281	-1.10	1.74	2.06	0.75	125
AQUA _{SW-gen}	-1.16	3.41	3.60	0.48	281	-0.97	1.85	2.07	0.73	125
AQUA _{SW-simpl}	-1.57	3.23	3.59	0.49	281	-0.36	1.77	1.81	0.76	125
VIIRS _{TES}	0.40	2.63	2.66	0.76	273	-0.06	3.23	3.23	0.79	164
VIIRS _{SW-gen}	-0.81	1.55	1.75	0.85	273	-1.25	1.82	2.2	0.88	164
VIIRS_{SW-simpl}	-0.47	1.49	1.56	0.88	273	-0.90	1.89	2.10	0.89	164
SLSTR _{L2}	-1.94	4.22	4.65	0.42	26	-1.90	4.03	4.47	0.43	28
SLSTR _{SW-gen}	-3.07	4.28	5.27	0.41	26	-3.05	4.09	5.11	0.43	28
SLSTR _{SW-simpl}	-2.32	4.16	4.77	0.44	26	-2.30	3.98	4.61	0.45	28

Table A.3.3 . Daytime validation results of the LST algorithms considered in this study at Tambopata in-situ station. Metrics presented correspond to the bias, standard deviation and RMSE value together with the correlation coefficient and the number of points used to perform the validation. Validation is performed separately for the radiometer and pyrgeometer. In bold, it is highlighted the best performing algorithm for each sensor. An absolute difference of 3 K between LST estimate and LST-insitu was used in order to screen clouds.

Daytime	Radiometer					Pyrgeometer				
	Bias (K)	σ (K)	RMSE (K)	R	N	Bias (K)	σ (K)	RMSE (K)	R	N
TERRA _{MODIS-SW}	-1.64	0.83	1.84	0.97	127	-1.63	0.88	1.85	0.95	102
TERRA _{SW-gen}	-1.65	0.85	1.85	0.96	127	-1.75	0.85	1.94	0.96	102
TERRA _{SW-simpl}	-0.85	0.81	1.18	0.96	127	-0.91	0.82	1.22	0.96	102
TERRA _{MODIS-DN}	-1.51	0.93	1.77	0.96	109	-1.62	0.92	1.87	0.96	91
TERRA _{SW-gen}	-1.69	0.79	1.87	0.97	109	-1.92	0.93	2.13	0.96	91
TERRA _{SW-simpl}	-0.90	0.76	1.18	0.98	109	-1.08	0.89	1.40	0.96	91
AQUA _{MODIS-SW}	-1.17	1.02	1.55	0.95	92	-1.67	0.77	1.84	0.96	60
AQUA _{MODIS-TES}	1.46	0.99	1.53	0.95	92	1.15	0.86	1.89	0.96	60
AQUA _{SW-gen}	-0.52	1.23	1.33	0.92	92	-1.17	1.12	1.62	0.92	60
AQUA _{SW-simpl}	-0.05	1.05	1.05	0.95	92	-0.64	0.94	1.14	0.94	60
AQUA _{MODIS-DN}	-1.07	1.07	1.52	0.94	70	-1.63	0.83	1.83	0.96	47
AQUA _{SW-gen}	0.36	1.21	1.27	0.94	70	-0.83	1.18	1.44	0.93	47
AQUA _{SW-simpl}	-0.15	1.20	1.22	0.94	70	-0.25	1.32	1.34	0.92	47
VIIRS _{TES}	0.65	1.31	1.47	0.90	264	0.41	1.35	1.41	0.90	152
VIIRS _{SW-gen}	-1.25	1.45	1.92	0.89	264	-1.61	1.36	2.12	0.90	152
VIIRS _{SW-simpl}	-0.29	1.45	1.48	0.90	264	-0.65	1.45	1.60	0.90	152
SLSTR _{L2}	0.27	0.97	1.01	0.91	16	0.43	1.17	1.25	0.86	17
SLSTR _{SW-gen}	-2.30	0.96	2.49	0.91	16	-1.93	0.94	2.15	0.92	17
SLSTR _{SW-simpl}	-1.47	0.90	1.73	0.92	16	-1.08	0.94	1.43	0.93	17

Table A.3.4 . Nighttime validation results of the LST algorithms considered in this study at Tambopata in-situ station. Metrics presented correspond to the bias, standard deviation and RMSE value together with the correlation coefficient and the number of points used to perform the validation. Validation is performed separately for the radiometer and pyrgeometer. In bold, it is highlighted the best performing algorithm for each sensor. An absolute difference of 3 K between LST estimate and LST-insitu was used in order to screen clouds.

Nighttime	Radiometer					Pyrgeometer				
	Bias (K)	σ (K)	RMSE (K)	R	N	Bias (K)	σ (K)	RMSE (K)	R	N
TERRA _{MODIS-SW}	-0.66	0.80	1.04	0.96	203	-0.93	0.71	1.17	0.96	118
TERRA _{SW-gen}	-0.78	0.65	1.01	0.97	203	-1.03	0.57	1.17	0.98	118
TERRA _{SW-simpl}	-0.19	0.56	0.60	0.98	203	-0.41	0.51	0.66	0.98	118
TERRA _{MODIS-DN}	-0.59	0.93	1.11	0.94	212	-0.81	0.82	1.16	0.94	131
TERRA _{SW-gen}	-0.76	0.79	1.09	0.96	212	-1.00	0.69	1.22	0.96	131
TERRA _{SW-simpl}	-0.29	0.73	0.79	0.96	212	-0.54	0.69	0.88	0.96	131
AQUA _{MODIS-SW}	-0.22	1.00	1.02	0.94	154	-0.55	0.86	1.02	0.94	96
AQUA _{MODIS-TES}	1.20	1.04	1.06	0.95	154	0.90	1.16	1.29	0.92	96
AQUA _{SW-gen}	-0.05	0.77	0.77	0.97	154	-0.39	0.64	0.74	0.97	96
AQUA _{SW-simpl}	0.47	0.63	0.78	0.98	154	0.13	0.57	0.59	0.98	96
AQUA _{MODIS-DN}	-0.34	1.02	1.08	0.93	212	-0.63	0.83	1.03	0.94	112
AQUA _{SW-gen}	-0.18	0.87	0.99	0.94	212	-0.49	0.78	0.92	0.95	112
AQUA _{SW-simpl}	0.32	0.85	0.91	0.95	212	0.11	0.70	0.71	0.96	112
VIIRS _{TES}	0.34	1.16	1.21	0.91	238	0.01	1.07	1.07	0.91	133
VIIRS _{SW-gen}	-0.53	0.90	1.05	0.94	238	-0.75	0.68	1.01	0.95	133
VIIRS _{SW-simpl}	-0.23	0.77	0.81	0.95	238	-0.44	0.64	0.78	0.96	133
SLSTR _{L2}	0.28	0.74	0.79	0.98	19	0.1	0.78	0.79	0.95	21
SLSTR _{SW-gen}	-0.80	0.70	1.07	0.98	19	-1.00	0.76	1.26	0.96	21
SLSTR _{SW-simpl}	-0.11	0.61	0.63	0.98	19	-0.3	0.72	0.78	0.96	21

APPENDIX A.4

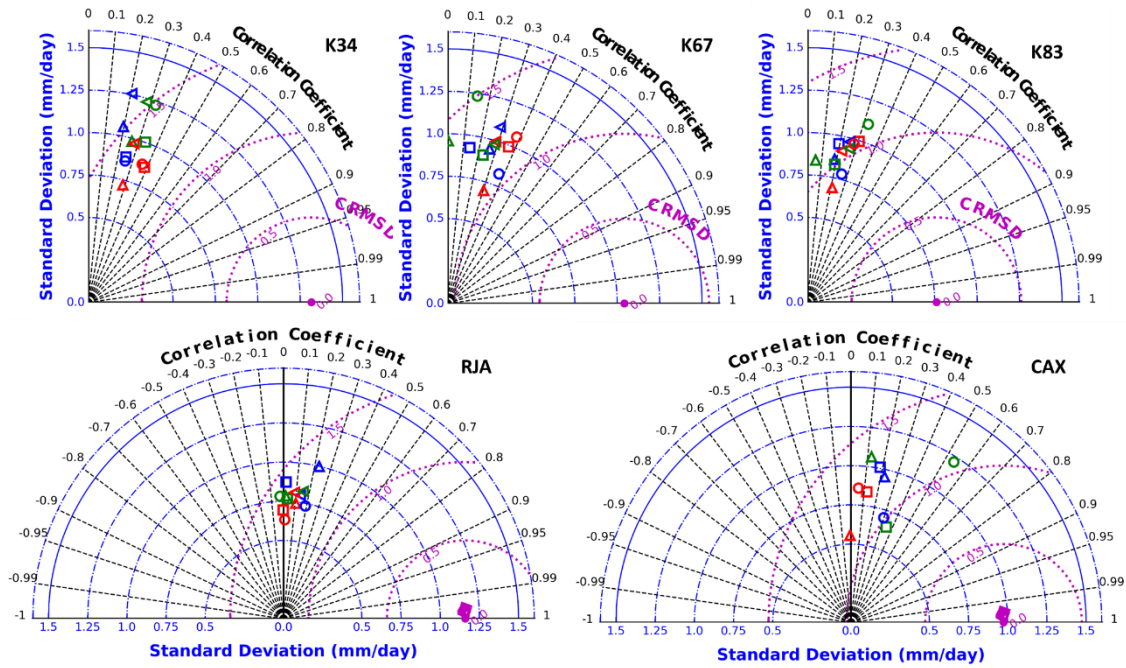


Figure A.4.1. Taylor diagrams considering Scenario-II and Bowen-Ratio corrected values.

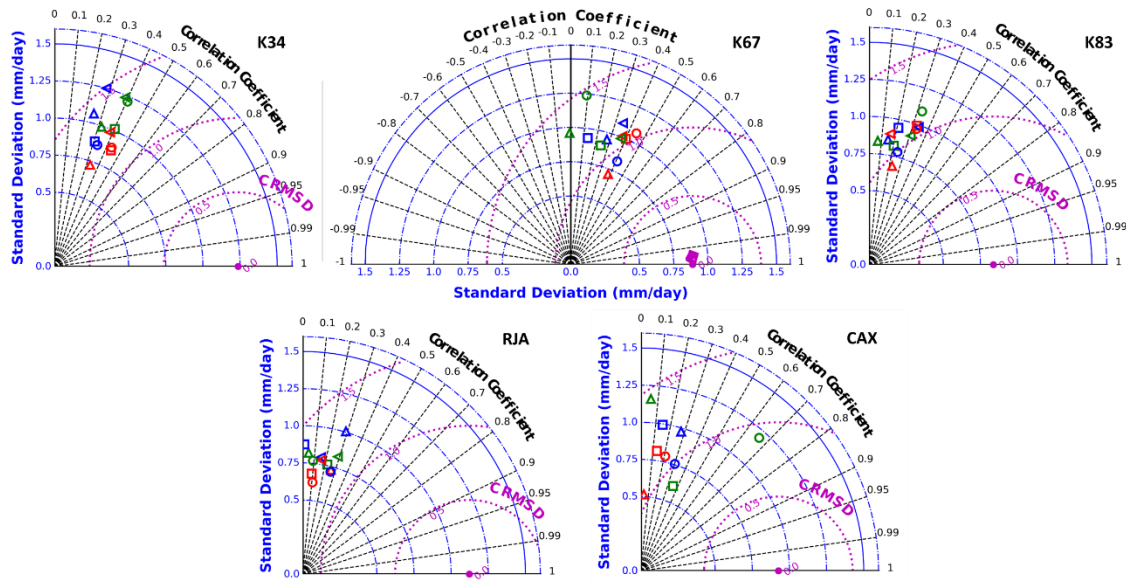


Figure A.4.2. Taylor diagrams considering Scenario-II and Energy-Residual corrected values.

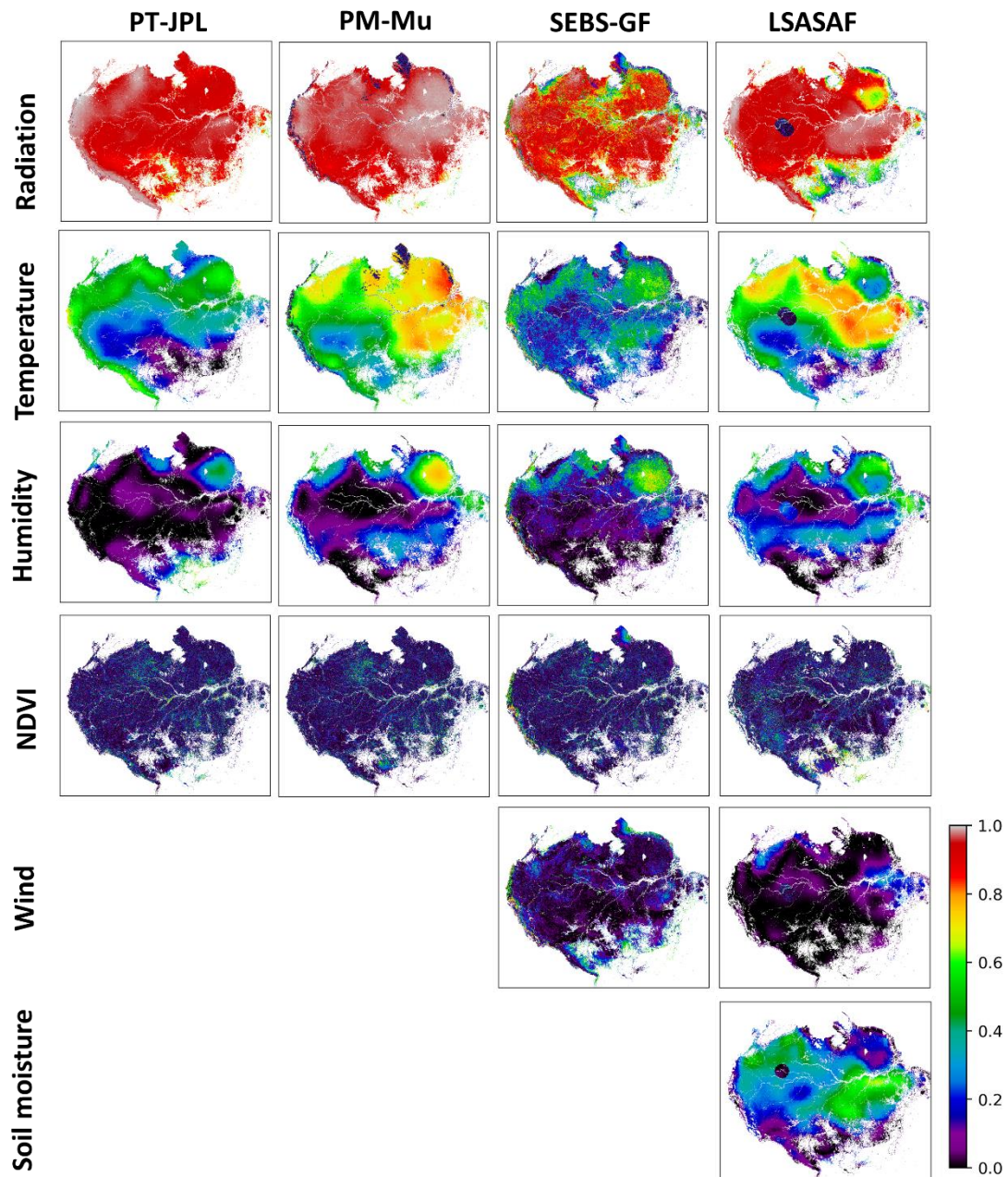


Figure A.4.3. R² value derived from the linear regression of ET model estimates against model inputs (ERA-Interim forcing). Radiation inputs refer to Rn₂₄ (PT-JPL and SEBS-GF) and SR_{in} (PM-Mu and LSASAF). Temperature and humidity inputs refer to T_a and e_a forced at the temporal scale indicated by the models. Soil moisture refers to the root zone soil moisture for LSASAF model. Non significant values (p < 0.05) are displayed in black.

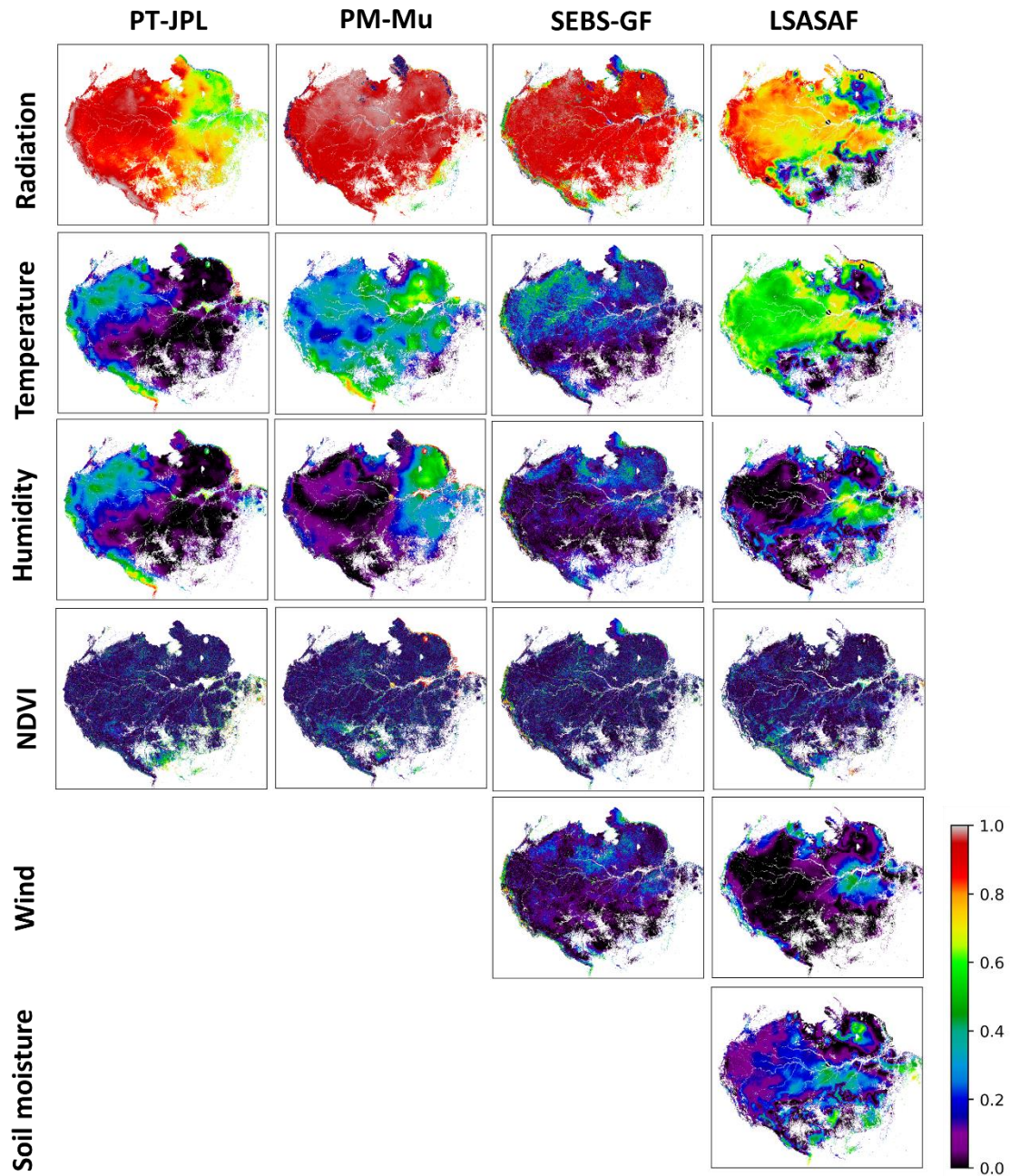


Figure A.4.4. R² value derived from the linear regression of ET model estimates against model inputs (GLDAS 2.1 forcing). Radiation inputs refer to Rn₂₄ (PT-JPL and SEBS-GF) and SR_{in} (PM-Mu and LSASAF). Temperature and humidity inputs refer to T_a and e_a forced at the temporal scale indicated by the models. Soil moisture refers to the root zone soil moisture for LSASAF model. Non significant values (p<0.05) are displayed in black.

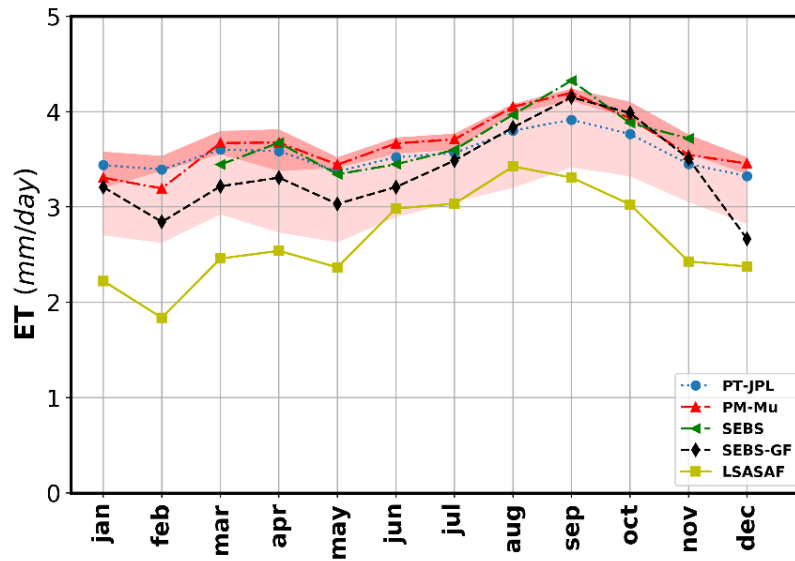


Figure A.4.5 . Time series of ET model monthly mean values. For PM-Mu a vegetation fraction cover value of 0.85 (same as f_{apar}) was considered. In-situ ET observations are represented by the shadowed area (lower, intermediate and upper limit indicating uncorrected, BR and ER ET observations respectively).

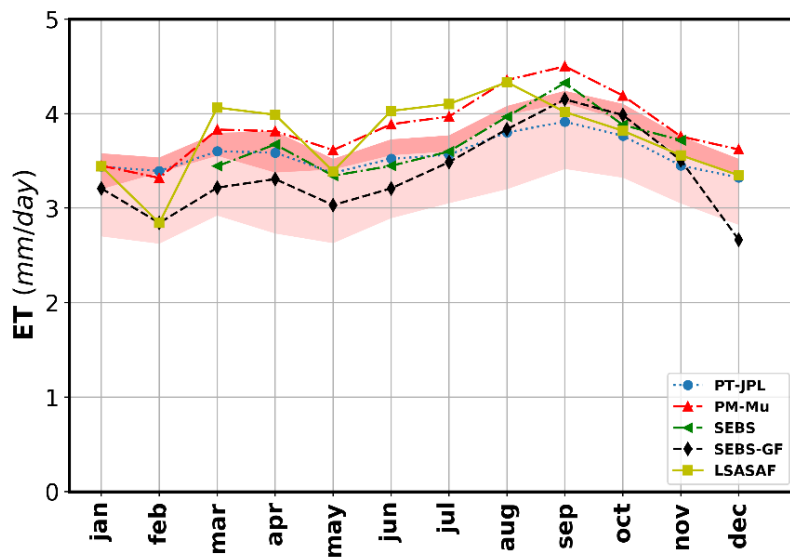


Figure A.4.6. Time series of ET model monthly mean values. For LSASAF, an interception term was added in the total latent heat flux calculation. In-situ ET observations are represented by the shadowed area (lower, intermediate and upper limit indicating uncorrected, BR and ER ET observations respectively).

Table A.4.1 Validation metrics for PM-Mu with vegetation cover fraction assumed equal as f_{apar} (0.85). Metrics considered were the bias, the root mean square error (RMSE), the correlation coefficient (R), the Taylor Skill Score (S) and the number of points used (N). All stations were used in this validation. ET refers to uncorrected in-situ ET observations, BR and ER to Bowen Ratio and Energy Residual correction methods.

	BIAS (mm/day)	RMSE (mm/day)	R	S	N
ET	0.70	1.10	0.63	0.82	1305.00
BR	0.06	1.02	0.54	0.73	1084.00
ER	-0.26	0.78	0.74	0.85	1169.00

Table A.4.2. Validation metrics for LSASAF considering the inclusion of an interception term to the total latent heat flux calculation. Metrics considered were the bias, the root mean square error (RMSE), the correlation coefficient (R), the Taylor Skill Score (S) and the number of points used (N). All stations were used in this validation. ET refers to uncorrected in-situ ET observations, BR and ER to Bowen Ratio and Energy Residual correction methods.

	BIAS (mm/day)	RMSE (mm/day)	R	S	N
ET	0.92	1.51	0.61	0.66	1602.00
BR	0.29	1.32	0.61	0.68	1084.00
ER	-0.04	1.04	0.75	0.77	1320.00

APPENDIX B

List of publications

- Gomis-Cebolla, J., Jimenez, J. C., & Sobrino, J. A. (2019). MODIS probabilistic cloud masking over the Amazonian evergreen tropical forests: a comparison of machine learning-based methods. *International Journal of Remote Sensing*, 1-26.

- Gomis-Cebolla, J., Jimenez, J. C., Sobrino, J. A., Corbari, C., & Mancini, M. (2019). Intercomparison of remote-sensing based evapotranspiration algorithms over amazonian forests. *International Journal of Applied Earth Observation and Geoinformation*, 80, 280-294.

- Gomis-Cebolla, J., Jimenez, J. C., & Sobrino, J. A. (2018). LST retrieval algorithm adapted to the Amazon evergreen forests using MODIS data. *Remote Sensing of Environment*, 204, 401-411.

- Gomis-Cebolla, J., Jiménez-Muñoz, J., & Sobrino, J. (2016). MODIS-based monthly LST products over Amazonia under different cloud mask schemes. *Data*, 1(2), 2.

REFERENCES

- Ackerman, S. A., Strabala, K. I., Menzel, W. P., Frey, R. A., Moeller, C. C., & Gumley, L. E. (1998). Discriminating clear sky from clouds with MODIS. *Journal of Geophysical Research: Atmospheres*, *103*(D24), 32141-32157.
- Ackerman, S., Strabala, K., Menzel, P., Frey, R., Moeller, C., ... & Riggs, G. (2010). Discriminating clear-sky from cloud with modis algorithm theoretical basis document (mod35).
- Allen, R. G., Tasumi, M., Morse, A., Trezza, R., Wright, J., Bastiaanssen, W., Kramber, W., Lorite, I., & Robison, C. (2007). Satellite-Based Energy Balance for Mapping Evapotranspiration with Internalized Calibration (METRIC)—Applications. *Journal of Irrigation and Drainage Engineering*, *133*(4), 395-406. [https://doi.org/10.1061/\(ASCE\)0733-9437\(2007\)133:4\(395\)](https://doi.org/10.1061/(ASCE)0733-9437(2007)133:4(395))
- Amato, U., Antoniadis, A., Cuomo, V., Cuttillo, L., Franzese, M., Murino, L., & Serio, C. (2008). Statistical cloud detection from SEVIRI multispectral images. *Remote Sensing of Environment*, *112*(3), 750-766.
- Ambaum, M. H. (2010). *Thermal physics of the atmosphere* (p. 239). Chichester, UK: Wiley-Blackwell.
- Anderson, M. C., Norman, J. M., Diak, G. R., Kustas, W. P., & Mecikalski, J. R. (1997). A two-source time-integrated model for estimating surface fluxes using thermal infrared remote sensing. *Remote Sensing of Environment*, *60*(2), 195-216.
- Anderson, M. C., Norman, J. M., Mecikalski, J. R., Otkin, J. A., & Kustas, W. P. (2007). A climatological study of evapotranspiration and moisture stress across the continental United States based on thermal remote sensing: 1. Model formulation. *Journal of Geophysical Research: Atmospheres*, *112*(D10).
- Andreae, M. O., Artaxo, P., Brandao, C., Carswell, F. E., Ciccioli, P., Da Costa, A. L., ... & Kabat, P. (2002). Biogeochemical cycling of carbon, water, energy, trace gases, and aerosols in Amazonia: The LBA-EUSTACH experiments. *Journal of Geophysical Research: Atmospheres*, *107*(D20), LBA-33.
- Andreae, M. O., Rosenfeld, D., Artaxo, P., Costa, A. A., Frank, G. P., Longo, K. M., & Silva-Dias, M. A. F. D. (2004). Smoking rain clouds over the Amazon. *Science*, *303*(5662), 1337-1342.
- Aragao, L. E., Poulter, B., Barlow, J. B., Anderson, L. O., Malhi, Y., Saatchi, S., ... & Gloor, E. (2014). Environmental change and the carbon balance of Amazonian forests. *Biological Reviews*, *89*(4), 913-931.
- Araujo, A.C., Nobre, A.D., Kruijt, B., Elbers, A., Dallorosa, R., Stefani, P., von Randow, C., Manazi, A.O., Culf, A.D., Gash, J.H.C., Valentini, R., Kabat, P., (2002). Comparative measurements of carbon dioxide fluxes from two nearby towers in a central Amazonian rainforest: the Manaus LBA site. *Journal Geophysical Research*. *107*, <http://dx.doi.org/10.1029/2001JD000676>.
- Asner, G. P., & Alencar, A. (2010). Drought impacts on the Amazon forest: the remote sensing perspective. *New phytologist*, *187*(3), 569-578.

- Atkinson, P. M., Dash, J., & Jeganathan, C. (2011). Amazon vegetation greenness as measured by satellite sensors over the last decade. *Geophysical Research Letters*, 38(19).
- Avissar, R., & Pielke, R. A. (1989). A parameterization of heterogeneous land surfaces for atmospheric numerical models and its impact on regional meteorology. *Monthly Weather Review*, 117(10), 2113-2136.
- Ayer, M., Brunk, H., Ewing, G., Reid, W., & Silverman, E. (1955). An empirical distribution function for sampling with incomplete information. *Annals of Mathematical Statistics*, 5, 641-647.
- Badgley, G., Fisher, J., Jiménez, C., Tu, K., & Vinukollu, R. (2015). On Uncertainty in Global Terrestrial Evapotranspiration Estimates from Choice of Input Forcing Datasets*. *Journal of Hydrometeorology*, 16(4), 1449-1455. doi: 10.1175/jhm-d-14-0040.1
- Bagley, J. E., Desai, A. R., Harding, K. J., Snyder, P. K., & Foley, J. A. (2014). Drought and deforestation: Has land cover change influenced recent precipitation extremes in the Amazon?. *Journal of Climate*, 27(1), 345-361.
- Balch, J. K., Nepstad, D. C., Curran, L. M., Brando, P. M., Portela, O., Guilherme, P., ... & de Carvalho Jr, O. (2011). Size, species, and fire behavior predict tree and liana mortality from experimental burns in the Brazilian Amazon. *Forest Ecology and Management*, 261(1), 68-77.
- Baldassarre, G. D., & Montanari, A. (2009). Uncertainty in river discharge observations: a quantitative analysis. *Hydrology and Earth System Sciences*, 13(6), 913-921.
- Baldocchi, D., Falge, E., Gu, L., Olson, R., Hollinger, D., Running, S., ... & Fuentes, J. (2001). FLUXNET: A new tool to study the temporal and spatial variability of ecosystem-scale carbon dioxide, water vapor, and energy flux densities. *Bulletin of the American Meteorological Society*, 82(11), 2415-2434.
- Baldridge, A.M., Hook, S. J., Grove, C. I., & Rivera, G. (2009). The ASTER spectral library version 2.0. *Remote Sensing of Environment*, 113, 711-715.
- Balsamo, G., Beljaars, A., Scipal, K., Viterbo, P., van den Hurk, B., Hirschi, M., & Betts, A. K. (2009). A revised hydrology for the ECMWF model: Verification from field site to terrestrial water storage and impact in the Integrated Forecast System. *Journal of hydrometeorology*, 10(3), 623-643.
- Barry, R. G., & Carleton, A. M. (2001). *Synoptic and dynamic climatology* (Vol. 620). London: Routledge.
- Bastiaanssen, W. G. M., Menenti, M., Feddes, R. A., & Holtslag, A. A. M. (1998). A remote sensing surface energy balance algorithm for land (SEBAL). 1. Formulation. *Journal of Hydrology*, 212-213, 198-212. [https://doi.org/10.1016/S0022-1694\(98\)00253-4](https://doi.org/10.1016/S0022-1694(98)00253-4)
- Becker, F., & Li, Z. L. (1990). Towards a local split window method over land surfaces. *Remote Sensing*, 11(3), 369-393.

- Beljaars, A. C. M., & Holtslag, A. A. M. (1991). Flux parameterization over land surfaces for atmospheric models. *Journal of Applied Meteorology*, 30(3), 327-341.
- Beljaars, A. C., & Viterbo, P. (1994). The sensitivity of winter evaporation to the formulation of aerodynamic resistance in the ECMWF model. *Boundary-Layer Meteorology*, 71(1-2), 135-149.
- Berk, A., Anderson, G. P., Acharya, P. K., & Shettle, E. P. (2008). MODTRAN5. 2.0. 0 user's manual. Spectral Sciences Inc., Burlington MA, Air Force Research Laboratory, Hanscom MA.
- Berrisford, P., Dee, D. P. K. F., Fielding, K., Fuentes, M., Kallberg, P., Kobayashi, S., & Uppala, S. (2009). The ERA-interim archive. *ERA report series*, (1), 1-16.
- Betts, R. A., Cox, P. M., Collins, M., Harris, P. P., Huntingford, C., & Jones, C. D. (2004). The role of ecosystem-atmosphere interactions in simulated Amazonian precipitation decrease and forest dieback under global climate warming. *Theoretical and applied climatology*, 78(1-3), 157-175.
- Bishop, C. M. (2006). *Pattern recognition and machine learning*. springer.
- Bonan, G. B. (1998). The land surface climatology of the NCAR Land Surface Model coupled to the NCAR Community Climate Model. *Journal of Climate*, 11(6), 1307-1326.
- Borbas, E.E, Seemann, S.W, Kern, Moy, Li, J, Gumley, L.E. and Menzel, W.P. (2011) "MODIS Atmospheric Profile Retrieval Algorithm Theoretical Basis Document (version 7)." Available at http://modisatmos.gsfc.nasa.gov/reference_atbd.html.
- Bosilovich, M. G., Lucchesi, R., & Suarez, M. (2015). MERRA-2: File specification.
- Brando, P. M., Nepstad, D. C., Davidson, E. A., Trumbore, S. E., Ray, D., & Camargo, P. (2008). Drought effects on litterfall, wood production and belowground carbon cycling in an Amazon forest: results of a throughfall reduction experiment. *Philosophical Transactions of the Royal Society B: Biological Sciences*, 363(1498), 1839-1848.
- Brando, P. M., Balch, J. K., Nepstad, D. C., Morton, D. C., Putz, F. E., Coe, M. T., ... & Alencar, A. (2014). Abrupt increases in Amazonian tree mortality due to drought–fire interactions. *Proceedings of the National Academy of Sciences*, 111(17), 6347-6352.
- Broxton, P. D., Zeng, X., Scheftic, W., & Troch, P. A. (2014). A MODIS-based global 1-km maximum green vegetation fraction dataset. *Journal of Applied Meteorology and Climatology*, 53(8), 1996-2004.
- Brutsaert, W., (1982). *Evaporation into the atmosphere*. D. Reidel, 299pp.
- Brutsaert, W. (1999). Aspects of bulk atmospheric boundary layer similarity under free-convective conditions. *Reviews of Geophysics*, 37(4), 439-451.
- Brutsaert, W. (2005). *Hydrology: an Introduction*. Cambridge University Press.
- Brutsaert, W (2013) *Evaporation into the atmosphere: Theory, history and applications*. (Vol.1) Springer Science & Business Media.

- Bulgin, C., Mittaz, J., Embury, O., Eastwood, S., & Merchant, C. (2018). Bayesian cloud detection for 37 years of Advanced Very High Resolution Radiometer (AVHRR) global area coverage (GAC) data. *Remote Sensing*, 10(1), 97.
- Campbell, G. S., & Norman, J. M. (2012). *An introduction to environmental biophysics*. Springer Science & Business Media.
- Carlson, T. N., Capehart, W. J., & Gillies, R. R. (1995). A new look at the simplified method for remote sensing of daily evapotranspiration. *Remote Sensing of Environment*, 54(2), 161-167.
- Carswell, F.E., A.L. Costa, M. Palheta, Y. Malhi, P. Meir, J.D.R. Costa, M.D. Ruivo, L.D.M. Leal, J.M.N. Costa, R.J. Clement, and J. Grace- (2002). Seasonality in CO₂ and H₂O flux at an eastern Amazonian rain forest, *Journal of Geophysical Research*, 107 (D20), 8076.
- Chai, D., Newsam, S., Zhang, H. K., Qiu, Y., & Huang, J. (2019). Cloud and cloud shadow detection in Landsat imagery based on deep convolutional neural networks. *Remote Sensing of Environment*, 225, 307-316.
- Chen, F., Mitchell, K., Schaake, J., Xue, Y., Pan, H. L., Koren, V., ... & Betts, A. (1996). Modeling of land surface evaporation by four schemes and comparison with FIFE observations. *Journal of Geophysical Research: Atmospheres*, 101(D3), 7251-7268.
- Chen, N., Li, W., Gatebe, C., Tanikawa, T., Hori, M., Shimada, R., ... & Stamnes, K. (2018). New neural network cloud mask algorithm based on radiative transfer simulations. *Remote Sensing of Environment*, 219, 62-71.
- Choudhury, B. J., & Monteith, J. L. (1988). A four-layer model for the heat budget of homogeneous land surfaces. *Quarterly Journal of the Royal Meteorological Society*, 114(480), 373-398.
- Christodoulou, C.I., Michaelides, S.C., Pattichis, C.S., (2003). Multifeature texture analysis for the classification of clouds in satellite imagery. *IEEE Transactions on Geoscience and Remote Sensing* 41, 2662–2668.
- Clark, D. B. (1996). Abolishing virginity. *Journal of Tropical Ecology*, 12(5), 735-739.
- Clark, D. A., Piper, S. C., Keeling, C. D., & Clark, D. B. (2003). Tropical rain forest tree growth and atmospheric carbon dynamics linked to interannual temperature variation during 1984–2000. *Proceedings of the national academy of sciences*, 100(10), 5852-5857.
- Cleugh, H. A., Leuning, R., Mu, Q., & Running, S. W. (2007). Regional evaporation estimates from flux tower and MODIS satellite data. *Remote Sensing of Environment*, 106(3), 285-304.
- Cohen, J. C., Silva Dias, M. A., & Nobre, C. A. (1995). Environmental conditions associated with Amazonian squall lines: A case study. *Monthly Weather Review*, 123(11), 3163-3174.

- Coll, C., Caselles, V., Valor, E., Niclòs, R., Sánchez, J. M., Galve, J. M., et al. (2007). Temperature and emissivity separation from ASTER data for low spectral contrast surfaces. *Remote Sensing of Environment*, 110, 162–175.
- Courault, D., Seguin, B., & Olioso, A. (2005). Review on estimation of evapotranspiration from remote sensing data: From empirical to numerical modeling approaches. *Irrigation and Drainage systems*, 19(3-4), 223-249.
- Cox, P. M., Betts, R. A., Jones, C. D., Spall, S. A., & Totterdell, I. J. (2000). Acceleration of global warming due to carbon-cycle feedbacks in a coupled climate model. *Nature*, 408(6809), 184.
- Cox, P. M., Betts, R. A., Collins, M., Harris, P. P., Huntingford, C., & Jones, C. D. (2004). Amazonian forest dieback under climate-carbon cycle projections for the 21st century. *Theoretical and applied climatology*, 78(1-3), 137-156.
- Cox, P. M., Harris, P. P., Huntingford, C., Betts, R. A., Collins, M., Jones, C. D., ... & Nobre, C. A. (2008). Increasing risk of Amazonian drought due to decreasing aerosol pollution. *Nature*, 453(7192), 212.
- Crosson, W. L., Al-Hamdan, M. Z., Hemmings, S. N., & Wade, G. M. (2012). A daily merged MODIS Aqua–Terra land surface temperature data set for the conterminous United States. *Remote Sensing of Environment*, 119, 315-324.
- da Costa, A. C. L., Galbraith, D., Almeida, S., Portela, B. T. T., da Costa, M., Junior, J. D. A. S., ... & Phillips, O. L. (2010). Effect of 7 yr of experimental drought on vegetation dynamics and biomass storage of an eastern Amazonian rainforest. *New Phytologist*, 187(3), 579-591.
- Da Rocha, H. R., Goulden, M. L., Miller, S. D., Menton, M. C., Pinto, L. D., de Freitas, H. C., & e Silva Figueira, A. M. (2004). Seasonality of water and heat fluxes over a tropical forest in eastern Amazonia. *Ecological applications*, 14(sp4), 22-32.
- Da Rocha, H. R., Manzi, A. O., Cabral, O. M., Miller, S. D., Goulden, M. L., Saleska, S. R., ... & Vourlitis, G. (2009). Patterns of water and heat flux across a biome gradient from tropical forest to savanna in Brazil. *Journal of Geophysical Research: Biogeosciences*, 114(G1).
- Dai, Y., Zeng, X., (1997). A land surface model (IAP94) for climate studies part I: Formulation and validation in off-line experiments. *Advances in Atmospheric Sciences*, 14(4), 433-460.
- Dai, Y., Zeng, X., Dickinson, R.E., Baker, I., Bonan, G.B., Bosilovich, M.G., Denning, A.S., Dirmeyer, P.A., Houser, P.R., Niu, G., Oleson, K.W., Schlosser, C.A., Yang, Z.L., (2003). The Common Land Model. *Bulletin of the American Meteorological Society* 84, 1013–1023. doi:10.1175/BAMS-84-8-1013
- Davidson, E. A., de Araújo, A. C., Artaxo, P., Balch, J. K., Brown, I. F., Bustamante, M. M., ... & Munger, J. W. (2012). The Amazon basin in transition. *Nature*, 481(7381), 321.
- DeBruin, H. A. (2009). Time to think: reflections of a pre-pensioned scintillometer researcher. *Bulletin of the American Meteorological Society*, 90(5), ES17-ES26.

- Dee, D. P., Uppala, S. M., Simmons, A. J., Berrisford, P., Poli, P., Kobayashi, S., ... & Bechtold, P. (2011). The ERA-Interim reanalysis: Configuration and performance of the data assimilation system. *Quarterly Journal of the royal meteorological society*, 137(656), 553-597.
- Di Vittorio, A. V., & Emery, W. J. (2002). An automated, dynamic threshold cloud-masking algorithm for daytime AVHRR images over land. *IEEE Transactions on Geoscience and Remote Sensing*, 40(8), 1682-1694.
- Dickinson, E., Henderson-Sellers, A., & Kennedy, J. (1993). Biosphere-atmosphere transfer scheme (BATS) version 1e as coupled to the NCAR community climate model.
- Dirzo, R., & Raven, P. H. (2003). *Global state of biodiversity and loss*. Annual review of Environment and Resources, 28.
- Dominguez, F., & Kumar, P. (2008). Precipitation recycling variability and ecoclimatological stability—A study using NARR data. Part I: Central US plains ecoregion. *Journal of Climate*, 21(20), 5165-5186.
- Doughty, C. E., & Goulden, M. L. (2008). Are tropical forests near a high temperature threshold?. *Journal of Geophysical Research: Biogeosciences*, 113(G1).
- El-Masri, B., Barman, R., Meiyappan, P., Song, Y., Liang, M., & Jain, A. K. (2013). Carbon dynamics in the Amazonian Basin: Integration of eddy covariance and ecophysiological data with a land surface model. *Agricultural and forest meteorology*, 182, 156-167.
- Ershadi, A., McCabe, M. F., Evans, J. P., Chaney, N. W., & Wood, E. F. (2014). Multi-site evaluation of terrestrial evaporation models using FLUXNET data. *Agricultural and Forest Meteorology*, 187, 46-61.
- Espinoza Villar, J. C., Ronchail, J., Guyot, J. L., Cochonneau, G., Naziano, F., Lavado, W., ... & Vauchel, P. (2009). Spatio-temporal rainfall variability in the Amazon basin countries (Brazil, Peru, Bolivia, Colombia, and Ecuador). *International Journal of Climatology: A Journal of the Royal Meteorological Society*, 29(11), 1574-1594.
- Espinoza, J. C., Ronchail, J., Marengo, J. A., & Segura, H. (2019). Contrasting North–South changes in Amazon wet-day and dry-day frequency and related atmospheric features (1981–2017). *Climate Dynamics*, 52(9-10), 5413-5430.
- FAO/IIASA/ISRIC/ISSCAS/JRC, (2012). *Harmonized World Soil Database (version 1.2)*. FAO, Rome, Italy and IIASA, Laxenburg, Austria.
- Feldpausch, T. R., Phillips, O. L., Brienen, R. J. W., Gloor, E., Lloyd, J., Lopez-Gonzalez, G., ... & Alvarez-Loayza, P. (2016). Amazon forest response to repeated droughts. *Global Biogeochemical Cycles*, 30(7), 964-982.
- Fisch, G., Marengo, J. A., & Nobre, C. A. (1998). Uma revisão geral sobre o clima da Amazônia. *Acta amazônica*, 28(2), 101-101.

- Fisher, J.B., Debiase, T.A., Qi, Y., Xu, M., Goldstein, A.H., (2005) Evapotranspiration models compared on a Sierra Nevada forest ecosystem. *Environmental Modelling & Software*, 20, 783–796.
- Fisher, J. B., Baldocchi, D. D., Misson, L., Dawson, T. E., & Goldstein, A. H. (2007). What the towers don't see at night: nocturnal sap flow in trees and shrubs at two AmeriFlux sites in California. *Tree Physiology*, 27(4), 597-610.
- Fisher, J. B., Tu, K. P., & Baldocchi, D. D. (2008). Global estimates of the land–atmosphere water flux based on monthly AVHRR and ISLSCP-II data, validated at 16 FLUXNET sites. *Remote Sensing of Environment*, 112(3), 901-919.
- Fisher, J. B., Malhi, Y., Bonal, D., Da Rocha, H. R., De Araujo, A. C., Gamo, M., ... & Kumagai, T. O. (2009). The land–atmosphere water flux in the tropics. *Global Change Biology*, 15(11), 2694-2714.
- Foken, T. (2008). The energy balance closure problem: an overview. *Ecological Applications*, 18(6), 1351-1367.
- Foken, T., Aubinet, M., Finnigan, J. J., Leclerc, M. Y., Mauder, M., & Paw U, K. T. (2011). Results of a panel discussion about the energy balance closure correction for trace gases. *Bulletin of the American Meteorological Society*, 92(4), ES13-ES18.
- Foken, T., Leuning, R., Oncley, S.R., Mauder, M., & Aubinet, M. (2012). Corrections and Data Quality Control. In M. Aubinet, T. Vesala & D. Papale (Eds.), *Eddy Covariance, A Practical Guide to Measurement and Data Analysis*: Springer
- Frantz, D., Haß, E., Uhl, A., Stoffels, J., & Hill, J. (2018). Improvement of the Fmask algorithm for Sentinel-2 images: Separating clouds from bright surfaces based on parallax effects. *Remote sensing of environment*, 215, 471-481.
- Fu, R., Zhu, B., & Dickinson, R. E. (1999). How do atmosphere and land surface influence seasonal changes of convection in the tropical Amazon?. *Journal of Climate*, 12(5), 1306-1321.
- Fu, R., Yin, L., Li, W., Arias, P. A., Dickinson, R. E., Huang, L., ... & Myneni, R. B. (2013). Increased dry-season length over southern Amazonia in recent decades and its implication for future climate projection. *Proceedings of the National Academy of Sciences*, 110(45), 18110-18115.
- Galbraith, D., Levy, P. E., Sitch, S., Huntingford, C., Cox, P., Williams, M., & Meir, P. (2010). Multiple mechanisms of Amazonian forest biomass losses in three dynamic global vegetation models under climate change. *New Phytologist*, 187(3), 647-665.
- Galve, J. M., Coll, C., Caselles, V., & Valor, E. (2008). An atmospheric radiosounding database for generating land surface temperature algorithms. *IEEE Transactions on Geoscience and remote Sensing*, 46(5), 1547-1557.
- García, M., Sandholt, I., Ceccato, P., Ridler, M., Mougin, E., & Kergoat, L. et al. (2013). Actual evapotranspiration in drylands derived from in-situ and satellite data: Assessing biophysical constraints. *Remote Sensing of Environment*, 131, 103-118.

- García-Santos, V., Valor, E., Caselles, V., Mira, M., Galve, J. M., & Coll, C. (2012). Evaluation of different methods to retrieve the hemispherical downwelling irradiance in the thermal infrared region for field measurements. *IEEE Transactions on Geoscience and Remote Sensing*, 51(4), 2155-2165.
- Garratt, J. R., & Hicks, B. B. (1973). Momentum, heat and water vapour transfer to and from natural and artificial surfaces. *Quarterly Journal of the Royal Meteorological Society*, 99(422), 680-687.
- Garreaud, R. D., & Aceituno, P. (2007). Atmospheric circulation over South America: mean features and variability. *The physical geography of South America*. Oxford University Press, Oxford, England.
- Garreaud, R. D., Vuille, M., Compagnucci, R., & Marengo, J. (2009). Present-day south american climate. *Palaeogeography, Palaeoclimatology, Palaeoecology*, 281(3-4), 180-195.
- Gatti, L. V., Gloor, M., Miller, J. B., Doughty, C. E., Malhi, Y., Domingues, L. G., ... & Freitas, S. (2014). Drought sensitivity of Amazonian carbon balance revealed by atmospheric measurements. *Nature*, 506(7486), 76.
- Gelaro, R., McCarty, W., Suárez, M. J., Todling, R., Molod, A., Takacs, L., ... & Wargan, K. (2017). The modern-era retrospective analysis for research and applications, version 2 (MERRA-2). *Journal of Climate*, 30(14), 5419-5454.
- Gellens-Meulenberghs, F., Arboleda, A., & Ghilain, N. (2007). Towards a continuous monitoring of evapotranspiration based on MSG data. *IAHS PUBLICATION*, 316, 228.
- Ghilain, N., Arboleda, A., & Gellens-Meulenberghs, F. (2011). Evapotranspiration modelling at large scale using near-real time MSG SEVIRI derived data. *Hydrology & Earth System Sciences*, 15(3).
- Ghosh, A., Pal, N. R., & Das, J. (2006). A fuzzy rule based approach to cloud cover estimation. *Remote Sensing of Environment*, 100(4), 531-549.
- Gillespie, A. R. (1995). Lithologic mapping of silicate rocks using TIMS. TIMS Data Users' Workshop. Pasadena, CA: Jet Propul. Lab., JPL Publication 86-38, 29-44.
- Gillespie, A. R., Rokugawa, S., Hook, S. J., Matsunaga, T., & Kahle, A. B. (1996). Temperature/emissivity separation algorithm theoretical basis document, Version 2.4. In (pp. 1-64). Maryland, USA: NASA/GSFC.
- Gillespie, A., Rokugawa, S., Matsunaga, T., Cothorn, J. S., Hook, S., & Kahle, A. B. (1998). A temperature and emissivity separation algorithm for Advanced Spaceborne Thermal Emission and Reflection Radiometer (ASTER) images. *IEEE transactions on geoscience and remote sensing*, 36(4), 1113-1126.
- Gillies, R. R., Kustas, W. P., & Humes, K. S. (1997). A verification of the « triangle » method for obtaining surface soil water content and energy fluxes from remote

measurements of the Normalized Difference Vegetation Index (NDVI) and surface e. *International Journal of Remote Sensing*, 18(15), 3145-3166.

Godin, R. (2014). Joint Polar Satellite System (JPSS) VIIRS cloud mask (VCM) algorithm theoretical basis document (ATBD). *Joint Polar Satellite System (JPSS) Ground Project Code*, 474, 474-00033.

Gómez-Chova, L., Camps-Valls, G., Calpe-Maravilla, J., Guanter, L., & Moreno, J. (2007). Cloud-screening algorithm for ENVISAT/MERIS multispectral images. *IEEE Transactions on Geoscience and Remote Sensing*, 45(12), 4105-4118.

Gomis-Cebolla, J., Jimenez, J. C., & Sobrino, J. A. (2018). LST retrieval algorithm adapted to the Amazon evergreen forests using MODIS data. *Remote Sensing of Environment*, 204, 401-411.

Gonçalves, L. G. G., Borak, J. S., Costa, M. H., Saleska, S. R., Baker, I., Restrepo-Coupe, N., ... & Arain, M. A. (2013). Overview of the large-scale biosphere-atmosphere experiment in Amazonia Data Model Intercomparison Project (LBA-DMIP). *Agricultural and Forest meteorology*, 182, 111-127.

Goulden, M.L., Miller, S.D., Rocha, H.R., Menton, M.C., Freitas, H.C., Figueira, A.M.S., Sousa, C.A.D., (2004). Diel and seasonal patterns of tropical forest CO₂ exchange. *Ecological Applications*. 14, 42–54, <http://dx.doi.org/10.1890/02-6008>.

Güntner, A. (2008). Improvement of global hydrological models using GRACE data. *Surveys in geophysics*, 29(4-5), 375-397.

Hagolle, O., Huc, M., Pascual, D. V., & Dedieu, G. (2010). A multi-temporal method for cloud detection, applied to FORMOSAT-2, VEN μ S, LANDSAT and SENTINEL-2 images. *Remote Sensing of Environment*, 114(8), 1747-1755.

Hasler, N., & Avissar, R. (2007). What controls evapotranspiration in the Amazon basin?. *Journal of Hydrometeorology*, 8(3), 380-395.

Hastenrath, S., & Heller, L. (1977). Dynamics of climatic hazards in northeast Brazil. *Quarterly Journal of the Royal Meteorological Society*, 103(435), 77-92.

Hastie, T., Tibshirani, R., Friedman, J., & Franklin, J. (2005). The elements of statistical learning: data mining, inference and prediction. *The Mathematical Intelligencer*, 27(2), 83-85.

Heidinger, A. K., Evan, A. T., Foster, M. J., & Walther, A. (2012). A naive Bayesian cloud-detection scheme derived from CALIPSO and applied within PATMOS-x. *Journal of Applied Meteorology and Climatology*, 51(6), 1129-1144.

Herman, J. D., & Usher, W. (2017). SALib: An open-source Python library for Sensitivity Analysis. *J. Open Source Software*, 2(9), 97.

Hernandez Filho, P, Y. E. Shimabukuro, and D. C. L. Lee. (1993). Final report on the forest inventory project at the Tapajos National Forest. Instituto Nacional de Pesquisas Espaciais, Sdlo Jos6 dos Campos, SP, Brazil

- Hersbach, H., & Dee, D. (2016). ERA5 reanalysis is in production. *ECMWF newsletter*, 147(7), 5-6.
- Hilker, T., Lyapustin, A. I., Tucker, C. J., Sellers, P. J., Hall, F. G., & Wang, Y. (2012). Remote sensing of tropical ecosystems: Atmospheric correction and cloud masking matter. *Remote Sensing of Environment*, 127, 370-384.
- Hilker, T., Lyapustin, A. I., Tucker, C. J., Hall, F. G., Myneni, R. B., Wang, Y., ... & Sellers, P. J. (2014). Vegetation dynamics and rainfall sensitivity of the Amazon. *Proceedings of the National Academy of Sciences*, 111(45), 16041-16046.
- Hilker, T., Lyapustin, A. I., Hall, F. G., Myneni, R., Knyazikhin, Y., Wang, Y., ... & Sellers, P. J. (2015). On the measurability of change in Amazon vegetation from MODIS. *Remote Sensing of Environment*, 166, 233-242.
- Hollstein, A., Fischer, J., Henken, C. C., & Preusker, R. (2014). Bayesian cloud detection for MERIS, AATSR, and their combination. *Atmospheric Measurement Techniques Discussions*, 7(11).
- Hollstein, A., Segl, K., Guanter, L., Brell, M., & Enesco, M. (2016). Ready-to-use methods for the detection of clouds, cirrus, snow, shadow, water and clear sky pixels in Sentinel-2 MSI images. *Remote Sensing*, 8(8), 666.
- Holmes, J. W. (1984). Measuring evapotranspiration by hydrological methods. *Agricultural Water Management*, 8(1-3), 29-40.
- Howard, L (1804). On the Modification of Clouds, 1802. *The Philosophical Magazine*, 16:97-107.
- Hughes, M., & Hayes, D. (2014). Automated detection of cloud and cloud shadow in single-date Landsat imagery using neural networks and spatial post-processing. *Remote Sensing*, 6(6), 4907-4926.
- Hulley, G. C., & Hook, S. J. (2009). The North American ASTER Land Surface Emissivity Database (NAALSED) Version 2.0. *Remote Sensing of Environment*, 113, 1967–1975.
- Hulley, G. C., & Hook, S. J. (2011). Generating consistent land surface temperature and emissivity products between ASTER and MODIS data for Earth science research. *IEEE Transactions on Geoscience and Remote Sensing*, 49, 1304–1315.
- Hulley, G. C., Hook, S. J., & Hughes, C. (2012). *MODIS MOD21 land surface temperature and emissivity algorithm theoretical basis document*. Pasadena, CA: Jet Propulsion Laboratory, National Aeronautics and Space Administration, 2012..
- Huntingford, C., Zelazowski, P., Galbraith, D., Mercado, L. M., Sitch, S., Fisher, R., ... & Malhi, Y. (2013). Simulated resilience of tropical rainforests to CO₂-induced climate change. *Nature Geoscience*, 6(4), 268.
- Hutchison, K. D., Roskovensky, J. K., Jackson, J. M., Heidinger, A. K., Kopp, T. J., Pavolonis, M. J., & Frey, R. (2005). Automated cloud detection and classification of data

collected by the Visible Infrared Imager Radiometer Suite (VIIRS). *International Journal of Remote Sensing*, 26(21), 4681-4706.

Hutyra, L.R., Munger, J.W., Saleska, S.R., Gottlieb, E., Daube, B.C., Dunn, A.L., Amaral, D.F., Camargo, P.B., Wofsy, S.C., (2007). Seasonal controls on the exchange of carbon and water in an Amazonian rain forest. *Journal of Geophysical Research. Biogeosciences*. 112, 1–16.

Irish, R. R. (2000, August). Landsat 7 automatic cloud cover assessment. In *Algorithms for Multispectral, Hyperspectral, and Ultraspectral Imagery VI* (Vol. 4049, pp. 348-355). International Society for Optics and Photonics.

Irish, R. R., Barker, J. L., Goward, S. N., & Arvidson, T. (2006). Characterization of the Landsat-7 ETM+ automated cloud-cover assessment (ACCA) algorithm. *Photogrammetric engineering & remote sensing*, 72(10), 1179-1188.

Ishida, H., Oishi, Y., Morita, K., Moriwaki, K., & Nakajima, T. Y. (2018). Development of a support vector machine based cloud detection method for MODIS with the adjustability to various conditions. *Remote Sensing of Environment*, 205, 390-407.

Jang, J. D., Viau, A. A., Anctil, F., & Bartholomé, E. (2006). Neural network application for cloud detection in SPOT VEGETATION images. *International Journal of Remote Sensing*, 27(4), 719-736.

Jardim, F. C. D. S., & Hosokawa, R. T. (1987). Estrutura da floresta equatorial úmida da estação experimental de silvicultura tropical do INPA. *Acta Amazonica*, 17, 411-534.

Jarvis, P. G. (1976). The interpretation of the variations in leaf water potential and stomatal conductance found in canopies in the field, *Philosophical Transactions of the Royal Society of London B*, 593–610.

Jiang, L., & Islam, S. (1999). A methodology for estimation of surface evapotranspiration over large areas using remote sensing observations. *Geophysical Research Letters*, 26(17), 2773-2776. <https://doi.org/10.1029/1999GL006049>

Jiménez-Muñoz, J. C., & Sobrino, J. A. (2008). Split-window coefficients for land surface temperature retrieval from low-resolution thermal infrared sensors. *IEEE geoscience and remote sensing letters*, 5(4), 806-809.

Jiménez-Muñoz, J. C., Sobrino, J. A., Mattar, C., & Malhi, Y. (2013). Spatial and temporal patterns of the recent warming of the Amazon forest. *Journal of Geophysical Research: Atmospheres*, 118(11), 5204-5215.

Jiménez-Muñoz, J. C., Mattar, C., Sobrino, J. A., & Malhi, Y. (2015). A database for the monitoring of thermal anomalies over the Amazon forest and adjacent intertropical oceans. *Scientific data*, 2, 150024.

Jiménez-Muñoz, J. C., Mattar, C., Barichivich, J., Santamaría-Artigas, A., Takahashi, K., Malhi, Y., ... & Van Der Schrier, G. (2016a). Record-breaking warming and extreme drought in the Amazon rainforest during the course of El Niño 2015–2016. *Scientific reports*, 6, 33130.

- Jiménez-Muñoz, J. C., Mattar, C., Sobrino, J. A., & Malhi, Y. (2016b). Digital thermal monitoring of the Amazon forest: an intercomparison of satellite and reanalysis products. *International journal of digital earth*, 9(5), 477-498.
- Jimenez, J. C., Barichivich, J., Mattar, C., Takahashi, K., Santamaría-Artigas, A., Sobrino, J. A., & Malhi, Y. (2018). Spatio-temporal patterns of thermal anomalies and drought over tropical forests driven by recent extreme climatic anomalies. *Philosophical Transactions of the Royal Society B: Biological Sciences*, 373(1760), 20170300.
- Jung, M., Reichstein, M., & Bondeau, A. (2009). Towards global empirical upscaling of FLUXNET eddy covariance observations: validation of a model tree ensemble approach using a biosphere model. *Biogeosciences*, 6(10), 2001-2013. <https://doi.org/10.5194/bg-6-2001-2009>
- Kalma, J. D., & Jupp, D. L. B. (1990). Estimating evaporation from pasture using infrared thermometry: evaluation of a one-layer resistance model. *Agricultural and Forest Meteorology*, 51(3-4), 223-246.
- Kalma, J. D., McVicar, T. R., & McCabe, M. F. (2008). Estimating land surface evaporation: A review of methods using remotely sensed surface temperature data. *Surveys in Geophysics*, 29(4-5), 421-469.
- Kanamitsu, M. (1989). Description of the NMC global data assimilation and forecast system. *Weather and Forecasting*, 4(3), 335-342.
- Kanamitsu, M., Ebisuzaki, W., Woollen, J., Yang, S. K., Hnilo, J. J., Fiorino, M., & Potter, G. L. (2002). Ncep–doe amip-ii reanalysis (r-2). *Bulletin of the American Meteorological Society*, 83(11), 1631-1644.
- Karlsson, K. G., Johansson, E., & Devasthale, A. (2015). Advancing the uncertainty characterisation of cloud masking in passive satellite imagery: Probabilistic formulations for NOAA AVHRR data. *Remote Sensing of Environment*, 158, 126-139.
- Keller, M., Alencar, A., Asner, G. P., Braswell, B., Bustamante, M., Davidson, E., ... & Kruijt, B. (2004). Ecological research in the large-scale biosphere–atmosphere experiment in Amazonia: early results. *Ecological Applications*, 14(sp4), 3-16.
- Kilpatrick, K. A., Podestá, G., Williams, E., Walsh, S., & Minnett, P. J. (2019). Alternating Decision Trees for Cloud Masking in MODIS and VIIRS NASA Sea Surface Temperature Products. *Journal of Atmospheric and Oceanic Technology*, 36(3), 387-407.
- Kleist, D. T., Parrish, D. F., Derber, J. C., Treadon, R., Errico, R. M., & Yang, R. (2009). Improving incremental balance in the GSI 3DVAR analysis system. *Monthly Weather Review*, 137(3), 1046-1060.
- Kljun, N., Calanca, P., Rotach, M., and Schmid, H. (2004). A Simple Parameterisation for Flux Footprint Predictions, *Boundary-Layer Meteorology*, 112, 503–523.
- Kondratyev, K. Y. *Radiation in the Atmosphere Academic*. New York, page 915, 1969

Koster, R. D., & Suarez, M. J. (1996). *Energy and water balance calculations in the Mosaic LSM*. National Aeronautics and Space Administration, Goddard Space Flight Center, Laboratory for Atmospheres, Data Assimilation Office.

Kruijt, B., Elbers, J. A., Von Randow, C., Araujo, A. C., Oliveira, P. J., Culf, A., ... & Moors, E. J. (2004). The robustness of eddy correlation fluxes for Amazon rainforest conditions: Ecological Archives A014-024-A1. *Ecological Applications*, 14(sp4), 101-113.

Kumar, S. V., Peters-Lidard, C. D., Tian, Y., Houser, P. R., Geiger, J., Olden, S., ... & Adams, J. (2006). Land information system: An interoperable framework for high resolution land surface modeling. *Environmental modelling & software*, 21(10), 1402-1415.

Kustas, W. P., Choudhury, B. J., Moran, M. S., Reginato, R. J., Jackson, R. D., Gay, L. W., & Weaver, H. L. (1989). Determination of sensible heat flux over sparse canopy using thermal infrared data. *Agricultural and Forest Meteorology*, 44(3), 197-216. [https://doi.org/10.1016/0168-1923\(89\)90017-8](https://doi.org/10.1016/0168-1923(89)90017-8)

Kustas, W. P. (1990). Estimates of evapotranspiration with a one-and two-layer model of heat transfer over partial canopy cover. *Journal of Applied Meteorology*, 29(8), 704-715.

Kustas, W. P., & Norman, J. M. (1999). Evaluation of soil and vegetation heat flux predictions using a simple two-source model with radiometric temperatures for partial canopy cover. *Agricultural and Forest Meteorology*, 94(1), 13-29.

Lafont, D., Jourdan, O., & Guillemet, B. (2006). Mesoscale cloud pattern classification over ocean with a neural network using a new index of cloud variability. *International Journal of Remote Sensing*, 27(16), 3533-3552.

Lagouarde, J. P., Bonnefond, J. M., Kerr, Y. H., McAneney, K. J., & Irvine, M. (2002). Integrated sensible heat flux measurements of a two-surface composite landscape using scintillometry. *Boundary-layer meteorology*, 105(1), 5-35.

Le Hégarat-Masclé, S., & André, C. (2009). Use of Markov random fields for automatic cloud/shadow detection on high resolution optical images. *ISPRS Journal of Photogrammetry and Remote Sensing*, 64(4), 351-366.

L'Ecuyer, T. S., Wood, N. B., Haladay, T., Stephens, G. L., & Stackhouse Jr, P. W. (2008). Impact of clouds on atmospheric heating based on the R04 CloudSat fluxes and heating rates data set. *Journal of Geophysical Research: Atmospheres*, 113(D8).

Lee, Y., Wahba, G., & Ackerman, S. A. (2004). Cloud classification of satellite radiance data by multicategory support vector machines. *Journal of Atmospheric and Oceanic Technology*, 21(2), 159-169.

Leinenkugel, P., Kuenzer, C., & Dech, S. (2013). Comparison and enhancement of MODIS cloud mask products for Southeast Asia. *International journal of remote sensing*, 34(8), 2730-2748.

- Leitold, V., Morton, D. C., Longo, M., dos-Santos, M. N., Keller, M., & Scaranello, M. (2018). El Niño drought increased canopy turnover in Amazon forests. *New Phytologist*, 219(3), 959-971.
- Lettenmaier, D. P., & Famiglietti, J. S. (2006). Hydrology: Water from on high. *Nature*, 444(7119), 562.
- Leuning, R., Zhang, Y. Q., Rajaud, A., Cleugh, H., & Tu, K. (2008). A simple surface conductance model to estimate regional evaporation using MODIS leaf area index and the Penman-Monteith equation. *Water Resources Research*, 44(10), W10419.
- Li, J., Menzel, W. P., Yang, Z., Frey, R. A., & Ackerman, S. A. (2003). High-spatial-resolution surface and cloud-type classification from MODIS multispectral band measurements. *Journal of Applied Meteorology*, 42(2), 204-226.
- Li, Z. L., Tang, R., Wan, Z., Bi, Y., Zhou, C., Tang, B., ... & Zhang, X. (2009). A review of current methodologies for regional evapotranspiration estimation from remotely sensed data. *Sensors*, 9(5), 3801-3853.
- Li, Z. L., Tang, B. H., Wu, H., Ren, H., Yan, G., Wan, Z., ... & Sobrino, J. A. (2013). Satellite-derived land surface temperature: Current status and perspectives. *Remote sensing of environment*, 131, 14-37.
- Li, Z., Shen, H., Li, H., Xia, G., Gamba, P., & Zhang, L. (2017). Multi-feature combined cloud and cloud shadow detection in GaoFen-1 wide field of view imagery. *Remote sensing of environment*, 191, 342-358.
- Li, Z., Shen, H., Cheng, Q., Liu, Y., You, S., & He, Z. (2019). Deep learning based cloud detection for medium and high resolution remote sensing images of different sensors. *ISPRS Journal of Photogrammetry and Remote Sensing*, 150, 197-212.
- Liang, X., Lettenmaier, D. P., Wood, E. F., & Burges, S. J. (1994). A simple hydrologically based model of land surface water and energy fluxes for general circulation models. *Journal of Geophysical Research: Atmospheres*, 99(D7), 14415-14428.
- Liebmann, B., & Marengo, J. (2001). Interannual variability of the rainy season and rainfall in the Brazilian Amazon Basin. *Journal of Climate*, 14(22), 4308-4318.
- Liu, Y., Xia, J., Shi, C. X., & Hong, Y. (2009). An improved cloud classification algorithm for China's FY-2C multi-channel images using artificial neural network. *Sensors*, 9(7), 5558-5579.
- Liu, R., & Liu, Y. (2013). Generation of new cloud masks from MODIS land surface reflectance products. *Remote Sensing of Environment*, 133, 21-37.
- Long, D., Singh, V. P., & Scanlon, B. R. (2012). Deriving theoretical boundaries to address scale dependencies of triangle models for evapotranspiration estimation. *Journal of Geophysical Research: Atmospheres*, 117(D5), D05113.

- Long, D., Longuevergne, L., & Scanlon, B. R. (2014). Uncertainty in evapotranspiration from land surface modeling, remote sensing, and GRACE satellites. *Water Resources Research*, 50(2), 1131-1151.
- Lumley, J. L., & Panofsky, H. A. (1964). The structure of atmospheric turbulence. *Interscience Monographs and Texts in Physics and Astronomy*, New York: Wiley, 1964.
- Luo, Y., Trishchenko, A. P., & Khlopenkov, K. V. (2008). Developing clear-sky, cloud and cloud shadow mask for producing clear-sky composites at 250-meter spatial resolution for the seven MODIS land bands over Canada and North America. *Remote Sensing of Environment*, 112(12), 4167-4185.
- Lyapustin, A., & Wang, Y. (2007). MAIAC: multi-angle implementation of atmospheric correction for MODIS. *Algorithm Theoretical Basis Document*, <http://neptune.gsfc.nasa.gov/bsb/subpages/index.php>, 69.
- Lyapustin, A., Wang, Y., & Frey, R. (2008). An automatic cloud mask algorithm based on time series of MODIS measurements. *Journal of Geophysical Research: Atmospheres*, 113(D16).
- Mace, G. G., & Zhang, Q. (2014). The CloudSat radar-lidar geometrical profile product (RL-GeoProf): Updates, improvements, and selected results. *Journal of Geophysical Research: Atmospheres*, 119(15), 9441-9462.
- Maidment, D. R. (1993). *Handbook of hydrology*: McGraw-Hill. ISBN: 0070397325/9780070397323.
- Malhi, Y., Pegoraro, E., Nobre, A. D., Pereira, M. G. P., Grace, J., Culf, A. D., & Clement, R. (2002). Energy and water dynamics of a central Amazonian rain forest. *Journal of Geophysical Research: Atmospheres*, 107(D20), LBA-45.
- Malhi, Y., Roberts, J., Betts, R., Killeen, T., Li, W. and Nobre, C. (2008). Climate Change, Deforestation, and the Fate of the Amazon. *Science*, 319, 169-172.
- Mantua NJ, Hare SR, Zhang Y, Wallace JM, Francis RC. (1997). A Pacific interdecadal climate oscillation with impacts on salmon production. *Bulletin of the American Meteorological Society* **78**: 1069–1079.
- Marchand, R., Mace, G. G., Ackerman, T., & Stephens, G. (2008). Hydrometeor detection using CloudSat—An Earth-orbiting 94-GHz cloud radar. *Journal of Atmospheric and Oceanic Technology*, 25(4), 519-533.
- Marengo, J. A. (1992). Interannual variability of surface climate in the Amazon basin. *International Journal of Climatology*, 12(8), 853-863.
- Marengo, J. A., Liebmann, B., Kousky, V. E., Filizola, N. P., & Wainer, I. C. (2001). Onset and end of the rainy season in the Brazilian Amazon Basin. *Journal of Climate*, 14(5), 833-852.

- Marengo, J. A. (2004). Interdecadal variability and trends of rainfall across the Amazon basin. *Theoretical and applied climatology*, 78(1-3), 79-96.
- Marengo, J. A., Tomasella, J., Alves, L. M., Soares, W. R., & Rodriguez, D. A. (2011). The drought of 2010 in the context of historical droughts in the Amazon region. *Geophysical Research Letters*, 38(12).
- Marengo, J. A., & Espinoza, J. C. (2016). Extreme seasonal droughts and floods in Amazonia: causes, trends and impacts. *International Journal of Climatology*, 36(3), 1033-1050.
- Marengo, J. A., Souza, C. A., Thonicke, K., Burton, C., Halladay, K., Betts, R. A., & Soares, W. R. (2018). Changes in climate and land use over the Amazon Region: current and future variability and trends. *Frontiers in Earth Science*, 6, 228.
- Martens, B., Miralles, D.G., Lievens, H., van der Schalie, R., de Jeu, R.A.M., Fernández-Prieto, D., Beck, H.E., Dorigo, W.A., and Verhoest, N.E.C. (2017). GLEAM v3: satellite-based land evaporation and root-zone soil moisture, *Geoscientific Model Development*, 10, 1903–1925, doi: 10.5194/gmd-10-1903-2017.
- Martin, S. T., Artaxo, P., Machado, L. A. T., Manzi, A. O., Souza, R. A. F., Schumacher, C., ... & Fisch, G. (2016). Introduction: Observations and modeling of the green ocean Amazon (GoAmazon2014/5). *Atmospheric Chemistry and Physics*, 16(8).
- Mather, J. H., & Voyles, J. W. (2013). The ARM Climate Research Facility: A review of structure and capabilities. *Bulletin of the American Meteorological Society*, 94(3), 377-392.
- Mather, P., & Tso, B. (2016). *Classification methods for remotely sensed data*. CRC press.
- Matsunaga, T. (1994). A temperature-emissivity separation method using an empirical relationship between the mean, the maximum, and the minimum of the thermal infrared emissivity spectrum. *Journal of the Remote Sensing Society of Japan*, 14(3), 230-241.
- Mazzoni, D., Garay, M. J., Davies, R., & Nelson, D. (2007). An operational MISR pixel classifier using support vector machines. *Remote Sensing of Environment*, 107(1-2), 149-158.
- McMillin, L. M. (1975). Estimation of sea surface temperatures from two infrared window measurements with different absorption. *Journal of Geophysical Research*, 80(36), 5113-5117.
- Michel, D., Jiménez, C., Miralles, D. G., Jung, M., Hirschi, M., Ershadi, A., ... & Seneviratne, S. I. (2016). The WACMOS-ET project—Part 1: Tower-scale evaluation of four remote-sensing-based evapotranspiration algorithms. *Hydrology and Earth System Sciences*, 20(2), 803-822.
- Miller, S. D., Goulden, M. L., Menton, M. C., da Rocha, H. R., de Freitas, H. C., Figueira, A. M. E. S., & Dias de Sousa, C. A. (2004). Biometric and micrometeorological measurements of tropical forest carbon balance. *Ecological Applications*, 14(sp4), 114-126

- Miller, S. D., de Sousa, C. A. D., Menton, M. C., Maia, A. R., da Rocha, H. R., & Goulden, M. L. (2008). Effects of selective logging on tropical forest tree growth. *Journal of Geophysical Research: Biogeosciences*, 113(G1).
- Miralles, D. G., Holmes, T. R. H., De Jeu, R. A. M., Gash, J. H., Meesters, A. G. C. A., & Dolman, A. J. (2011). Global land-surface evaporation estimated from satellite-based observations. *Hydrology and Earth System Sciences*, 15(2), 453-469. <https://doi.org/10.5194/hess-15-453-2011>
- Miralles, D. G., Jiménez, C., Jung, M., Michel, D., Ershadi, A., McCabe, M. F., ... & Mu, Q. (2016). The WACMOS-ET project-Part 2: Evaluation of global terrestrial evaporation data sets. *Hydrology and Earth System Sciences*, 20(2), 823-842.
- Moene, A. F., & Van Dam, J. C. (2014). *Transport in the atmosphere-vegetation-soil continuum*. Cambridge University Press.
- Molod, A., Takacs, L., Suarez, M., & Bacmeister, J. (2015). Development of the GEOS-5 atmospheric general circulation model: Evolution from MERRA to MERRA2. *Geoscientific Model Development*, 8(5), 1339-1356.
- Monin, A. S., & Obukhov, A. M. (1954). Basic laws of turbulent mixing in the atmosphere near the ground. *Tr. Akad. Nauk SSSR Geofiz. Inst*, 24(151), 163-187.
- Monteith, J.L. (1965). Evaporation and environment. Symposium of the society if experimental biology, 19:205-224.
- Moore, C. J., & Fisch, G. (1986). Estimating heat storage in Amazonian tropical forest. *Agricultural and Forest Meteorology*, 38(1-3), 147-168.
- Mu, Q., Heinsch, F. A., Zhao, M., & Running, S. W. (2007). Development of a global evapotranspiration algorithm based on MODIS and global meteorology data. *Remote sensing of Environment*, 111(4), 519-536.
- Mu, Q.Z., Zhao, M.S., Running, S.W. (2011). Improvements to a MODIS global terrestrial evapotranspiration algorithm. *Remote Sensing of Environment*. 115, 1781–1800.
- Musial, J. P., Hüsler, F., Sütterlin, M. B., Neuhaus, C., & Wunderle, S. (2014). Probabilistic approach to cloud and snow detection on Advanced Very High Resolution Radiometer (AVHRR) imagery. *Atmospheric Measurement Techniques (AMT)*, 7(3), 799-822.
- Nepstad, D. C., Stickler, C. M., Filho, B. S., & Merry, F. (2008). Interactions among Amazon land use, forests and climate: prospects for a near-term forest tipping point. *Philosophical Transactions of the Royal Society B: Biological Sciences*, 363(1498), 1737-1746.
- Nishida, K., Nemani, R. R., Glassy, J. M., & Running, S. W. (2003). Development of an evapotranspiration index from Aqua/MODIS for monitoring surface moisture status. *IEEE Transactions on Geoscience and Remote Sensing*, 41(2), 493-501.

- Nobre, C. A., Obregón, G. O., Marengo, J. A., Fu, R., & Poveda, G. (2009). Characteristics of Amazonian climate: Main features. *Amazonia and Global Change*, edited by: Keller, M., Bustamante, M., Gash, J., Silva Dias, P., *Geophys. Mon. Ser.*, 186, 149-162.
- Nobre, C. A., Sampaio, G., Borma, L. S., Castilla-Rubio, J. C., Silva, J. S., & Cardoso, M. (2016). Land-use and climate change risks in the Amazon and the need of a novel sustainable development paradigm. *Proceedings of the National Academy of Sciences*, 113(39), 10759-10768.
- Norman, J. M., & Becker, F. (1995). Terminology in thermal infrared remote sensing of natural surfaces. *Agricultural and Forest Meteorology*, 77(3-4), 153-166.
- Norman, J. M., Kustas, W. P., & Humes, K. S. (1995). Source approach for estimating soil and vegetation energy fluxes in observations of directional radiometric surface temperature. *Agricultural and Forest Meteorology*, 77(3-4), 263-293.
- Norman, J. M., Anderson, M. C., Kustas, W. P., French, A. N., Mecikalski, J., Torn, R., ... & Tanner, B. C. W. (2003). Remote sensing of surface energy fluxes at 101-m pixel resolutions. *Water Resources Research*, 39(8).
- Oyama, M. D., & Nobre, C. A. (2003). A new climate-vegetation equilibrium state for tropical South America. *Geophysical research letters*, 30(23).
- Pedregosa, F., Varoquaux, G., Gramfort, A., Michel, V., Thirion, B., Grisel, O., ... & Vanderplas, J. (2011). Scikit-learn: Machine learning in Python. *Journal of machine learning research*, 12(Oct), 2825-2830.
- Perry, E. M., & Moran, M. S. (1994). An evaluation of atmospheric corrections of radiometric surface temperatures for a semiarid rangeland watershed. *Water resources research*, 30(5), 1261-1269.
- Phillips, O. L., Aragão, L. E., Lewis, S. L., Fisher, J. B., Lloyd, J., López-González, G., ... & Van Der Heijden, G. (2009). Drought sensitivity of the Amazon rainforest. *Science*, 323(5919), 1344-1347.
- Platt, J. (1999). Probabilistic outputs for support vector machines and comparisons to regularized likelihood methods. *Advances in large margin classifiers*, 10(3), 61-74.
- Prata, A. J. (2002). Land surface temperature measurement from space: AATSR algorithm theoretical basis document. *Contract Report to ESA, CSIRO Atmospheric Research, Aspendale, Victoria, Australia, 2002*, 1-34.
- Price, J. C. (1990). Using spatial context in satellite data to infer regional scale
- Priestley, C.H.B., Taylor, R.J.(1972). On the assessment of surface heat flux and evaporation using large-scale parameters. *Monthly Weather Review*. 100, 81–92.
- Rammig, A., Jupp, T., Thonicke, K., Tietjen, B., Heinke, J., Ostberg, S., ... & Cox, P. (2010). Estimating the risk of Amazonian forest dieback. *New Phytologist*, 187(3), 694-706.

- Rana, G., & Katerji, N. (2000). Measurement and estimation of actual evapotranspiration in the field under Mediterranean climate: a review. *European Journal of agronomy*, 13(2-3), 125-153.
- Reichle, R., R. Koster, G. De Lannoy, B. Forman, Q. Liu, S. Mahanama, and A. Toure, (2011). Assessment and enhancement of MERRA land surface hydrology estimates. *Journal of Climate*, 24, 6322–6338, doi:10.1175/JCLI-D-10-05033.1
- Remedios, J. (2012). SLSTR ATBD Land Surface Temperature, Sentinel-3 Optical Products and Algorithm Definition, Version 2.3, ref. S3-L2-SD-03-T03-ULNILU-ATBD_L2LST, Oct. 10, 2012, https://sentinel.esa.int/documents/247904/349589/SLSTR_Level-2_LST_ATBD.pdf.
- Restrepo-Coupe, N., da Rocha, H. R., Hutyra, L. R., da Araujo, A. C., Borma, L. S., Christoffersen, B., ... & Fitzjarrald, D. R. (2013). What drives the seasonality of photosynthesis across the Amazon basin? A cross-site analysis of eddy flux tower measurements from the Brasil flux network. *Agricultural and Forest Meteorology*, 182, 128-144.
- Ricciardelli, E., Romano, F., & Cuomo, V. (2008). Physical and statistical approaches for cloud identification using meteosat second generation-spinning enhanced visible and infrared imager data. *Remote sensing of environment*, 112(6), 2741-2760.
- Rienecker, M. M., Suarez, M. J., Gelaro, R., Todling, R., Bacmeister, J., Liu, E., ... & Bloom, S. (2011). MERRA: NASA's modern-era retrospective analysis for research and applications. *Journal of climate*, 24(14), 3624-3648.
- Roads, J. (2003). The NCEP–NCAR, NCEP–DOE, and TRMM tropical atmosphere hydrologic cycles. *Journal of Hydrometeorology*, 4(5), 826-840.
- Rodell, M., Houser, P.R., Jambor, U., Gottschalck, J., Mitchell, K.E., Meng, C.-J., Arsenault, K., Cosgrove, B.A., Radakovich, J., Bosilovich, M.G., Entin, J.K., Walker, J.P., Lohmann, D., Toll, D., (2004). The Global Land Data Assimilation System. *Bulletin of the American Meteorological Society* 85, 381–394. doi:10.1175/BAMS-85-3-381
- Roerink, G. J., Su, Z., & Menenti, M. (2000). S-SEBI: A simple remote sensing algorithm to estimate the surface energy balance. *Physics and Chemistry of the Earth, Part B: Hydrology, Oceans and Atmosphere*, 25(2), 147-157. [https://doi.org/10.1016/S1464-1909\(99\)00128-8](https://doi.org/10.1016/S1464-1909(99)00128-8)
- Ronchail, J., Cochonneau, G., Molinier, M., Guyot, J. L., De Miranda Chaves, A. G., Guimarães, V., & De Oliveira, E. (2002). Interannual rainfall variability in the Amazon basin and sea-surface temperatures in the equatorial Pacific and the tropical Atlantic Oceans. *International Journal of Climatology: A Journal of the Royal Meteorological Society*, 22(13), 1663-1686.
- Rothman, L. S., Gamache, R. R., Tipping, R. H., Rinsland, C. P., Smith, M. A. H., Benner, D. C., ... & Goldman, A. (1992). The HITRAN molecular database: editions of 1991 and 1992. *Journal of Quantitative Spectroscopy and Radiative Transfer*, 48(5-6), 469-507.

- Rothman, L. S., Rinsland, C. P., Goldman, A., Massie, S. T., Edwards, D. P., Flaud, J. M., ... & Schroeder, J. (1998). The HITRAN molecular spectroscopic database and HAWKS (HITRAN atmospheric workstation): 1996 edition. *Journal of Quantitative Spectroscopy and Radiative Transfer*, 60(5), 665-710.
- Ryu, Y., Baldocchi, D. D., Kobayashi, H., van Ingen, C., Li, J., Black, T. A., ... & Rouspard, O. (2011). Integration of MODIS land and atmosphere products with a coupled-process model to estimate gross primary productivity and evapotranspiration from 1 km to global scales. *Global Biogeochemical Cycles*, 25(4).
- Saitwal, K., Azimi-Sadjadi, M. R., & Reinke, D. (2003). A multichannel temporally adaptive system for continuous cloud classification from satellite imagery. *IEEE transactions on geoscience and remote sensing*, 41(5), 1098-1104.
- Saleska, S. R., Didan, K., Huete, A. R., & Da Rocha, H. R. (2007). Amazon forests green-up during 2005 drought. *Science*, 318(5850), 612-612.
- Saleska, S. R., da Rocha, H. R., Huete, A. R., Nobre, A. D., Artaxo, P., and Shimabukuro, Y. E. (2013). LBA-ECO CD-32 Flux Tower Network Data Compilation, Brazilian Amazon: 1999–2006, Data set, available at: <http://daac.ornl.gov> from Oak Ridge National Laboratory Distributed Active Archive Center, Oak Ridge, Tennessee, USA, doi:10.3334/ORNLDAAAC/1174.
- Saltelli, A. (2002). Making best use of model evaluations to compute sensitivity indices. *Computer physics communications*, 145(2), 280-297.
- Saltelli, A., Ratto, M., Andres, T., Campolongo, F., Cariboni, J., Gatelli, D., ... & Tarantola, S. (2008). *Global sensitivity analysis: the primer*. John Wiley & Sons.
- Saltelli, A., Annoni, P., Azzini, I., Campolongo, F., Ratto, M., & Tarantola, S. (2010). Variance based sensitivity analysis of model output. Design and estimator for the total sensitivity index. *Computer Physics Communications*, 181(2), 259-270.
- Samanta, A., Ganguly, S., Hashimoto, H., Devadiga, S., Vermote, E., Knyazikhin, Y., ... & Myneni, R. B. (2010). Amazon forests did not green-up during the 2005 drought. *Geophysical research letters*, 37(5).
- Samanta, A., Ganguly, S., Vermote, E., Nemani, R. R., & Myneni, R. B. (2012). Why is remote sensing of amazon forest greenness so challenging?. *Earth Interactions*, 16(7), 1-14.
- Sampaio, G., Nobre, C., Costa, M. H., Satyamurty, P., Soares-Filho, B. S., & Cardoso, M. (2007). Regional climate change over eastern Amazonia caused by pasture and soybean cropland expansion. *Geophysical Research Letters*, 34(17).
- Sassen, K., & Wang, Z. (2008). Classifying clouds around the globe with the CloudSat radar: 1-year of results. *Geophysical research letters*, 35(4).
- Scaramuzza, P. L., Bouchard, M. A., & Dwyer, J. L. (2011). Development of the Landsat data continuity mission cloud-cover assessment algorithms. *IEEE Transactions on Geoscience and Remote Sensing*, 50(4), 1140-1154.

- Sellers, P. J., Mintz, Y. C. S. Y., Sud, Y. E. A., & Dalcher, A. (1986). A simple biosphere model (SiB) for use within general circulation models. *Journal of the Atmospheric Sciences*, 43(6), 505-531.
- Senay, G. B., Bohms, S., Singh, R. K., Gowda, P. H., Velpuri, N. M., Alemu, H., & Verdin, J. P. (2013). Operational Evapotranspiration Mapping Using Remote Sensing and Weather Datasets: A New Parameterization for the SSEB Approach. *Journal of the American Water Resources Association*, 49(3), 577-591.
- Senna, M. C., Costa, M. H., & Shimabukuro, Y. E. (2005). Fraction of photosynthetically active radiation absorbed by Amazon tropical forest: A comparison of field measurements, modeling, and remote sensing. *Journal of Geophysical Research: Biogeosciences*, 110(G1).
- Silver, W. L., Neff, J., McGroddy, M., Veldkamp, E., Keller, M., & Cosme, R. (2000). Effects of soil texture on belowground carbon and nutrient storage in a lowland Amazonian forest ecosystem. *Ecosystems*, 3(2), 193-209.
- Simard, M., Pinto, N., Fisher, J. B., & Baccini, A. (2011). Mapping forest canopy height globally with spaceborne lidar. *Journal of Geophysical Research: Biogeosciences*, 116(G4).
- Skokovic, D. (2017). Calibration and Validation of Thermal Infrared Remote Sensing Sensors and Land/Sea Surface Temperature algorithms over the Iberian Peninsula.
- Snyder, W. C., Wan, Z., Zhang, Y., & Feng, Y. Z. (1998). Classification-based emissivity for land surface temperature measurement from space. *International Journal of Remote Sensing*, 19(14), 2753-2774.
- Sobol', I. Y. M. (1967). On the distribution of points in a cube and the approximate evaluation of integrals. *Zhurnal Vychislitel'noi Matematiki i Matematicheskoi Fiziki*, 7(4), 784-802.
- Sobol', I. Y. M. (1990). On sensitivity estimation for nonlinear mathematical models. *Matematicheskoe modelirovanie*, 2(1), 112-118.
- Sobol, I. M. (2001). Global sensitivity indices for nonlinear mathematical models and their Monte Carlo estimates. *Mathematics and Computers in Simulation*, 55(1-3):271-280, doi:10.1016/S0378-4754(00)00270-6.
- Sobrino, J. A., Li, Z. L., Stoll, M. P., & Becker, F. (1996). Multi-channel and multi-angle algorithms for estimating sea and land surface temperature with ATSR data. *International Journal of Remote Sensing*, 17(11), 2089-2114.
- Sobrino, J. A., & Cuenca, J. (1999). Angular variation of thermal infrared emissivity for some natural surfaces from experimental measurements. *Applied optics*, 38(18), 3931-3936.

- Sobrino, J. A., & Raissouni, N. (2000). Toward remote sensing methods for land cover dynamic monitoring: Application to Morocco. *International journal of remote sensing*, 21(2), 353-366.
- Sobrino, J. A., Jiménez-Muñoz, J. C., Sòria, G., Romaguera, M., Guanter, L., Moreno, J., ... & Martínez, P. (2008). Land surface emissivity retrieval from different VNIR and TIR sensors. *IEEE Transactions on Geoscience and Remote Sensing*, 46(2), 316-327.
- Song, X., Bryan, B. A., Paul, K. I., & Zhao, G. (2012). Variance-based sensitivity analysis of a forest growth model. *Ecological Modelling*, 247, 135-143.
- Souza Filho, J. D. D. C., Ribeiro, A., Costa, M. H., & Cohen, J. C. P. (2005). Control mechanisms of the seasonal variation of transpiration in a northeast Amazonian tropical rainforest. *Acta Amazonica*, 35(2), 223-229.
- Stephens, G., Winker, D., Pelon, J., Trepte, C., Vane, D., Yuhas, C., ... & Lebsock, M. (2018). CloudSat and CALIPSO within the A-Train: Ten years of actively observing the Earth system. *Bulletin of the American Meteorological Society*, 99(3), 569-581.
- Stoy, P. C., Mauder, M., Foken, T., Marcolla, B., Boegh, E., Ibrom, A., ... & Cescatti, A. (2013). A data-driven analysis of energy balance closure across FLUXNET research sites: The role of landscape scale heterogeneity. *Agricultural and forest meteorology*, 171, 137-152.
- Su, Z. (2002). The Surface Energy Balance System (SEBS) for estimation of turbulent heat fluxes. *Hydrology and earth system sciences*, 6(1), 85-100.
- Sun, Z., Wang, Q., Matsushita, B., Fukushima, T., Ouyang, Z., & Watanabe, M. (2009). Development of a Simple Remote Sensing EvapoTranspiration model (Sim-ReSET): Algorithm and model test. *Journal of Hydrology*, 376(3-4), 476-485.
- Sun, L., Wei, J., Wang, J., Mi, X., Guo, Y., Lv, Y., ... & Tian, X. (2016). A universal dynamic threshold cloud detection algorithm (UDTCDA) supported by a prior surface reflectance database. *Journal of Geophysical Research: Atmospheres*, 121(12), 7172-7196.
- Talsma, C. J., Good, S. P., Jimenez, C., Martens, B., Fisher, J. B., Miralles, D. G., ... & Purdy, A. J. (2018). Partitioning of evapotranspiration in remote sensing-based models. *Agricultural and forest meteorology*, 260, 131-143.
- Taiz, L., Zeiger, E., Møller, I. M., & Murphy, A. (2015). Plant physiology and development. *Sunderland, MA: Sinauer Associates*.
- Tang, R., Li, Z. L., & Tang, B. (2010). An application of the Ts–VI triangle method with enhanced edges determination for evapotranspiration estimation from MODIS data in arid and semi-arid regions: Implementation and validation. *Remote Sensing of Environment*, 114(3), 540-551.
- Taylor, K. E. (2001). Summarizing multiple aspects of model performance in a single diagram. *Journal of Geophysical Research: Atmospheres*, 106(D7), 7183-7192.

Ter Steege, H., Pitman, N. C., Sabatier, D., Baraloto, C., Salomão, R. P., Guevara, J. E., ... & Monteagudo, A. (2013). Hyperdominance in the Amazonian tree flora. *Science*, 342(6156), 1243092.

Tian, B., Azimi-Sadjadi, M. R., Haar, T. V., & Reinke, D. (2000). Temporal updating scheme for probabilistic neural network with application to satellite cloud classification. *IEEE Transactions on Neural networks*, 11(4), 903-920.

Timmermans, J., Su, Z., van der Tol, C., Verhoef, A., & Verhoef, W. (2013). Quantifying the uncertainty in estimates of surface-atmosphere fluxes through joint evaluation of the SEBS and SCOPE models. *Hydrology Earth System Sciences*, 17, 1561-1573

Tonooka, H. (2005). Accurate atmospheric correction of ASTER thermal infrared imagery using the WVS method. *IEEE Transactions on Geoscience and Remote Sensing*, 43(12), 2778-2792.

Toomey, M., Roberts, D. A., Still, C., Goulden, M. L., & McFadden, J. P. (2011). Remotely sensed heat anomalies linked with Amazonian forest biomass declines. *Geophysical Research Letters*, 38(19).

Twine TE, Kustas WP, Norman JM et al. (2000) Correcting eddy-covariance flux underestimates over a grassland. *Agricultural and Forest Meteorology*, 103, 279–300.

Van den Hurk, B. J. J. M., & Holtslag, A. A. M. (1997). On the bulk parameterization of surface fluxes for various conditions and parameter ranges. *Boundary-Layer Meteorology*, 82(1), 119-133.

Van den Hurk, B. J., Viterbo, P., Beljaars, A. C. M., & Betts, A. K. (2000). Offline validation of the ERA40 surface scheme (p. 43). European Centre for Medium-Range Weather Forecasts.

Van der Kwast, J., Timmermans, W., Gieske, A., Su, Z., Olioso, A., Jia, L., Elbers, J., Karssenbergh, D., & de Jong, S. (2009). Evaluation of the Surface Energy Balance System (SEBS) applied to ASTER imagery with flux-measurements at the SPARC 2004 site (Barrax, Spain). *Hydrology Earth System Science*, 13, 1337-1347

Vemury, S., Stowe, L. L., & Anne, V. R. (2001). AVHRR pixel level clear-sky classification using dynamic thresholds (CLAVR-3). *Journal of Atmospheric and Oceanic Technology*, 18(2), 169-186.

Vera, C., Higgins, W., Amador, J., Ambrizzi, T., Garreaud, R., Gochis, D., ... & Nogues-Paegle, J. (2006). Toward a unified view of the American monsoon systems. *Journal of climate*, 19(20), 4977-5000.

Viterbo, P. & Beljaars, A. C. M. (1995). An improved land surface parameterization scheme in the ECMWF model and its validation, *Journal of Climate*, 8, 2716–2748.

VIIRS LST ATBD (2011), Joint Polar Satellite System (JPSS) VIIRS Land Surface Temperature Algorithm Theoretical Basis Document (ATBD) http://npp.gsfc.nasa.gov/sciencedocuments/ATBD_122011/47400051_LandSurfTemp_Rev-20110422.pdf

- Von Randow C, Manzi AO, Kruijt B et al. (2004) Comparative measurements and seasonal variations in energy and carbon exchange over forest and pasture in South West Amazonia. *Theoretical and Applied Climatology*, 78, 5–26.
- Wagner F. H., Herault B., Rossi V., Hilker T., Maeda E. E., Sanchez A., Lyapustin A. I., Galvão L. S., Wang Y. & Aragão L. E. O. C. (2017) Climate drivers of the Amazon forest greening. *PLOS One* 12, e01800932. doi; 10.1371/journal.pone.0180932
- Wan, Z., & Dozier, J. (1996). A generalized split-window algorithm for retrieving land-surface temperature from space. *IEEE Transactions on geoscience and remote sensing*, 34(4), 892-905.
- Wan, Z., & Li, Z. L. (1997). A physics-based algorithm for retrieving land-surface emissivity and temperature from EOS/MODIS data. *IEEE Transactions on Geoscience and Remote Sensing*, 35(4), 980-996
- Wan, Z. (2008). New refinements and validation of the MODIS land-surface temperature/emissivity products. *Remote sensing of Environment*, 112(1), 59-74.
- Wan, Z. & Li, Z. (2008). Radiance-based validation of the V5 MODIS land-surface temperature product. *International Journal of Remote Sensing*, 29, 5373-5395.
- Wan, Z. (2014). New refinements and validation of the collection-6 MODIS land-surface temperature/emissivity product. *Remote sensing of Environment*, 140, 36-45.
- Wan, Z., Zhang, K., Xue, X., Hong, Z., Hong, Y., & Gourley, J. J. (2015). Water balance-based actual evapotranspiration reconstruction from ground and satellite observations over the conterminous U nited S tates. *Water Resources Research*, 51(8), 6485-6499.
- Wang, K., Li, Z., & Cribb, M. (2006). Estimation of evaporative fraction from a combination of day and night land surface temperatures and NDVI: A new method to determine the Priestley–Taylor parameter. *Remote Sensing of Environment*, 102(3-4), 293-305.
- Wang, K., Wang, P., Li, Z., Cribb, M., & Sparrow, M. (2007). A simple method to estimate actual evapotranspiration from a combination of net radiation, vegetation index, and temperature. *Journal of Geophysical Research: Atmospheres*, 112(D15).
- Wang, J., & Bras, R. L. (2011). A model of evapotranspiration based on the theory of maximum entropy production. *Water Resources Research*, 47(3).
- Wang, K., & Dickinson, R. E. (2012). A review of global terrestrial evapotranspiration: Observation, modeling, climatology, and climatic variability. *Reviews of Geophysics*, 50(2).
- Werth, D., & Avissar, R. (2002). The local and global effects of Amazon deforestation. *Journal of Geophysical Research: Atmospheres*, 107(D20), LBA-55.
- Williamson, S.N., Hilk,D.S., Garnon, J.A., Kavanaugh, J.L., and Koh, S. (2013). Evaluating cloud contamination in clear-sky MODIS Terra daytime land surface temperatures using ground-based meteorology observations. *Journal of Climate*, 26(5), 1551-1600.

Wilson, K., Goldstein, A., Falge, E., Aubinet, M., Baldocchi, D., Berbigier, P., ... & Grelle, A. (2002). Energy balance closure at FLUXNET sites. *Agricultural and Forest Meteorology*, 113(1-4), 223-243.

Wilson, A., Parmentier, B. and Jetz, W. (2014). Systematic land cover bias in Collection 5 MODIS cloud mask and derived products — A global overview. *Remote Sensing of Environment*, 141, 149-154.

World Meteorological Organization (WMO) (2008), Measurement of evaporation, in WMO Guide to Meteorological Instruments and Methods of Observation, 7th ed., chap. 10, pp. I10-1–I10-10, Geneva, Switzerland. [Available at http://www.wmo.int/pages/prog/www/IMOP/publications/CIMO-Guide/CIMO_Guide-7th_Edition-2008.html.]

World Meteorological Organization (WMO) (2017), International Cloud Atlas Manual on the Observation of Clouds and Other Meteors (WMO-No.407) available at <https://cloudatlas.wmo.int//definition-of-a-cloud.html>

Wu, W. S., Purser, R. J., & Parrish, D. F. (2002). Three-dimensional variational analysis with spatially inhomogeneous covariances. *Monthly Weather Review*, 130(12), 2905-2916.

Yang, Y., Di Girolamo, L., & Mazzoni, D. (2007). Selection of the automated thresholding algorithm for the Multi-angle Imaging SpectroRadiometer Radiometric Camera-by-Camera Cloud Mask over land. *Remote Sensing of Environment*, 107(1-2), 159-171.

Yang, Y., Long, D., & Shang, S. (2013). Remote estimation of terrestrial evapotranspiration without using meteorological data. *Geophysical Research Letters*, 40(12), 3026-3030. <https://doi.org/10.1002/grl.50450>

Yao, Y., Liang, S., Li, X., Chen, J., Liu, S., & Jia, K. et al. (2017). Improving global terrestrial evapotranspiration estimation using support vector machine by integrating three process-based algorithms. *Agricultural And Forest Meteorology*, 242, 55-74. doi: 10.1016/j.agrformet.2017.04.011

Yu, Y., Privette, J. L., & Pinheiro, A. C. (2005). Analysis of the NPOESS VIIRS land surface temperature algorithm using MODIS data. *IEEE Transactions on Geoscience and Remote Sensing*, 43(10), 2340-2350.

Yuan, W., Liu, S., Yu, G., Bonnefond, J. M., Chen, J., Davis, K., ... & Suyker, A. E. (2010). Global estimates of evapotranspiration and gross primary production based on MODIS and global meteorology data. *Remote Sensing of Environment*, 114(7), 1416-1431.

Zadrozny, B., & Elkan, C. (2001, June). Obtaining calibrated probability estimates from decision trees and naive Bayesian classifiers. In *Icml* (Vol. 1, pp. 609-616).

Zadrozny, B., & Elkan, C. (2002, July). Transforming classifier scores into accurate multiclass probability estimates. In *Proceedings of the eighth ACM SIGKDD international conference on Knowledge discovery and data mining* (pp. 694-699). ACM.

Zemp, D. C., Schleussner, C. F., Barbosa, H. M. J., Van der Ent, R. J., Donges, J. F., Heinke, J., ... & Rammig, A. (2014). On the importance of cascading moisture recycling in South America. *Atmospheric Chemistry and Physics*, *14*(23), 13337-13359.

Zeng, Z., Piao, S., Lin, X., Yin, G., Peng, S., Ciais, P., & Myneni, R. B. (2012). Global evapotranspiration over the past three decades: estimation based on the water balance equation combined with empirical models. *Environmental Research Letters*, *7*(1), 014026.

Zhai, H., Zhang, H., Zhang, L., & Li, P. (2018). Cloud/shadow detection based on spectral indices for multi/hyperspectral optical remote sensing imagery. *ISPRS journal of photogrammetry and remote sensing*, *144*, 235-253.

Zhang, K., Kimball, J. S., Mu, Q., Jones, L. A., Goetz, S. J., & Running, S. W. (2009). Satellite based analysis of northern ET trends and associated changes in the regional water balance from 1983 to 2005. *Journal of Hydrology*, *379*(1-2), 92-110.

Zhang, X., Jia, X., Yang, J., & Hu, L. (2010). Evaluation of MOST functions and roughness length parameterization on sensible heat flux measured by large aperture scintillometer over a corn field. *Agricultural and forest meteorology*, *150*(9), 1182-1191.

Zhang, K., Kimball, J. S., Nemani, R. R., Running, S. W., Hong, Y., Gourley, J. J., & Yu, Z. (2015). Vegetation greening and climate change promote multidecadal rises of global land evapotranspiration. *Scientific reports*, *5*, 15956.

Zhang, K., Kimball, J. S., & Running, S. W. (2016). A review of remote sensing based actual evapotranspiration estimation. *Wiley Interdisciplinary Reviews: Water*, *3*(6), 834-853.

Zhang, K., Ma, J., Zhu, G., Ma, T., Han, T., & Feng, L. L. (2017). Parameter sensitivity analysis and optimization for a satellite-based evapotranspiration model across multiple sites using Moderate Resolution Imaging Spectroradiometer and flux data. *Journal of Geophysical Research: Atmospheres*, *122*(1), 230-245.

Zhu, Z., & Woodcock, C. E. (2012). Object-based cloud and cloud shadow detection in Landsat imagery. *Remote sensing of environment*, *118*, 83-94.

Zhu, Z., & Woodcock, C. E. (2014). Automated cloud, cloud shadow, and snow detection in multitemporal Landsat data: An algorithm designed specifically for monitoring land cover change. *Remote Sensing of Environment*, *152*, 217-234.

